

Molecular Dynamics Modelling of Barium Silicate and Barium Fluorozirconate Glasses

A thesis presented

by

Maha Rai

to

The School of Physical Science

in partial fulfilment of the requirements for the degree of Doctor of
Philosophy in the subject of

Physics

University of Kent
Canterbury
Kent, UK
CT2 7NZ

December 2017

University of
Kent

This thesis is dedicated to my wonderful parents Sumanchandra Rai and Purnalachhi Rai.

And in memory of my grandfather Nirpati Rai and
grandmother Shubhawati Rai.

Abstract

Advancement in science and technology has profoundly depended on new types of glass innovation. The glasses that were studied in this project are binary barium silicate glasses, binary barium fluorozirconate glasses, *ZBLAN* glasses and Eu^{3+} doped *ZBLAN* glass (the *ZBLAN* glasses are based on binary barium fluorozirconate glass). The high atomic number of barium in the barium silicate glasses provides high mass and high electron density providing its applications for heat and X-ray shielding. The phenomena such as phase separation in the barium silicate glass will affect its properties of durability and electrical conductivity. On the other hand, *ZBLAN* glasses have a broad infrared optical transmission window due to the weaker bonding/interaction of F^- ions. Due to the presence of lanthanum in the composition *ZBLAN* glass can be easily doped with rare-earth ions such as Eu^{3+} giving it many optical applications such as optical amplifier and fibre lasers.

Hence, it's essential to study the structure of these glasses to understand their properties for applications. This thesis used the classical molecular dynamics modelling technique to study the static atomic structure of glass. Generally, fluoride glasses can be formed by totally replacing oxygen atoms in oxide glasses by fluorine atoms. The oxide silicate glasses are common glasses that follow the Zachariasen rules of glass formation but the fluorozirconate glasses do not and lack fixed structural units.

The structure analysis was performed at short-range order (e.g. coordination number, bond length and bond angle), medium-range order (e.g. network connectivity) and long-range order (e.g. phase separation). The related crystals were also simulated in similar conditions to the glasses to compare their atomic structure. Normally at short-range order glass structure is similar to its related crystal but the differences between them starts from the position and number of next nearest neighbours and increases thereafter. Additionally, the

new methods such as rotational invariants and grid analysis were used to scrutinise structural units and phase separation respectively.

The model of barium silicate glass shows good agreement with experimental diffraction data. The typical bond length and coordination number for *Ba* were 2.97 Å and approximately 7 respectively. The model did not show any phase separation at low *Ba* content and hence for further investigation very large models of alkaline earth silicate glasses were studied to see how *Ba*, *Ca* and *Mg* are distributed in the glass. The grid analysis was used to see the distributions which show homogeneity for *Ba* and *Ca* and inhomogeneity for *Mg* cation.

The structural units of fluorozirconate glasses were carefully studied as they do not follow the Zachriassen glass model. The coordination number for *Zr* was mixture of 7 and 8. The rotational invariant analysis shows that the structural units of ZrF_n polyhedra for coordination number 7 and 8 were similar to Augmented Triangular Prism and Biaugmented Triangular Prism respectively. However, rotational invariant values for BaF_n polyhedra tend more towards random.

The large complex model of Eu^{3+} doped *ZBLAN* glass was made as it is studied for optical applications. The initial analysis was to observe whether *Zr* and *Ba* has similar structural roles as in binary fluorozirconate glass system which they do. Considering the extra elements in *ZBLAN* glass, *Al* behaves like a network former and has octahedra structural units whereas *La* and *Na* behave like modifiers. In the glass *Eu* was uniformly distributed with predominantly coordination number of 8 and does not have well defined structural units.

Acknowledgements

My sincere gratitude to Dr Gavin Mountjoy who initially accepted me as one of his PhD students. He has been a great teacher, imparting his expert knowledge in the project that I have undertaken. He has always been there to answer any questions that I have thrown at him and he has gone beyond the call of his duty. His encouragement and patience is truly commendable. I will always be grateful for his support and valuable guidance during challenging situations that arose while undertaking my PhD.

I am also very grateful to Dr Tim Kinnear from the School of Physical Science who has not only become a good friend but assisted me to understand and write new computational code that I have used in this project. I would also like to thank Professor Paul Strange for access to Mathematica library of polyhedra.

My deepest gratitude to my parents Sumanchandra Rai and Purnalachhi Rai without whom this PhD would not have been possible. I am grateful to my siblings Mandika Rai, Yadav Rai and Roshan Rai for their love and support. It would be incomplete if I do not mention my fiancé Kalpana Rai who has believed in me, supported me and encouraged me to complete my thesis.

I would like to thank all my Nepalese relatives and friends that are in the UK, Nepal and around the world who have had good words and good wishes towards me. Finally, I would like to extend my thanks to Kirat Rai Yayokkha (KRY) UK and Folkestone Gurkha (Nepalese) Community (FNC) UK, the community organisation with whom I was voluntarily involved.

Contents

Title page.....	i
Dedication	ii
Abstract	iii
Acknowledgements	v
1. Introduction	1
1.1 Glasses.....	1
1.1.1 Crystalline and non-crystalline solids.....	2
1.1.2 The glass transition	3
1.1.3 Applications of glasses.....	3
1.2 Barium silicate and barium fluorozirconate glasses.....	4
1.2.1 Barium silicate $BaO - SiO_2$ glasses and alkaline earth silicate glasses.....	4
1.2.2 Barium fluorozirconate $ZrF_2 - BaF_2$ glasses.....	5
1.2.3 ZBLAN glasses	6
1.3 Describing the structures of glasses	7
1.3.1 Zachariasen rules for glasses	7
1.3.2 Modified random network model	8
1.3.3 Random closed packed model	9
1.3.4 Modelling of glass structures	11
1.4 References	13
2. Modelling method	18
2.1 Interatomic potential	18
2.1.1 Empirical force field	20
2.1.2 Two body potential	21
2.1.3 Coulomb interaction and short-range interaction	22
2.1.4 Principle of energy minimisation	24
2.2 Use of GULP to test potential	26
2.2.1 Input files for GULP	27
2.2.2 Control parameters for GULP	28
2.2.3 Initial structural parameters.....	28
2.2.4 Potential parameters.....	28
2.2.5 Output files from GULP	29
2.3 Theory and algorithms of molecular dynamics	29
2.3.1 Equations of motion.....	30
2.3.2 Thermal equilibrium	32

2.3.3 Berendsen thermostat.....	34
2.3.4 Boundary conditions.....	35
2.3.5 Force calculation.....	36
2.4 Use of DL_POLY for molecular dynamics modelling.....	41
2.4.1 Control parameters for DL_POLY_2.....	41
2.4.2 Field files for DL_POLY_2.....	41
2.4.3 Output from DL_POLY_2.....	42
2.5 Molecular dynamics modelling of glasses.....	42
2.5.1 Initial configuration.....	43
2.5.2 Temperature stages.....	43
2.5.3 Quenching.....	44
2.5.4 Sampling.....	44
2.6 Analysing structures of MD models of glasses.....	45
2.6.1 Pair distribution function.....	45
2.6.2 Nearest neighbour distances and coordination numbers.....	49
2.6.3 Bond angle distribution functions.....	50
2.6.4 Network connectivity.....	50
2.6.5 X-ray and neutron diffraction structure factors.....	52
2.7 References.....	59
3. The method of rotational invariants.....	63
3.1 Introduction.....	63
3.2 Calculation of rotational invariants.....	64
3.3 Reference polyhedra.....	68
3.4 Nearest neighbour distances, bond angle distributions and coordination numbers for reference polyhedra.....	73
3.5 Rotational invariants values of reference polyhedra.....	75
3.6 Conclusions.....	82
3.7 References.....	82
4. Molecular dynamics modelling of barium silicate BaO – SiO₂ glasses.....	84
4.1 Introduction.....	84
4.2 Method.....	86
4.2.1 Structure of barium silicate crystals.....	86
4.2.2 Potentials for barium silicate systems.....	90
4.2.3 Testing of potentials.....	91
4.2.4 Initial configurations for barium silicate glasses.....	95
4.2.5 Parameters for MD modelling of barium silicate glasses.....	96
4.3 Results.....	96

4.3.1 Pair distribution function, nearest neighbour distances and coordination numbers	97
4.3.2 Bond angle distribution functions.....	100
4.3.3 Network connectivity.....	102
4.3.4 Neutron and X-ray diffraction structure factors	104
4.3.5 Rotational invariants for <i>Si</i> and <i>Ba</i> in <i>BaO – SiO₂</i> binary glasses	106
4.4 Discussion	108
4.5 Conclusions	113
4.6 References	113
5. Modifier cation distribution in large models of alkaline earth silicate glasses.....	116
5.1 Introduction	116
5.2 Method	119
5.2.2 Interatomic potentials for <i>MO – SiO₂</i> systems with <i>M = Mg, Ca</i> and <i>Ba</i> ..	119
5.2.2 Initial configurations for <i>MO – SiO₂</i> glasses with <i>M = Mg, Ca</i> and <i>Ba</i>	120
5.2.3 Parameters for MD modelling of <i>MO – SiO₂</i> glasses with <i>M = Mg, Ca</i> and <i>Ba</i>	120
5.2.4 Sphere grid and cubic grid sampling of cation distributions.....	121
5.2.5 Theory of Poisson and binomial distributions.....	122
5.3 Results	123
5.3.1 Modifier cation distribution in initial configurations	123
5.3.2 Modifier cation distribution in <i>50MO – 50SiO₂</i> glasses with <i>M = Mg, Ca</i> and <i>Ba</i>	125
5.3.3 Modifier cation distribution in <i>25MO – 75SiO₂</i> glasses with <i>M = Mg, Ca</i> and <i>Ba</i>	127
5.4 Discussion	129
5.5 Conclusions	133
5.6 References	134
6. Molecular dynamics modelling of barium zirconium fluoride <i>ZrF₄ – BaF₂</i> glasses	136
6.1 Introduction	136
6.2 Method	142
6.2.1 Structure of barium fluorozirconate crystals.....	142
6.2.2 Potentials for barium fluorozirconate systems	146
6.2.3 Testing of potentials.....	146
6.2.4 Initial configurations for barium fluorozirconate glasses	150
6.2.5 Parameters for MD modelling of barium fluorozirconate glasses.....	150
6.3 Results	151

6.3.1 Pair distribution function, nearest neighbour distances and coordination numbers	152
6.3.2 Bond angle distribution functions.....	155
6.3.3 Network connectivity.....	158
6.3.4 Neutron and X-ray diffraction structure factors	160
6.3.5 Rotational invariants for <i>Zr</i> and <i>Ba</i> in <i>ZrF₄ – BaF₂</i> binary glasses	162
6.4 Discussion	167
6.5 Conclusions	173
6.6 References	174
7. Molecular dynamics modelling of <i>Eu³⁺</i> doped <i>ZBLAN</i> glasses.....	177
7.1 Introduction	177
7.2 Method	179
7.2.1 Structure of multicomponent fluorozirconate crystals.....	179
7.2.2 Potentials for <i>ZBLAN</i> systems including <i>Eu³⁺</i>	184
7.2.3 Testing of potentials.....	184
7.2.4 Initial configurations for <i>Eu³⁺</i> doped <i>ZBLAN</i> glasses.....	189
7.2.5 Parameters for MD modelling of <i>Eu³⁺</i> doped <i>ZBLAN</i> glasses	190
7.3 Results	191
7.3.1 Pair distribution functions, nearest neighbour distances and coordination numbers	195
7.3.2 Bond angle distribution functions.....	203
7.3.3 Network connectivity.....	204
7.3.4 X-ray diffraction structure factor for <i>ZBLA</i> and <i>ZBLAN</i> glasses	206
7.3.5 Rotational invariants for <i>Zr</i> , <i>Ba</i> , <i>La</i> , <i>Al</i> , <i>Na</i> and <i>Eu</i> cations in <i>ZBLAN</i> and <i>Eu³⁺</i> doped <i>ZBLAN</i> glasses	208
7.4 Discussion	217
7.5 Conclusions	226
7.5 References	228
8. Conclusions	231
8.1 References	234

Chapter 1

Introduction

1.1 Glasses

Glasses often go unnoticed, but they are an essential part of our everyday life. Glasses are all around us and their use and production are carried out on an industrial scale. Centuries ago, humans discovered these special materials that have formed naturally by certain thermodynamics conditions [1]. Since then humans have been producing glasses for thousands of years by melting and cooling (quenching) appropriate raw materials [2]. For centuries, no other man-made materials have shown these special qualities that are transparent, chemically inert, environmentally friendly (recycling) and strong [3].

Science has profoundly depended on glass instruments. Developments of new types of glasses has helped to accelerate the remarkable acquisition of knowledge about the natural and physical worlds by enabling the development new scientific instruments [4]. Its's also an indispensable and essential component in the field of optics, photonics and electronic technology [5]. Hence, it's a fascinating material both scientifically and technologically.

In principle, many kinds of material, inorganic, organic, or metallic, can form a glass by many techniques such melt-quenching, vapor deposition, sol-gel processing of solutions, and neutron irradiation of crystalline materials [2]. Multicomponent materials can also form a glass resulting in huge variety of glass types, families, or groups, which properties depend on the varieties of materials compositions, thus making glasses very universal engineering materials [6].

Therefore, to study the structure of such noble materials is essential. The materials under study are inorganic glasses that can be made traditionally by the method of melt-quenching.

1.1.1 Crystalline and non-crystalline solids

Most inorganic elements and compounds melt to form liquids and when this liquid is cooled either crystallization may take place at the melting point temperature, T_m , or it will become a ‘supercooled liquid’, i.e. more viscous with decreasing temperatures and may eventually form a glass [7]. Thus, glasses have numerous properties common with crystalline solids, such as hardness and elasticity of shape [8]. Generally, glasses are defined as amorphous materials or non-crystalline materials that lack the long-range periodic atomic arrangements whereas crystal can be defined by both short-range and long-range order of periodic atomic arrangements. The inter-relationship between crystal and glass, i.e. non-crystalline solid that has liquid-like structure, can be explained using the volume-temperature diagram shown in Figure 1.1 [9] for a glass-forming substance.

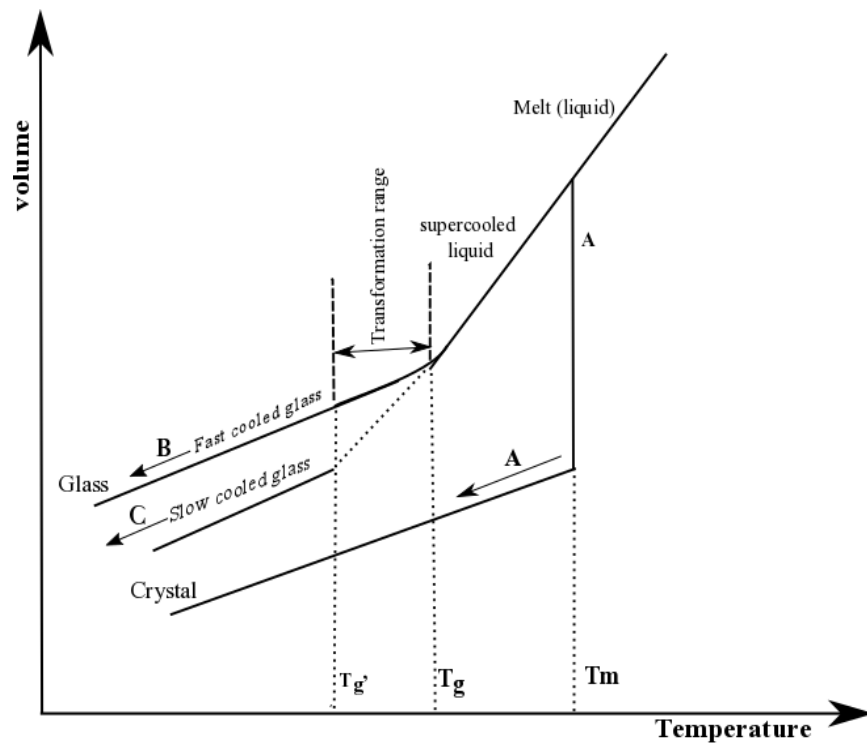


Figure 1.1 Schematic illustration of the volume-temperature diagram for a glass forming liquid [9]. Crystallization is shown by the path **A** and the glass formations are shown by path **B** and **C**.

1.1.2 The glass transition

The path **A** in Figure 1.1 shows the crystallization process as the volume of liquid decreases slowly until it reaches melting point i.e. T_m and the volume changes abruptly as liquid is transformed into a crystalline solid. But if the change in the volume below T_m is gradual, which is shown by the path **B** and **C** in Figure 1.1 then a ‘supercooled liquid’ is formed until it reaches the glass transition temperature, T_g , and below this point it loses its liquid properties and form a solid glass. Hence, the glass transition is the phenomenon when many liquids are cooled below their melting temperatures, T_m , and solidify into an amorphous solid [10]. This region where such changes occur (the transformation region shown in Figure 1.1) can be defined by the glass transition temperature, T_g . Similar characteristics shown by the volume-temperature relation can also be exhibited by other thermodynamic variables such as entropy and energy [11]. Faster cooling leads to a greater T_g and a less dense glass [12] illustrated by the path **B** in Figure 1.1. Also, the T_g depends upon the cooling rate and the typical cooling rate in laboratory experiments are between 0.1 – 100 Kelvin per minute [13].

1.1.3 Applications of glasses

Glasses are isotropic materials, i.e. if the glass is free from stress and strain, its macroscopic properties like optical transmission and absorption, refraction of light, and thermal expansion, are observed equally in all directions [14]. Furthermore, if electrical neutrality is maintained over the whole structure glass has a flexibility of chemical composition [15]. Because of these unique structural and thermodynamic properties of glass the material has an advantage over the application of crystalline materials in certain applications.

Almost all the commercially important glasses are based on silica, SiO_2 , such as flat glasses, technical specialty glasses, and optical and fiber glasses. The flat glasses are manufactured mostly for glazing and containers which are still mainly based on sodium calcium silicates as they are cheap ingredients, and can easily be melted [16].

Phosphate glasses that are not based on silica are used as hosts for lasers [17] and borate glasses for luminescence [18]. Other non-silica-based oxide glasses that are commercially important are boro-aluminates that have high electrical resistivity exceeding that of silica, and alkaline earth aluminates used as a high-temperature sealant and IR-transmitting glass [19].

1.2 Barium silicate and barium fluorozirconate glasses

These glasses can be considering as barium containing inorganic binary glasses. The project is effectively based on studying the structure of these glasses by classical molecular dynamic technique. Since the silicate based glasses are the most common kind and heavily studied it can be an initial base to understand the structure of such glasses. One of the interests to study heavy metal fluoride glasses (HMG) mainly based on binary 'ZB' system, i.e. barium zirconium fluoride glass, $ZrF_4 - BaF_2$, is that it does not follow the common Zachariasen criteria of glass formation.

1.2.1 Barium silicate $BaO - SiO_2$ glasses and alkaline earth silicate glasses

Barium silicate glasses, $BaO - SiO_2$, are members of the alkaline earth silicate glass family $xMO - (100 - x)SiO_2$ (i.e. $M = Mg, Ca, Ba$). Barium is less common than the lighter alkaline earths Mg and Ca in naturally occurring silicate systems. The higher atomic number of barium provides high mass for thermal resistance, and high electron density for radiation resistance. This makes barium silicate compounds of interest for applications of

heat shielding (e.g. in fuel cell seals [20]), and X-ray shielding (e.g. in nuclear engineering [21]).

The sequence of increasing alkaline earth size, i.e. $M = Mg, Ca$ and Ba , can be expected to influence properties of alkaline earth silicates. The phase diagrams [22] show a shift in the regions of low melting temperature, T_m , indicative of glass forming, from $x = 50 - 55$ for Mg ($T_m \sim 1560^\circ C$), to $x = 40 - 60$ for Ca ($T_m \sim 1450^\circ C$), to $x = 25 - 40$ for Ba ($T_m \sim 1650^\circ C$). There is liquid-liquid phase [23] at low MO content for Mg ($x < 33.4$), Ca ($x < 27.4$) and Ba ($x < 19.5$). For the $BaO - SiO_2$ system there is sub-liquidus phase separation for $x < 30$ [24] which borders on the glass forming region. Hence $BaO - SiO_2$ glasses with $x < 30$ have been studied for phase separation, nucleation, and crystallisation, particularly by Zanotto et al [25].

In alkaline earth silicate systems, the tendency towards phase separation increases with a decrease in the basicity (capability to give electrons) of the modifier cation (i.e. $Ba < Ca < Mg$) [23]. The viscosity of a phase separated glasses is usually greater than that of a homogeneous glass of the same compositions. The phase separated glasses usually provide different chemical durability and the electrical conductivity properties [16].

1.2.2 Barium fluorozirconate $ZrF_4 - BaF_2$ glasses

Fluoride glasses based on the fluorozirconate system were first reported in 1975 [26]. This is an uncommon glass as it does not follow the Zachariasen rules, which is a generally admitted as a criterion for glass formation [27]. However, researchers were attracted to fluoride glasses based on $ZrF_4 - BaF_2$ because of their high potential ability for mid infrared optical application [28] and interesting electrical properties due to the F^- ion mobility [29].

The binary glass system $ZrF_4 - BaF_2$ has the widest glass forming region and only this system gives glasses in comparatively large size compared to the other binary fluorozirconate glasses system [24] $MF_2 - ZrF_4$ where $M = Ca, Sr, Ba,$ and Pb . Hence, the best of fluorozirconate glass-forming compositions are based on the binary glass system $ZrF_4 - BaF_2$ [30], such as well-known multicomponent fluorozirconate ‘*ZBLAN*’ glasses, containing $ZrF_4, BaF_2, LaF_3, AlF_3$ and NaF [31]. These multicomponent fluorozirconate glasses and other ternary glasses consist of more than 70% to 90% of ZrF_4 and BaF_2 [32]. Therefore, the binary barium fluorozirconate can be considered as prototype for fluorozirconate glasses [33].

Unlike the well-known classical tetrahedral network of silicate glasses system, the nature of the fluoride ion arrangement around zirconium is not known with certainty [34]. The major problem is due to the lack of fixed structural units and the average coordination number of fluorine about zirconium is not integer [35], making it a puzzling glass system.

1.2.3 *ZBLAN* glasses

Since the discovery of heavy metal fluoride glasses in 1975, these glasses specially based on ZrF_4 were heavily studied because of their broad infrared optical transmission window [36]. Among the fluoride glasses the *ZBLAN* glass composition is the most stable against devitrification [37] and it has better ability for fiber drawing [38]. *ZBLAN* fiber optics are used in a number of applications, such as optical amplifiers and fiber laser [39]. It has a low optical dispersion, low refractive index, low phonon energy, lesser thermal dependence of the optical properties, and ease of machining and polishing [40], and is a good host for doping rare-earth ions [41].

Heavy rare-earth-doped *ZBLAN* glasses are good candidates for upconversion process, which converts photons from the near infrared into the visible [42]. It has many prac-

tical applications in solid-state lasers [43], photonics [44], white light generation by simultaneous red, blue and green emissions [45] and medical applications (e.g. surgical knife) [46].

1.3 Describing the structure of glasses

The knowledge of atomic-scale structure is essential to understand the physical and chemical properties of materials that form glasses. Structural theories and kinetic theory are the two types of theories that generally try to explain the glass forming materials. Here we concentrate only on the structural theory proposed by Zachariasen, which was mainly developed in the oxide glass systems. Zachariasen rules for glass formation are the most commonly used for formulating models for glass structures. The glass forming cations can be classified into network formers, network modifiers and intermediates which may either reinforce the network (e.g. coordination number 4) or loosen the network (e.g. coordination number 6 – 8) [5]. The network former and network modifier cations will be sequentially described below.

1.3.1 Zachariasen rules for glasses

The interatomic forces in crystal and non-crystalline materials can be considered to be similar, which indicates that they have a similar atomic structure in certain regards [7]. Zachariasen realized that the structural differences in oxide glass and crystal is due to the distorted network of glass at long-range, which is due to the variation in bond length, bond angles and torsion angle [2]. Figure 1.2 is the schematic illustration in two-dimensions for a pure glass-forming oxide to describe the structure of conventional oxide glasses by the random network theory which was first introduced by Zachariasen [47]. The following set of criteria for glass formation were proposed by Zachariasen, which are widely used as a set of rules for formulating a model for glass structures.

- I. Not more than two cations (network former) are linked by an oxygen
- II. The oxygen coordination number that surrounded the network forming cations should be small (three or four)
- III. The oxygen polyhedra share only corners and not edges or faces
- IV. To have a three-dimensional network then at least three corners of each oxygen polyhedron must be shared.

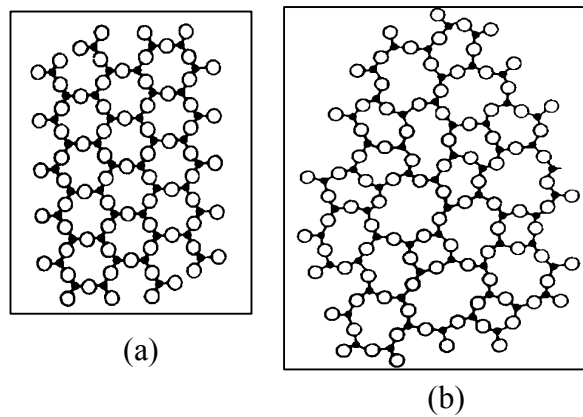


Figure 1.2 Schematic two-dimensional structural representation of hypothetical crystal A_2O_3 (a) and Zachariasen model of glassy A_2O_3 (b) [47].

1.3.2 Modified random network model

In a multicomponent oxide glass system network modifier are the cations that do not form a glass themselves but modify the network structure created by the network forming cations. It forms negatively-charged non-bridging oxygen (O_{nb}) by breaking linkage of bridging oxygen (O_b) that connects network former cations. For example, if modifier Na_2O is added to network former SiO_2 then $Si - O - Si$ linkage will break to form $Si - O^-$ termination. Also, it has been noticed that the modifier cations will adapt their local environment to have their own desired coordination polyhedron as found in associated crystalline materials, which is generally coordination number ≥ 6 [48].

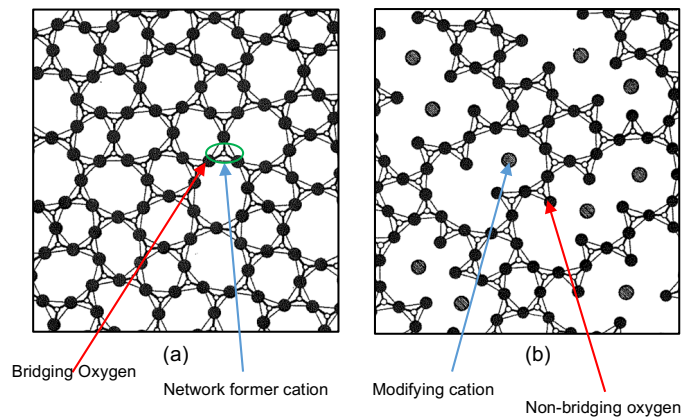


Figure 1.3 Random network (a) and Random network with network modifying cations (b) [48].

1.3.3 Random closed packed model

In metallic and ionic systems, there is not strong directional bonding so the structural description in terms of network former and network modifier may be less appropriate [7]. However, it can be described by random closed packed model (RCP) which was initiated by Bernal in 1959 [49]. The important concept in such structures are those of radius ratio, packing density and hole filling (holes large enough to admit another atom) [48]. First it was approached by an empirical method, building models with plasticine balls, ball-bearings, as well as ball-and-spoke [50].

Consider polyhedron AX_n , where A is a cation and X is an anion (i.e. usually larger than a cation). The coordination polyhedra present can be determined by the relative sizes of their constituent ions by the radius ratio r_A/r_X . For stability, the A atom should fill the cavity defined by the X atoms that give the critical radius $(r_A/r_X)_C$, at which this criterion is just fulfilled with the A atom just in contact with all the X atoms and below which the AX_n polyhedron is unstable [35]. However, above this value the AX_n polyhedron will remain stable until the point is reached where extra X atoms can be added [48]. The common coordination polyhedra critical radius $(r_A/r_X)_C$ are given in Table 1.1 [35, 51].

In general, small radius ratios (for e.g. $n = 3$ or 4) tend to result in well-defined structural units whereas larger radius ratios i.e. large values of n allow a greater latitude for distortion and often lead to the existence of more than one type of polyhedra [35]. The random close packing model can also be characterized by the distribution of void polyhedra [49] and the types of hole in a random close packing can be classified into one of five types of polyhedra and these polyhedra holes are illustrated in Figure 1.4 [7, 35]. These Bernal holes represent convex deltahedra in which every face is an equilateral triangle [35].

Table 1.1 Critical radius for some of the common coordination polyhedra [35, 51].

Polyhedron (Geometrical structures)	n	$(r_A/r_X)_c$
Triangle	3	0.155
Tetrahedron	4	0.225
Octahedron	6	0.414
Trigonal Prism	6	0.528
Archimedean Antiprism	8	0.645
Cube	8	0.732
Icosahedron	12	0.902

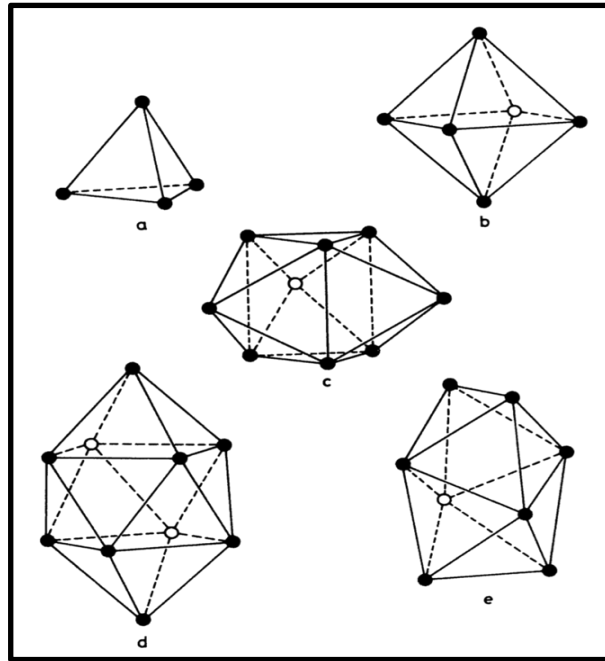


Figure 1.4 The five canonical holes of a random closed packing [7, 35] (a) Tetrahedron; (b) Octahedron; (c) Trigonal Prism; (d) Archimedean Anti Prism and (e) Snub Disphenoid.

1.3.4 Modelling of glass structures

The experimental results from a non-crystalline system are usually smooth and rather featureless due to its isotropic nature and the most commonly measured quantities are averaged over macroscopic number of atoms, each with a unique environment [51]. Because of this reason it can only provide limited information. Also, the optimum information that can be extracted from the conventional diffraction experiment is a one-dimensional correlation function i.e. distances between atoms [52]. Experimental investigations are best at providing structural information on short range order but provides sparse information at medium range and long range.

However, the structure of non-crystalline system such as pair distribution function and structure factor can be evaluated theoretically at a given temperature and pressure by

theories which are based on interactions between particles i.e. atoms [53]. Therefore, computer simulations and modelling is a complement to experimental methods and it can disclose new insights into medium range order, surface structures, and dynamic changes in local structures [54].

Computer simulations are carried out to understand the properties of assemblies of atoms in term of the microscopic interactions between them and their structures [55]. Computer simulations require a mathematical-physical model and its solutions are obtained approximately by numerical computing and this allows the study of significantly more complex models realistically rather than by analytical means [56]. The specific input parameters, which are used in the simulations that characterize the model or the system, are derived from theoretical considerations or from experimental data [57]. These methods have become an indispensable tool for investigating and predicating physical and chemical properties of glassy materials. Hence one can also test a theory either by conducting a simulation using the same model or by performing the experiments.

The computer simulation modelling techniques applied in glassy materials are Molecular Dynamics (MD), Monte Carlo (MC), Reverse Monte Carol (RMC), and Empirical Potential Structure Refinement (EPSR).

MC modelling simulations explore the configuration space by trial moves of particles by method of metropolis algorithm and it uses the potential to describe the interaction between the particles [58]. Whereas RMC modelling technique does not require interatomic potentials but uses the available experimental data directly, and predominantly diffraction data [59]. EPSR technique is evolved from the RMC technique as it uses both a purely pairwise interaction potential and diffraction data [60].

MD modelling techniques can be classified into *ab initio* MD method and classical MD method. The basic idea in *ab initio* MD is to consider the force acting on the nuclei from electronic structure and also selecting a particular approximation for solving the Schrödinger

equation [61]. In classical molecular dynamics, the state of the particles at any time is characterized by their position and momentum and it changes in time according to the Newton equations of motion [62].

MD is the study of how molecules or atoms move, deform and interact over time. It is also about developing quantitative predictions of molecular size and shape, flexibilities, interactions with other molecules, behavior under pressure, and the relative frequency of one state or conformation compared to another. The complex nature of the force field involved and the large size of typical molecular systems mean that MD is almost always chaotic [63].

The MD simulation procedure can be performed in three steps: model the individual particles, simulate the movements of large number of the model particles and finally analyse the simulation data for the required collective phenomenon [64]. The analysis can be a static structure such as pair distribution function and rotational invariants (i.e. spherical harmonic). The latter is one way to explore the angular dependence of the correlations between atom positions.

1.4 References

- [1] D.R. Uhlmann, N.J. Kreidl, *Glass Science and Technology, Vol. 4 A: Structure, Microstructure, and Properties*, (1989).
- [2] J.E. Shelby, *Introduction to Glass Science and Technology*, Royal Society of Chemistry, 2005.
- [3] E. Le Bourhis, *Glass: Mechanics and Technology*, John Wiley & Sons, 2008.
- [4] A. Macfarlane, G. Martin, Beyond the ivory tower. A world of glass, *Science*. 305 (2004) 1407-1408.
- [5] Z. Jiang, Q. Zhang, The structure of glass: A phase equilibrium diagram approach, *Progress in Materials Science*. 61 (2014) 144-215.
- [6] W. Martienssen, H. Warlimont, *Springer Handbook of Condensed Matter and Materials Data*, Springer Science & Business Media, 2006.
- [7] S.R. Eliot, *Physics of amorphous materials*, (1990).

- [8] A. Feltz, *Amorphous Inorganic Materials and Glasses*, VCH, 1993.
- [9] H. Rawson, *Inorganic glass forming system: Nonmetallic solids*, (1967).
- [10] K. Binder, W. Kob, *Glassy Materials and Disordered Solids: An Introduction to their Statistical Mechanics*, World Scientific, 2011.
- [11] G.N. Greaves, S. Sen, *Inorganic glasses, glass-forming liquids and amorphizing solids*, *Adv. Phys.* 56 (2007) 1-166.
- [12] D.C. Boyd, P.S. Danielson, A. Thompson, M. Velez, S.T. Reis, R.K. Brow, *Glass*, *Kirk-Othmer Encyclopedia of Chemical Technology*. 12 (2004).
- [13] M.D. Ediger, C.A. Angell, S.R. Nagel, *Supercooled liquids and glasses*, *J. Phys. Chem.* 100 (1996) 13200-13212.
- [14] M. Yamane, Y. Asahara, *Glasses for Photonics*, Cambridge University Press, 2000.
- [15] L. Stoch, *Flexibility of structure and glass-forming ability: A chemical approach*, *Glass physics and chemistry*. 27 (2001) 167-174.
- [16] R.H. Doremus, *Glass Science*, 2nd ed., Wiley, 1994.
- [17] J.E. Marion, M.J. Weber, *Phosphate laser glasses*, *European Journal of Solid State and Inorganic Chemistry*. 28 (1991) 271-287.
- [18] K. Mariselvam, R.A. Kumar, *Borate Glasses for Luminescence Applications—Potential Materials for White LEDs and Laser Sources*, (2016).
- [19] A.K. Varshneya, *Fundamentals of Inorganic Glasses*, Elsevier, 2013.
- [20] C. Lara, M.J. Pascual, A. Durán, *Glass-forming ability, sinterability and thermal properties in the systems RO–BaO–SiO₂ (R = Mg, Zn)*, *J. Non Cryst. Solids*. 348 (2004) 149-155.
- [21] N. Chanthima, J. Kaewkhao, C. Kedkaew, W. Chewpraditkul, A. Pokaipist, P. Limsuwan, *Study on interaction of Bi₂O₃, PbO and BaO in silicate glass system at 662 keV for development of gamma-rays shielding materials*, *Progress in Nuclear Science and Technology*. (2011) 15-17.
- [22] Z.G. Tyurnina, S.I. Lopatin, S.M. Shugurov, V.L. Stolyarova, *Thermodynamic properties of silicate glasses and melts: 1. System BaO–SiO₂*, *Russ. J. Gen. Chem.* 76 (2006) 1522-1530.
- [23] P. Hudon, D.R. Baker, *The nature of phase separation in binary oxide melts and glasses. I. Silicate systems*, *J. Non Cryst. Solids*. 303 (2002) 299-345.
- [24] A.H. Ramsden, P.F. James, *The effects of amorphous phase separation on crystal nucleation kinetics in BaO–SiO₂ glasses*, *J. Mater. Sci.* 19 (1984) 2894-2908.
- [25] E.D. Zanutto, P.F. James, A.F. Craievich, *The effects of amorphous phase separation on crystal nucleation kinetics in BaO–SiO₂ glasses*, *J. Mater. Sci.* 21 (1986) 3050-3064.

- [26] M. Poulain, M. Poulain, J. Lucas, Verres fluores au tetrafluorure de zirconium proprietes optiques d'un verre dope au Nd^{3+} , Mater. Res. Bull. 10 (1975) 243-246.
- [27] Y. Kawamoto, Progress in Structural Study of ZrF_4 -Based Glasses, 5 (1985) 417-425.
- [28] B. Boulard, A. Le Bail, J.P. Laval, C. Jacoboni, Local Environment of Zr in Barium Fluorozirconate Glasses: The EXAFS point of view, Le Journal de Physique Colloques. 47 (1986) 794.
- [29] J. Senegas, J.M. Bobe, J.M. Reau, ^{19}F NMR comparative investigation of some ZrF_4 -based fluoride glasses and some crystalline phases in the BaF_2 - ZrF_4 system, Solid State Commun. 89 (1994) 983-988.
- [30] R.M. Almeida, M.I. Marques, M.C. Gonçalves, EXAFS study of Ba and La structural environments in fluorozirconate glasses, J. Non Cryst. Solids. 168 (1994) 144-149.
- [31] R.E. Youngman, S. Sen, A high-resolution ^{19}F NMR spectroscopic study of barium fluorozirconate glasses and related crystals, Solid State Nucl. Magn. Reson. 27 (2005) 77-89.
- [32] W. Wang, Y. Chen, T. Hu, The short-range order in ternary ZrF_4 - BaF_2 - ErF_3 glasses, J. Non Cryst. Solids. 180 (1995) 285-291.
- [33] Y. Kawamoto, T. Horisaka, K. Hirao, N. Soga, A molecular dynamics study of barium meta-fluorozirconate glass, J. Chem. Phys. 83 (1985) 2398-2404.
- [34] C.C. Phifer, D.J. Gosztola, J. Kieffer, C.A. Angell, Effects of coordination environment on the Zr-F symmetric stretching frequency of fluorozirconate glasses, crystals, and melts, J. Chem. Phys. 94 (1991) 3440-3450.
- [35] J.H. Simmons, C.J. Simmons, R. Ochoa, A.C. Wright, Fluoride Glass Structure, Academic Press, San Diego, 1991.
- [36] S. Aasland, M. Einarsrud, T. Grande, P.F. McMillan, Spectroscopic investigations of fluorozirconate glasses in the ternary systems ZrF_4 - BaF_2 - AF (A= Na, Li), J. Phys. Chem. 100 (1996) 5457-5463.
- [37] F.A. Santos, J. Delben, A. Delben, L. Andrade, S.M. Lima, Thermal stability and crystallization behavior of TiO_2 doped ZBLAN glasses, J. Non Cryst. Solids. 357 (2011) 2907-2910.
- [38] J. Adam, Fluoride glass research in France: fundamentals and applications, J. Fluorine Chem. 107 (2001) 265-270.
- [39] D.S. Tucker, E.C. Ethridge, G.A. Smith, G. Workman, Effects of gravity on ZBLAN glass crystallization, Ann. N. Y. Acad. Sci. 1027 (2004) 129-137.
- [40] X. Zhu, N. Peyghambarian, High-power ZBLAN glass fiber lasers: review and prospect, Advances in OptoElectronics. 2010 (2010).

- [41] S. Gross, D.G. Lancaster, H. Ebendorff-Heidepriem, T.M. Monro, A. Fuerbach, M.J. Withford, Femtosecond laser induced structural changes in fluorozirconate glass, *Optical Materials Express*. 3 (2013) 574-583.
- [42] U. Skrzypczak, M. Miclea, A. Stalmashonak, B. Ahrens, B. Henke, G. Seifert, J.A. Johnson, S. Schweizer, Time-resolved investigations of erbium ions in ZBLAN-based glasses and glass ceramics, *physica status solidi (c)*. 8 (2011) 2649-2652.
- [43] E. Downing, L. Hesselink, J. Ralston, R. Macfarlane, A three-color, solid-state, three-dimensional display, *Science*. 273 (1996) 1185.
- [44] A. Herrmann, D. Ehrt, Green and Red Er^{3+} Photoluminescence Behavior in Various Fluoride Glasses, *International Journal of Applied Glass Science*. 1 (2010) 341-349.
- [45] J. Méndez-Ramos, P. Acosta-Mora, J.C. Ruiz-Morales, T. Hernandez, M.E. Borges, P. Esparza, Heavy rare-earth-doped ZBLAN glasses for UV-blue up-conversion and white light generation, *J Lumin*. 143 (2013) 479-483.
- [46] T. Sumiyoshi, H. Sekita, T. Arai, S. Sato, M. Ishihara, M. Kikuchi, High-power continuous-wave 3- and 2-/spl mum/m cascade Ho/sup 3+/: ZBLAN fiber laser and its medical applications, *IEEE Journal of Selected Topics in Quantum Electronics*. 5 (1999) 936-943.
- [47] K.J. Rao, *Structural Chemistry of Glasses*, Elsevier, 2002.
- [48] C.J. Simmons, O.H. El-Bayoumi, *Experimental Techniques of Glass Science*, Amer Ceramic Society, 1993.
- [49] D. Feng, G. Jin, *Introduction to Condensed Matter Physics*, World Scientific, 2005.
- [50] R. Zallen, *The Physics of Amorphous Solids*, John Wiley & Sons, 1998.
- [51] D.A. Drabold, Topics in the theory of amorphous materials, *The European Physical Journal B*. 68 (2009) 1-21.
- [52] B. Vessal, 12 - Amorphous Solids, in: C.R.A. Catlow (Ed.), *Computer Modeling in Inorganic Crystallography*, Academic Press, London, 1997, pp. 295-332.
- [53] Y. Waseda, *The structure of non-crystalline materials: liquids and amorphous solids*, (1980).
- [54] A. Takada, A.N. Cormack, Computer simulation models of glass structure, *Physics and Chemistry of Glasses-European Journal of Glass Science and Technology Part B*. 49 (2008) 127-135.
- [55] M.P. Allen, *Introduction to molecular dynamics simulation, Computational soft matter: from synthetic polymers to proteins*. 23 (2004) 1-28.
- [56] M. Griebel, S. Knapek, G. Zumbusch, *Numerical Simulation in Molecular Dynamics: Numerics, Algorithms, Parallelization, Applications*, Springer Science & Business Media, 2007.
- [57] G. Sutmann, *Classical Molecular Dynamics*, Citeseer, 2002.

- [58] J.C. Mauro, A.K. Varshneya, Monte Carlo simulation of SexTe_{1-x} glass structure with ab initio potentials, *Phys. Rev. B.* 72 (2005) 024212.
- [59] G. Evrard, L. Pusztai, Reverse Monte Carlo modelling of the structure of disordered materials with RMC: a new implementation of the algorithm in C, *Journal of Physics: Condensed Matter.* 17 (2005) S1.
- [60] A.K. Soper, Partial structure factors from disordered materials diffraction data: An approach using empirical potential structure refinement, *Physical Review B.* 72 (2005) 104204.
- [61] D. Marx, J. Hutter, Ab initio molecular dynamics: Theory and implementation, *Modern methods and algorithms of quantum chemistry.* 1 (2000) 141.
- [62] C. Lubich, *From Quantum to Classical Molecular Dynamics: Reduced Models and Numerical Analysis*, European Mathematical Society, 2008.
- [63] C.M. Ben Leimkuhler, *Molecular Dynamics: With Deterministic and Stochastic Numerical Methods*, 1st ed., Springer International Publishing, 2015.
- [64] J.M. Haile, Molecular dynamics simulation: Elementary methods, *Comput. Phys.* 7 (1993) 625.

Chapter 2

Modelling method

2.1 Interatomic potential

The phases of matter are the consequences of competition between thermal energy and intermolecular/interatomic forces and the struggle between these defines whether a given substance under given conditions is a gas, a liquid or a solid [1]. When the atoms are a certain distance apart there may be an attractive interatomic force but weak and when they are too close together there is strong repulsive force. Interatomic force is overcome when the thermal energy is a very high amount and partially overcome when it is medium amount. When thermal energy is a small amount, the interatomic force is stronger and atoms are bound to form a solid.

Almost all physical phenomena except the world inside the atomic nucleus, may attributed directly or indirectly to the forces between atoms and this inter atomic interaction can be expressed in term of their potential energy of interaction, or interatomic potentials [2]. Figure 2.1 illustrates the relationship between the potential energy and interatomic force as a function of distance [3].

The nature of interatomic potentials determines the static and dynamical properties of all phases of matter and it also governs the properties of chemical complexes and reaction mechanisms and the stability of biological compounds [4]. Although the physical and chemical properties are based on interatomic forces that bind the atoms together, these forces are not measured directly in any experiment. However, the features that are related to interatomic forces such as viscosity coefficient, transport coefficient, phonon spectra, and elastic constants are measured to extract the information about interatomic forces from the experiment [5].

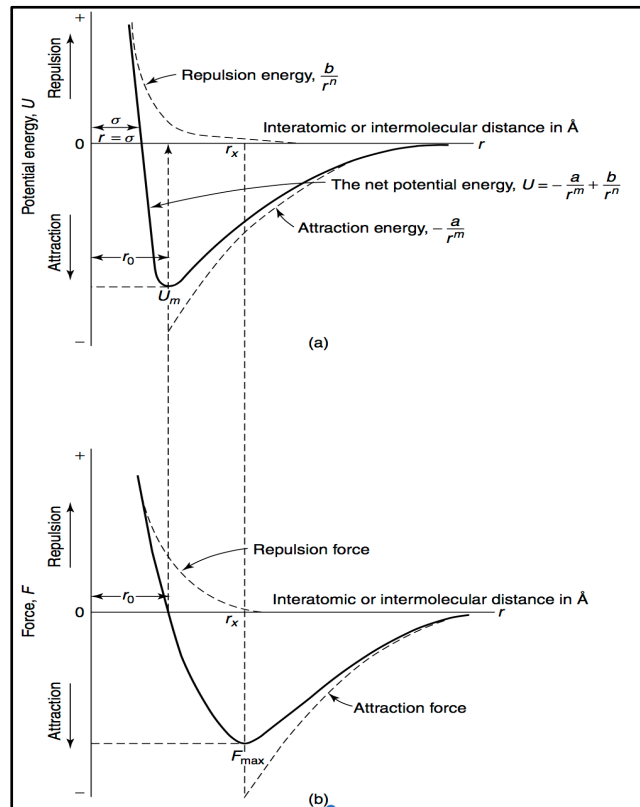


Figure 2.1 Interatomic (a) potential energy and (b) force diagram [3].

Matter is a system that is described by the interacting atoms that consist of electrons and nuclei. Due to the quantum nature of the electronic and nuclear motion only the quantum-mechanical principles can provide the detailed theory of interatomic forces [6]. There is also many-particle problem which does not have an exact quantum mechanical solution. However, it can be simplified by considering the electrons having a much higher kinetic energy than the nuclei, which allows us to separate electrons and nuclear motions and treat them independently [7]. This approach is valid at a given condition and known as Born-Oppenheimer or adiabatic approximation [4-7].



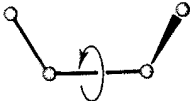
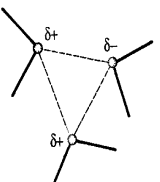
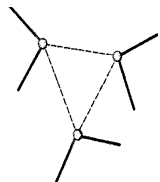
The Born-Oppenheimer approximation not only makes it easier to solve the Schrödinger equation by simplifying the nuclear and electronic interaction but it also allows us to describe the atomic system by the classical force field method [8]. Generally, it is sufficient

to assume that the nuclei behave like classical particles and the Newtonian equations of motions can be used to describe them. In the case of electrons, which are responsible for the bonds between atoms, if these bonds are characterized by some classical or semi-empirical potential model then only studying the arrangement of the atomic nuclei is sufficient [9]. But the effects that are caused by the electrons, e.g. optical spectrum, cannot be studied by this method.

2.1.1 Empirical force field

The force field (FF) of a molecular system describes the interaction between bonded parts and non-bonded parts of the system that are responsible for classical interatomic potential shown in Table 2.1 [10]. The three components that form the bonded parts are bond stretching, bond bending and bond rotation. The non-bonded parts are formed by the electrostatic interaction and van der-Waals interaction.

Table 2.1 Schematic representation of the four key contributions to a molecular mechanics force field in a N -body system [10].

N -body system	2-body system	3-body system	4-body system
Bonded parts	 Bond stretch	 Bond bend	 Bond rotation (torsion)
Non-bonded parts	  Electrostatic and van der Waals	Not applicable	Not applicable

In an organic system, the bonds are covalent and directed, i.e. the potential are the functions of bond length, bond angles and torsion angles, and the non-bonded interaction.

However, in an ionic system or an inorganic material the bonds between atoms are mainly due to electrostatic interaction and are not directed [9]. In a simple force field, the non-bonded function can be defined by electrostatic force induced by the charges present on atoms and van der Waals interaction due to the electron-electron attraction and repulsion due to Pauli principle.

Inorganic matter is often modelled by so called rigid ion model where the Coulomb potential function describes the electrostatic interaction and Lennard-Jones type or Buckingham type potential function describes the van der Waals interactions. In some cases, the shell-model is used to describe the ion polarizability. In this model, each ion is treated as a core and shell, coupled by harmonic spring and the strength of harmonic spring corresponds to the polarizability of the ions [9, 10].

2.1.2 Two body potential

Based on the Born-Oppenheimer approximation, the interatomic potential energy of a classical system only depends on the coordinates of atoms [11]. The force field approach subsumed the knowledge of electronic structure into effective interatomic potential, U , which describes in analytical or numerical form the variation in the energy of the molecule or solid as a function of the nuclear coordinates, $r_1 \dots r_N$, of the N atoms present in the molecule or solid [12]. The potential energy is given by the series of pair U^2 , three-body U^3 , four-body U^4 , and higher terms which is shown in Equation 2.1, where $r_{ij} = |r_i - r_j|$.

$$U(r_1 \dots r_N) = \sum_{i,j=1}^N U^2(r_{ij}) + \sum_{i,j,k=1}^N U^3(r_i, r_j, r_k) + \sum_{i,j,k=1}^N U^4(r_i, r_j, r_k, r_l) + \dots$$

Equation 2.1

The potential energy, U , is mainly approximated by the pair potential term, U^2 , that depends only on the distance, r_{ij} , of the pair separation of nuclei i and j . This is generally a good approximation for the ionic system but not for the covalent solids as illustrated in Table 2.1. Also, if the series on the right-hand side of the equation has a quick convergence, the higher terms in the expression can be neglected [12]. Practically it is demanding to calculate multi-body atomic interactions and it is equally difficult to define it theoretically. Therefore, these many body potentials are usually truncated after three-body term and the contribution of the truncated terms are included by inserting various parameters (linear and/or non-linear parameters) to the remaining terms [13].

Although the quantum mechanical approach is known to be theoretically rigorous, the empirical interatomic potential function is still essential due to their simpler execution and practicality in dealing with many-body dynamical systems in large models [14]. Therefore, the pair potential function simplifies the statistical mechanical formalism used in calculating various thermodynamical properties [13]. The classical system can be approximated by many different potential models such as the hard-sphere, square-well and soft-sphere and the interaction of atoms in these models can be evaluated by the typical pair potential functions like Lenard-Jones, Morse, Rydberg and Buckingham potential functions [15].

2.1.3 Coulomb interaction and short-range interaction

The materials under studies are of ionic character. The percentages of ionic characters of the bond are related to the electronegativity of the individual atoms [3]. In ionic pair potential model, the material is described as composed of spherically symmetric positive and negative ions that interact according to their interatomic separations and Coulomb's Law gives the value of their energetic interactions [9]. The columbic interactions between these ions are also the long-range potential function in an ionic material. The Columbic potential is given by Equation 2.2,

$$\phi(r_{ij}) = \frac{q_i q_j}{4\pi r_{ij} \epsilon_0} \quad \text{Equation 2.2}$$

where r_{ij} is the relative distance between the effective charges of ions q_i and q_j , and ϵ_0 is the permittivity of free space (dielectric constant).

The non-bonded interactions of the two-body potential not only consist of Coulomb energy, i.e. long-range interaction, but also embedded with short-range repulsive and the weakly attractive energy components. So, for the binary ionic glasses system, the Buckingham potential function can be used to describe the short-range interactions, which has an exponential repulsion term and an inverse power attractive term to account for the van der Waals dispersion interactions [16]. Theoretical description of the Buckingham potential, which is the function of an interatomic distance only, can be found elsewhere [9, 10], which is expressed in Equation 2.3,

$$V_{ij}(r_{ij}) = A_{ij} \exp\left(\frac{-r_{ij}}{\rho_{ij}}\right) - \frac{C_{ij}}{r_{ij}^6} \quad \text{Equation 2.3}$$

where i and j are the ions with separations r , and A_{ij} , C_{ij} and ρ_{ij} are the adjustable parameters of the model. A_{ij} and ρ_{ij} determine the degree of the repulsion due to the electron cloud density (i.e. Pauli exclusion principle) and C_{ij} is the attraction term related to Van der Waals interaction. The parameters can be calculated directly by quantum mechanical methods or by empirical fitting [17]. All the ionic systems studied here, are treated as the soft-sphere model and the total interatomic potential energy, $U_{ij}(r)$, for rigid ion is given by Equation 2.4.

$$U_{ij}(r_{ij}) = A_{ij} \exp\left(\frac{-r_{ij}}{\rho_{ij}}\right) - \frac{C_{ij}}{r_{ij}^6} + \phi_{ij} \quad \text{Equation 2.4}$$

The pair potential most commonly used in molecular modelling is thus ‘effective’ pairwise potentials as they do not represent the true interaction energy between two isolated atoms but are parameterised to include many-body effects in the pairwise energy [10]. In

this project, generally the interactions between the atoms are described as shown in Table 2.2.

Table 2.2 The long-range and the short-range interaction of an ionic system in two body potential.

Interactions	Electrostatic (Coulomb) and $\propto N^2$	Pauli Principle (Repulsive) and $\propto N$	Van der Walls (weakly attractive) and $\propto N$
Cation – Anion e.g. $Zr - F$ (close together)	(–) Strong attraction	(+) Repulsive	(–) weakly attractive
Anion – Anion e.g. $F - F$ (close together)	(+) Repulsion	(+) Repulsive	(–) Weakly attractive
Cation – Cation e.g. $Zr - Zr$ (further apart)	(+) Repulsion	Not applied (very weak)	Not applied (very weak)
Term	$(\pm) \frac{q_i q_j}{4\pi r_{ij} \epsilon_0}$	$(+) A_{ij} \exp\left(\frac{-r_{ij}}{\rho_{ij}}\right)$	$-\frac{C_{ij}}{r_{ij}^6}$

2.1.4 Principle of energy minimization

The geometrical arrangement of atoms in space manifest the structure of a molecule and for a given structure and electronic state, the molecule has a specific energy. The energy of molecule varies with the coordinates or geometry and this can be described by the potential-energy surface (PES). The geometry corresponds to bond-length, bond-angles, torsions and other internal coordinates. The PES is a natural consequence from the Born-Oppenheimer approximation, which can be obtained by solving for the electronic energy at series of fixed nuclear positions [18].

A simple representation of PES is shown in Figure 2.2 for a diatomic molecule, which is the basis of the force field method [19]. The saddle point in the PES is the minimum point, which indicates the minimum energy arrangements of the atoms, i.e. zero net force on atoms. This corresponds to the stable state of the system and the process of finding this

saddle point in PES is referred as an energy minimization or commonly known as geometry optimization.

This saddle point can be a local minimum, the lowest point in some limited region, or it can be a global minimum, the lowest point anywhere on the PES. In a system with N atoms the energy is the function of $3N - 6$ internal (the rotational and translation internal coordinates are excluded as it does not vary the energy of the system) or $3N$ Cartesian coordinates. Therefore, it is impossible to visualise the entire energy surface except for simple cases where the energy is a function of one or two coordinates [10]. Clearly, it is difficult task to find a global energy minimum compared to a local minimum as multidimensional PSE produces a complex curvature.

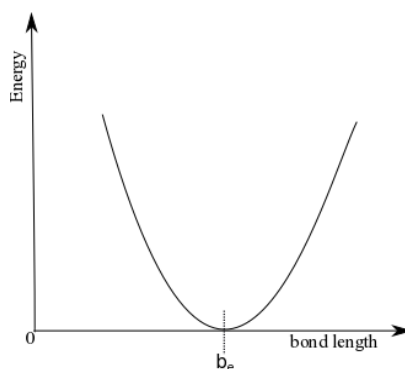


Figure 2.2 One-dimensional PES for a diatomic molecule. The PES increases if the bond length is stretched or compressed away from the equilibrium value b_e [19].

There are several methods that perform the geometry optimization to find the minimum energy. Generally, these methods are based on simple iterative formula given by the formula, $x_{new} = x_{old} + \gamma$, where, x_{new} is the next new position, x_{old} is the current position and γ is adjustment parameter made to the position. Simply analysing from Figure 2.2 numerical test (derivatives) is applied to new position to reach the minimum value b_e .

Methods such as steepest descent, conjugate gradient and Newton-Raphson can be implemented. Their algorithms are based on the order of the derivatives of the total energy

function [20]. So, at any given point of PES, the internal energy can be expanded by a Taylor series [21], which is shown in Equation 2.5.

$$U(x + \delta x) = U(x) + \frac{\partial U}{\partial x} \delta x + \frac{1}{2!} \frac{\partial^2 U}{\partial x^2} (\delta x)^2 + \dots, \quad \text{Equation 2.5}$$

Steepest descent method works by estimating the first derivative of the strain energy with respect to each coordinate of each atom and the second derivative is assumed zero. The initial direction in which it chooses to be minimized is in the direction that has largest gradient, hence named steepest descent method. The gradient at each point has to be calculated until it reaches the minimum. The main problem with the steepest descent method is that of determining the appropriate step size for atom movement during the derivative estimation steps and the atom movement steps.

The conjugate gradient method is a first-order minimization technique. It uses both the current gradient and the previous search direction to drive the minimization. Because the conjugated gradient method uses the minimization history to calculate the search direction and contains a scaling factor for determining step size, the method converges faster and makes the step sizes optimal as compared to the steepest descent technique. However, the number of computing cycles required for a conjugated gradient calculation is approximately proportional to the number of atoms N , and the time per cycle is proportional to N^2 [10, 20].

2.2 Use of GULP to test potential

The General Utility Lattice Program (GULP) software was used to test the interatomic potential parameters. The GULP uses the Newton-Rapson energy minimisation method, which uses both first and second derivatives, i.e. gradient and the curvatures of PES for γ correction parameters. In Equation 2.5, if the first derivative is given by a gradient vector, g , then second derivative matrix is referred as the Hessian Matrix, H [22]. Expanding

energy to second order, then the displacement vector, Δx , from the current position to the minimum is given by Equation 2.6.

$$\Delta x = -H^{-1} g \quad \text{Equation 2.6}$$

The most expensive step of the Newton-Raphson method, particularly once the size of the system increases, is the inversion of the Hessian. Also, the Hessian may only vary slowly from one step to the next. It is therefore wasteful and undesirable to invert this matrix at every step of the optimization and it can be avoided through the use of updating formulae [21,22] that use the change in the gradient and variables between cycles to modify the inverse Hessian such that it approaches the exact matrix.

Furthermore, there is the danger that if the energy surface is close to some other stationary point, such as a transition state, then simply applying this formula iteratively may lead to a maximum, rather than the minimum. Therefore, the expression is modified in Equation 2.7,

$$\Delta x = -\alpha H^{-1} g \quad \text{Equation 2.7}$$

where α is a scalar quantity, which is determined by performing a line search along the search direction to find the one-dimensional minimum, and the procedure becomes iterative again [21].

2.2.1 Input files for GULP

The details of software user manual are in [23]. Here, some of the important details to test potentials are highlighted. The GULP Input consists of **control parameters**, **structural parameters** and **potential parameters** and there are several types of standard minimization that are available in GULP. The most commonly used being to optimise at constant pressure, in which all internal and cell variables are included, or at constant volume, where the unit cell remains frozen [21].

2.2.2 Control parameters for GULP

This section provides GULP control parameters on how and what properties to deduce, i.e. structural control and calculation type, method and algorithm, and output control.

Some of the keywords required are:

optimize = minimize the energy with respect to geometrical variables

angle = calculate valid three body angles

bond = calculate valid bond lengths based on covalent radii

distance = calculate interatomic distances

property = calculate the bulk lattice properties

comp = perform constant pressure calculation – cell to vary

nosymmetry = turn off after symmetry once unit cell has been generated

cutd = cutoff distance for calculating the average bond length

average = output average bond lengths

compare = produce a table comparing the initial and final geometries

2.2.3 Initial structural parameters

The structure parameters of three-dimensional crystal are the unit cell, the fractional Cartesian coordinates, types of atoms, and the space group symmetry. These were obtained from CDS National Chemical database [24].

2.2.4 Potential parameters

The type of the interatomic potential should be defined as GULP has various other types of potential. Also, one has to mention whether the interaction is between core-core or core-shell. Throughout this project core-core Buckingham potential is used which is ob-

tained from Teter [25]. Teter potential has not been published however it is a well-established potential as there are considerable published literatures that have used it for both rigid ion model (e.g. [26]) and shell model (e.g. [27]). It has been also used to model the structure of other materials that is not glass (e.g. [28]).

2.2.5 Output files from GULP

In a constant pressure calculation where the initial coordinate parameters of a crystal are obtained experimentally, the energy minimization algorithm stipulates the comparison result between the input (initial) and output or final energy minimized structural parameters. The result largely depends on the interatomic potential parameters. The output file provides bond length, and coordination number.

2.3 Theory and algorithms of molecular dynamics

The Molecular dynamics (MD) method allows one to accurately predict properties of materials provided that the interatomic interactions are known and classically the essence of MD is simply to numerically solve an N -body problem. This is an excellent technique to approximate for wide range of materials and only when the translational or rotational motion of light atoms or molecules (e.g. He , H_2 , D_2) or vibrational motion with the frequency, ν , such that $h\nu > K_B T$ are considered one does has to worry about quantum effects [29].

Numerical integration of the Newton's equations of motion generates the configuration of the system which allows one to investigate both equilibrium (time-independent) and non-equilibrium (time-dependent) properties. Hence, the phase-space trajectory computed allows us to evaluate thermodynamic (temperature, energy), static structures (radial distribution function) and dynamic properties (time correlation coefficient, transport coefficient, space- time correlation function ($G(r, t)$) of a system [30].

2.3.1 Equations of motion

Initially, the starting point of a MD simulation is a well-defined microscopic description of the physical system in terms of a Hamiltonian or Lagrangian from which the Newton's equations of motion are derived [31]. In a classical system to know how the system evolves in time, or the trajectory of motion one has to know the coordinates, $\mathbf{r}_i = x_i, y_i, z_i$, and all the velocities, $\mathbf{v}_i = [v_x, v_y, v_z]_i$, of all the particles i in the system at any moment of time and this information can be obtained by solving the Newton's equation of motion given in Equation 2.8,

$$\mathbf{F}_i = m_i \mathbf{a}_i \quad i = 1, 2, \dots, N \quad \text{Equation 2.8}$$

where $\mathbf{F}_i = [F_x, F_y, F_z]_i$ is total force acting on particle i by all the other particles (classical mechanical system free from the external force), m_i is the mass of particle i and $\mathbf{a}_i = [a_x, a_y, a_z]_i$ is the acceleration of the particle i in the direction of net forces. The forces can be derived from the potential energy, U , which corresponds to the pair potential in this modelling system given by Equation 2.9.

$$\mathbf{F}_i = - \frac{\partial}{\partial \mathbf{r}_i} U(\mathbf{r}_1, \dots, \mathbf{r}_N) \quad \text{Equation 2.9}$$

From the force, we can determine the acceleration of the particles, which are the combined with the positions and velocities at time, t , to calculate the positions and velocities at a new time, $t + \Delta t$. The experience of force on any particle is assumed constant for a short period of time, time-step, Δt , then the position of a particle at new time, $t + \Delta t$, can be obtain from a Taylor series expansion. Therefore, the change in coordinates of a particle, around time, t , is given at time forward, $t + \Delta t$, and time backward, $t - \Delta t$, by Equation 2.10 and 2.11,

$$\mathbf{r}(t + \Delta t) = \mathbf{r}(t) + \mathbf{v}(t)\Delta t + \frac{\mathbf{F}(t)}{2m} \Delta t^2 + \frac{\Delta t^3}{3!} \ddot{\mathbf{r}} + \mathcal{O}(\Delta t^4) \quad \text{Equation 2.10}$$

$$r(t - \Delta t) = r(t) - V(t)\Delta t + \frac{F(t)}{2m}\Delta t^2 - \frac{\Delta t^3}{3!}\ddot{r} + \mathcal{O}(\Delta t^4) \quad \text{Equation 2.11}$$

Summing this two Equations 2.10 and 2.11 gives the Equation 2.12 or 2.13.

$$r(t + \Delta t) + r(t - \Delta t) = 2r(t) + \frac{F(t)}{m}\Delta t^2 + \mathcal{O}(\Delta t^4) \quad \text{Equation 2.12}$$

or

$$r(t + \Delta t) \approx 2r(t) - r(t - \Delta t) + \frac{F(t)}{m}\Delta t^2 \quad \text{Equation 2.13}$$

A simple Verlet algorithm can integrate the equations of motion. The approximation of the new position contains an error that is order Δt^4 . Newton's equations are time reversible and reversing the velocities should result in a trajectory that re-traces itself. The Verlet and Verlet-derived integrators all satisfy this property [29]. But the Verlet algorithm has disadvantages as it lacks explicit velocity terms in the equation and it is only possible to calculate the velocity after the positions have computed in the next step.

For the Verlet "leapfrog", it requires values of position, r , and force, F , at time, t , while the velocities, v , are half a time-step behind. Therefore, at first the velocities are defined from the Verlet scheme at half-integer time-steps to compute the new positions as given by Equation 2.14 and 2.15.

$$v\left(t - \frac{\Delta t}{2}\right) = \frac{r(t) - r(t - \Delta t)}{\Delta t} \quad \text{Equation 2.14}$$

and

$$v\left(t + \frac{\Delta t}{2}\right) = \frac{r(t + \Delta t) - r(t)}{\Delta t} \quad \text{Equation 2.15}$$

The new position based on the old positions and velocities, and also the new update expressions of the velocities from the Verlet algorithm are given by Equation 2.16 and 2.17.

$$r(t + \Delta t) = r(t) + V\left(t + \frac{\Delta t}{2}\right)\Delta t \quad \text{Equation 2.16}$$

$$v\left(t + \frac{\Delta t}{2}\right) = v\left(t - \frac{\Delta t}{2}\right) + \Delta t \frac{F(t)}{m} \quad \text{Equation 2.17}$$

The current velocity at time, t , is obtained as the mean from the mid step values as given by Equation 2.18. Therefore, the velocities ‘leapfrog’ over the positions to give their values at $t + \frac{1}{2}\Delta t$ and positions also leap over the velocities to give their new values at $t + \Delta t$ to produce the velocities at $t + \frac{3}{2}\Delta t$ and so on [10, 29, 30].

$$v(t) = \frac{1}{2} \left[v\left(t + \frac{1}{2}\Delta t\right) + v\left(t - \frac{1}{2}\Delta t\right) \right] \quad \text{Equation 2.18}$$

However, “leapfrog” algorithm doesn’t compute velocities and positions at the same time as a result kinetic energy and potential energy are not defined at the same time. Therefore, the updating of positions and velocities is synchronized in the velocity Verlet algorithm given by Equation 2.19 and 2.20, that gives positions, velocities and accelerations at the same time and also does not compromise precision [32]. Hence, one does not need to apply a more complex Verlet algorithm than velocity Verlet algorithm [33].

$$r(t + \Delta t) = r(t) + v(t)\Delta t + \frac{F(t)}{2m} \Delta t^2 \quad \text{Equation 2.19}$$

$$v(t + \Delta t) = v(t) + \frac{1}{2}\Delta t \left[\frac{F(t)}{m} + \frac{F(t + \Delta t)}{m} \right] \quad \text{Equation 2.20}$$

2.3.2 Thermal equilibrium

MD is typically applied to an isolated system, containing a fixed number of N particles in a fixed volume, V , and the total energy, E , of the system is constant. The equations of motion are solved until the properties of the system no longer change with time and only after achieving the equilibration are the actual measurements are taken [34]. Equilibrium thermodynamical properties of the simulated system can be obtained by averaging certain dynamical variables, which are the functions of the computed coordinates and velocities both

over time and over all particles [35]. The calculation of time averages in MD is not possible due to the macroscopic number of atoms, i.e. in order of 10^{23} , which is not even realistic to determine an initial configuration of the system. Hence to overcome these problems the time average is replaced by the ensemble average [29, 33]. Equation 2.21 below describes the thermodynamic averages that can be obtained from the MD ensemble averages [10],

$$\langle A \rangle = \frac{1}{M} \sum_{i=1}^M A(p^N, r^N) \quad \text{Equation 2.21}$$

where, $\langle A \rangle$ is an ensemble average of the property, A over all replication of the ensemble generated by the simulation, M is the number of MD time-step, Δt , and, p and r are the momenta and positions of N particles. This statistical ensemble can also control thermodynamics quantities like pressure, temperature or the number of particles [30].

Characteristically, in MD simulation the total energy, E , and the total linear momentum, p , are constants of motion hence the ensemble average measured is a microcanonical (constant NVE) ensemble [30]. The microcanonical ensemble is the simplest and most fundamental of the equilibrium ensembles of an isolated system of fixed N particles in a constant volume, V , and total energy, E , from which other equilibrium ensembles are also derived [36]. However, to compare result directly between MD simulations and the experiments canonical ensemble is preferred where the number of particles N , the volume, V , and the temperature, T , are fixed (i.e. constant NVT) [37].

The other types of equilibrium ensembles are grand canonical and isothermal isobaric. In isothermal isobaric NPT the number of particles, pressure and temperature are fixed. Also in general laboratory experiments are typically carried out at constant temperature and pressure. The microcanonical, canonical and isothermal isobaric ensembles describe closed systems for which there is no change in the number of particles whereas the grand canonical ensembles can describe the open system in which the number of particles can change [38].

Thus, thermodynamics quantities provide the link between the microscopic and macroscopic world of a molecular system. In a classical mechanical system, the total energy is conserved and the temperature is rather considered the average temperature, $\langle T \rangle$, derived from the average velocities of all the particles in the system. The average kinetic energy, $\langle \frac{1}{2} m v_i^2 \rangle$, and instantaneous temperature, T , of system can be obtained from the velocity, $v(t)$, assuming that the system atomic velocities have no net momentum as given by Equation 2.22 and 2.23,

$$\langle \frac{1}{2} m v_i^2 \rangle = \frac{1}{2} k_B T \quad \text{Equation 2.22}$$

$$T = \frac{\sum_{i=1}^N m_i v_i^2(t)}{K_B f} \quad \text{Equation 2.23}$$

where k_B is the Boltzmann constant and f is the number of degrees of freedom in the system. Since the system is equilibrated at microcanonical (NVE) ensembles where thermodynamic properties N and V is fixed and the total energy is conserved by calculating the instantaneous temperature, T , the total energy, H_{NVE} , given by Equation 2.24, of the system is conserved where U is the potential energy of the system and KE the kinetic energy at time, t .

$$H_{NVE} = U + KE \quad \text{Equation 2.24}$$

2.3.3 Berendsen thermostat

In canonical (NVT) ensembles the system average temperatures should be kept close to the target Temperature, T_{ext} . Therefore, to modulate the temperature varieties of thermostat are introduced. The DL_POLY_2 uses Berendsen thermostat algorithm to modulate the temperature which is obtained by modifying the equations of motion where the instantaneous temperature, T , is pushed towards the target temperature, T_{ext} , by scaling the velocities, v , at each step [39] as given by Equation 2.25 and 2.26,

$$\chi \leftarrow \left[1 + \frac{\Delta t}{t_{relax}} \left(\frac{T_{ext}}{T} - 1 \right) \right]^{1/2} \quad \text{Equation 2.25}$$

$$v \left(t + \frac{\Delta t}{2} \right) \leftarrow v \left[\left(t - \frac{\Delta t}{2} \right) + \Delta t \frac{F(t)}{m} \right] \chi \quad \text{Equation 2.26}$$

where χ is the scaling factor for velocity, v , and t_{relax} is a relaxation time (i.e. in range of 0.5 – 2 pico seconds). If $T > T_{ext}$ and $\chi < 1$ then, $v\chi < v$ therefore v is reduced.

2.3.4 Boundary conditions

In MD studies the surface effects have a huge impact while trying to study the bulk phenomena of any material [10]. Practically, material structures are built with at least 10^{23} atoms therefore, the boundary condition defines the thermodynamic environment in the MD models. Hence the problem of surface effects can be overcome by implementing periodic boundary conditions. The model box, for example cubic box, is replicated throughout space to form an infinite lattice so that during the course of the simulation as a molecule moves in the original box, its periodic image in each of the neighboring boxes moves in exactly the same way. The central box (original box) has to be surrounded by 26 virtual copies in 3D space so that a particle that exits the box from one face re-enters the box from its opposite face (see Figure 2.3) without changing the velocity vector.

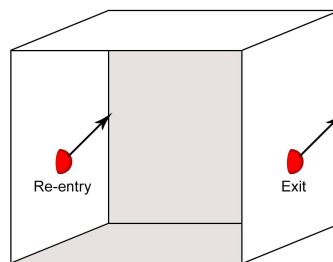


Figure 2.3 Periodic boundary condition where a particle is going to leave the simulation box and its position is set immediately to the opposite face and velocity vector remains unchanged [7].

The interatomic forces are computed not only for the atoms within the central box but by including all the particles of its virtual images. Adding or subtracting according the

box length from the coordinate of the particle position vectors can easily create these images. If the range of the potential is longer than the box length, a particle would interact with itself. Therefore, to avoid this problem a cutoff radius i.e., maximum interaction distance is introduced to limit the range of the potentials. These particles positions ensure the constancy of energy, particle number and volume [33]. The cutoff radius for the cubic simulation box is no greater than half of the box length.

2.3.5 Force calculation

In a model system where the pairwise additive interactions are considered then the force on a particle is contributed by all the neighbouring particles. That is for a system of N particles, one has to evaluate $N(N - 1)/2$ pair interactions and compute all $N(N - 1)/2$ pair distances to describe which pairs can interact. Hence the time to calculate the energy of the system scales as N^2 . Therefore, one has to adopt an efficient technique to calculate the short-range interaction and long-range interaction.

2.3.5.1 Short-range force calculation

The two-body pair potential, nonbonding interactions are contributed by dispersion, repulsion and electrostatic potential. The Buckingham potential represents the dispersion and repulsion parts, and is the function of interatomic distances as given by Equation 2.3. This is also known as short-range interaction as the potential energy decays rapidly with increasing interatomic separations. The total potential energy of the whole system is given by Equation 2.27, which is the sum of pairwise interactions over all atoms pairs from Equation 2.4.

$$U_{tot} = \frac{1}{2} \sum_{i=1}^N \sum_{\substack{j=1 \\ j \neq i}}^N U_{ij} \quad \text{Equation 2.27}$$

The time required calculating the forces in each particle scales to $O(N^2)$. One of the ways to reduce the calculations of inter-atomic potentials is by introducing the cutoff distance, r_{cut} , in potential functions and by assuming that both potential functions and forces beyond the cutoff distance are zero [40]. However, truncating the potential one still has to compute all $N(N - 1)/2$ pair distances to describe which pairs can interact. Thus, to effectively reduce unnecessary interatomic distance evaluation can be achieved by constructing the Verlet neighbouring list method, the cell-linked method, and the multiple time-step method.

2.3.5.1.1 Verlet neighbouring list

Theory behind the Verlet neighbouring list is to construct and maintain a list of neighbouring atoms for each atom in the system by defining the skin radius, r_s , which serves as a reservoir of particles [41]. Interactions between particles are always calculated for each particle within the interaction sphere (see Figure 2.4) [42]. This significantly reduces the time to calculate the forces on each particle because between the update of neighbouring list it has to only check the particle pair which appear in the list. The frequency at which the table must be updated depends on the thermodynamic state point, the time step, the cutoff distance and thickness of skin radius [41]. The overall procedure scales as $O(N \times N_{NL})$, where N_{NL} is the average number of neighbours of an atom in the material and is independent to the system size N .

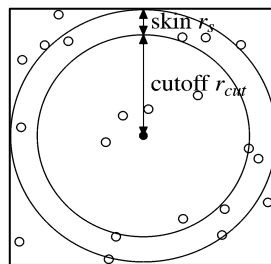


Figure 2.4 Illustration of the basic idea of Verlet table algorithm [42].

2.3.5.1.2 Cell-linked method

For the large numbers of particles, the conventional neighbouring list becomes inefficient and the alternative method of keeping track of neighbours for large systems is the cell index method [33]. The idea behind this method is that the computational domain is subdivided into cells of length at least equal to the r_{cut} and every time steps, atoms are assigned to one of these cells according to their spatial coordinates [40]. If the particle distribution is assumed to be homogeneous then each cell contains N/c particles, where c denotes the number of cells and thus, construction of assigning each atom to appropriate cells, scales time require by $O(N)$ as long as the particle density is kept constant [43].

Though, this method is fast and efficient for constructing of the “neighbouring list” but inefficient in calculating the force as there are too many particles to be checked. The total number of pairs that can be constructed for an atom by using all neighbouring atoms is equal to $27\rho r_{cut}^3$ where ρ is the atom density, but only $\frac{4\pi}{3}\rho r_{cut}^3$ of them have atoms within the cutoff distance, hence this method generates a number of pairs about $\frac{81}{4\pi} = 6.45$ times greater than necessary calculation of interatomic distance. Therefore, the software DL_POLY_2 usually uses cell-linked method only for the complicated intermolecular interaction[44]. Several improvements and optimizations made in both methods [40, 42] are found in elsewhere [45].

2.3.5.1.3 Multiple time-step method

The book-keeping methods discussed above considerably reduce the time for examining the complete set of $\frac{1}{2}N(N - 1)$ pairs, identifying those pairs separated by less than cutoff distance, r_{cut} , and computing the forces for this subset [33]. It is assumed the remaining pair interaction do not influence the dynamics of the system. Only by cutting down the

time spent in calculating the forces between pairs within cutoff range can further increase in the speed be obtained.

As shown in Figure 2.5 the multiple time-step method is designed to have two cutoffs for the pair interactions. They are the primary cutoff, r_{prim} , for the primary neighbour's atoms and the secondary cutoff for the secondary particles that lies in distances between r_{prim} and r_{cut} . The motions of primary regions' particles largely influence force in a particle whereas the secondary forces are smaller and change slowly with the time and hence the multiple time step evaluates the interactions arising from the primary particles at every time-step. However, the interactions arising from the secondary particles are calculated much less frequently, and merely extrapolated over the interval [39].

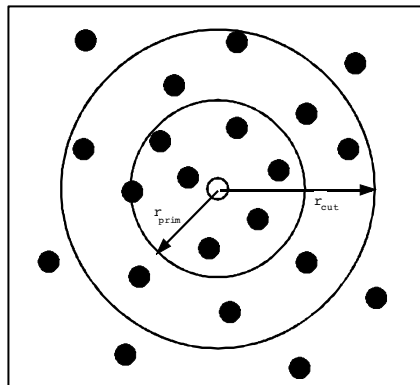


Figure 2.5 Illustration of multiple time-step algorithm [39].

2.3.5.2 Ewald summation

The long-range electrostatic interaction between the particles considers how charge may be distributed in space and is given by the Coulomb's law as expressed in Equation 2.2. One of the problems with electrostatic interaction is the charge-charge interaction that depends on $1/r$ and it decays very slowly with r , the interatomic distance. Also, another problem is in the system of periodic boundary conditions where the long-range force influence is much greater than half the length of the simulation box. If we consider a periodic boundary

condition system of N particles with charges, q_i , at positions, r_i , in an overall neutral and cubic simulation box of length, L , and volume, L^3 , then the total electrostatic energy of the system [43], is given by Equation 2.28,

$$E = \frac{1}{2} \sum'_{|n|=0} \sum_{i=1}^N \sum_{j=1}^N \frac{q_i q_j}{4\pi\epsilon_0 |\mathbf{r}_{ij} + \mathbf{n}L|} \quad \text{Equation 2.28}$$

where \mathbf{n} is the lattice vector/cell-coordinate vector. The first sum over n takes into the account the periodic images of the charges and the prime indicates the terms with $i = j$ are excluded when $n = 0$. The distance between a particle in the origin cell and another at an image cell is given by $\mathbf{r}_{ij} + \mathbf{n}L$ where $\mathbf{r}_{ij} = \mathbf{r}_i - \mathbf{r}_j$. The above sum is conditionally convergent which means the result depends on the order of summation and conceptually the infinitely periodic system is built approximately in spherical layers that will converge however other shapes are also possible [47].

Therefore, the technique is to sum the long-range interactions between particles and all their infinite periodic images and expresses the long-range potentials by splitting slowly converging sums into two rapidly converging sums in both real and reciprocal space. In Equation 2.28 the Coulomb part of the equation is effectively separated into two parts using a Gaussian error function, $erf(\alpha r)$, and $erfc(\alpha r) = 1 - erf(\alpha r)$ [48]. The fundamental mathematical trick is to split the term $\frac{1}{r}$ as given by Equation 2.29,

$$\frac{1}{r} = \frac{erf(\alpha r)}{r} + \frac{erfc(\alpha r)}{r} \quad \text{Equation 2.29}$$

where α is a parameter that is chosen so that an optimal split between the real-space sum and the reciprocal-space is obtained [49]. The first term on the right-hand side will correspond to a summation in real space and converges rapidly. The second term will be summation in reciprocal space and is a smooth function, hence its Fourier transforms decays rapidly [47]. The complete derivation of the Ewald summation can be found elsewhere [10, 33].

2.4 Use of DL_POLY for molecular dynamics modelling

Modelling and simulation of the material under study in this project is performed by a parallel molecular dynamics simulation package DL_POLY_2 developed at Daresbury Laboratory by W. Smith and T.R Forester [39]. For simulating a glass model in the DL_POL_2 requires following input files:

- (a) Config file - (see section 2.5.1)
- (b) Control file
- (c) Field file

2.4.1 Control parameters for DL_POLY_2

This file contains the commands to control the condition under which the simulation is performed. They are the parameters of temperature, pressure, type of thermodynamic ensemble (e.g. *NVT*), number of simulation steps and equilibration steps.

Here we also illustrate the time-step of MD simulation which is typically 1 *fs* (10^{-15} s) for a stable simulation with rigid ions. For the canonical *NVT* ensemble to modulate the temperature a Berendsen thermostat algorithm with a relaxation time 2 *ps* (2×10^{-12} s) is defined so as to obtain final densities compatible with the measured densities. The other specified parameters are “skin” width for Verlet neighbour list, cutoff for short-range potential, primary cutoff for multiple time step algorithm, Coulomb potential cutoff, and Ewald precession (which is specified for the electrostatic force calculation by the Ewald summation method).

2.4.2 Field files for DL_POLY_2

In this file, the total number of atoms species are given with their partial charges and atomic mass numbers. The Teter potential parameters are based on 60% partial charges of ion species to account valence electron density formed due to partial covalence in the system.

The parameters of the Buckingham potential taken from Teter are also specified for each pairwise interaction between the atom species to calculate the short-range forces.

2.4.3 Output from DL_POLY_2

After the successful run the DL_POLY_2 generates output data files and the details of these files are given in [39]. However, some of the key output files such as OUTPUT, REVCON, CONFIG and HISTORY that are important to this modelling project is discussed in short here. OUTPUT consists of the job summary of the simulation such as the sample of initial and final configuration. According to number of time-step used instantaneous and rolling-average thermodynamic data and the radial distribution function are generated as well. REVCON consists of the final configuration of atom species positions. It has to be renamed as the CONFIG if it is to be used as the initial configuration in the next stage of simulation. The HISTORY file is one of the key output data for analysis as it consists of atomic coordinates, velocities and forces during the simulation. It can be generated formatted or unformatted but usually the formatted HISTORY file is very large.

The pair distribution function, the average coordination numbers and the bond angle distribution functions are obtained from the OUTPUT and HISTORY files using the “xanal_02” and “xhst-hsc” programs from Jincheng Du of Alfred State University [50]. From the REVCON file we can obtain the final image of the model and the diffraction results from Material Studio [51] and I.S.A.A.C.S. [52] software package respectively.

2.5 Molecular dynamics modelling of glasses

The modelling of glasses is performed in aid of understanding the relation between the glass properties and the underlying atomic structure. It can be done in two ways by energy minimisation or geometry optimization method and by molecular dynamics methods.

However, if interest is in the behaviour of a material at finite temperatures then the molecular dynamics modelling is favoured technique to study [9]. This can be achieved through simulating the properties of materials by determining the position of each atom in space and their motion as function of time. Molecular dynamics methods are extensively used to model the structure of network glass-forming materials. Here we examine some of the steps involved in performing a molecular dynamic modelling in canonical ensemble.

2.5.1 Initial configuration

In the model cubic box, the correct number of atoms species in the system is given by the chemical composition of the glass. The length of the box can be determined by the experimental density values of the glass. The initial positions of atom species are randomly generated but do not overlap each other by choosing a minimum value for the inter-atomic distance. Initial velocities of atoms can be randomly assigned from the Maxwell-Boltzmann distribution at the temperature of interest.

2.5.2 Temperature stage

The most commonly used procedure to generate glass structures is a simulated melt and quenching process. This is performed in the six stages of progressively lower temperatures. During the first three stages before the melt temperature, T_{melt} , the system is heated in very high temperature and equilibrated to completely have the random configuration. Also, trajectory of 40,000 time-steps at 6000 K is sufficient to allow diffusion over the box length for models of few thousand atoms. The six stages barium silicate and barium fluorozirconate based glasses are given in Table 2.3. In the simulation, melt temperature, T_{melt} , is higher than experiment glass melting temperature because it represents a liquid before quenching.

Table 2.3 The typical MD stages for melt-quenched glass.

Stages	Temperature (K)	Time-steps	Process
1	6000	40000	Equilibrate
2	3000	40000	Equilibrate
3	T_{melt} (e.g. 2000)	40000	Equilibrate
4	T_{melt} (e.g. 2000)	$\frac{(T_{melt} - 300)K}{0.02 K}$ e.g. 85000	Quench ($10^{13} Ks^{-1}$)
5	300	40000	Equilibrate
6	300	40000	Collect or Sampling

2.5.3 Quenching

The typical quench rate of glasses in the molecular dynamics modelling used here is between $10^{12} - 10^{13} Ks^{-1}$. The MD study of all the glasses uses quench rates several orders of magnitude higher than the experimental due to constraints on computing time. For quench rate $10^{12} Ks^{-1}$, the number of time-step is $\frac{(T_{melt}-300)K}{0.002 K}$, as temperature drops 0.002 K every time-step.

2.5.4 Sampling

The calculation of the thermodynamic properties such as static structure from the time average of MD is not feasible due the complexity of the time evolution of large number of molecules. However, the successive snapshots of dynamic trajectory of the system are calculated in specified time-steps which will be used in sampling a probability distribution. Thus, in many molecular simulations, the dynamics trajectory is used as a method of sampling a desired ensemble, for example to compute the average of some function of the phase space variables. In such cases, it is important that the trajectory produces a representative

collection of phase points for all variables of the model. A common ensemble used in biomolecular simulation is the NVT ensemble, which weights points of phase space according to the Gibbs density [29].

2.6 Analysing structures of MD models of glasses

The final phase space particle trajectories of the model glass obtained from the MD simulation can be analyzed to obtain static structure, thermodynamic and dynamic properties [53]. Here we investigate their time independent structural properties such as pair distribution functions, bond lengths, bond angle distribution functions and the coordination numbers, which are compared with the experimental results. The diffraction data produced from the models were also compared with the experiments to scrutinise the validity of a model.

2.6.1 Pair distribution function

Glasses are isotropic in nature and their structures can be described in term of 1-dimensional, spatially averaged, radial distribution function (RDF), $R(r)$. It's defined as the number of atoms lying at distances between r and $r + dr$ from the centre of an arbitrary origin atom. The $R(r)$ is defined in term of the function $\rho(r)$, by Equation 2.30,

$$R(r)dr = 4\pi r^2 \rho(r)dr \quad \text{Equation 2.30}$$

where $\rho(r)$ is an atomic pair density correlation function. The normalized function is also known as pair distribution function (PDF), $g(r)$. When $r \rightarrow \infty$, $g(r) \rightarrow 1$ and if r is shorter than the distance of closet approach of pairs of atoms (i.e. $r \rightarrow 0$) $g(r) \rightarrow 0$. The $\rho(r)$ and $g(r)$ are closely related functions, which is given in Equation 2.31,

$$g(r) = \frac{\rho(r)}{\rho^0} = \frac{R(r)}{4\pi r^2 \rho^0} \quad \text{Equation 2.31}$$

where ρ^0 is the average number density of the material. The $\rho(r)$ oscillates about and then asymptotes to ρ^0 at high r and becomes zero as $r \rightarrow 0$ as illustrated in Figure 2.6 [54].

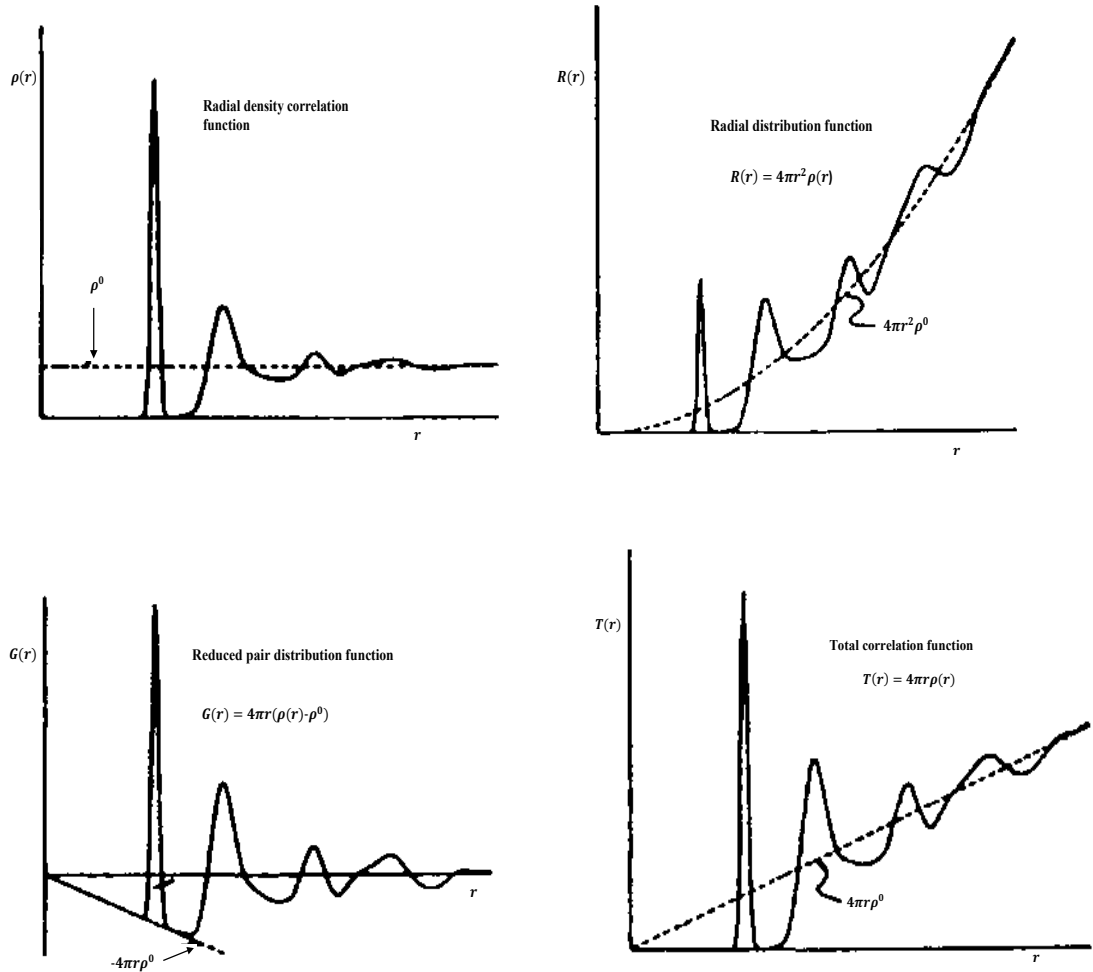


Figure 2.6 Real space correlation functions for a monatomic amorphous material [54]. (*Top-left*) Radial density, $\rho(r)$, (*top-right*) radial distribution function, $R(r)$, (*bottom-left*) reduced pair distribution function, $G(r)$, and (*bottom-right*) total correlation function, $T(r)$.

The other correlation function generally used to represent data that are useful for analysing the diffraction data are the total correlation function, $T(r)$, which is related to $R(r)$, given by Equation 2.32.

$$T(r) = \frac{R(r)}{r} = 4\pi r \rho(r) = 4\pi r \rho^0 g(r) \quad \text{Equation 2.32}$$

The differential correlation function or the reduced pair distribution function, $G(r)$, which is obtained on subtracting the average density contribution, $t^0(r) = 4\pi r \rho^0$, from the total correlation function (i.e. $T(r) - t^0(r)$) [52] is given by Equation 2.33.

$$G(r) = 4\pi r [\rho(r) - \rho^0] = 4\pi r \rho^0 (g(r) - 1) \quad \text{Equation 2.33}$$

Aforementioned are the real space correlation functions for a monatomic amorphous material. They all convey the same structural information and really only differ in their asymptotic behaviour at large r , as shown by Figure 2.5, $R(r) \propto r^2$, $T(r) \propto r$ and $G(r) \rightarrow 0$. In a multicomponent system containing more than one element type such as in a binary system which contains atom i and j types the partial pair distribution function g_{ij} is defined in terms of $\rho_{ij}(r)$ by Equation 2.34,

$$g_{ij}(r) = \frac{\rho_{ij}(r)}{\rho^0 c_j} = \frac{\rho_{ij}(r)}{\rho_j} \quad \text{Equation 2.34}$$

where $\rho_j = \frac{N_j}{V}$, the number density for the j type atoms and c_j the concentration of atom type j in the material. When r is large, there is no $i - j$ correlation and $g_{ij}(r) \rightarrow 1$ whereas for very small r , $g_{ij}(r) \rightarrow 0$ as atoms does not interpenetrate. We can also deduce the partial correlation function, T_{ij} , which is given by Equation 2.35,

$$T_{ij}(r) = 4\pi r \rho_{ij}(r) = 4\pi r \rho_j g_{ij}(r) \quad \text{Equation 2.35}$$

and the partial differential function or partial reduced pair distribution, $G_{ij}(r)$, is given by Equation 2.36.

$$G_{ij}(r) = 4\pi r \rho_j [g_{ij}(r) - 1] \quad \text{Equation 2.36}$$

For n types of atoms in a system the structure may be described in terms of $n(n + 1)/2$ independent partial correlation functions, i.e. n pairs for $i = j$ and $\frac{n^2 - n}{2}$ pairs for $i \neq j$ without repeating, which will give the total correlation function, $T(r)$, expressed in Equation 2.37.

$$T(r) = \sum_i \sum_j c_i T_{ij}(r) \quad \text{Equation 2.37}$$

MD provides positions of individual atoms as function of time, hence $g(r)$ can be obtained from the simulations. This local structure function is proportional to the probability of finding a pair of atoms separated by distance, $r \pm dr$, and the expression by which $g(r)$

is evaluated by taking an ensemble average over pairs. It is defined as the number of atom at distance $(r, r + dr)$ from a central atom over average number of atoms in same volume and its mathematical form of $g(r)$ is given by Equation 2.38 or 2.39,

$$g(r) = \frac{\frac{1}{N} \sum_{i=1}^N \sum_{j \neq i}^N \delta(r - R_{ij})}{4\pi r^2 \rho^0} \quad \text{Equation 2.38}$$

$$4\pi r^2 \rho^0 g(r) = \frac{1}{N} \left\langle \sum_i^N \sum_{j \neq i}^N \delta(r - R_{ij}) \right\rangle \quad \text{Equation 2.39}$$

where $\rho^0 = N/V$ is the average number density, $(\frac{1}{N} \sum_{i=1}^N)$ gives the average over all central atoms and R_{ij} is the distance between centres of atoms i and j . The term $\sum_{j \neq i}^N \delta(r - R_{ij})$ is the counting function and the δ is the delta function described elsewhere [29, 34] and it takes the following values:

$\delta(x - x_i) = 1$, if centre of atom i is located at x and

$\delta(x - x_i) = 0$, if centre of atom i is not at x .

On any radial direction, $g(r)$ can be expressed in terms of $T(r)$ by Equation 2.40,

$$4\pi r^2 \rho^0 g(r) = r T(r) \quad \text{Equation 2.40}$$

and hence, the pair distribution function (PDF), $T_{ij}(r)$, of model is given by Equation 2.41.

The result obtained for the $33BaF_2 - 67ZrF_4$ glass and its associated crystal $BaZr_2F_{10}$ is given in Figure 2.7.

$$T_{ij}(r) = \frac{1}{r} \left(\frac{1}{N_i} \sum_i^N \sum_{j \neq i}^N \delta[r - R_{ij}] \right) \quad \text{Equation 2.41}$$

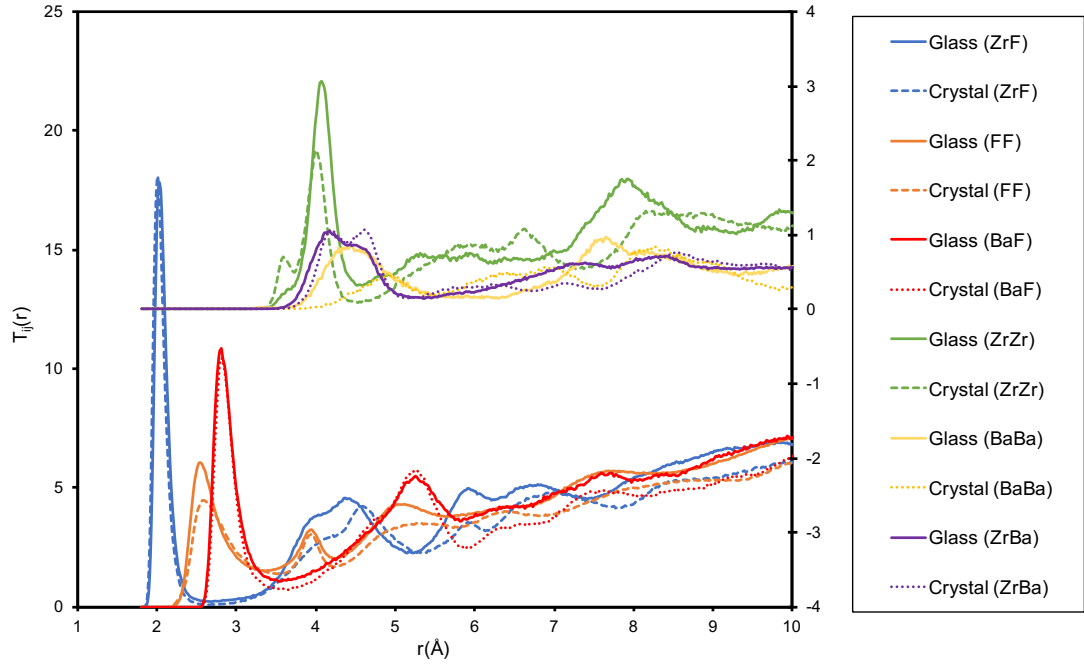


Figure 2.7 The PDF of $33\text{BaF}_2 - 67\text{ZrF}_4$ glass and its related $\text{BaZr}_2\text{F}_{10}$ crystal.

2.6.2 Nearest neighbor distances and coordination numbers

The statistical information for the non-crystalline structure like inter atomic distances and coordination numbers are contained in a set of pair distribution function. Therefore, from the T_{ij} , the coordination number, $N_{ij}(r)$, that is the number of atoms j surrounding the atom i at distance between R_1 and R_2 can be deduced by Equation 2.42,

$$N_{ij} = \int_{R_1}^{R_2} r T_{ij}(r) dr \quad \text{Equation 2.42}$$

where R_1 and R_2 define the beginning, and ending positions of the peak. Interatomic distance between atom i and j contributes to both n_{ij} and n_{ji} . This gives the relationship between the coordination number N_{ij} and N_{ji} given by Equation 2.43.

$$c_i N_{ij} = c_j N_{ji} \quad \text{Equation 2.43}$$

2.6.3 Bond angle distribution functions

In amorphous material, the bond angle distribution functions (BAD) describes the randomness in the structure. If we consider the atom types i and j then the bond angle, θ is the angle subtended between atoms $i - j - i, j$ being the central atom type and hence the inter-connections between atoms inside the structural units can be analysed in term of BAD. Figure 2.8 shows the BAD subtend by two oxygen, O , atoms at silicon, Si , atoms i.e. is $O - Si - O$. The crystalline structure will have a narrow distribution centred on a single value however the amorphous will have a broad angle distribution due to the static variation, structural and thermal disorder.

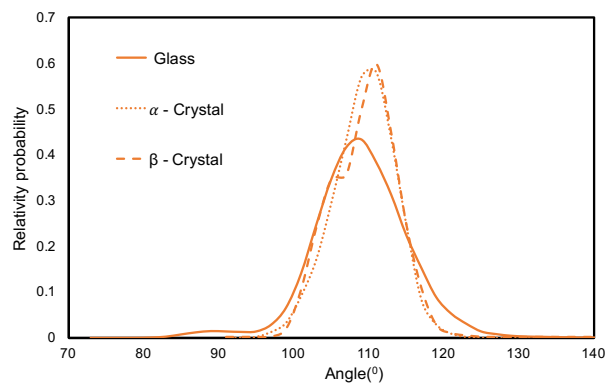


Figure 2.8 The BAD of $33BaO - 67SiO_2$ glass and its two related α and $\beta - BaSi_2O_5$ crystals.

2.6.4 Network connectivity

The averaged Q^n structure of the glass is called the network connectivity, which can be understood as the number of bridging and non-bridging bonds in the glass structures that link each of the building blocks to their neighbours. Here Q^n represents the structure unit and n is the number of bridging atoms (i.e. oxygen or fluorine in this project). This can easily be calculated from the stoichiometric composition of glasses and the number of bridging bonds that are destroyed for each network modifier added.

There are two methods used to analyse the network connectivity of the glass models. The first is a direct method from the pair distribution function, $T_{ij}(r)$. For example, from Figure 2.7, the area under the first peak of $T_{ZrZr}(r)$ gives CN_{ZrZr} which is an average connectivity, at cutoff 4.55 Å. The other method is “xhst-hsc” software [50], which looks for the $Zr - F - Zr$ (i.e. corner sharing) and edge sharing fluorine in the model, which is illustrated by $Zr_{(1)}$ and $Zr_{(2)}$ in Figure 2.9. In the direct method (i.e. from PDF), $Zr_{(2)}$ and $Zr_{(4)}$ are counted once each from the $Zr_{(1)}$ at certain cutoff but $Zr_{(3)}$ is not counted. However, in “xhst-hsc” method, $Zr_{(2)}$ is counted twice as connection is edge sharing (two fluorine) and $Zr_{(3)}$ is counted once as corner sharing but $Zr_{(4)}$ is not counted. The “xhst-hsc” method particularly looks for the number $\langle n \rangle$ of fluorine ion bridging between two zirconium ions whereas in direct method it is not necessary.

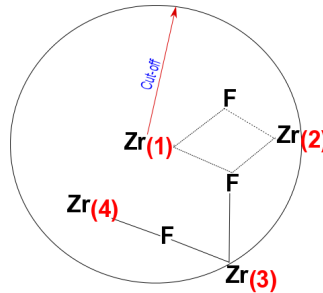


Figure 2.9 Illustration of $Zr - Zr$ connectivity calculation from the PDF and "xhst-hsc" program.

From these two methods, percentage of corner sharing and edge sharing can be calculated for the modelled glasses or crystals by Equation 2.44.

$$\% \text{ corner sharing} = \frac{CN_{ZrZr} - \frac{\langle n \rangle}{2}}{\langle n \rangle - \frac{\langle n \rangle}{2}} \quad \text{Equation 2.44}$$

2.6.5 X-ray and neutron diffraction structure factor

X-ray and neutron diffraction structure factors can be deduced from the $g(r)$ function from the MD models of the glasses and compared with experimental diffraction results. This is an essential process to validate the MD models of glasses. X-rays are high energy electromagnetic waves that consist of oscillating electric and magnetic field which interact with the electron cloud of atoms in a material. Neutrons are the neutral particles that will only interact with the nucleus of an atom via the strong nuclear force. It has the advantage of deep penetration to probe the bulk material but requires a large sample for strong scattering signal [55].

In theory X-ray and neutron diffraction formalism can be similar. In a single crystal if constructive interference is to occur among outgoing beams of X-rays of wavelength λ , then elastically scattered from regular plane of atoms, will obey the Bragg condition, given by Equation 2.45,

$$n\lambda = 2d\sin\theta \quad \text{Equation 2.45}$$

where d is the spacing of planes and n is an integer and the resultant diffracted X-rays are observed only for scattering angles 2θ and wavelengths λ that satisfy the scattering geometry for a point shown in Figure 2.10 [56].

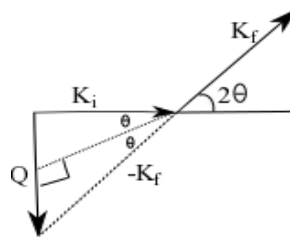


Figure 2.10 The vector diagram for elastic scattering geometry $|\mathbf{K}_i| = |\mathbf{K}_f|$ through an angle of 2θ [56].

The diffraction pattern produced by crystalline material is characteristically very different to glassy material. The diffraction experiments conducted with a non-crystalline sample is no different from that with a crystalline material however, observed diffraction pattern by non-crystalline materials are diffuse haloes in character [57]. Hence the Bragg's law is inappropriate and different conditions for diffraction should be derived for a non-crystalline structure material.

The scattering of both X-rays and neutrons from samples are characterised by the resultant change in the momentum and energy. If we consider the elastic scattering where energy is conserved then the scattering law will only depend on scattering vector or wave-vector transfer, \mathbf{Q} . The vector diagram for elastic scattering is shown in Figure 2.10 where \mathbf{K}_i is the incident wavevector on the sample and \mathbf{K}_f is the final wave vector scattered by the sample through an angle of 2θ . Intensities of the diffracted beams are recorded as a function of 2θ .

In a scattering theory X-rays or neutrons momentum and energy change as follows given by Equation 2.46 and 2.47,

$$\hbar\mathbf{Q} = \hbar\mathbf{K}_i - \hbar\mathbf{K}_f \quad \text{Equation 2.46}$$

$$\hbar\omega = E_i - E_f \quad \text{Equation 2.47}$$

where Planck constant $\hbar = h/2\pi$, angular frequency $\omega = 2\pi f$ and $\mathbf{Q} = \mathbf{K}_i - \mathbf{K}_f$. If there is no exchange of energy then after scattering, the modulus of the wave vector \mathbf{K} and the wavelength λ remains unchanged as given by Equation 2.48.

$$|\mathbf{K}_i| = |\mathbf{K}_f| = \frac{2\pi}{\lambda} \quad \text{Equation 2.48}$$

The parameter Q can be deduced by elementary trigonometry as given by Equation 2.49 and 2.50,

$$\frac{|\mathbf{Q}|}{2} = |\mathbf{K}_i| \sin\theta \quad \text{Equation 2.49}$$

$$Q = \frac{4\pi \sin\theta}{\lambda} \quad \text{Equation 2.50}$$

where $Q = |\mathbf{Q}|$ and this links the magnitude of the momentum transfer to the wavelength and scattering angle. This is known by the scattering vector in neutron diffraction and symbol k is conventionally used to represent the scattering vector in X-ray diffraction.

If the scatters are point charges, then the scattering intensity, I_{eu} , in terms of ‘electron units’ (eu) is given by modulus squared of amplitude as expressed in Equation 2.51,

$$I_{eu} = f_e f_e^* \quad \text{Equation 2.51}$$

f_e is the scattering factor which is given Equation 2.52.

$$f_e = \int \exp[\mathbf{Q} \cdot \mathbf{r}] \rho_e(\mathbf{r}) dV \quad \text{Equation 2.52}$$

Here, atomic electron charge is assumed to be distributed in a small volume dV , and $\rho_e(\mathbf{r})$ is the corresponding density variation as a function of \mathbf{r} . Assuming the electron distribution to have spherical symmetry so that r is simply treated as a scalar [53] gives Equation 2.53.

$$f_e = \int_0^\infty 4\pi r^2 \rho_e(r) \frac{\sin Qr}{Qr} dr \quad \text{Equation 2.53}$$

For an atom containing several electrons, the ‘atomic scattering factor’ is simply the sum of the individual amplitudes as given by Equation 2.54,

$$f = \sum_n f_{en} = \sum_n \int_0^\infty 4\pi r^2 \rho_{e_n}(r) \frac{\sin Qr}{Qr} dr \quad \text{Equation 2.54}$$

where $\rho_{e_n}(r)$ is the density distribution of electrons and $\sin Qr/Qr$ tends to 1 for small value of Q and so integral will give the total number of electrons in the atom or atomic num-

ber Z . Hence f itself tends to Z as Q tends to zero. The atomic scattering factor, f , is a function of Q and the variation of $f(Q)$ as function of Q is shown in Figure 2.11 [58] for X-rays and neutrons.

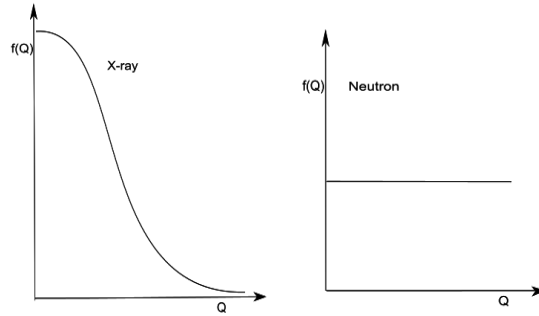


Figure 2.11 Schematic diagram of Q dependence of atomic form factor, f , for X-ray and neutron diffraction [58].

In an amorphous material, the scattered intensity $I(Q)$ is given by the overall summation of the scattered amplitude $A(Q)$ from all atoms, i , having positions, \mathbf{r}_i , multiplied by its complex conjugate. Equation 2.55 and 2.56 defines $A(Q)$ and $I(Q)$ respectively,

$$A(Q) = \sum_i f_i \exp(i\mathbf{Q} \cdot \mathbf{r}_i) \quad \text{Equation 2.55}$$

$$I(Q) = \sum_i f_i \exp(i\mathbf{Q} \cdot \mathbf{r}_i) \sum_j f_j \exp(-i\mathbf{Q} \cdot \mathbf{r}_j) \quad \text{Equation 2.56}$$

where subscript i is number of atoms $1 \dots N$. By introducing the vector, $\mathbf{r}_{ij} = \mathbf{r}_i - \mathbf{r}_j$, and Equation 2.56 can be written as Equation 2.57.

$$I(Q) = \sum_i \sum_j f_i f_j \exp(\mathbf{Q} \cdot \mathbf{r}_{ij}) \quad \text{Equation 2.57}$$

The probability of finding two atomic scatters at distance r_{ij} from a given atom is identical in all directions assuming the isotropic nature of the amorphous solid and taking the average of the exponential term in above equation yields the ‘Debye equation’ [54, 55] for an isotropic collection of scattering atoms, which is given in Equation 2.58.

$$I(Q) = \sum_i \sum_j f_i f_j \frac{\sin Q r_{ij}}{Q r_{ij}} \quad \text{Equation 2.58}$$

If the type of atom in a material is monoatomic, i.e. one type of atoms, then $I(Q)$ is given by Equation 2.59.

$$I(Q) = \sum_i f^2 + \sum_i \sum_{i \neq j} f^2 \frac{\sin Q r_{ij}}{Q r_{ij}} \quad \text{Equation 2.59}$$

In the above Equation 2.59, the density function $\rho_i(r_{ij})$ is introduced considering i as the atom at the origin and the summation over j can be replaced by the integral over the sample volume with an assumed spherical symmetry to give Equation 2.60.

$$I(Q) = \sum_i f^2 + \sum_i f^2 \int \rho_i(r_{ij}) \frac{\sin Q r_{ij}}{Q r_{ij}} dV_j \quad \text{Equation 2.60}$$

If the density is expressed as an appropriate isotropic function of r and taking into consideration that at sufficiently large distance, r , $\rho(r)$ tends to ρ^0 , which is the constant average density then the Equation 2.60 can be written as Equation 2.61,

$$I(Q) = N f^2 + N f^2 \int_0^\infty 4\pi r^2 [\rho(r) - \rho^0] \frac{\sin Q r}{Q r} dr \quad \text{Equation 2.61}$$

where the effect of ρ^0 can be ignored at $Q = 0$, which is not measured and N is the total number of atoms in the sample. The reduced scattering function, $F(Q)$, is given by Equation 2.62.

$$F(Q) = Q \left[\frac{I(Q)}{N f^2} - 1 \right] \quad \text{Equation 2.62}$$

The differential or reduced radial distribution function, $G(r)$, is given by Equation 2.33 and $F(Q)$ and $G(r)$ oscillate about zero instead of being an increasing or decreasing function of Q or r . Thus $F(Q)$ can be written as Equation 2.63.

$$F(Q) = \int_0^\infty G(r) \sin Q r dr \quad \text{Equation 2.63}$$

The function $F(Q)$ is obtained from the experimental scattering intensity in Q -space. The reduced pair distribution function, $G(r)$, is related to $F(Q)$ through a sine Fourier transform as given by Equation 2.64.

$$G(r) = \frac{2}{\pi} \int_0^{\infty} F(Q) \sin Qr \, dQ \quad \text{Equation 2.64}$$

The structure factor, $S(Q)$ is related to $F(Q)$ by the expression given by Equation 2.65,

$$F(Q) = Q[S(Q) - 1] \quad \text{Equation 2.65}$$

and the $S(Q)$ is defined in Equation 2.66.

$$S(Q) = \frac{I(Q)}{Nf^2} \quad \text{Equation 2.66}$$

The structure factor can be calculated from the pair distribution function (PDF) as given by Equation 2.67.

$$Q[S(Q) - 1] = \int_0^{\infty} (T(r) - 4\pi r \rho^0) \sin Qr \, dr \quad \text{Equation 2.67}$$

In a monoatomic system, all the atoms are chemically identical providing no correlation between scattering length, and atomic position in the sample. In a polyatomic system scattering length distribution is different for neutron for given chemical species, i , and for X-ray scattering length depends on Z_i . Different chemical species also have different interatomic correlations so to describe the structure factor for polyatomic system one has to consider several partial structure factors, $S_{ij}(Q)$ [53]. Therefore, for more than one type of atoms, the $T_{ij}(r)$ contribution to $S(Q)$ depends on concentration of atoms and the atomic scattering factors. Hence, in Equation 2.67, weighting factor w_{ij} is added to generate $S(Q)$ from T_{ij} , which is expressed in Equation 2.68,

$$Q(S(Q) - 1) = \sum_{ij} w_{ij} (Q) \int_0^{\infty} (T_{ij}(r) - 4\pi r \rho_j) \sin Qr \, dr \quad \text{Equation 2.68}$$

where, w_{ij} is defined by Equation 2.78,

$$w_{ij} = \frac{c_i c_j f_i f_j}{\langle f \rangle^2} \quad \text{Equation 2.69}$$

and defining $\langle f \rangle = \sum_{i=1}^N c_i f_i$. The monoatomic system is expressed in polyatomic system by using the weighted values for the scattering factors and $\rho(r)$ is expressed as function of scattering factors by the w_{ij} as shown by Equation 2.70,

$$\rho(r) = \sum_{ij} c_i \rho_{ij}(r) \quad \text{Equation 2.70}$$

where $\rho_{ij}(r)$ is the average number of j atoms per unit volume at distance r from any i atom.

The w_{ij} are the main factors that causes the different scattering results for X-ray and neutron diffraction. The calculation of w_{ij} for X-ray is given by Equation 2.71,

$$w_{ij} = \frac{(2 - \delta_{ij}) c_i c_j Z_i Z_j}{\langle Z^2 \rangle} \quad \text{Equation 2.71}$$

where δ_{ij} is the Kronecker delta function, $\delta_{ij} = 1$ for $i = j$ and $\delta_{ij} = 0$ for $i \neq j$. Referring to Figure 2.11, this is a good approximation for X-ray, as $f \rightarrow Z$ as $Q \rightarrow 0$ but for the neutrons the weighting factor is true because it only depends on the scattering length, b , which is given by Equation 2.72.

$$w_{ij} = \frac{(2 - \delta_{ij}) c_i c_j b_i b_j}{\langle b^2 \rangle} \quad \text{Equation 2.72}$$

In the diffraction experiments, the value of maximum Q measured is finite and hence this Q_{max} leads to peak broadening in real space after Fourier transformation as well as to non-physical oscillation in $g(r)$ and in other r -space functions. Therefore, the termination of the data can be represented by the modification function $M(Q)$ describing the experimental Q -range, with $M(Q > Q_{max}) = 0$. This is Fourier-transformed to produce the r -

space modification function with which theoretical r -space function is convolved before comparison or fitting to Fourier-transformed diffraction data [53]. However, in this thesis only at Chapter 4 the Waser modification function (see Figure 1. *c* in [59]) is used to show $T(r)$ from X-ray diffraction data for the barium silicate glass.

2.7 References

- [1] D. Tabor, *Gases, Liquids and Solids*, 2nd ed., Cambridge University Press, Cambridge, 1979.
- [2] I.M. Torrens, *Interatomic Potentials*, Academic Press, New York and London, 1972.
- [3] B.S. Mitchell, *An Introduction to Materials Engineering and Science for Chemical and Materials Engineers*, John Wiley and Sons, New Jersey, 2003.
- [4] J.C. Xie, S.K. Mishra, T. Kar, R. Xie, Generalized interatomic pair-potential function, *Chemical Physics Letters*. 605–606 (2014) 137-146.
- [5] I.G. Kaplan, *Intermolecular Interactions: Physical Picture, Computational Methods and Model Potentials*, 1st ed., John Wiley & Sons Ltd, England, 2006.
- [6] G. Bonny, L. Malerba, Overview of interatomic potentials, Open Report of The Belgian Nuclear Research Centre. (2005).
- [7] M. Rieth, *Nano-Engineering in Science and Technology: An Introduction to the World of Nano-Design*, World Scientific, New Jersey, 2003.
- [8] J. Hill, C.M. Freeman, L. Subramanian, Use of Force Fields in Materials Modelling, *Reviews in Computational Chemistry*. 16 (2000) 141-216.
- [9] J.R. Hill, L. Subramanian, A. Maiti, *Molecular Modelling Techniques in Material Sciences*, Taylor & Francis Group, 2005.
- [10] A.R. Leach, *Molecular Modelling: Principles and Applications*, Prentice Hall, Harlow, 2001.
- [11] J.H. Li, X.D. Dai, S.H. Liang, K.P. Tai, Y. Kong, B.X. Liu, Interatomic potentials of the binary transition metal systems and some applications in materials physics, *Physics Reports*. 455 (2008) 1-134.
- [12] C.R.A. Catlow, *Computer Modeling in Inorganic Crystallography*, Academic Press, 1997.
- [13] Ş. Erkoç, Empirical many-body potential energy functions used in computer simulations of condensed matter properties, *Physics Reports*. 278 (1997) 79-105.

- [14] T.C. Lim, Relationship and discrepancies among typical interatomic potential functions, *Chinese Physics Letters*. 21 (2004) 2167-2170.
- [15] T.C. Lim, Connection among classical interatomic potential functions, *Journal of Mathematical Chemistry*. 36 (2004) 261-269.
- [16] C. Massobrio, J. Du, M. Bernasconi, P.S Salmon, *Molecular Dynamics Simulations of Disordered Materials: From Network Glasses*, 215 (2015).
- [17] R.A. Jackson, P.A. Meenan, G.D. Price, K.J. Roberts, G.B. Telfer, P.J. Wilde, Deriving empirical potentials for molecular ionic materials, *Mineralogical Magazine*. 59 (1995) 617-622.
- [18] H.B. Schlegel, *Geometry optimization*, Wiley Interdisciplinary Reviews: Computational Molecular Science. 1 (2011) 790-809.
- [19] E.G. Lewars, *Computational Chemistry: Introduction to the Theory and Applications of Molecular and Quantum Mechanics*, 2nd ed., Springer, Netherlands, 2011.
- [20] C.S. Tsai, *An Introduction to Computational Biochemistry*, John Wiley & Sons, 2003.
- [21] J.D. Gale, A.L. Rohl, The General Utility Lattice Program (GULP), *Molecular Simulation*. 29 (2003) 291-341.
- [22] J.D. Gale, GULP: A computer program for the symmetry-adapted simulation of solids, *Journal of the Chemical Society, Faraday Transactions*. 93 (1997) 629-637.
- [23] J.D. Gale, *General Utility Lattice Program, GULP manual*. (1998).
- [24] "We wish to acknowledge the use of the EPSRC funded National Chemical Database Service hosted by the Royal Society of Chemistry".
- [25] D. Teter, Private communication, (2004).
- [26] J. Du, R. Devanathan, L.R. Corrales, W.J. Weber, A.N. Cormack, Short- and medium-range structure of amorphous zircon from molecular dynamics simulations, *Phys. Rev. B*. 74 (2006) 214204.
- [27] A. Tilocca, N.H. de Leeuw, A.N. Cormack, Shell-model molecular dynamics calculations of modified silicate glasses, *Phys. Rev. B*. 73 (2006) 104209.
- [28] S. Sperinck, P. Raiteri, N. Marks, K. Wright, Dehydroxylation of kaolinite to metakaolin a molecular dynamics study, *J. Mater. Chem*. 21 (2011) 2118-2125.
- [29] D. Frenkel, B. Smit, *Understanding Molecular Simulation: From Algorithms to Applications*, 2nd ed., Academic Press, 2001.
- [30] G. Sutmann, *Classical Molecular Dynamics*, Citeseer, 2002.
- [31] U. Landman, *Molecular Dynamics Simulations in Material Science and Condensed Matter Physics*, in: Landau, David P. and Mon, K. K. and Schüttler, Heinz-Bernd (Ed.),

Computer Simulation Studies in Condensed Matter Physics, Springer Berlin Heidelberg, 1988, pp. 108-123.

[32] K. Binder, J. Horbach, W. Kob, W. Paul, F. Varnik, Molecular dynamics simulations, *Journal of Physics: Condensed Matter*. 16 (2004) S429.

[33] M.P. Allen, D.J. Tildesley, *Computer Simulation of Liquids*, Clarendon Press; 1990, Oxford [England], 1987.

[34] J.M. Haile, *Molecular Dynamics Simulation: Elementary Methods*, Wiley, New York, 1992.

[35] S.I. Simdyankin, M. Dzugutov, *Case Study: Computational Physics-The Molecular Dynamics Method*, Royal Institute of Technology, Stockholm. (2003).

[36] M. Tuckerman, *Statistical Mechanics: Theory and Molecular Simulation*, Oxford University Press, 2010.

[37] S. Nosé, Molecular dynamics simulations at constant temperature and pressure, in: *Anonymous Computer Simulation in Materials Science*, Springer, 1991, pp. 21-41.

[38] R.J. Sadus, *Molecular Simulation of Fluids: Theory, Algorithms, and Object-Oriented*, Elsevier, 2002.

[39] T.R. Forester, W. Smith, *The DL_POLY_2.0 user manual*, CCLRC, Daresbury Laboratory, Warrington WA4 4AD, UK. (1997).

[40] W. Li, T. Ying, W. Jian, D. Yu, Comparison research on the neighbor list algorithms: Verlet table and linked-cell, *Comput. Phys. Commun.* 181 (2010) 1682-1686.

[41] G.S. Grest, B. Dünweg, K. Kremer, Vectorized link cell Fortran code for molecular dynamics simulations for a large number of particles, *Comput. Phys. Commun.* 55 (1989) 269-285.

[42] Z. Yao, J. Wang, G. Liu, M. Cheng, Improved neighbor list algorithm in molecular simulations using cell decomposition and data sorting method, *Comput. Phys. Commun.* 161 (2004) 27-35.

[43] A. Heinecke, W. Eckhardt, M. Horsch, H. Bungartz, *Molecular Dynamics Simulation*, in: *Anonymous Supercomputing for Molecular Dynamics Simulations*, Springer, 2015, pp. 11-29.

[44] W. Smith, I.T. Todorov, A short description of DL_POLY, *Molecular Simulation*. 32 (2006) 935-943.

[45] G. Sutmann, V. Stegailov, Optimization of neighbor list techniques in liquid matter simulations, *Journal of Molecular Liquids*. 125 (2006) 197-203.

[46] M. Deserno, C. Holm, How to mesh up Ewald sums. I. A theoretical and numerical comparison of various particle mesh routines, *J. Chem. Phys.* 109 (1998) 7678.

- [47] A.Y. Toukmaji, J.A. Board, Ewald summation techniques in perspective: a survey, *Comput. Phys. Commun.* 95 (1996) 73-92.
- [48] X. Qian, T. Schlick, Efficient multiple-time-step integrators with distance-based force splitting for particle-mesh-Ewald molecular dynamics simulations, *J. Chem. Phys.* 116 (2002) 5971-5983.
- [49] E.R. Hernández, *Molecular Dynamics: from basic techniques to applications (A Molecular Dynamics Primer)*, (2008).
- [50] D. Jincheng, Private Communication, Alfred State University, USA.
- [51] Accelrys Software Inc, *MS Modelling*, Version 3.2 (2005).
- [52] S. Le Roux, V. Petkov, ISAACS—interactive structure analysis of amorphous and crystalline systems, *Journal of Applied Crystallography*. 43 (2010) 181-185.
- [53] H.E. Fischer, A.C. Barnes, P.S. Salmon, Neutron and x-ray diffraction studies of liquids and glasses, *Reports on Progress in Physics*. 69 (2005) 233.
- [54] K.J. Rao, *Structural Chemistry of Glasses*, Elsevier, 2002.
- [55] C.J. Simmons, O.H. El-Bayoumi, *Experimental Techniques of Glass Science*, Amer Ceramic Society, 1993.
- [56] D.S. Sivia, *Elementary Scattering Theory: For X-Ray and Neutron Users*, 1st ed., Oxford University Press, New York, 2011.
- [57] S.R. Eliot, *Physics of amorphous materials*, (1990).
- [58] Y. Waseda, *The structure of non-crystalline materials: liquids and amorphous solids*, (1980).
- [59] J. Waser, The Fourier Inversion of Diffraction Data, *Rev. Mod. Phys.* 25 (1953) 671-690.

Chapter 3

The method of rotational invariants

3.1 Introduction

The pair distribution function and structure factor (i.e. obtained from its Fourier transformation), coordination number, network connectivity and bond angle distribution functions are some of the conventional techniques for local structure analysis of simulated glass models. In an atomistic model, the bond angle distribution functions (BAD) can describe the coordination geometries of atoms. The alternative parameters, known as rotational invariants, Q_l , can also describe the type of and degree of order in coordination geometries [1]. In previous studies, they were used to describe liquid and amorphous structures, and were also referred to as “bond orientational order parameters” [2] and “spherical invariants” [3].

Notably Q_l were used to characterise the order in coordination geometries of atoms in Lennard-Jones (LJ) liquids and dense random packing of hard spheres models. Remarkably, Q_l were reported only for l even (despite that Q_l for l odd will be non-zero when there is lack of centrosymmetry) and thus proposing resemblance to icosahedral geometry [1]. There was a later study [4] done on LJ liquids that reported values for both l even and odd but large values were found for l odd, challenging the previous hypothesis of icosahedral geometry [1]. Perhaps, the most accepted previous study was done by Steinhardt et al. [2] as there are number of published studies such as [5-9], which are based on their work looking at different bond orientational order parameters.

Network former and modifier cations of glasses form a polyhedral structure with the nearest neighbouring anions and these cations coordination polyhedra have vertices, which are defined by the nearest neighbour anions to which the cations are ionically bonded (i.e. in the case of ionic glasses). Cations coordination polyhedra can be compared with the all

the possible reference convex polyhedra structures in terms of rotational invariant parameters, Q_l . The reference convex polyhedra of Johnson solids, Platonic solids and Archimedean solids with the vertices, N , between 4 and 12 are investigated. The Platonic solids are regular convex polyhedra with equivalent faces composed of congruent convex regular polygons, and the Archimedean solids are the convex polyhedra that have similar arrangement of non-intersecting regular convex polygons of two or more different types arranged in the same way about each vertex with all sides the same length. The rest of the convex polyhedra with regular faces and equal length edges can be defined as the Johnson solids [10].

3.2 Calculation of rotational invariants

In the glass, an atom at position, R_i , is given by $\mathbf{R}_i = (x_i, y_i, z_i)$. However, this can also be represented by the angular coordinate function or spherical function, $f(r, \theta, \phi)$ pictured in Figure 3.1.

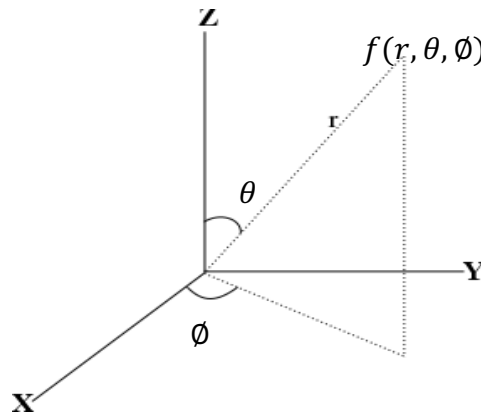


Figure 3.1 Polar coordinates, where $0 \leq \theta \leq \pi$ and $0 \leq \phi \leq 2\pi$.

The information between the neighbouring atoms j relative to a given central atom i can be expressed in Equation 3.1,

$$T_{ij}(x, y, z) = \sum_{j \neq i} \delta(x - x_{ij}) \delta(y - y_{ij}) \delta(z - z_{ij}) \quad \text{Equation 3.1}$$

where $x_{ij} = (x_j - x_i)$ and for an isotropic material like glass, the correlation in radial position of neighbouring atoms R_{ij} can be described using the pair distribution function, $T_{ij}(r)$, given by Equation 2.41 (see Chapter 2), which is the orientational average of $T_{ij}(x, y, z)$ over all atoms i [1] and given by Equation 3.2.

$$T(r) = \frac{1}{N} \sum_i \sum_{j \neq i} \delta(r - R_{ij}) \quad \text{Equation 3.2}$$

In $T(r)$, bond length, r (radial distance), corresponds to nearest neighbours. Alternatively, the correlation can be also expressed in angular positions of nearest neighbour atoms, θ_{ij} and ϕ_{ij} , by using the bond angle distribution function. The part of the function, $T_{ij}(x, y, z)$, that depends on angular positions, θ_{ij} and ϕ_{ij} , [1] is given by Equation 3.3,

$$\tau_{ij}(\theta, \phi) = \sum_{j \neq i} \delta(\theta - \theta_{ij}) \delta(\phi - \phi_{ij}) \quad \text{Equation 3.3}$$

where θ_{ij} gives the angular position of atom j when atom i is at the origin.

The BAD as a function of θ describing the coordinate geometries from the distribution of neighbouring atoms 1 and 2 relative to central atom can normally be calculated by Equation 3.4,

$$\mathbf{r}_1 \cdot \mathbf{r}_2 = |\mathbf{r}_1| |\mathbf{r}_2| \cos \theta \quad \text{Equation 3.4}$$

where \mathbf{r}_1 is the vector between centre atom and the first neighbouring atom and \mathbf{r}_2 is the vector between centre atom and the second neighbouring atom.

From the theory of spherical harmonics [11], the spherical function, $f(\theta, \phi)$, can be decomposed as the sum of its harmonics [12], given by Equation 3.5,

$$f(\theta, \phi) = \sum_l \sum_m C_{lm} Y_{lm}(\theta, \phi) \quad \text{Equation 3.5}$$

where radial factors r can be ignored assuming it's approximately equidistance from central atom to the nearest neighbour atoms and $Y_{lm}(\theta, \phi)$ is the spherical harmonic function with $l = 0, 1, 2, 3, \dots$, and $m = -l, -l + 1, \dots, l - 1, l$.

From the properties of completeness and orthogonality [13], the value of coefficient C_{lm} is given by Equation 3.6,

$$C_{lm} = \iint f(\theta, \phi) Y_{lm}^*(\theta, \phi) \sin\theta d\theta d\phi \quad \text{Equation 3.6}$$

where $*$ denotes the complex conjugate. Normalization of $f(\theta, \phi)$ gives Equation 3.7,

$$\sum_{l=0}^{\infty} |C_{lm}|^2 = 1 \quad \text{Equation 3.7}$$

where C_{lm} depend on the axis orientation.

The function from Equation 3.3 is equal to Equation 3.5 [1] and are considered discrete functions. The presence of the delta function in Equation 3.3 complicates the normalisation and for convenience $\tau_{ij}(\theta, \phi)$ is not normalised. From Equations 3.3, 3.5 and 3.6, i.e. substituting $\tau_{ij}(\theta, \phi)$ into the expression for C_{lm} gives Equation 3.8.

$$C_{lm} = \sum_{j \neq i} Y_{lm}^*(\theta_{ij}, \phi_{ij}) \quad \text{Equation 3.8}$$

The coefficients C_{lm} in their complex number form are rotationally-dependent [14], which cannot be important in an isotropic material. They can be converted to a rotationally invariant form by computing the magnitude of each coefficient. Therefore, the second order rotational invariant, Q_l , is deduced by Equation 3.9,

$$Q_l = \left(\frac{1}{2l+1} \sum_m |C_{lm}|^2 \right)^{\frac{1}{2}} \quad \text{Equation 3.9}$$

here, the invariant circular 4π factor is not included whereas in other literature it is included in calculation of the Q_l values. The fact that Q_l does not depend on axis orientation can be demonstrated by using the example function given by Equation 3.10,

$$f(\theta, \phi) = \cos(2\theta) = \cos 2\hat{z} \quad \text{Equation 3.10}$$

as this function has the spherical harmonic coefficients $C_{00} = 0.489$, $C_{20} = 0.874$ and comparing with the example function given by the Equation 3.11,

$$f(\theta, \phi) = \sin(2\theta) \cos(2\phi) = \cos 2\hat{x} \quad \text{Equation 3.11}$$

which has the spherical harmonic coefficients $C_{00} = 0.489$, $C_{20} = -0.438$ and $C_{22} = C_{-2-2} = 0.536$. As illustrated in Figure 3.2 these two functions differ only in the axis orientation and both functions have the same rotational invariants $Q_0 = 0.489$ and $Q_2 = 0.391$. Figure 3.3 is another example of functions having same Q_l but different spherical harmonics coefficients.

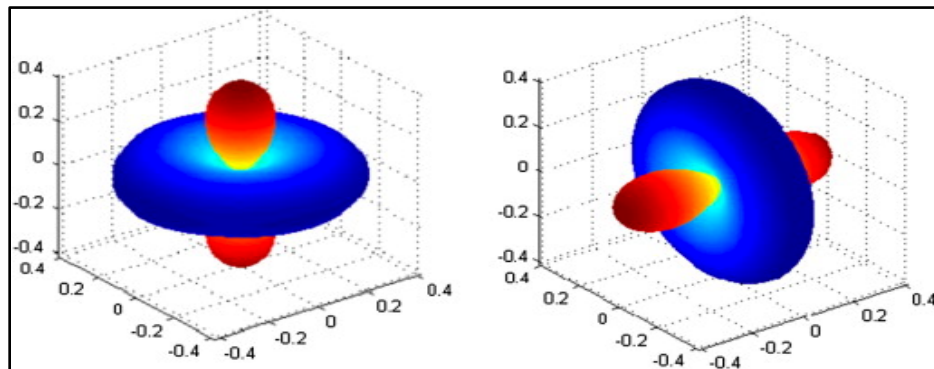


Figure 3.2 (Left) first example smooth function oriented along the z -axis $f(\theta, \phi) = \cos(2\theta)$ and (right) second example smooth function oriented along the x -axis $f(\theta, \phi) = \sin(2\theta) \cos(2\phi)$. Both functions have same rotational invariants $Q_0 = 0.489$ and $Q_2 = 0.936$ but the spherical harmonic coefficients are different [1].

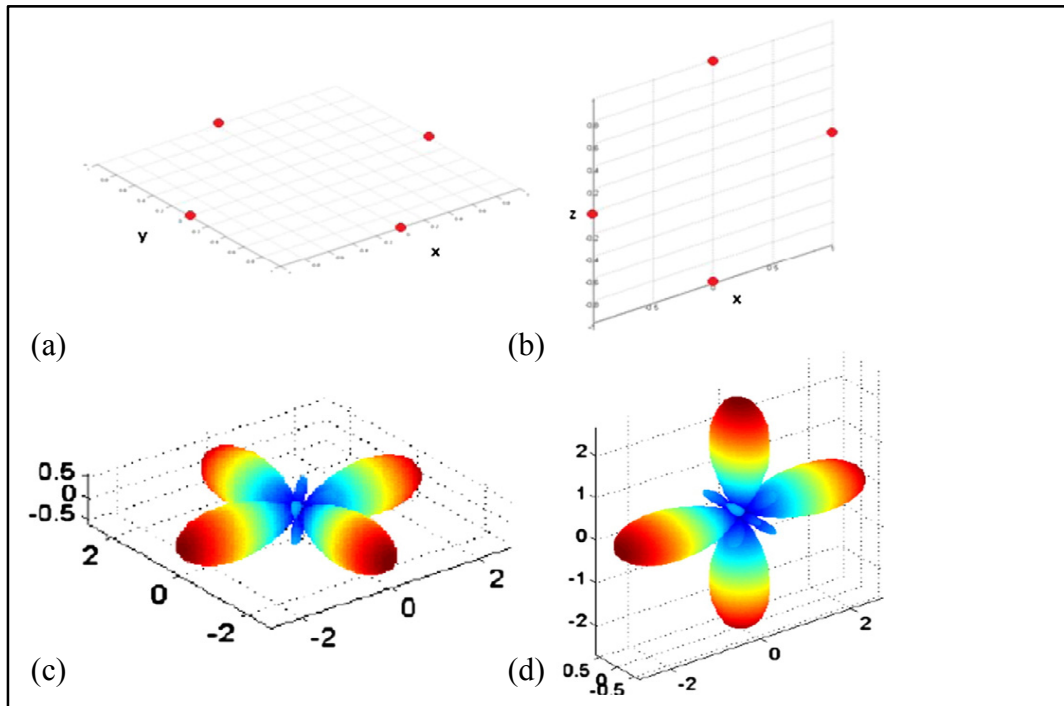


Figure 3.3 The discrete function (four points in a cross) orientated in the (a) horizontal x, y plane and (b) vertical x, y plane. The (c) and (d) are the reconstructions using spherical harmonics coefficient C_{lm} for $l = 1$ to 5. Both have different spherical harmonics coefficients but have same rotational invariants $Q_0 = 1.128$, $Q_2 = 0.564$ and $Q_4 = 0.936$ [1].

3.3 Reference polyhedra

All the possible convex polyhedra with vertices, $4 \leq N \leq 12$ were extracted from the Wolfram Mathematica [15]. One way to distinguish polyhedra with the same vertices, N , is by the values of their Q_l and l can be thought of as the order of “nodal” symmetry. The names and the 3D pictures of the all reference convex polyhedra, $4 \leq N \leq 12$ are illustrated in Figures 3.4 – 3.7.

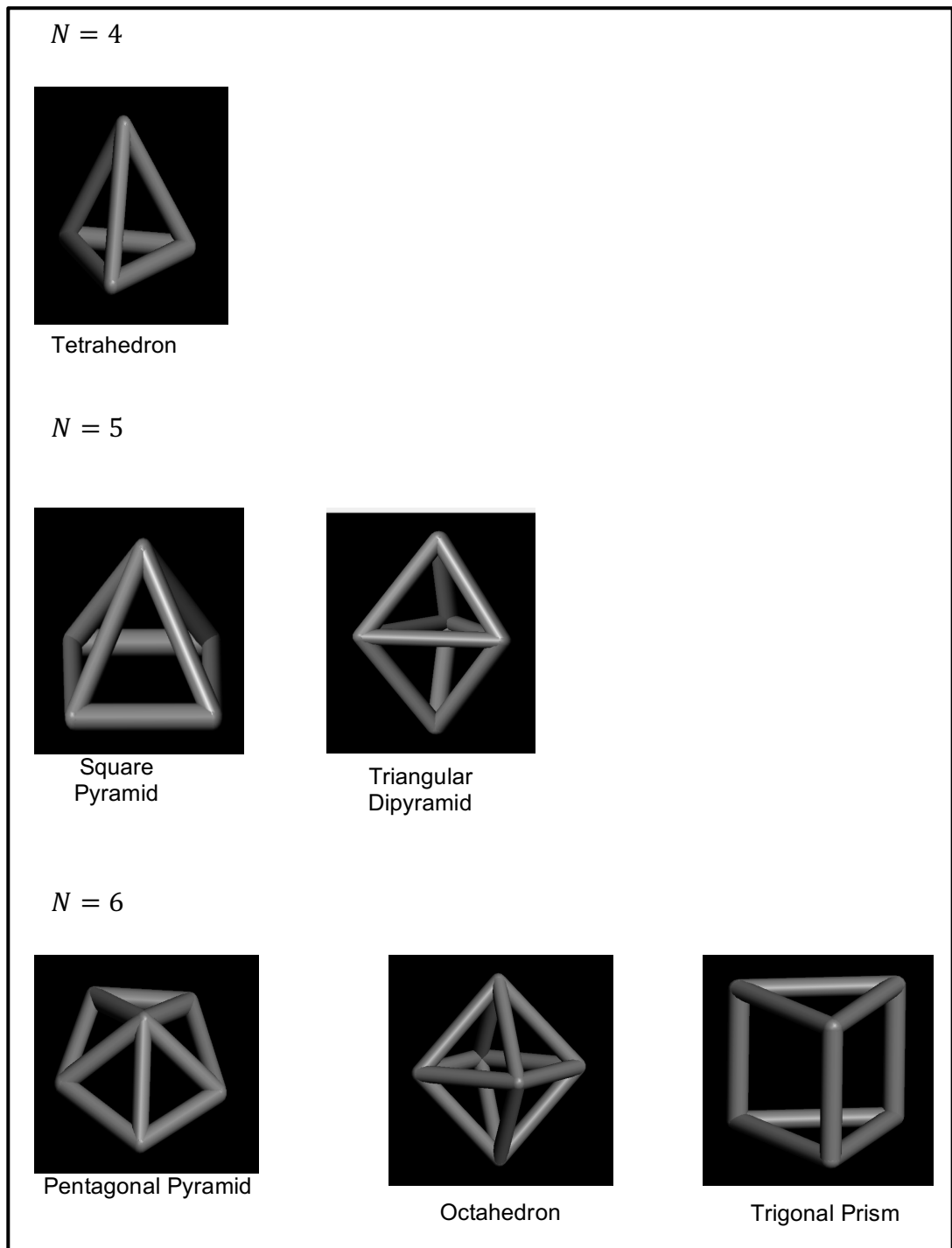


Figure 3.4 Reference convex polyhedra $4 \leq N \leq 6$.

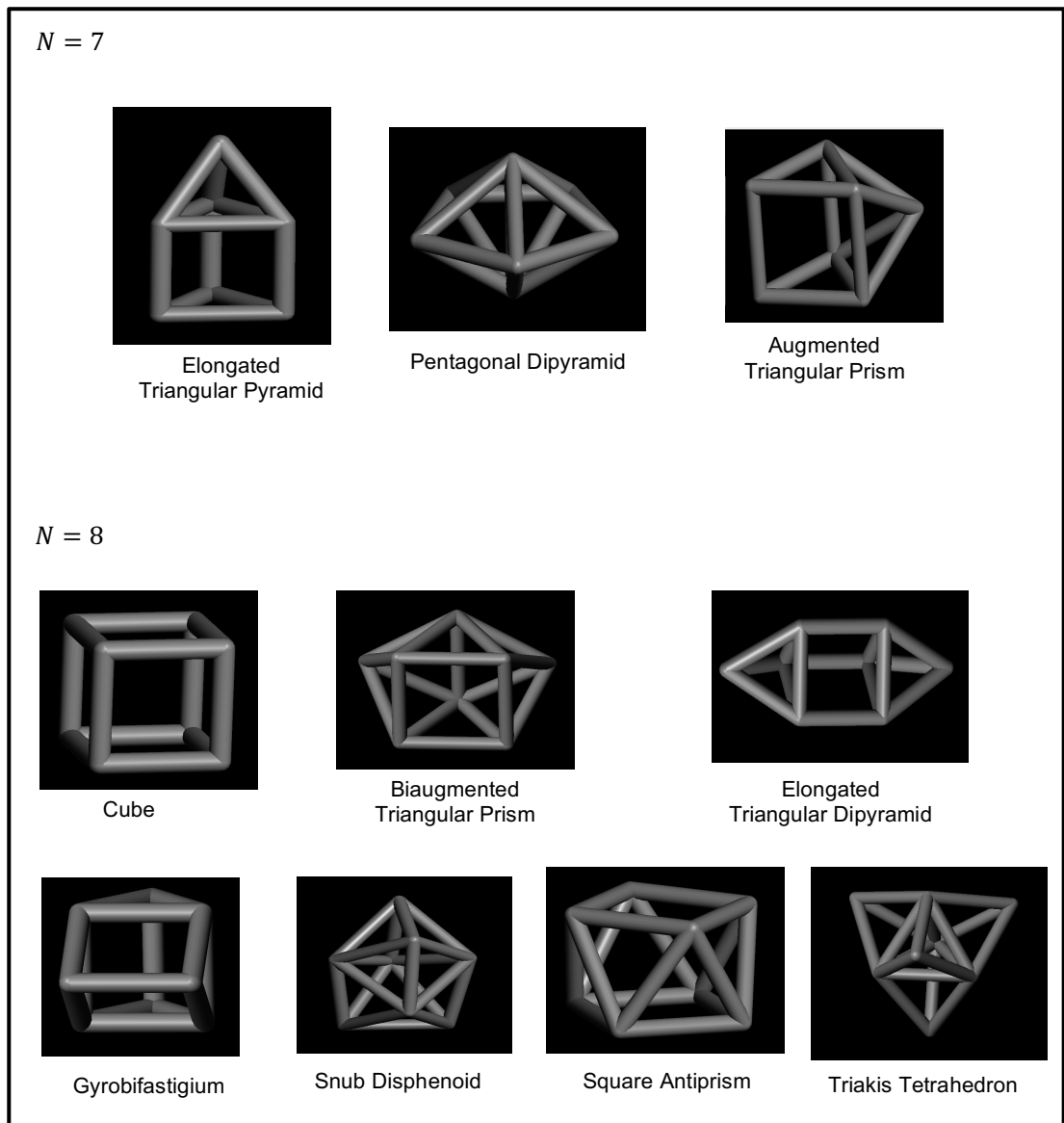


Figure 3.5 Reference convex polyhedra $7 \leq N \leq 8$.

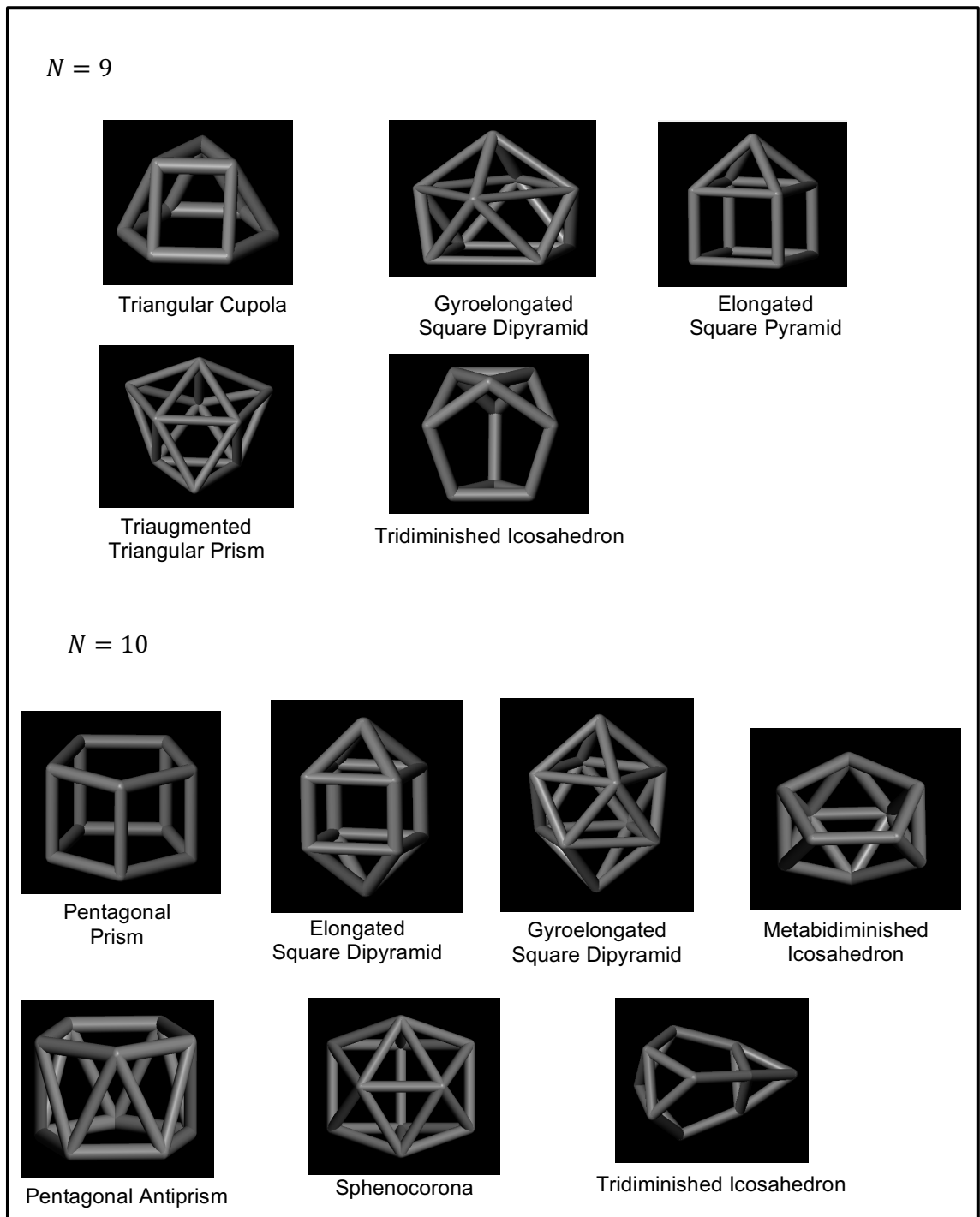


Figure 3.6 Reference convex polyhedra $9 \leq N \leq 10$.

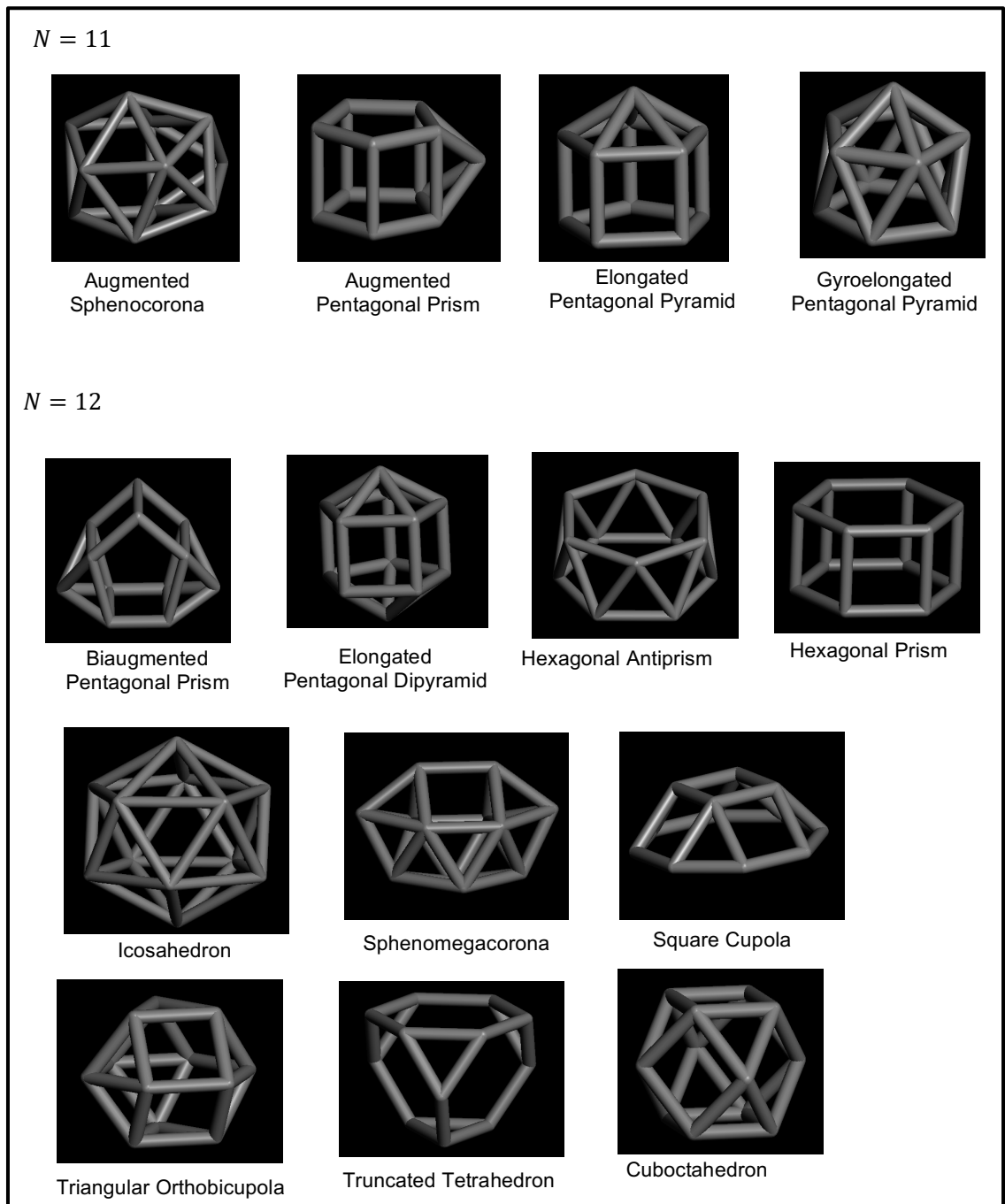


Figure 3.7 Reference convex polyhedra $11 \leq N \leq 12$.

3.4 Nearest neighbour distances, bond angle distributions and coordination numbers for reference polyhedra

In the following Figures 3.8 – 3.13 are the examples of reference polyhedra with their parameters such as the number of vertices, N , or the coordination numbers, CN , the vertices distances from the centre of the mass (COM), i.e. the neighbouring distances from the central position, and the angles subtend by each vertex with another vertex.

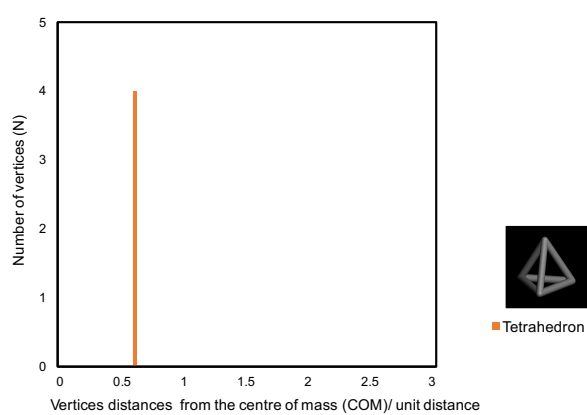


Figure 3.8 Tetrahedron vertices, $N = 4$, i.e. $CN = 4$ and the vertices distances from the COM.

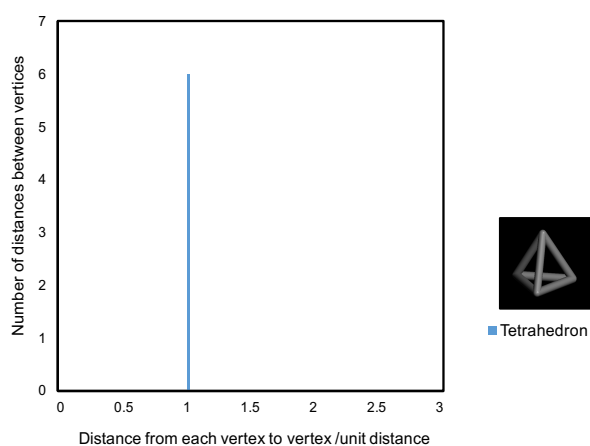


Figure 3.9 Tetrahedron distances from each vertex to another vertex and the number of distances between the vertices.

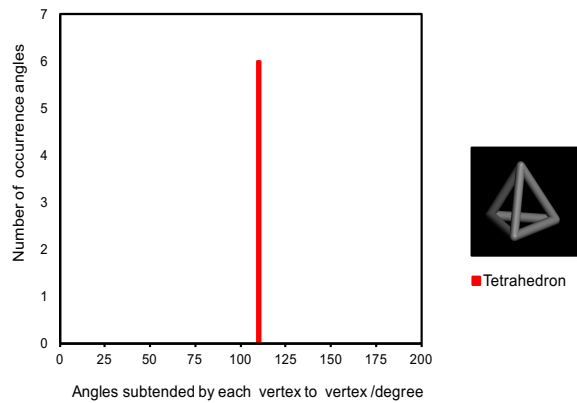


Figure 3.10 Angles subtended by each vertex to another vertex in a tetrahedron polyhedron.

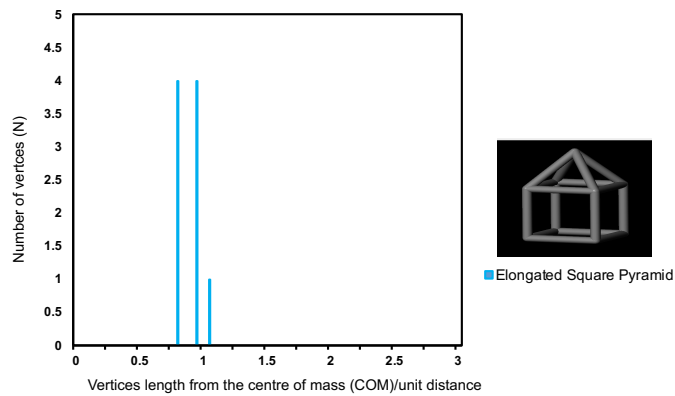


Figure 3.11 Elongated Square Pyramid vertices, $N = 9$, i.e. $CN = 9$ and the vertices distances from the COM.

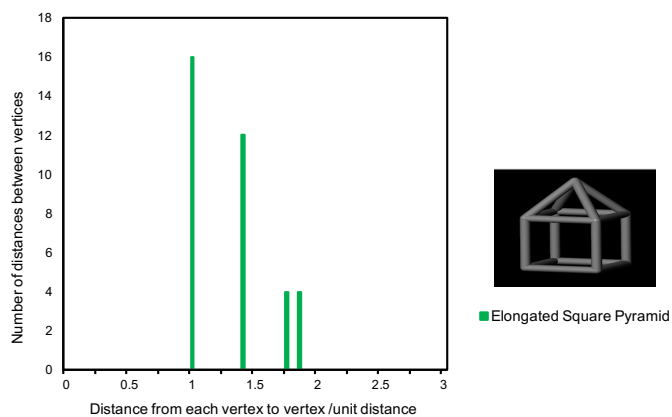


Figure 3.12 Elongated Square Pyramid distances from each vertex to another vertex and number of distances between vertices.

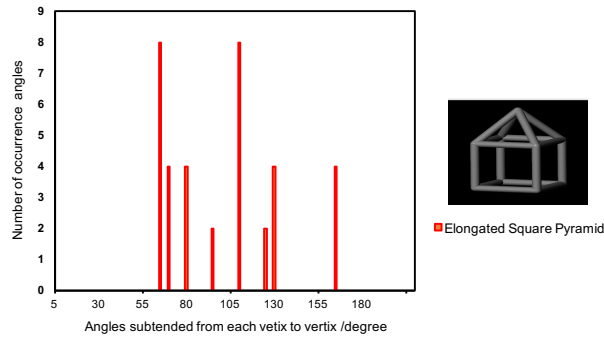


Figure 3.13 Angles subtended by each vertex to another vertex in Elongated Square Pyramid polyhedron.

3.5 Rotational invariants values of the reference polyhedra

As aforementioned, the Cartesian coordinates of all possible convex polyhedra, $4 \leq N \leq 12$ were extracted from Wolfram Mathematica [15] and they were converted to polar coordinates to evaluate the spherical harmonics coefficients, C_{lm} . Then using equation 3.9 the Q_l values of the reference polyhedra were evaluated, which are shown in Tables 3.1 – 3.13.

Table 3.1 Q_l values for $l = 1$ to 10 of convex polyhedra with vertices, $N = 4$.

Q_l	Tetrahedron ($N = 4$)
l	
0	1.128
1	0.000
2	0.000
3	0.841
4	0.575
5	0.000
6	0.709
7	0.691
8	0.240
9	0.584
10	0.734

Table 3.2 Q_l values for $l = 1$ to 10 of convex polyhedra with vertices, $N = 5$.

Q_l l	Square Pyramid ($N = 5$)	Triangular Dipyramid ($N = 5$)
0	1.410	1.410
1	0.061	0.000
2	0.217	0.141
3	0.593	0.669
4	0.947	0.881
5	0.458	0.442
6	0.350	0.643
7	0.782	0.364
8	0.655	0.885
9	0.654	0.605
10	0.455	0.482

Table 3.3 Q_l values for $l = 1$ to 10 of convex polyhedra with vertices, $N = 6$.

Q_l l	Octahedron ($N = 6$)	Pentagonal Pyramid ($N = 6$)	Trigonal Prism ($N = 6$)
0	1.693	1.693	1.693
1	0.000	0.138	0.000
2	0.000	0.401	0.242
3	0.000	0.495	0.578
4	1.293	0.756	0.725
5	0.000	0.964	1.092
6	0.598	0.334	0.215
7	0.000	0.801	0.102
8	1.215	0.662	0.942
9	0.000	0.379	0.747
10	0.696	0.909	0.770

Table 3.4 Q_l values for $l = 1$ to 10 of convex polyhedra with vertices, $N = 7$.

Q_l	Elongated Triangular Pyramid ($N = 7$)	Pentagonal Dpyramid ($N = 7$)	Augmented Triangular Prism ($N = 7$)
l			
0	1.975	1.975	1.957
1	0.036	0.000	0.048
2	0.468	0.141	0.176
3	0.637	0.000	0.317
4	0.291	1.093	0.932
5	1.113	0.990	1.091
6	0.787	0.123	0.573
7	0.617	0.670	0.317
8	0.846	0.950	0.697
9	0.312	0.559	1.052
10	0.818	0.865	0.666

Table 3.5 Q_l values for $l = 1$ to 10 of convex polyhedra with vertices, $N = 8$.

Q_l	Biaugmented Triangular Prism ($N = 8$)	Cube ($N = 8$)	Elongated Triangular Dpyramid ($N = 8$)
l			
0	2.257	2.257	2.257
1	0.034	0.000	0.000
2	0.232	0.000	0.806
3	0.109	0.000	0.578
4	0.725	1.149	0.161
5	1.385	0.000	1.092
6	0.562	1.418	0.635
7	0.442	0.000	0.102
8	0.708	0.480	1.339
9	0.778	0.000	0.747
10	1.144	1.467	0.852

Table 3.6 Q_l values for $l = 1$ to 10 of convex polyhedra with vertices, $N = 8$. (Note: the values of Q_l for Cube and Triakis Tetrahedron is similar due to similar angular position).

Q_l	Gyrobifastigium ($N = 8$)	Snub Disphenoid ($N = 8$)	Square Antiprism ($N = 8$)	Triakis Tetrahedron ($N = 8$)
l				
0	2.257	2.257	2.257	2.257
1	0.000	0.303	0.000	0.000
2	0.141	0.500	0.244	0.000
3	0.473	0.485	0.000	0.000
4	0.902	0.870	0.690	1.149
5	0.782	1.418	1.397	0.000
6	1.123	0.557	0.713	1.418
7	0.641	0.698	0.236	0.000
8	0.716	0.896	0.432	0.480
9	0.188	0.737	0.944	0.000
10	1.191	1.228	1.243	1.467

Table 3.7 Q_l values for $l = 1$ to 10 of convex polyhedra with vertices, $N = 9$.

Q_l	Elongated Square Pyramid ($N = 9$)	Gyroelongated Square Pyramid ($N = 9$)	Triangular Cupola ($N = 9$)
l			
0	2.539	2.539	2.539
1	0.047	0.027	0.136
2	0.266	0.037	0.497
3	0.069	0.182	0.478
4	0.897	0.396	0.484
5	0.850	1.532	1.031
6	1.297	0.868	0.943
7	0.711	0.206	1.254
8	0.572	0.764	0.358
9	0.517	0.555	0.417
10	0.978	1.235	1.023

Table 3.8 Q_l values for $l = 1$ to 10 of convex polyhedra with vertices, $N = 9$.

Q_l l	Triaugmented Triangular Prism ($N = 9$)	Tridiminished Icosahedron ($N = 9$)
0	2.539	2.539
1	0.000	0.068
2	0.181	0.348
3	0.091	0.670
4	0.408	0.441
5	1.535	0.466
6	0.814	1.668
7	0.261	0.432
8	0.851	0.393
9	0.606	0.631
10	1.139	1.001

Table 3.9 Q_l values for $l = 1$ to 10 of convex polyhedra with vertices, $N = 10$.

Q_l l	Augmented Tridiminished Icosahedron ($N = 10$)	Elongated Square Dipyramid ($N = 10$)	Gyroelongated Square Dipyramid ($N = 10$)
0	2.539	2.821	2.821
1	0.027	0.000	0.000
2	0.037	0.564	0.320
3	0.182	0.000	0.000
4	0.396	0.805	0.126
5	1.532	0.000	1.397
6	0.868	1.702	1.277
7	0.206	0.000	0.236
8	0.764	0.969	0.630
9	0.555	0.000	0.944
10	1.235	1.338	1.151

Table 3.10 Q_l values for $l = 1$ to 10 of convex polyhedra with vertices, $N = 10$.

Q_l	Metabidminished Icoshedron ($N = 10$)	Pentagonal Antiprism ($N = 10$)	Pentagonal Prism ($N = 10$)	Sphenocorona ($N = 11$)
l				
0	2.821	2.821	2.821	2.821
1	0.099	0.000	0.000	0.035
2	0.316	0.564	0.324	0.207
3	0.465	0.000	0.000	0.156
4	0.438	0.564	0.845	0.224
5	0.697	0.000	0.942	1.332
6	1.746	1.918	0.900	1.363
7	0.475	0.000	1.492	0.510
8	0.366	0.564	0.154	0.513
9	0.595	0.000	0.585	0.676
10	0.995	1.151	0.688	0.921

Table 3.11 Q_l values for $l = 1$ to 10 of convex polyhedra with vertices, $N = 11$.

Q_l	Augmented Sphenocorona ($N = 11$)	Augmented Pentagonal Prism ($N = 11$)	Elongated Pentagonal Pyramid ($N = 11$)	Gyroelongated Pentagonal Pyramid ($N = 11$)
l				
0	3.103	3.103	3.103	3.103
1	0.027	0.054	0.084	0.077
2	0.271	0.518	0.042	0.276
3	0.208	0.192	0.203	0.285
4	0.257	0.751	0.501	0.239
5	0.968	0.683	1.196	0.675
6	1.746	1.181	1.072	1.949
7	0.482	1.455	1.380	0.443
8	0.546	0.557	0.659	0.158
9	0.728	0.798	0.505	0.576
10	0.987	0.809	0.426	0.971

Table 3.12 Q_l values for $l = 1$ to 10 of convex polyhedra with vertices, $N = 12$.

Q_l	Biaugmented Pentagonal Prism ($N = 12$)	Elongated Pentagonal Dipyramid ($N = 12$)	Hexagonal Antiprism ($N = 12$)	Hexagonal Prism ($N = 12$)	Icosahedron ($N = 12$)
l					
0	3.385	3.385	3.385	3.385	3.385
1	0.017	0.000	0.000	0.000	0.000
2	0.736	0.240	0.907	0.677	0.000
3	0.326	0.000	0.000	0.000	0.000
4	0.687	0.281	0.340	0.677	0.000
5	0.555	0.942	0.000	0.000	0.000
6	0.899	1.464	0.965	1.609	2.245
7	1.741	1.492	1.948	0.000	0.000
8	0.451	0.410	0.922	1.725	0.000
9	0.914	0.585	0.305	0.001	0.000
10	1.002	0.380	0.388	1.003	1.229

Table 3.13 Q_l values for $l = 1$ to 10 of convex polyhedra with vertices, $N = 12$.

Q_l	Cuboctahedron ($N = 12$)	Sphenomegacorona ($N = 12$)	Square Cupola ($N = 12$)	Triangular Orthobicupola ($N = 12$)	Truncated Tetrahedron ($N = 12$)
l					
0	3.385	3.385	3.385	3.385	3.385
1	0.000	0.046	0.225	0.000	0.000
2	0.000	0.596	1.065	0.000	0.000
3	0.000	0.267	0.112	0.258	1.078
4	0.646	0.301	0.438	0.329	0.556
5	0.000	0.902	0.958	0.852	0.000
6	1.945	1.351	0.640	1.641	0.158
7	0.000	1.233	1.030	1.052	1.690
8	1.367	0.931	1.106	1.073	1.399
9	0.000	0.739	1.575	0.467	0.866
10	0.044	0.705	0.967	0.034	0.572

3.6 Conclusions

The method of rotational invariants can be used to describe the arrangement of nearest neighbour atoms. This method is suitable for isotropic materials like glass by comparing with the complete set of reference polyhedra. For the first time, all rotational invariants have been presented for $4 \leq N \leq 12$, including values for odd l and in the following Chapters they will be used to analyse models of glasses.

3.7 References

- [1] D. Scott, G. Mountjoy, Rotational invariants of network former and modifier cations in silicate glasses, *J. Non Cryst. Solids*. 401 (2014) 54-59.
- [2] P.J. Steinhardt, D.R. Nelson, M. Ronchetti, Bond-orientational order in liquids and glasses, *Physical Review B*. 28 (1983) 784.
- [3] A. Baranyai, A. Geiger, P.R. Gantrell-Mills, K. Heinzinger, R. McGreevy, G. Plinks, I. Ruff, Invariants of spherical harmonics as order parameters in liquids, *Journal of the Chemical Society, Faraday Transactions 2: Molecular and Chemical Physics*. 83 (1987) 1335-1365.
- [4] P.C. Whitford, G.D. Phillips, Enhanced septahedral ordering in cold Lennard-Jones fluids, *Physical Review E*. 72 (2005) 021203.
- [5] M. Ronchetti, G. Jacucci, Computer Simulation Studies of Atomic Structure and Dynamics Relevant to Liquid and Amorphous Alloys, in: *Anonymous Amorphous and Liquid Materials*, Springer, 1987, pp. 82-98.
- [6] A.Z. Patashinski, A.C. Mitus, M.A. Ratner, Towards understanding the local structure of liquids, *Physics reports*. 288 (1997) 409-434.
- [7] A.S. Keys, C.R. Iacovella, S.C. Glotzer, Harmonic order parameters for characterizing complex particle morphologies, *arXiv preprint arXiv:1012.4527*. (2010).
- [8] T. Kawasaki, A. Onuki, Construction of a disorder variable from Steinhardt order parameters in binary mixtures at high densities in three dimensions, *J. Chem. Phys.* 135 (2011) 174109.
- [9] W. Mickel, S.C. Kapfer, G.E. Schröder-Turk, K. Mecke, Shortcomings of the bond orientational order parameters for the analysis of disordered particulate matter, *J. Chem. Phys.* 138 (2013) 044501.
- [10] E.W. Weisstein, "Johnson Solid" From Wolfram MathWorld, 2016 (2016).

-
- [11] C.G. Gray, K.E. Gubbins, *Theory of Molecular Fluids, Volume 1: Fundamentals* Clarendon, Oxford, 1984.
- [12] M. Kazhdan, T. Funkhouser, S. Rusinkiewicz, Rotation invariant spherical harmonic representation of 3 d shape descriptors, 6 (2003) 156-164.
- [13] W. Tung, *Group Theory in Physics*, World Scientific, 1985.
- [14] A.S. Keys, C.R. Iacovella, S.C. Glotzer, Characterizing Structure Through Shape Matching and Applications to Self-Assembly, *Annual Review of Condensed Matter Physics*. 2 (2011) 263-285.
- [15] Wolfram Research Inc, *Mathematica*, 10.3 (2015).

Chapter 4

Molecular dynamics modelling of barium silicate $BaO - SiO_2$ glasses

4.1 Introduction

Oxide glasses are the most widely used and extensively studied inorganic glasses. In the alkaline earth series of silicate systems, barium silicate minerals are very rare [1] compared to the lighter alkaline earth magnesium silicate and calcium silicate minerals. In the glass formation of binary silicate systems such as $BaO - SiO_2$ glasses, silica acts as a network former and alkali earth cation barium acts as a modifier. Interestingly, silica itself can exist in vitreous form and its tetrahedron structure [2] is well understood and it keeps a persistent structure in both phases of crystal and glass. However, its amorphous structure is primarily described in a variation of the $Si - O - Si$ bond angles [3]. Si atoms are surrounded by four bridging oxygens, O_b , in silica but in silicate oxide glasses Si atoms can be surrounded by one, two, three or four non-bridging oxygen, O_{nb} , depending upon the concentration of the modifiers. Thus, the connectivity of the network former is described by Q^n distribution where Q is the tetrahedra unit and n is number of bridging oxygen atoms [4]. Therefore, introducing Ba increases O_{nb} that depolymerise the silicon network [5] hence varying the glass transition temperature and the glass-forming conditions [6]. A phase diagram of $BaO - SiO_2$ is shown in Figure 4.1 [7] that specifies the glass melting temperature, T_m , of $xBaO - (100 - x)SiO_2$ for $x = 25$ ($BS3$), 33.3 ($BS2$), 40 ($B2S3$) and 50 (BS).

The alkaline metal oxide (e.g. Ba , Ca , Mg) and SiO_2 chemically reacts with each other to form silicate melts and its thermodynamic stability largely depends upon the character of modifying oxide [7]. Also, in the $BaO - SiO_2$ system there is sub-liquid phase separation for $x < 33.3$ [8] which borders on the glass forming region. The glass structure of binary oxide silicate system has been described by modified random network (MRN) [9].

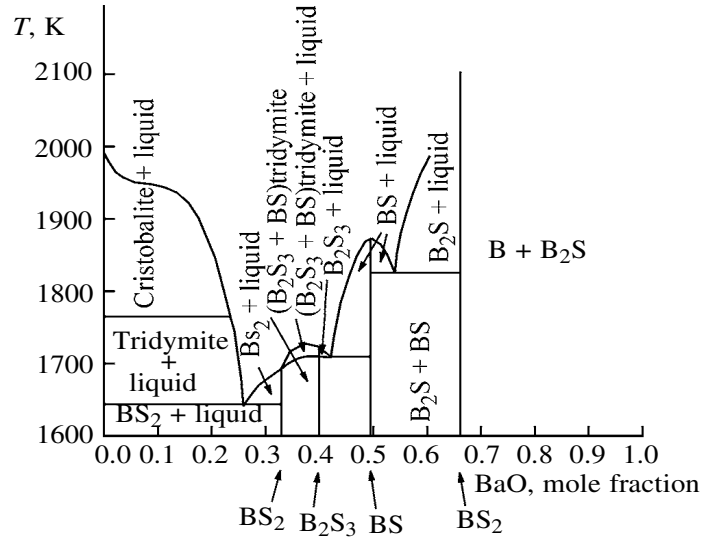


Figure 4.1 The phase diagram of $BaO - SiO_2$ binary system [7].

In the series of alkaline earth silicates system, $BaO - SiO_2$ glass structural studies by diffraction are less common compared to $MgO - SiO_2$ and $CaO - SiO_2$ binary glasses. Hasegawa and Yasui [10] studied $BaSi_2O_5$ ($x = 33.3$) glass by X-ray and neutron diffraction. They compared their results with the corresponding crystals as well and reported the bond length of 1.6 Å, 2.75 Å and 2.6 Å for nearest neighbours of $Si - O$, $Ba - O$ and $O - O$ pairs respectively. Cormier et al [11] reported the neutron diffraction result for $Ba_2Si_3O_8$ ($x = 40$) glass. They compared with the corresponding crystal structures obtained from simulation and reported the presence of quasi-lattice planes in the glass.

The depolymerisation (Q^n) in amorphous barium silicate glasses for composition $x = 33.3$ and $x = 33.7$ compared with corresponding crystal were studied by Bender et al [12] with X-ray absorption and photoemission electron spectroscopy. They reported an average Q^n between $n = 3$ and 4 for $x = 33.3$. Thompson et al [13] studied barium metasilicate glass ($BaSiO_3$, $x = 50$) by ^{17}O nuclear magnetic resonance (NMR) spectroscopy and reported that it contains roughly 67% of non-bridging oxygen, O_{nb} , as expected for a metasilicate.

Schlenz et al [14] studied the structure of barium silicates glasses for $x = 33.3$ and $x = 33.7$ by combined experimental (X-ray diffraction and ^{29}Si NMR) and molecular dynamics (MD) modelling but did not directly compare diffraction and modelling results or report $Ba - O$ bond lengths or coordination numbers. Therefore, here new MD models for $x = 25, 33.3, 40$ and 50 glasses are studied to analyse the local environments of Si and Ba cations in the glasses also by the method of rotational invariants, Q_l , presented in Chapter 3.

4.2 Method

4.2.1 Structure of barium silicate crystals

The inter atomic potential parameters used to model the glasses can be validated by first using them for barium silicate crystals structures. All the associated crystals available are studied to compare the structures with the glass structures from the models.

4.2.1.1 $\alpha-SiO_2$ (Quartz)

The quartz [15] tetrahedral crystal is shown in Figure 4.2. The lattice parameters are: $a = 4.902 \text{ \AA}$, $b = 4.902 \text{ \AA}$ and $c = 5.399 \text{ \AA}$ with $\alpha = 90^\circ$, $\beta = 90^\circ$ and $\gamma = 120^\circ$.

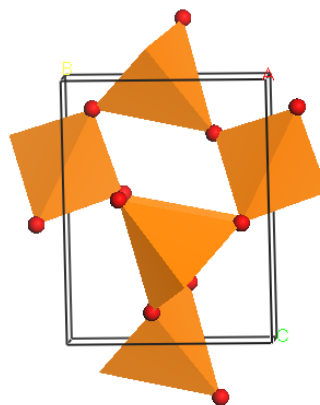


Figure 4.2 The unit cell of $\alpha - SiO_2$ tetrahedra (clay colour) and the red spheres are oxygen atoms.

4.2.1.2 $BaSi_4O_9$

The barium tecto-tetrasilicate ($BaSi_4O_9$) [16] crystal is shown in Figure 4.3. The lattice parameters are: $a = 6.495 \text{ \AA}$, $b = 6.495 \text{ \AA}$ and $c = 9.347 \text{ \AA}$ with $\alpha = 90^\circ$, $\beta = 90^\circ$ and $\gamma = 120^\circ$.

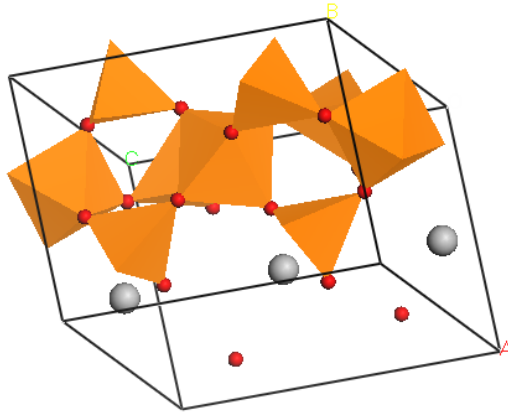


Figure 4.3 The unit cell of barium tecto-tetrasilicate where SiO_4 tetrahedra are indicated in clay colour, and red and grey spheres are oxygen and barium atoms respectively.

4.2.1.3 α - $BaSi_2O_5$

The α - Sanbornite [17] crystal is shown in Figure 4.4. The lattice parameters are: $a = 7.688 \text{ \AA}$, $b = 4.629 \text{ \AA}$ and $c = 13.523 \text{ \AA}$ with $\alpha = 90^\circ$, $\beta = 90^\circ$ and $\gamma = 90^\circ$.

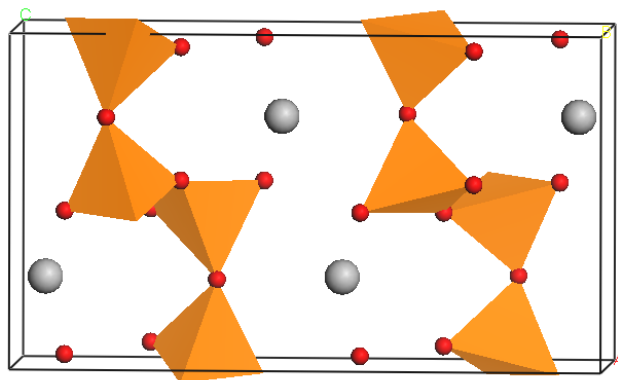


Figure 4.4 The unit cell of α - Sanbornite where SiO_4 tetrahedra are indicated in clay colour, and red and grey spheres are oxygen and barium atoms respectively.

4.2.1.4 β -BaSi₂O₅

The β - Sanbornite [18] crystal is shown in Figure 4.5. The lattice parameters are: $a = 23.202 \text{ \AA}$, $b = 4.661 \text{ \AA}$ and $c = 13.613 \text{ \AA}$ with $\alpha = 90^\circ$, $\beta = 97^\circ$ and $\gamma = 90^\circ$.

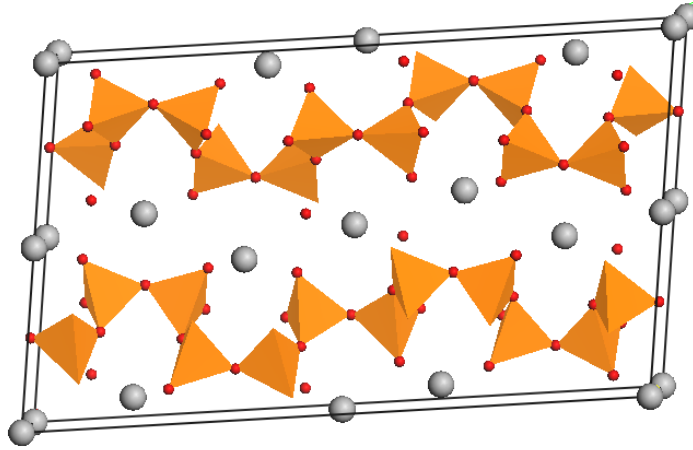


Figure 4.5 The unit cell of β - Sanbornite where SiO_4 tetrahedra are indicated in clay colour, and red and grey spheres are oxygen and barium atoms respectively.

4.2.1.5 $\text{Ba}_2\text{Si}_3\text{O}_7$

The $\text{Ba}_2\text{Si}_3\text{O}_7$ [19] crystal is shown in Figure 4.6. The lattice parameters are: $a = 12.476 \text{ \AA}$, $b = 13.962 \text{ \AA}$ and $c = 4.688 \text{ \AA}$ with $\alpha = 90^\circ$, $\beta = 90^\circ$ and $\gamma = 93.54^\circ$.

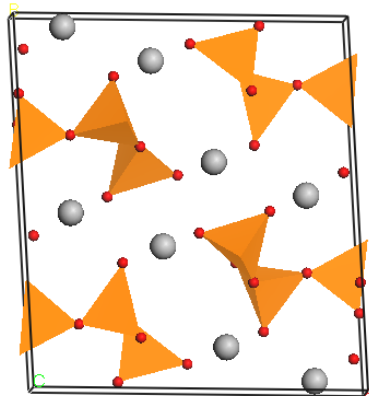


Figure 4.6 The unit cell of $\text{Ba}_2\text{Si}_3\text{O}_7$ crystal where SiO_4 tetrahedra are indicated in clay colour, and red and grey spheres are oxygen and barium atoms respectively.

4.2.1.6 $BaSiO_3$

The barium metasilicate ($BaSiO_3$) [20] crystal is shown in Figure 4.7. The lattice parameters are: $a = 4.58 \text{ \AA}$, $b = 5.611 \text{ \AA}$ and $c = 12.431 \text{ \AA}$ with $\alpha = 90^\circ$, $\beta = 90^\circ$ and $\gamma = 90^\circ$.

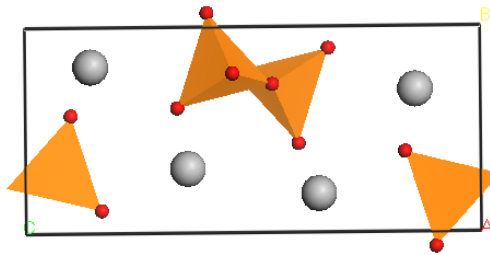


Figure 4.7 The unit cell of $BaSiO_3$ crystal where SiO_4 tetrahedra are indicated in clay colour, and red and grey spheres are oxygen and barium atoms respectively.

4.2.1.7 Ba_2SiO_4

The barium ortho silicate (Ba_2SiO_4) [21] crystal is shown in Figure 4.8. The lattice parameters are: $a = 5.805 \text{ \AA}$, $b = 10.20 \text{ \AA}$ and $c = 7.99 \text{ \AA}$ with $\alpha = 90^\circ$, $\beta = 90^\circ$ and $\gamma = 90^\circ$.

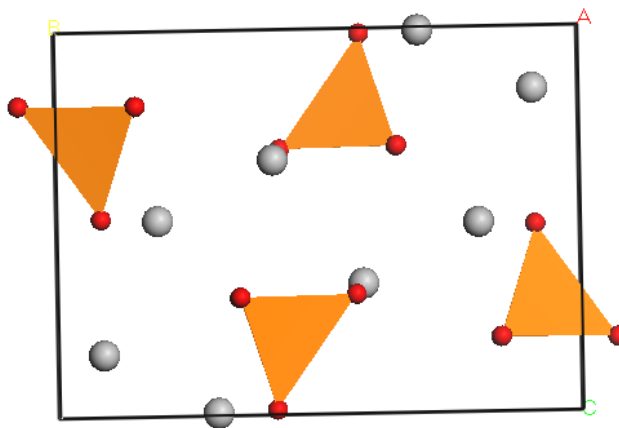


Figure 4.8 The unit cell of Ba_2SiO_4 crystal where SiO_4 tetrahedra are indicated in clay colour, and red and grey spheres are oxygen and barium atoms respectively.

4.2.1.8 BaO

The barium oxide BaO [22] crystal is shown in Figure 4.9. The lattice parameters are: $a = 5.538 \text{ \AA}$, $b = 5.538 \text{ \AA}$ and $c = 5.538 \text{ \AA}$ with $\alpha = 90^\circ$, $\beta = 90^\circ$ and $\gamma = 90^\circ$.

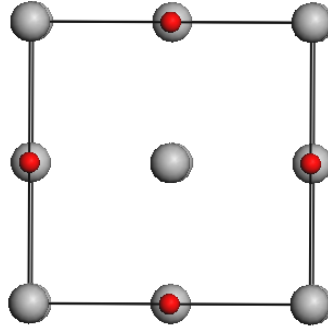


Figure 4.9 The unit cell of BaO crystal where red and grey spheres are oxygen and barium atoms respectively.

4.2.2 Potentials for barium silicate systems

The interaction between the pairs of ions in $BaO - SiO_2$ binary alkaline earth silicate glasses were model by using the Coulombic and Buckingham rigid ion potentials which were described in Equations 2.2 – 2.4. The potential parameters used were derived by Teter [23] and these are listed in Table 4.1 for $Si - O$, $Ba - O$ and $O - O$ interactions.

Table 4.1 Teter potential parameters for $BaO - SiO_2$ binary system.

$i - j$	$q_i (e)$	$A_{ij} (eV)$	$\rho_{ij} (\text{\AA})$	$C_{ij} (eV\text{\AA}^{-6})$
$Si - O$	2.4	13702.905	0.193817	54.681
$Ba - O$	1.2	8636.3836	0.275149	122.93
$O - O$	-1.2	1844.7458	0.343645	192.58

4.2.3 Testing of potentials

Teter interatomic potentials energy function parameters were tested by applying them in well-known barium silicate crystals structures of α - quartz (SiO₂), barium tectosilicate (BaSi₄O₉), α and β Sanbornite (BaSi₂O₅), Ba₂Si₃O₇, barium metasilicate (BaSiO₃), barium orthosilicate (Ba₂SiO₄) and barium oxide (BaO). These crystals correspond to $x = 0, 20, 33.3, 33.3, 40, 50, 80$ and 100. The General Utility Lattice Program (GULP) [24] software was used to evaluate the potential parameters. The GULP algorithm performs under the principle of energy minimisation described in Chapter 2 (see section 2.1.4 and 2.2). The results obtained from the GULP minimisation process are given in Table 4.2 – 4.9.

Table 4.2 The result from the GULP energy minimisation for $\alpha - SiO_2$ crystal initial and final structures displaying the low percentage errors.

Parameter	Unit	Initial Value	Final Value	Difference	Percent
Volume	Å ³	129.659	132.531	2.872	2.21
a	Å	4.901	4.934	0.033	0.67
b	Å	4.901	4.934	0.033	0.67
c	Å	5.398	5.444	0.046	0.85
α	Degree	90	90	0	0.00
β	Degree	90	90	0	0.00
γ	Degree	120	120	0	0.00
Si – O distance	Å	1.612	1.594	–0.018	–1.12

Table 4.3 The result from the GULP energy minimisation for BaSi₄O₉ crystal initial and final structures displaying the low percentage errors.

Parameter	Unit	Initial Value	Final Value	Difference	Percent
Volume	Å ³	341.490	347.509	6.019	1.76
<i>a</i>	Å	6.495	6.529	0.033	0.51
<i>b</i>	Å	6.495	6.529	0.033	0.51
<i>c</i>	Å	9.347	9.414	0.068	0.72
α	Degree	90.000	90.000	0.000	0.00
β	Degree	90.000	90.000	0.000	0.00
γ	Degree	120.000	120.000	0.000	0.00
<i>Si – O</i> distance	Å	1.626	1.573	–0.038	2.78
<i>Ba – O</i> distance	Å	3.0111	3.095	0.018	0.63
<i>Ba – O CN</i>		12	12	0	0.00

Table 4.4 The result from the GULP energy minimisation for α – BaSi₂O₅ crystal initial and final structures displaying the low percentage errors.

Parameter	Unit	Initial Value	Final Value	Difference	Percent
Volume	Å ³	481.253	479.609	–1.644	–0.34
<i>a</i>	Å	7.688	7.762	0.074	0.96
<i>b</i>	Å	4.629	4.745	0.116	2.51
<i>c</i>	Å	13.523	13.022	–0.501	–3.70
α	Degree	90	90	0.000	0.00
β	Degree	90	90	0.000	0.00
γ	Degree	90	90	0.000	0.00
<i>Si – O</i> distance	Å	1.614	1.588	–0.026	–1.61
<i>Ba – O</i> distance	Å	2.888	2.918	0.030	1.04
<i>Ba – O CN</i>		9	9	0.000	0.00

Table 4.5 The result from the GULP energy minimisation for $\beta - BaSi_2O_5$ crystal initial and final structures displaying the low percentage errors.

Parameter	Unit	Initial Value	Final Value	Difference	Percent
Volume	Å ³	1470.780	1470.647	-0.133	-0.01
<i>a</i>	Å	23.195	23.334	0.139	0.60
<i>b</i>	Å	4.658	4.742	0.084	1.80
<i>c</i>	Å	13.613	13.291	-0.322	-2.37
α	Degree	90	90	0.000	0.00
β	Degree	97.57	98.424	0.854	0.88
γ	Degree	90	90	0.000	0.00
<i>Si - O</i> distance	Å	1.616	1.586	-0.030	-1.86
<i>Ba - O</i> distance	Å	2.886	2.928	0.042	1.46
<i>Ba - O CN</i>		8.667	8.667	0.000	0.00

Table 4.6 The result from the GULP energy minimisation for $Ba_2Si_3O_7$ crystal initial and final structures displaying the low percentage errors.

Parameter	Unit	Initial Value	Final Value	Difference	Percent
Volume	Å ³	813.538	822.656	9.118	1.12
<i>a</i>	Å	12.477	12.218	-0.259	-2.10
<i>b</i>	Å	4.685	4.760	0.075	1.60
<i>c</i>	Å	13.944	14.176	0.232	1.50
α	Degree	90.000	90.000	0.000	0.00
β	Degree	93.540	93.926	0.386	0.40
γ	Degree	90.000	90.000	0.000	0.00
<i>Si - O</i> distance	Å	1.624	1.586	-0.038	-2.36
<i>Ba - O</i> distance	Å	2.882	2.900	0.018	0.63
<i>Ba - O CN</i>		7.500	8.000	0.500	6.67

Table 4.7 The result from the GULP energy minimisation for BaSiO₃ crystal initial and final structures displaying the low percentage errors.

Parameter	Unit	Initial Value	Final Value	Difference	Percent
Volume	Å ³	319.457	322.415	2.958	0.93
<i>a</i>	Å	4.58	4.578	-0.002	-0.04
<i>b</i>	Å	5.611	5.645	0.034	0.61
<i>c</i>	Å	12.431	12.476	0.045	0.36
α	Degree	90	90	0.000	0.00
β	Degree	90	90	0.000	0.00
γ	Degree	90	90	0.000	0.00
<i>Si - O</i> distance	Å	1.628	1.585	-0.043	-2.64
<i>Ba - O</i> distance	Å	2.775	2.839	0.064	2.31
<i>Ba - O CN</i>		7	7	0.000	0.00

Table 4.8 The result from the GULP energy minimisation for Ba₂SiO₄ crystal initial and final structures displaying the low percentage errors.

Parameter	Unit	Initial Value	Final Value	Difference	Percent
Volume	Å ³	444.023	446.117	2.094	0.47
<i>a</i>	Å	5.805	5.900	0.095	1.65
<i>b</i>	Å	10.200	10.203	0.003	0.03
<i>c</i>	Å	7.499	7.409	-0.089	-1.19
α	Degree	90.000	90.000	0.000	0.00
β	Degree	90.000	90.000	0.000	0.00
γ	Degree	90.000	90.000	0.000	0.00
<i>Si - O</i> distance	Å	1.633	1.578	-0.055	-3.37
<i>Ba - O</i> distance	Å	2.906	2.925	0.019	0.64
<i>Ba - O CN</i>		9.5	9.5	0	0

Table 4.9 The result from the GULP energy minimisation for BaO crystal initial and final structures displaying the low percentage errors.

Parameter	Unit	Initial Value	Final Value	Difference	Percent
Volume	\AA^3	169.939	160.812	-9.128	-5.37
a	\AA	5.539	5.438	-0.101	-1.82
b	\AA	5.539	5.438	-0.101	-1.82
c	\AA	5.539	5.438	-0.101	-1.82
α	Degree	90	90	0.000	0.00
β	Degree	90	90	0.000	0.00
γ	Degree	90	90	0.000	0.00
$Ba - O$ distance	\AA	2.769	2.719	-0.050	-1.81
$Ba - O$ CN		6	6	0.000	0.00

4.2.4 Initial configurations for barium silicate glasses

Models were made of $x(BaO) - (100 - x)SiO_2$ glasses with $x = 25, 33.3, 40$ and 50 . The initial random distribution of atoms numbers, cubic box lengths and densities of glasses are given in Table 4.10. Each model density is based on the experiential values [25-27].

Table 4.10 Initial configuration of the binary glasses $xBaO - (x - 100)SiO_2$ with the compositions $x = 25 - 50$.

Chemical compositions glasses (x)	Number of Si atoms	Number of Ba atoms	Density (gcm^{-3})	Box length (\AA)	T_m (K)
25($BS3$)	330	110	3.33	26.34	1950
33.3($BS2$)	335	165	3.74	27.21	2000
40 ($B2S3$)	282	188	4.00	28.95	2000
50 (BS)	240	240	4.21	27.21	2200

4.2.5 Parameters for MD modelling of barium silicate glasses

MD simulations were performed in DL_POLY_2 [28] (see details Chapter 2, section 2.4 – 2.5). The melt temperature, T_m , for $x = 25 - 50$ glasses were deduced from the phase diagram [7]. Typical control parameters for MD modelling of barium silicate glasses are given in Table 2.3 (see Chapter 2, section 2.5.2). The cutoff for short-range and long-range potentials were 9 Å and 12 Å respectively.

4.3 Results

Figure 4.10 displays the images of $xBaO - (x - 100)SiO_2$ alkaline earth silicate binary glass models for $x = 25, 33.3, 40$ and 50 . As expected the clay polyhedra are SiO_4 tetrahedra network formers. The dark grey spheres are barium atoms that are modifiers and the red spheres are oxygen atoms

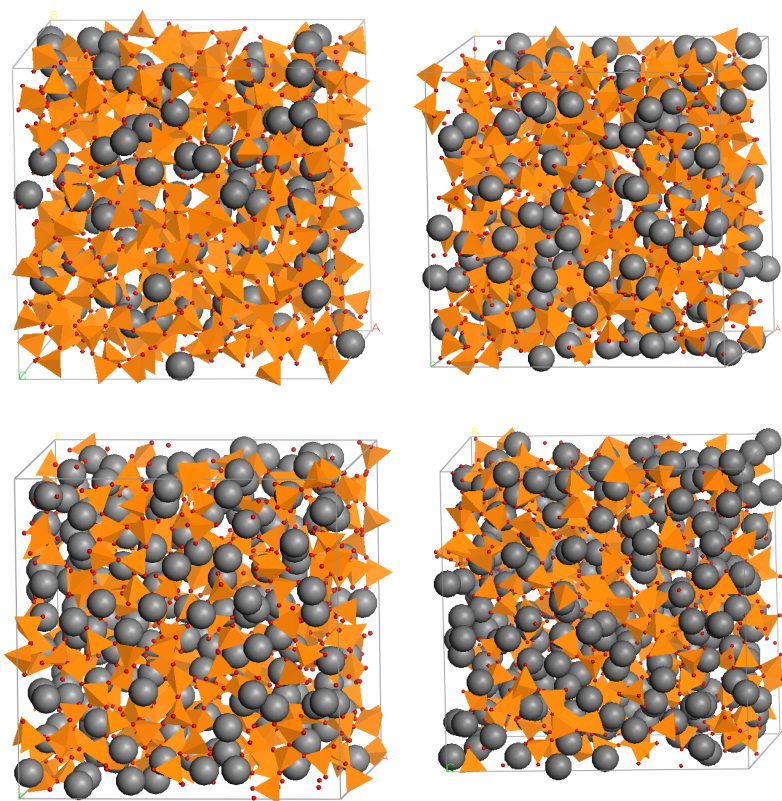


Figure 4.10 MD image of (*top-left*) $x = 25$, (*top-right*) $x = 33.3$, (*bottom-left*) $x = 40$ and (*bottom-right*) $x = 50$ glass models.

4.3.1 Pair distribution function, nearest neighbour distances and coordination numbers

Figure 4.11 displays the pair distribution function, $T_{ij}(r)$, for the binary glass model $x\text{BaO} - (x - 100)\text{SiO}_2$ for $x = 25, 33.3, 40$ and 50 . The position and width of the peak in $T_{ij}(r)$ indicates the distribution of the distances for different atomic correlations from which the average bond length, R_{ij} , can be calculated. The area under these peaks provides the average coordination number, N_{ij} . The first peak in $T_{SiO}(r)$ represent $Si - O$ nearest neighbours and is found to have $R_{SiO} = 1.59 \text{ \AA}$ and $N_{SiO} = 4$ in all the glass models which was expected.

In all the glass models, $T_{OO}(r)$ has the first peak at 2.59 \AA , which represent $O - Si - O$ configurations (i.e. O atom coordination Si atom). These first peaks are followed by the broad peak from $3.0 - 3.5 \text{ \AA}$ representing $O - Ba - O$ configurations. The first peaks of $T_{SiSi}(r)$ are roughly at 3.15 \AA representing $Si - O - Si$ linkages in the silica network in glass models from which the network connectivity (N_{SiSi}) can be calculated. The area under this peak decrease as x increases i.e. as the number of bridging oxygen, O_b , decreases.

The first peak in $T_{BaO}(r)$ also has roughly constant $R_{BaO} = 2.75 \text{ \AA}$ and $N_{BaO} = 6.7$. The correlation results for $T_{SiBa}(r)$ and $T_{BaBa}(r)$ has the first peaks at 3.7 \AA and 4.1 \AA respectively. These correlations have increasing area under the first peak as the number barium increases. The values of R_{ij} and N_{ij} for the glass models are given in Tables 4.11 and 4.12 where i and j are either Ba, Si or O atoms. The estimated errors in the results are $\pm 0.02 \text{ \AA}$ for average bond length and ± 0.1 for coordination numbers.

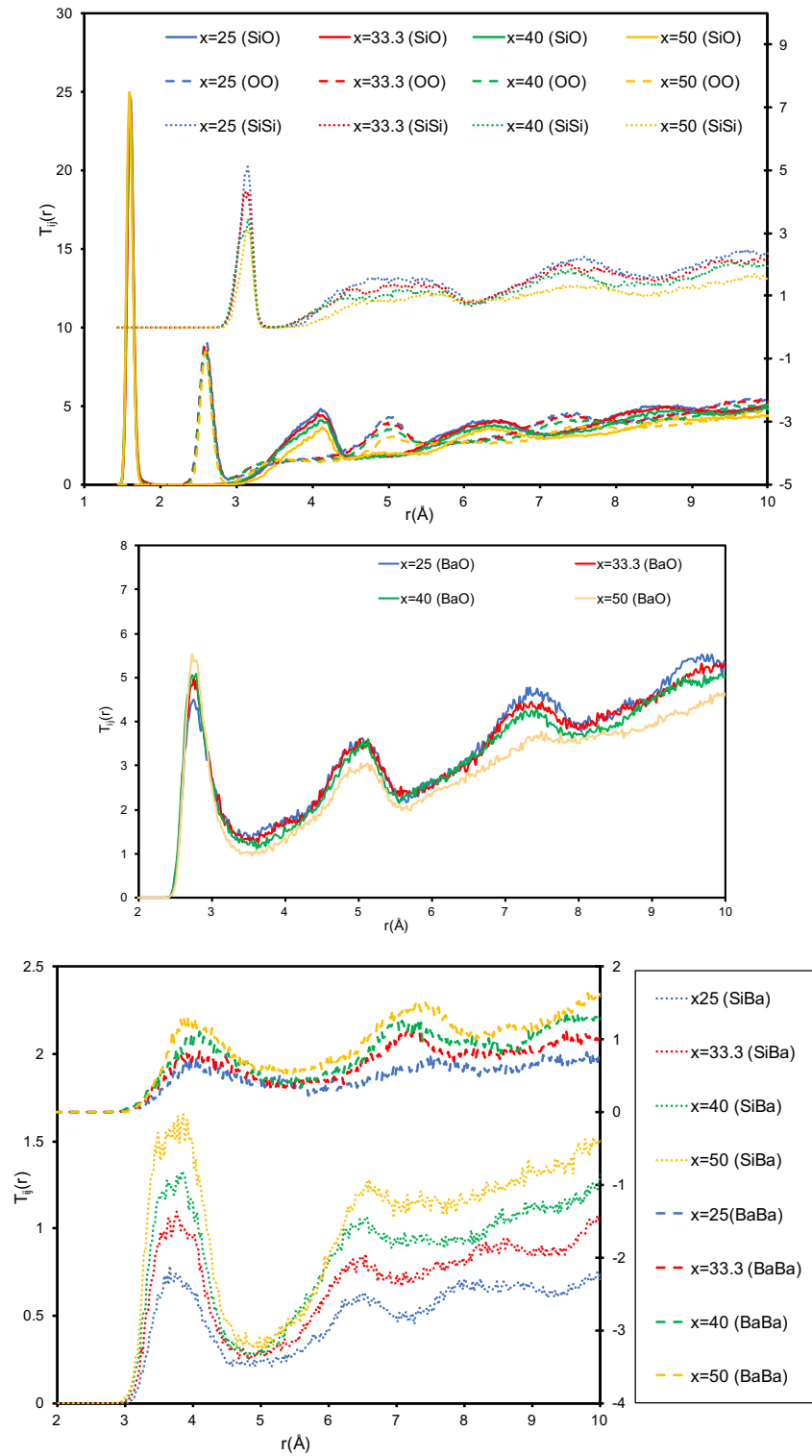


Figure 4.11 Pair distribution function, T_{ij} , for $x = 25, 33.3, 40$ and 50 glass models. Top figure shows T_{SiO} , T_{SiSi} and T_{OO} , middle figure displays T_{BaO} , and bottom figure shows T_{SiBa} and T_{BaBa} .

The average connectivity for N_{SiSi} can be also theoretically predicted, assuming the average connectivity, $\langle n \rangle$, is expected to vary from $\langle n \rangle = 4$ when $x = 0$ to $\langle n \rangle = 0$ when $x = 67.7$ (i.e. orthosilicate). Therefore, it can be predicted by using $\langle n \rangle = 4 - \frac{2x}{100-x}$. There are overlaps between the first peaks of $Si - Ba$ and $Ba - Ba$ correlations around the region 3.3 – 4.4 Å. There are predictable effects on the height of the first peak of $T_{ij}(r)$ while changing x . The changes in the height of the peaks are clearly visible in $Si - Ba$, $Ba - Ba$, $Ba - O$ and $Si - Si$ correlations due to the change in barium and non-bridging oxygen contents.

Table 4.11 Average bond length, R_{ij} , and coordination number, N_{ij} , of $BaO - SiO_2$ binary glass models. PDF indicates the result has been extracted from the area under the curve of $T_{ij}(r)$ functions. The cutoff distances were ~ 1.75 Å and ~ 3.33 Å for N_{SiO} and N_{SiSi} respectively.

x	$O:Si$	R_{SiO}	N_{SiO}	R_{SiSi}	$SiSi$ $\langle n \rangle$ Model	$SiSi$ $\langle n \rangle$ Theory	N_{SiSi} PDF
25	2.3	1.59Å	4.0	3.15 Å	3.37	3.33	3.36
33.3	2.3	1.59Å	4.0	3.15 Å	3.07	3.00	3.05
40	2.7	1.59Å	4.0	3.15 Å	2.68	2.67	2.68
50	3.0	1.59Å	4.0	3.15 Å	2.04	2.00	2.02

Table 4.12 R_{ij} and N_{ij} of $BaO - SiO_2$ binary glass models. The cutoff distances for N_{BaO} was 3.3 Å, for N_{BaBa} ranges from 5.09 – 5.33 Å, and for N_{SiBa} ranges from 4.61 – 4.71 Å.

x	R_{BaO}	N_{BaO}	R_{BaBa}	$BaBa$ $\langle n \rangle$ Model	N_{BaBa} PDF	R_{SiBa}	N_{SiBa}
25	2.75Å	6.5	4.27 Å	4.3	3.6	3.77 Å	2.67
33.3	2.79Å	6.9	4.27 Å	5.0	5.1	3.77 Å	4.04
40	2.79Å	6.8	4.29 Å	5.7	6.0	3.77 Å	4.95
50	2.79Å	6.7	4.25 Å	6.1	7.1	3.77 Å	6.37

4.3.2 Bond angle distribution functions

Figure 4.12 displays $O - Si - O$ (top) and $O - Ba - O$ (bottom) bond angle distribution functions (BAD) for $x(BaO) - (100 - x)SiO_2$ model glasses where $x = 25, 33.3, 40$ and 50 . The cutoff distances were 2.25 \AA and 3.3 \AA for $Si - O$ and $Ba - O$ respectively. As expected for the tetrahedral structure silicates, the primary peak of $O - Si - O$ for all glass models were at 109° . There is decrease in width of BAD relative probability with the increase of Ba content in the glass models. However, for $O - Ba - O$, there were two prominent peaks, a primary peak at 51° and a secondary peak around 80° . The secondary peaks have wider shoulder and there are minimum around 59° between these two peaks. In $O - Ba - O$, as Ba content increases the relative probability of primary peaks decreases whereas relative probability for secondary peaks increases with the increase of Ba content.

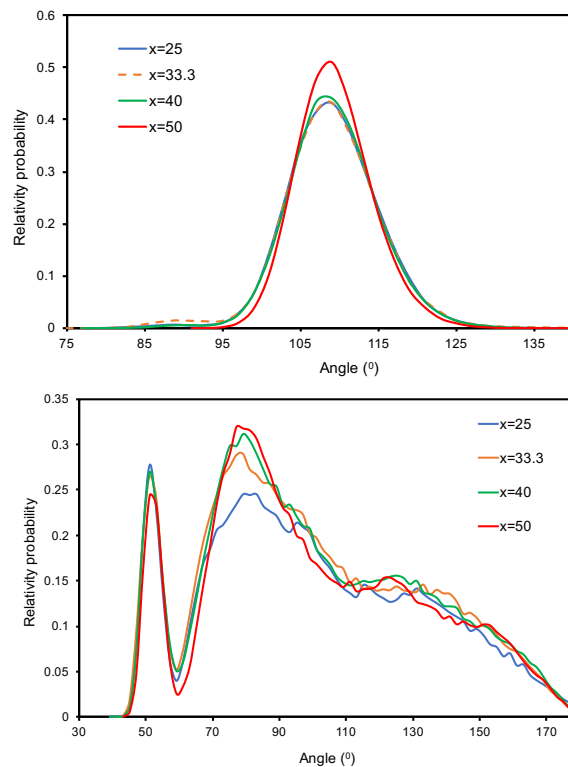


Figure 4.12 The BAD of $xBaO - x - (100)SiO_2$ glasses for $x = 25, 33.3, 40$ and 50 . (Top) $O - Si - O$ and (bottom) $O - Ba - O$.

Figure 4.13 displays BAD of $x(BaO) - (100 - x)SiO_2$ glasses and related crystals for $x = 33.3, 40$ and 50 . The $O - Si - O$ (*top*) of crystals have narrow sharp peaks compared to the glasses but $x = 50$ crystal has three distinctive peaks at $101^\circ, 109^\circ$ and 117° , indicating a distortion in tetrahedral angle. In $x = 33.3$ α -crystal primary peak is at 109° whereas for $x = 33.3$ β -crystal and $x = 40$ crystal the primary peak is around 111° due to some distortion of the tetrahedron.

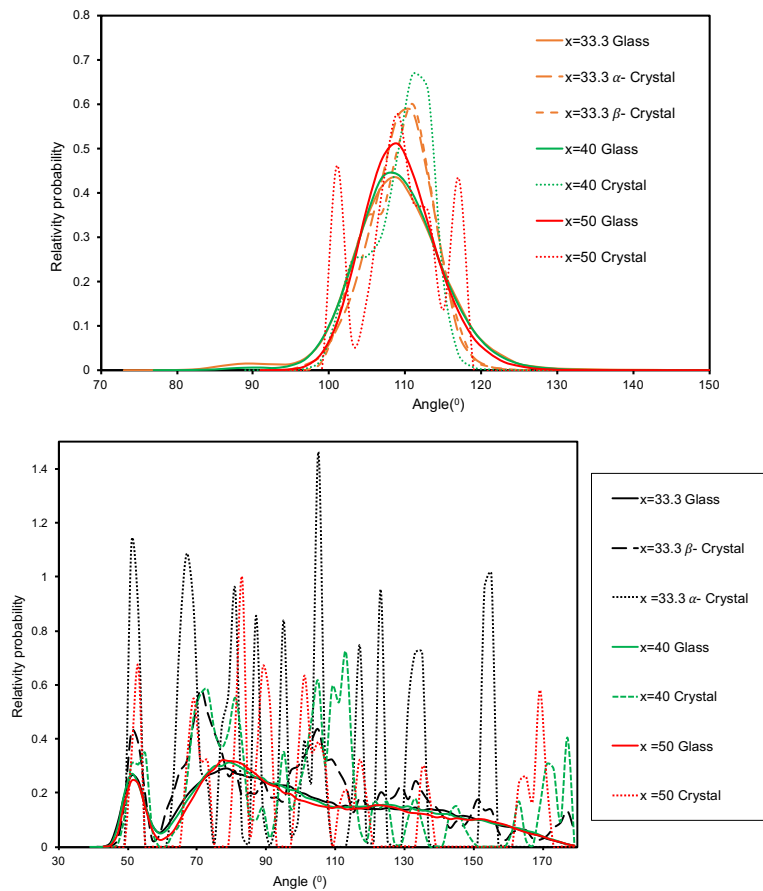


Figure 4.13 The BAD of $xBaO - x - (100)SiO_2$ glasses and related crystals for $x = 25, 33.3, 40$ and 50 . (*Top*) $O - Si - O$ and (*bottom*) $O - Ba - O$.

In $O - Ba - O$ (*bottom*) BAD crystals have range of several peaks compared to the smooth distribution of glasses. This is because in glass BaO_n polyhedra have various different shapes which on average give smooth curves. However, in crystals only few different Ba^{2+} ions local sites exist which are repeated and are indicated by several peaks. There is a

wider distribution for $O - Ba - O$ ranging from $50^\circ - 180^\circ$ in glasses due to $N_{BaO} \geq 6$. For example, in case of undistorted octahedra there is only two main peaks at 90° and 180° .

4.3.3 Network connectivity

Figure 4.14 shows as expected network connectivity, Q^n , for Si decreases with increase of x and with the increase of Ba content the $Ba - Ba$ connectivity increases.

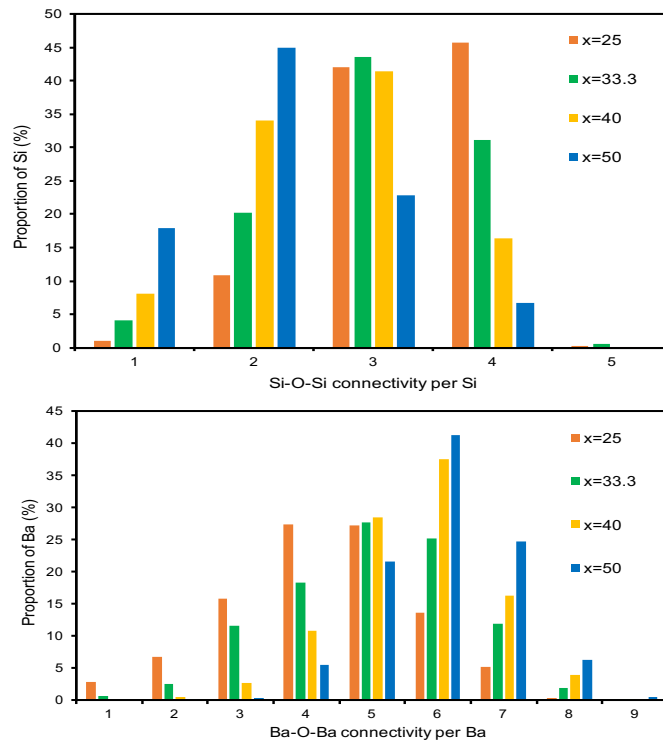


Figure 4.14 $Si - O - Si$ linkage per Si (top) and $Ba - O - Ba$ linkage per Ba (bottom) for $xBaO - (x - 100)SiO_2$ glasses.

Figure 4.15 shows the network connectivity calculated for the two methods described in Chapter 2 (see section 2.6.4). The $Si - Si$ (top) results from both methods give the same results signifying 100% corner sharing between SiO_2 tetrahedral structural units. However, for $Ba - Ba$ average connectivity as indicated by Table 4.12 (N_{BaBa}) there are differences of less than or equal to one between these two methods. When PDF is less than “xhst-hsc” which is case for $x = 25$, this is due to the edge sharing. When the PDF is greater

than “xhst-hsc” which is case for $x = 50$ this is due to mixture of edge sharing and non-bridging oxygen, O_{nb} , coordinated to three of Ba atoms. If PDF is equal to “xhst-hsc” in case of $x = 33.3$ and $x = 40$ this is due to both scenarios.

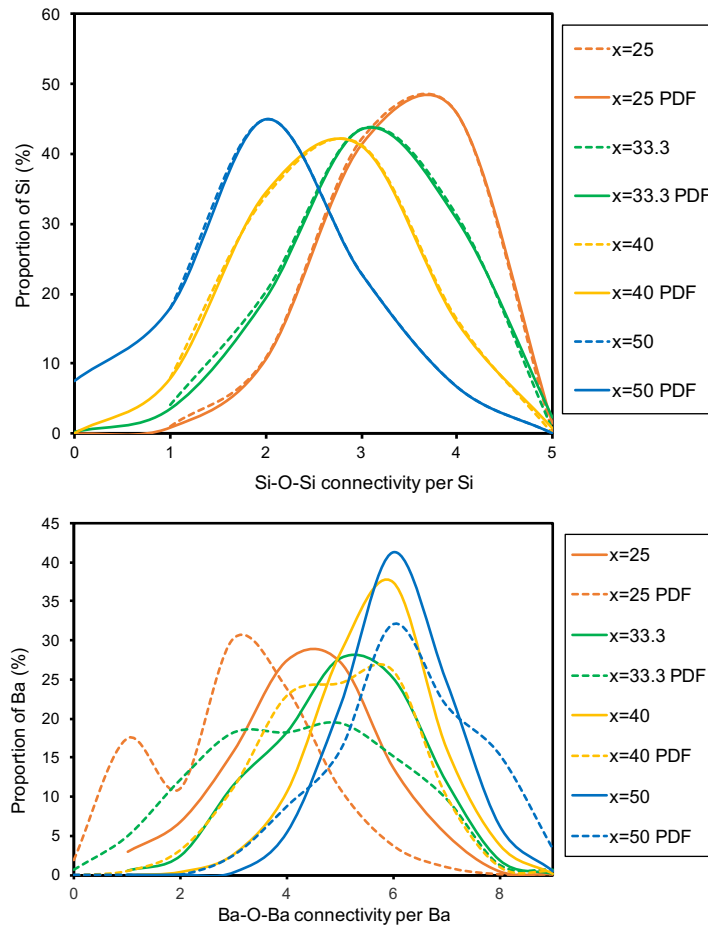


Figure 4.15 Comparisons of $Si - O - Si$ linkage per Si (*top*) and $Ba - O - Ba$ linkage per Ba (*bottom*) for $xBaO - x - (100)SiO_2$ glasses computed from pair distribution function (PDF) and “xhst-hsc” method.

Figure 4.16 shows $Si - Si$ (*top*) and $Ba - Ba$ (*bottom*) network connectivity between glasses and its related crystals. The result compares very well between them as crystals shows the narrow distribution (same connectivity) due to their more ordered structures whereas as glasses have wider distributions. There is an average $Ba - Ba$ connectivity of 6 similar in $x = 33.3$ - α , 40 and 50 crystals.

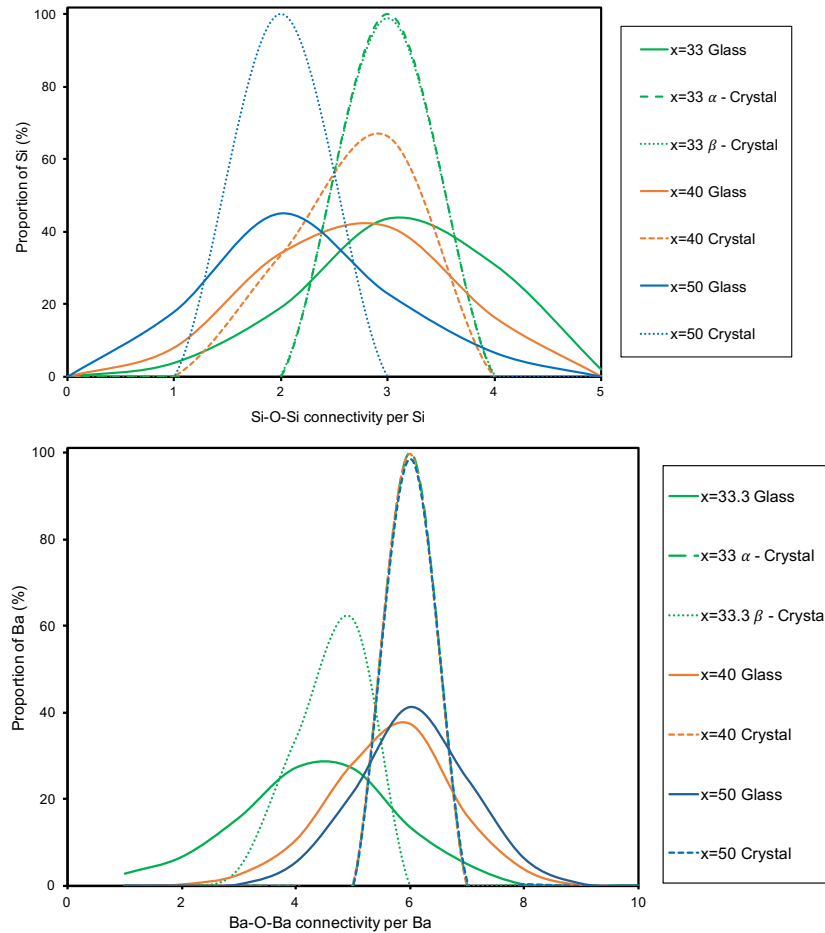


Figure 4.16 $Si - O - Si$ linkage per Si (top) and $Ba - O - Ba$ linkage per Ba (bottom) for $x = 33, 40$ and 50 glasses and crystals.

4.3.4 Neutron and X-ray diffraction structure factors

The changes occurring in T_{ij} lead to change in the diffraction structure factor $S(Q)$ [29] according to the relation given by Equation 2.68 (see Chapter 2). Figure 4.17 shows the neutron diffraction structure factors $S(Q)$ for the models with $x = 33.3$ and $x = 40$ compared to experimental results [10, 11]. For X-ray diffraction, only the total pair distribution function, $T(r)$, is reported for glass model $x = 33.3$ [10] which can be also obtained from Equation 2.68 (this equation is based on $r \rightarrow \infty$ but the calculation uses maximum $r = \frac{L}{2}$ where L is the model box length). There is also neutron $T(r)$ reported for $x = 33.3$ glass [10] and $T(r)$ for X-rays and neutron diffractions are compared with the model result in

Figure 4.18. There have not been reports of experimental diffraction data for $x = 25$ and $x = 50$ glasses due to the difficulty of preparing these glasses.

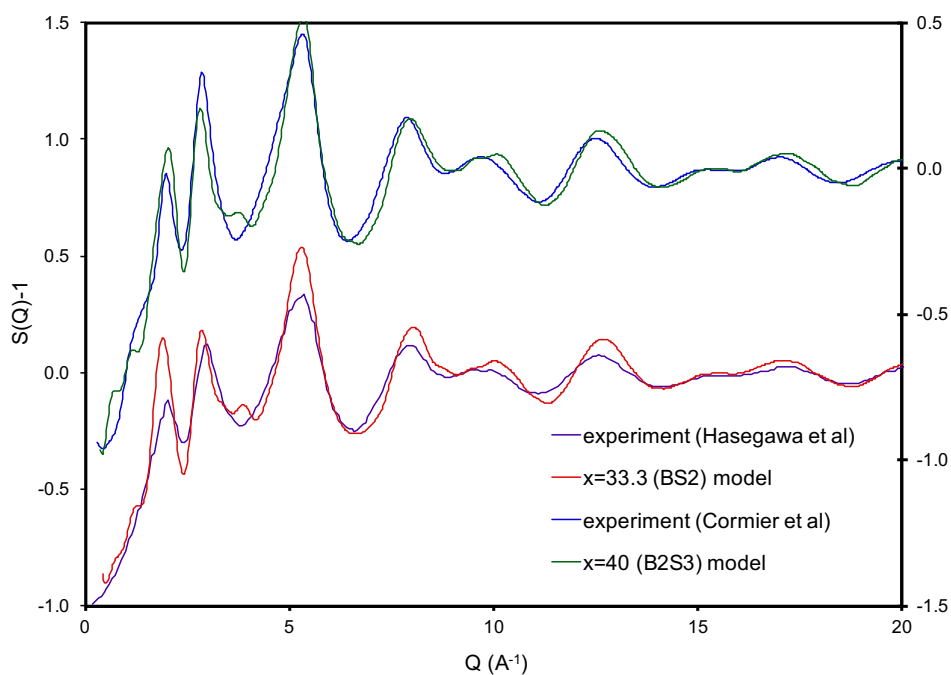


Figure 4.17 Neutron diffraction structure factor for $x = 33.3$ and $x = 40$ glass models and experiments [10, 11].

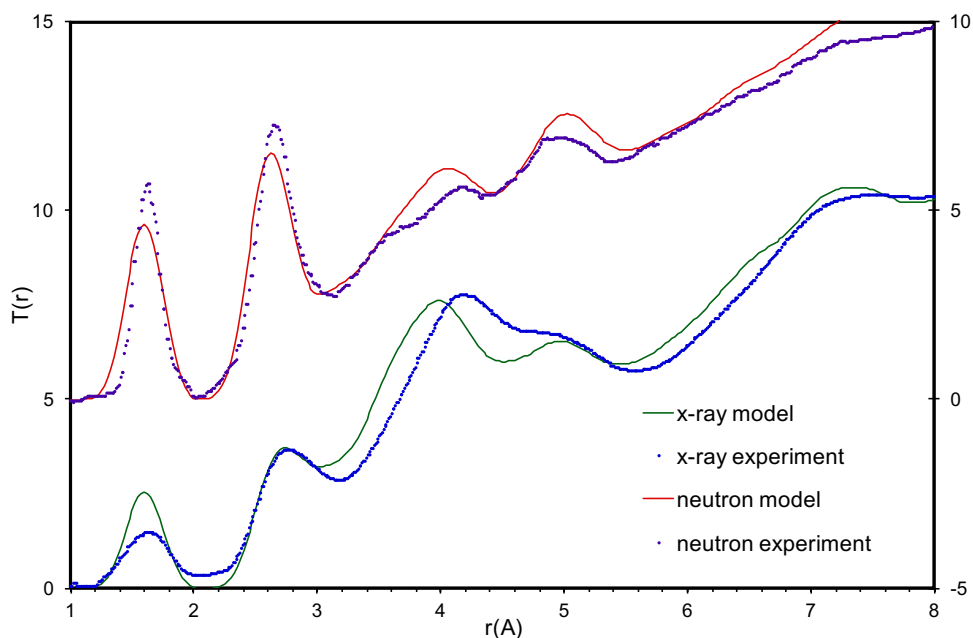


Figure 4.18 Total pair distribution function, $T(r)$, obtained from X-ray and neutron diffraction for $x = 33.3$ glass model and experiment [10].

4.3.5 Rotational invariants for Si and Ba in $BaO - SiO_2$ binary glasses

Figure 4.19 shows tetrahedron structural units of silicate glass models and its related crystal. As expected crystal Q_l values are closer to reference tetrahedron than glasses. Figure 4.20 compares the structure of BaO_n polyhedra in glasses with all the possible reference convex polyhedra. The CN for Ba in glasses are mostly between 6 and 7 with roughly 31% and 35% respectively. For $CN = 6$ and $CN = 7$ from $l = 4$ for glasses, Q_l are close to random. The uncertainty in the average Q_l for glasses were ± 0.05 (one standard deviation).

The average $Ba - O$ coordination number in crystals are found higher than 7 but the metasilicate crystal ($x = 50$) has 100% of $CN = 7$ and its Q_l result is closer to glasses than reference convex polyhedra for vertices, $N = 7$. The β -Sanbornite ($x = 33.3$) crystal and $x = 40$ crystal has $Ba - O$ coordination of 8.7 and 7.5 respectively. There was 27% of $CN = 7$ for β -Sanbornite and 19% of $CN = 7$ for $x = 40$ crystal. The shape of Q_l curve (see Figure 4.20) for $Ba - O$ with $CN = 7$ for $x = 40$ and $x = 50$ crystals have similar trend but β -Sanbornite is much more similar to that of glasses.

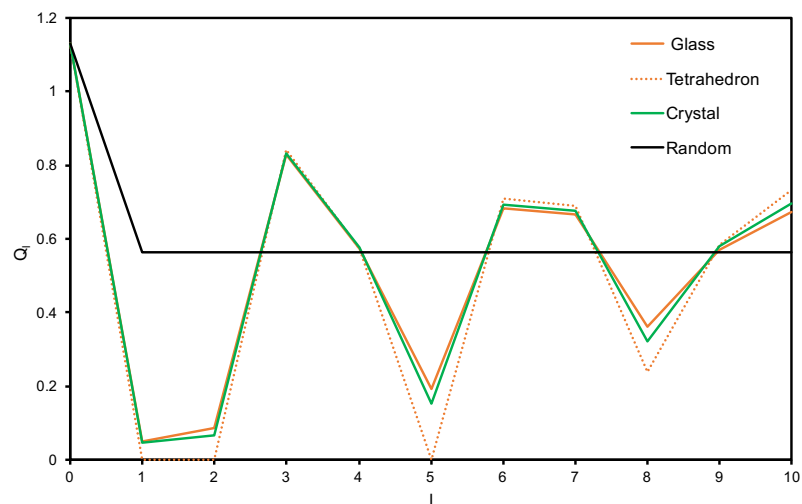


Figure 4.19 Rotational invariant, Q_l , of SiO_2 tetrahedra for glass, crystal and reference Tetrahedron.

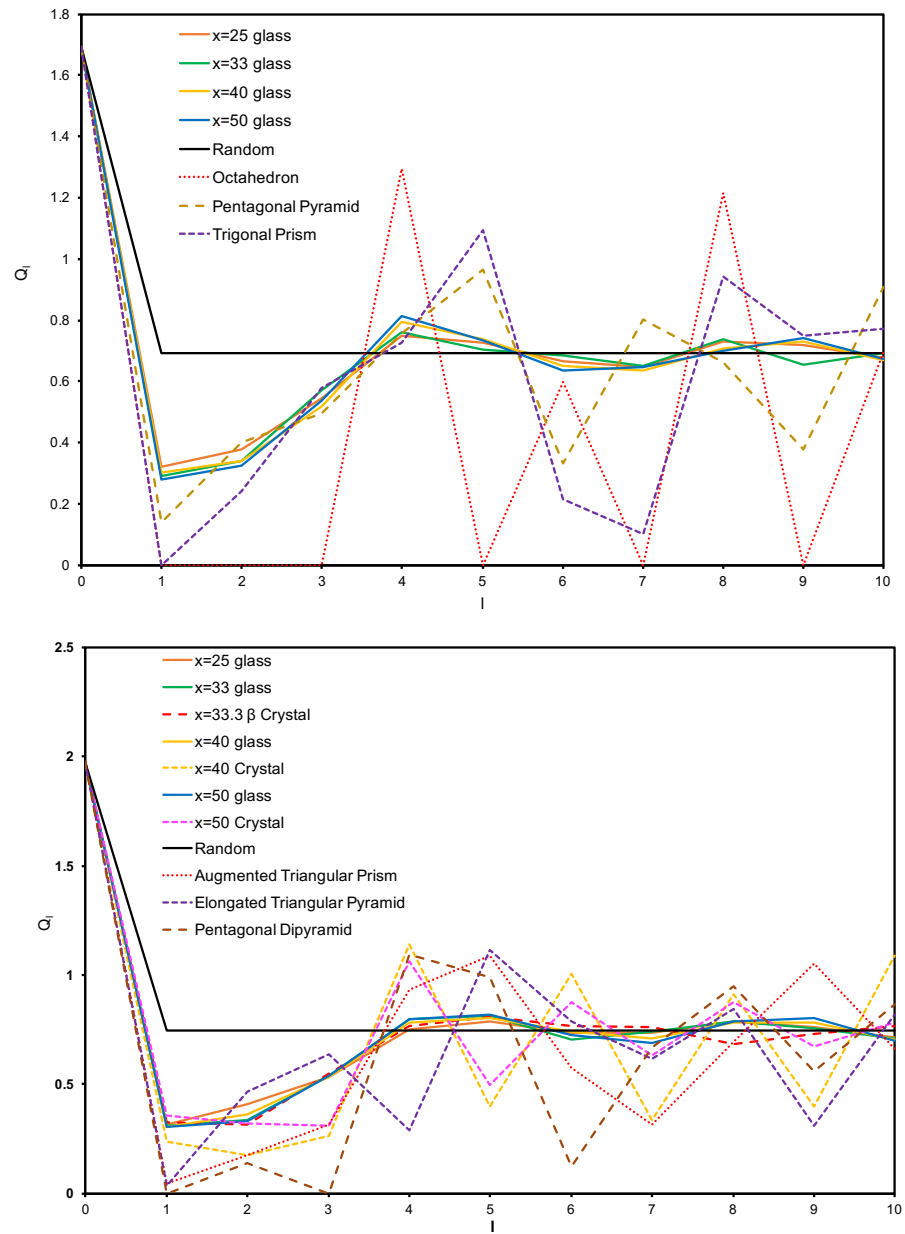


Figure 4.20 Rotational invariant Q_l of BaO polyhedra $CN = 6$ (top) and $CN = 7$ (bottom) for glasses and $x = 33.3$ (β) and $x = 50$ crystals compared with all the possible reference convex polyhedra of vertices, $N = 6$ and 7.

4.4 Discussion

The rigid ion potentials applied in this work have a good ability to reproduce short-range order found in $xBaO - (x - 100)SiO_2$ crystals for $x = 0, 25, 33.3, 40, 50, 75$ and 100. There were very low percentages of discrepancies in the volume of crystal structures overall less than 5%. The result from the glass pair distribution functions shows there are no significant change in nearest neighbour distance with changing compositions x . The present models have $Si - O$ average bond length of 1.59 Å which is slightly shorter than in the crystals but the tetrahedral silicate network found in crystals also existed in the glass models which have the expected amount of $Si - O - Si$ connectivity $\langle n \rangle$ shown in Table 4.11. Notable changes are seen in the increase of coordination numbers of $Ba - Ba$, $Si - Ba$ and decrease of coordination number in $Si - Si$ with increase of compositions x .

Generally, the crystals show higher BaO coordination number than glasses. The $T_{ij}(r)$ correlation of $x = 33.3$ - β crystal roughly matches to that of glasses rather than other crystals presented from the comparison of the pair distribution functions between MD model glasses and their related crystals in Figure 4.21 and Figure 4.22.

In crystals, the short-range order around Ba changes as x decreased from 50 to 25 with the $Ba - O$ average bond length increasing from 2.78 to 2.89 Å and the coordination number increases from 7 to 12. Over the same range of x from 50 to 25 glass models have $Ba - O$ average peak distance of 2.78 Å with coordination number of approximately 7, similar to the $x = 50$ crystal but clearly different to $x = 33.3$ and 40 crystals. In T_{BaO} correlations the broad peaks of glasses are due to the presence of multiple distances compared to the sharp narrow peaks of crystals. The short-range order for $Ba - O$ peak distance of 2.75 Å which was previously been reported from X-ray diffraction [10] for $x = 33.3$ is consistent with the result found here (Table 4.12).

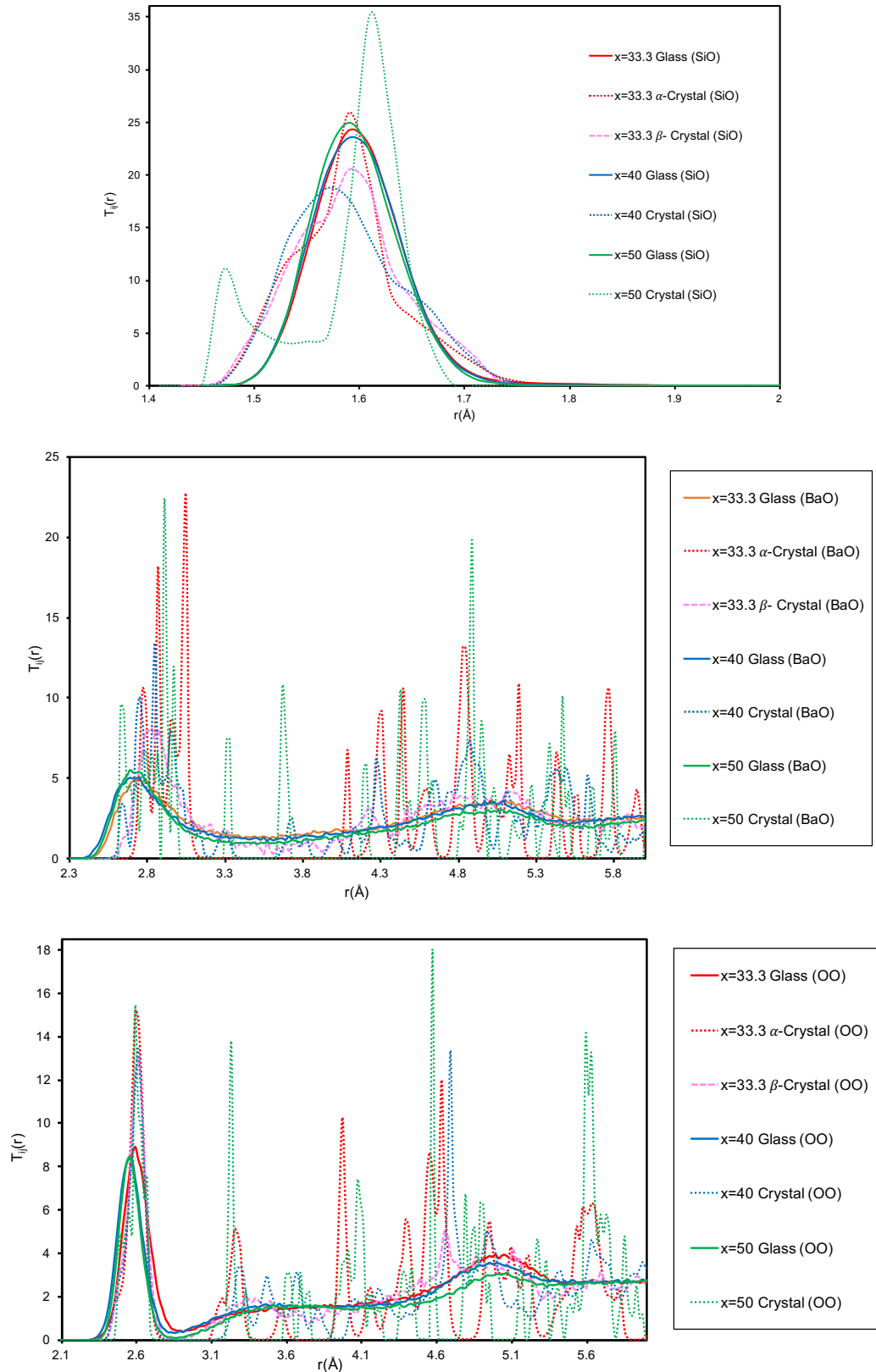


Figure 4.21 Comparison of $T_{ij}(r)$ between glasses and corresponding crystals for compositions $x = 33.3, 40$ and 50 . Correlations $T_{SiO}(r)$ (top), $T_{BaO}(r)$ (middle) and $T_{OO}(r)$ (bottom).

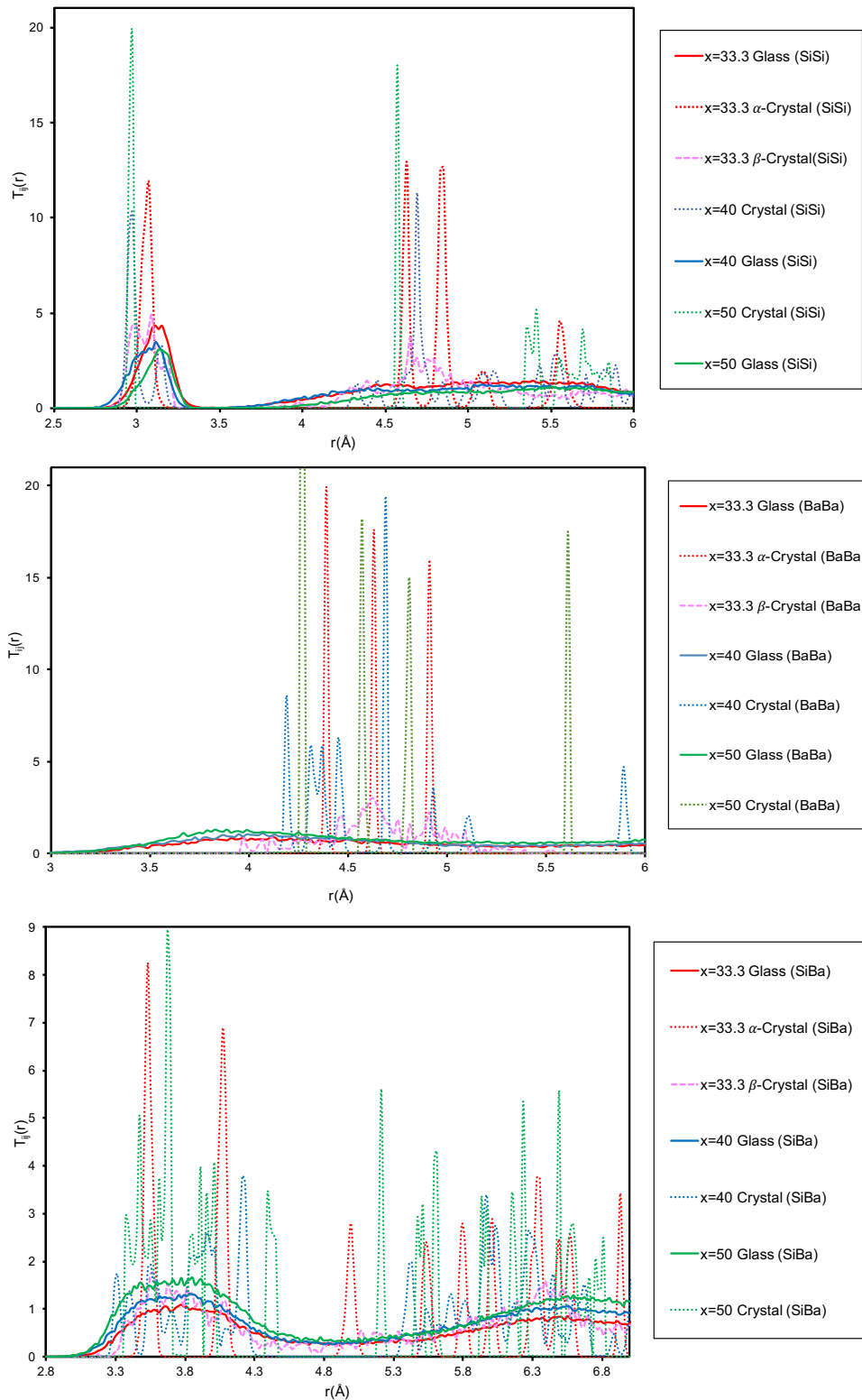


Figure 4.22 Comparison $T_{ij}(r)$ between glasses and corresponding crystals for compositions $x = 33.3, 40$ and 50 . Correlations $T_{SiSi}(r)$ (top), $T_{BaBa}(r)$ (middle) and $T_{SiBa}(r)$ (bottom).

The $T_{OO}(r)$ correlations curve is sharper in crystals at 2.6 Å indicating less distortion of tetrahedra $O - Si - O$ structures than found in glasses which is also followed by range of distinctive sharp peaks from 3.0 to 3.5 Å in crystals compared to the broad peaks of the glasses representing $O - Ba - O$ configurations due to mixture of BaO polyhedra present in glasses. In $T_{SiSi}(r)$ correlations $x = 40$ and 50 crystals has average primary peak $Si - Si$ at 2.97 Å compared to others crystals and glasses at 3.1 – 3.15 Å, which specify almost all $Si - Si$ connectivity $\langle n \rangle$ are corner sharing especially in $x = 50$ crystal. The previous MD study [14] had $\langle n \rangle = 2.7$ for $x = 33.3$ glass which is not consistent with the result here, $\langle n \rangle = 3$ but X-ray absorption spectroscopy [12] reported $\langle n \rangle = 3$. Glasses display the broad peaks for $T_{BaBa}(r)$ correlations compared to the sharp narrow peaks of crystals suggesting that barium is much more randomly sited in the glasses.

There is reasonable agreement between the present models and the experimental neutron diffraction structure factors. However, comparing with experimental pair distribution functions shows fair agreement up to 3.0 Å (see Figure 4.17). The models agree less well with X-ray diffraction data in the region of 3.5 – 5.0 Å (see Figure 4.18) and the reason may be due to the $Ba - Ba$ correlations that may influence X-ray diffraction data strongly.

The result from $Si - O - Si$ connectivity and $Ba - O - Ba$ connectivity indicates the present glass models are homogeneous because $\langle n \rangle$ remains approximately linear with x . However, previous studies suggested that the $x < 33.3$ has sub-liquidus phase separation [8]. Similarly, $Ba - O - Ba$ linkage per Ba (see Figure 4.14) which has been estimated from the numbers of $Ba - O - Ba$ correlations (see Table 4.12) corresponding to the first peak in $T_{BaBa}(r)$ shows that there is smooth progression from $x = 25$ to 50, with no deviation at $x = 25$. For phase separation, the $x = 25$ glass Ba rich silicate phase would have similar result for $Ba - O - Ba$ connectivity seen at higher values of x . But it was found

that all Ba are interconnected by $Ba - O - Ba$ linkages crossing the models, with no separated “clusters” of Ba . The absence of evidence for phase separation at $x = 25$ may be due to the high quench rates used in the modelling method and another reason may be that the phase separation is likely to be on length scales of several nanometer rather than the modelling box size presented here. This will be explored further in the following Chapter 5.

The neutron diffraction study of $x = 40$ glass [11] reported that the position of the “first sharp diffraction peak” in glass at 1.7 \AA^{-1} is very similar to the position of the (112 $-$) and (210) Bragg peaks for the $x = 40$ crystal. This was hypothesised to be evidence of “quasi-Bragg planes” in the glass structures, i.e. apparent layers with differing atomic density and an inter-layer spacing of 4.2 \AA [30] which is supposed to be an equivalent to (112 $-$) and (210) planes in the $x = 40$ crystal and are illustrated in Figure 4.23. However, this hypothesis is not supported by the present glass modelling result for $x = 40$ glass (see Figure 4.10) that clearly indicated Ba atoms are mixed with silicate tetrahedra structures and there is no layer-like ordering of Ba cations in the glass structures.

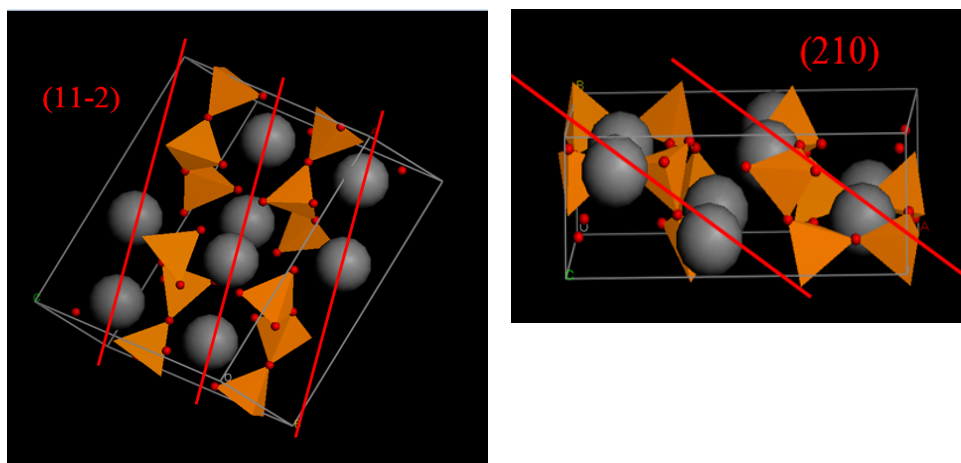


Figure 4.23 Illustration of $x = 40$ crystal showing (112 $-$) and (210) planes corresponding to pronounced layers with differing atomic density and an inter-layer spacing of 4.2 \AA [29]. In a previous study [11] it was noticed that the position of (112 $-$) and (210) Bragg peaks are similar to the “first sharp diffraction peak” in the $x = 40$ glass at $Q = 1.7 \text{ \AA}^{-1}$.

4.5 Conclusions

The new molecular dynamics models of $x(BaO) - (100 - x)SiO_2$ glasses presented here give fair agreement with experimental diffraction data for $x = 33.3$ and $x = 40$. The glass models have the expected silicate network and the short-range order around Ba typically has $Ba - O$ peak distance of 2.79 \AA and coordination of approximately 7, which is similar to $x = 50$ crystal and inconsistent with $x \leq 40$ crystals. The glasses gave the smooth bond angle distribution functions for $O - Ba - O$ signifying mixture of irregular BaO_n polyhedra in the glasses. The results of rotational invariants, Q_l , for Si cations, i.e. archetypal network former, is similar to tetrahedral geometry, and there was obvious variation in tetrahedral distortion between glasses and crystals. The Q_l values for glasses with $Ba - O$ coordination number 6 and 7 on average were closer to random values comparing directly with the convex polyhedra geometries. The $x = 25$ glass model did not show any evidence of sub-liquidus phase separation which may be due to the extremely high quench rate used and the small size box of the model. Furthermore, $x = 40$ glass model did not agree with the previous hypothesis [11] of layered structures with approximately 4.2 \AA spacing which were proposed to correspond between the first sharp diffraction peaks and the prominent Bragg peaks in $x = 40$ crystal.

4.6 References

- [1] F. Ferician, Z. Schlett, I. Jădăneanț, Synthesis of barium silicates by glow discharge electron gun, *Ceram. Int.* 28 (2002) 463-466.
- [2] S.J. Stevens, R.J. Hand, J.H. Sharp, Polymorphism of silica, *J. Mater. Sci.* 32 (1997) 2929-2935.
- [3] X. Yuan, A.N. Cormack, Si-O-Si bond angle and torsion angle distribution in vitreous silica and sodium silicate glasses, *J. Non Cryst. Solids.* 319 (2003) 31-43.
- [4] P.K. Ojha, S.K. Rath, T.K. Chongdar, N.M. Gokhale, A.R. Kulkarni, Structural Inversion and Behavioural Changes as a Function of Composition in Sr-La-Al-B-Si Based Glasses, *New Journal of Glass and Ceramics.* 1 (2011) 21.

- [5] A. Romero-Serrano, A. Cruz-Ramirez, B. Zeifert, M. Hallen-Lopez, A. Hernandez-Ramirez, Thermodynamic modelling of the BaO-SiO₂ and SrO-SiO₂ binary melts, *Glass Physics and Chemistry*. 36 (2010) 171-178.
- [6] G.N. Greaves, S. Sen, Inorganic glasses, glass-forming liquids and amorphizing solids, *Adv. Phys.* 56 (2007) 1-166.
- [7] Z.G. Tyurnina, S.I. Lopatin, S.M. Shugurov, V.L. Stolyarova, Thermodynamic properties of silicate glasses and melts: I. System BaO-SiO₂, *Russian journal of general chemistry*. 76 (2006) 1522-1530.
- [8] E.D. Zanotto, P.F. James, A.F. Craievich, The effects of amorphous phase separation on crystal nucleation kinetics in BaO-SiO₂ glasses, *J. Mater. Sci.* 21 (1986) 3050-3064.
- [9] G.N. Greaves, EXAFS and the structure of glass, *Journal of Non-Crystalline Solids*. 71 (1985) 203-217.
- [10] H. Hasegawa, I. Yasui, X-ray and neutron diffraction analyses of barium silicate glass, *J. Non Cryst. Solids*. 95 (1987) 201-208.
- [11] L. Cormier, P.H. Gaskell, S. Creux, Comparison of the low-Q features in diffraction data for silicate glasses and crystals containing Sr or Ba, *J. Non Cryst. Solids*. 248 (1999) 84-91.
- [12] S. Bender, R. Franke, E. Hartmann, V. Lansmann, M. Jansen, J. Hormes, X-ray absorption and photoemission electron spectroscopic investigation of crystalline and amorphous barium silicates, *J. Non Cryst. Solids*. 298 (2002) 99-108.
- [13] L.M. Thompson, R.J. McCarty, J.F. Stebbins, Estimating accuracy of ¹⁷O NMR measurements in oxide glasses: Constraints and evidence from crystalline and glassy calcium and barium silicates, *J. Non Cryst. Solids*. 358 (2012) 2999-3006.
- [14] H. Schlenz, A. Kirfel, K. Schulmeister, N. Wartner, W. Mader, W. Raberg, K. Wandelt, C. Oligschleger, S. Bender, R. Franke, Structure analyses of Ba-silicate glasses, *J. Non Cryst. Solids*. 297 (2002) 37-54.
- [15] M.G. Tucker, D.A. Keen, T. Dove, A detailed structural characterization of quartz on heating through the α - β phase transition, *Mineralogical Magazine*. 65 (2001) 489-507.
- [16] L.W. Finger, R.M. Hazen, B.A. Fursenko, Refinement of the crystal structure of BaSi₄O₉ in the benitoite form, *Journal of Physics and Chemistry of Solids*. 56 (1995) 1389-1393.
- [17] K. Hesse, F. Liebau, Crystal chemistry of silica-rich Barium silicates, *Zeitschrift für Kristallographie-Crystalline Materials*. 153 (1980) 3-18.
- [18] H. Katscher, G. Bissert, F. Liebau, The crystal structure of high-temperature Ba₂[Si₄O₁₀], *Zeitschrift für Kristallographie-Crystalline Materials*. 137 (1973) 146-158.
- [19] O.S. Filipenko, E.A. Pobedims., V.I. Ponomare., N.V. Belov, Crystalline Structure of Synthetic Barium Silicate, *Dokl. Akad. Nauk SSSR*. 196 (1971) 1337.

- [20] H.P. Grosse, E. Tillmanns, Bariummetasilicate, BaSiO₃(h), Cryst.Struct.Comm. 3 (1974) 603-605.
- [21] K.A. Denault, J. Brgoch, S.D. Klo, M.W. Gaultois, J. Siewenie, K. Page, R. Seshadri, Average and local structure, Debye temperature, and structural rigidity in some oxide compounds related to phosphor hosts, ACS applied materials & interfaces. 7 (2015) 7264-7272.
- [22] R.J. Zollweg, X-ray lattice constant of barium oxide, Physical Review. 100 (1955) 671.
- [23] D. Teter, Private communication, (2004).
- [24] J.D. Gale, A.L. Rohl, The General Utility Lattice Program (GULP), Molecular Simulation. 29 (2003) 291 - 341.
- [25] Y. Tang, Z. Jiang, Phase diagram model for the physical properties of silicate and borosilicate glass systems: density and refractive index analysis, J. Non Cryst. Solids. 189 (1995) 251-257.
- [26] S. Sridharan, M. Tomozawa, Effect of various oxide additives on sintering of BaO-SiO₂ system glass-ceramics, J. Mater. Sci. 27 (1992) 6747-6754.
- [27] H. Doweidar, Density-structure correlations in silicate glasses, J. Non Cryst. Solids. 249 (1999) 194-200.
- [28] W. Smith, T.R. Forester, DL_POLY_2. 0: A general-purpose parallel molecular dynamics simulation package, J. Mol. Graph. 14 (1996) 136-141.
- [29] H.E. Fischer, A.C. Barnes, P.S. Salmon, Neutron and x-ray diffraction studies of liquids and glasses, Reports on Progress in Physics. 69 (2005) 233.
- [30] M. Rai, G. Mountjoy, Molecular dynamics modelling of the structure of barium silicate glasses BaO-SiO₂, J. Non Cryst. Solids. 401 (2014) 159-163.

Chapter 5

Modifier cation distribution in large models of alkaline earth silicate glasses

5.1 Introduction

The region of glass formation in binary silicate system is limited by the separation of the melt within a certain composition range into two liquids of different composition [1]. The immiscibility or phase separation in the binary alkaline earth silicates glasses are common phenomena. The phase diagram for binary alkaline earth silicate system showing miscibility gaps is illustrated in Figure 5.1 [2] for $MO - SiO_2$ systems (i.e. $M = Mg, Ca$ and Ba). The tendency of phase separation depends on the strength of the ionic bond between the modifier cation and the non-bridging oxygen anions [1] and the ionic potential of cation can be defined by z/R , where z is the ion charge and R is its radius. Therefore, in $MO - SiO_2$ systems the tendency towards immiscibility phase separation increases (i.e. $Ba < Ca < Mg$) with a decrease in the basicity [3]. That is the width of immiscibility is larger for Mg and Ca than Ba .

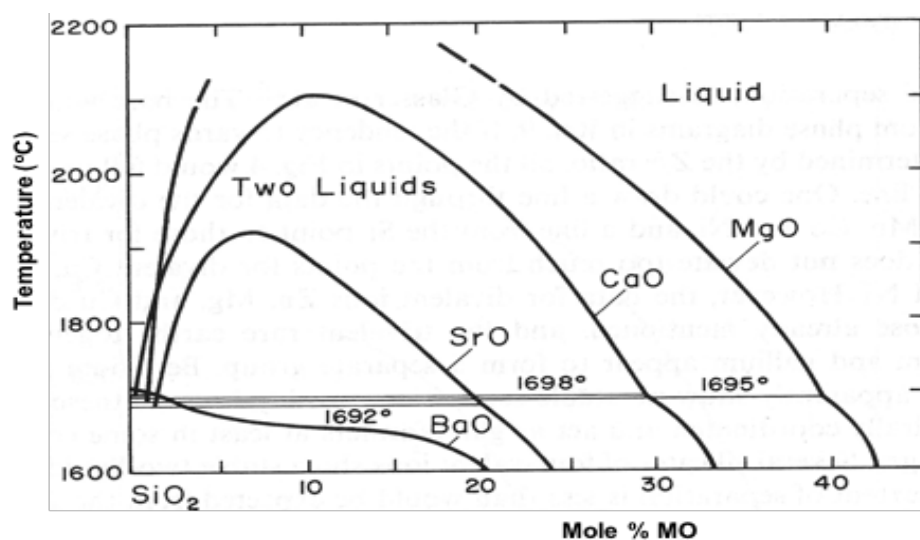


Figure 5.1 The phase diagram showing miscibility gaps for binary alkaline earth silicate glasses [2].

Usually, glasses are made by cooling homogenous (single phase) melts but many of them have a heterogeneous structure on sub-microscopic scale [4]. For the melts to form homogenous or heterogeneous glasses may depend on the free energy of the system. If mixing of two components yields a lower free energy, the mixture will remain homogenous but if the separation of the mixture into two components yields a lower free energy, separation will have occurred if allowed by kinetic consideration [5].

Previous MD structural studies were performed on $xMgO - (1 - x)SiO_2$ glasses for $x = 50, 54, 58, 62$ and 67 in [6, 7]. For the glasses $x = 50, 58$ and 67 the X-ray and neutron diffraction data from the experiments [8-11] were compared with the models with fair agreement. Previous MD structural studies were done on $xCaO - (1 - x)SiO_2$ glasses for $x = 10, 20, 30, 40$ and 50 in [12]. The X-ray diffraction data [13] for $x = 42$ and 50 glasses, and neutron diffraction [14] for $x = 42$ glass was compared to the model with a fair agreement. Both studies reported the bond length of $Si - O$ about 1.6 \AA and as expected Si retaining tetrahedra structure similar to the crystal. The bond length for $Mg - O$ and $Ca - O$ was reported to be about 2.0 \AA and 2.4 \AA respectively with coordination number for Mg between 4.5 to 5.5 and for Ca between 5 to 7 . In both glasses, the network of structural units was corner shared and $Si - Si$ connectivity drops as composition of x is increased. The MD structural studies for $xBaO - (1 - x)SiO_2$ glasses for $x = 25, 33.3, 40$ and 50 are presented in the previous Chapter 4.

In the binary alkaline earth silicate system, the glass properties such as viscosity, chemical durability and electrical conductivity are affected by phase separation [2]. The electron microscope can unveil the phase separation in the real glass (e.g. heat treatment of $BaO - SiO_2$ glasses [15] and see Figure 5.2 [5]). The MD studies on phase separation was done on $xCaO - (1 - x)SiO_2$ glasses for $x = 10$ and 20 [12] where the clustering of Ca cations was investigated by calculating the average number of neighbours Ca around a given Ca . For the $BaO - SiO_2$ system there is sub-liquidus phase separation for $x < 30$ which

borders on the glass forming region as shown in Figure 5.3 [15]. Hence $BaO - SiO_2$ glasses with $x < 30$ have been extensively studied in [15, 16] for phase separation, nucleation, and crystallisation.

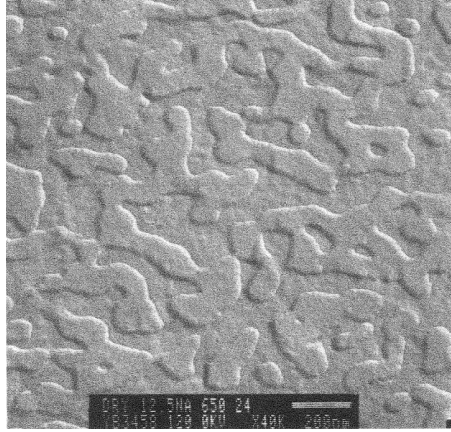


Figure 5.2 The phase separated glass showing interconnected morphology [5].

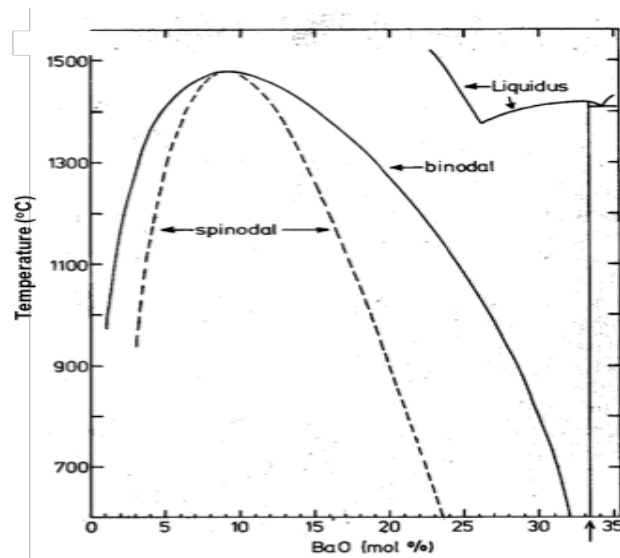


Figure 5.3 Part of $BaO - SiO_2$ phase diagram showing binodal (sub-liquidus liquid-liquid immiscibility) boundary [15].

On the basis of MD structural studies on $BaO - SiO_2$ system (Chapter 4) in $x = 25$ glass model all Ba cations were interconnected by $B - O - Ba$ linkages crossing the model homogeneously. The analysis of $Ba - O - Ba$ linkage per Ba shows that there is smooth progression from $x = 50$ to lower value of x , with no deviation at $x = 25$. This contrasts

with what was seen in $CaO - SiO_2$ system for $x = 10$ and $x = 20$ [12]. Subsequently, the $BaO - SiO_2$ glass for $x = 25$ model in Chapter 4 did not show the phase separation due the one reason being the model was made using a high quench rate (10^{13} K/s) and another reason might be that the phase separation is likely to be on length scales of several nanometre whereas the model box length was about 27 \AA . Therefore, here the new large models for $xMO - (1 - x)SiO_2$ glasses where $M = Mg, Ca$ and Ba for $x = 25$ and $x = 50$ were made to study this immiscibility phenomena including in $BaO - SiO_2$ system.

5.2 Method

5.2.1 Interatomic potentials for $MO - SiO_2$ systems with $M = Mg, Ca$ and Ba

The pair interaction between the ions in these three binary $MO - SiO_2$ systems (i.e. $M = Mg, Ca$ and Ba) are described by the Coulombic and Buckingham ion potentials given by Equations 2.2 to 2.4. The potential parameters used were derived by Teter [17] and they are listed in Table 5.1 for $Mg - O$, $Ca - O$, $Ba - O$ and $O - O$ interactions.

The testing of these potential parameters with its related crystals have already been done in the earlier work of [7] for $MgO - SiO_2$, and [12] for $CaO - SiO_2$ systems. For $BaO - SiO_2$ system the work is done in the previous Chapter 4.

Table 5.1 Teter potential parameters for $MO - SiO_2$ binary systems.

$i - j$	$q_i(e)$	$A_{ij}(eV)$	$\rho_{ij}(\text{\AA})$	$C_{ij}(eV\text{\AA}^{-6})$
$Mg - O$	1.2	7063.4907	0.210901	19.210
$Ca - O$	1.2	7747.1834	0.252623	93.109
$Ba - O$	1.2	8636.3836	0.275149	122.93
$Si - O$	2.4	13702.905	0.193817	54.681
$O - O$	-1.2	1844.7458	0.343645	192.58

5.2.2 Initial configurations for $MO - SiO_2$ glasses with $M = Mg, Ca$ and Ba

The large models made for the alkaline earth silicate glasses, $x(MO) - (100 - x)SiO_2$ (i.e. $M = Mg, Ca$ and Ba) are for the compositions of $x = 25$ and 50 . The atoms numbers, cubic box lengths and densities of glasses are given in Table 5.2. The densities of the models were based on the experimental values which were used in previous studies except for the $25MgO - 75SiO_2$ glass where it is estimated by linear trend progression.

Table 5.2 Initial configuration of the binary glasses $xMO - (x - 100)SiO_2$ for the compositions $x = 25$ and 50 .

Chemical compositions glasses (x)	Number of Mg atoms	Number of Ca atoms	Number of Ba atoms	Number of Si atoms	Density (gcm^{-3})	Box length (\AA)	T_{melt} (K)
$25MgO$	1650	–	–	4950	2.48	62.42	2100
$50MgO$	4000	–	–	4000	2.74	62.42	2000
$25CaO$	–	1650	–	4950	2.90	63.30	2000
$50CaO$	–	4000	–	4000	2.90	64.32	2000
$25BaO$	–	–	1650	4950	3.33	64.96	1950
$50BaO$	–	–	4000	4000	4.21	69.57	2200

5.2.3 Parameters for MD modelling of $MO - SiO_2$ glasses with $M = Mg, Ca$ and Ba

MD simulation on these binary glasses were performed in DL_POLY_2 [18] and the control parameters for MD modelling are given in Table 2.3 (see Chapter 2). The time-steps for quench stage for these glasses depended on melt temperature, T_{melt} , illustrated in Table 5.2 which are taken from the phase diagram for each of these glasses. The quench rate used was $10^{13} K/s$ and the cutoffs for the short-range and long-range potentials were 7.0 \AA and 12.0 \AA . However, at stage 3 of the ‘melt’ before quench a larger number of time-steps to

equilibrate were performed in some cases. As for $25MgO - 75SiO_2$ glass up to 2,720,000 time-steps was performed and for both $25CaO - 75SiO_2$ glass and $25BaO - 75SiO_2$ glass up to 1,840,000 time-steps were performed.

5.2.4 Sphere grid and cubic grid sampling of cation distributions

The clustering of cation or phase separation in the model can be surveyed by using sphere grid and cubic grid methods. That is a way to look for regions with different compositions in the glass structure. In the model based on random distribution, the number of modifier neighbours, N_{ii} , in term of atomic number density, ρ_i , can be deduced as; $N_{ii} = \rho_i \frac{4\pi d_{ii}^3}{3}$ where d_{ii} is the cutoff distance for $i - i$ modifier neighbours and $\rho_i = \frac{N_i}{V}$ for i modifier as illustrated in Figure 5.4.

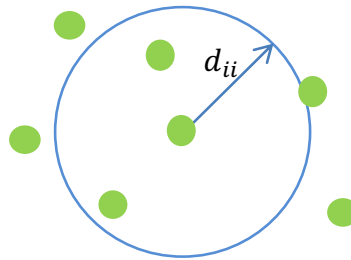


Figure 5.4 The neighbouring atoms sphere search with radius d_{ii} and the green spheres are modifiers.

In the glass model, the pair distribution function is averaged over whole structure that provides good statistics in number of neighbouring atoms, N , and neighbouring distances, R . However, the distribution of modifier cations in the glass model can be surveyed by measuring the local density of modifier particles in different regions of glass structure. Therefore, the local quantity is number of modifiers, N_i , in search volume, V_i . The search volume can be either a sphere or cube as shown in Figure 5.5. Then, the average number of modifiers locally is $\langle N_i \rangle = V_i \times (N_M/L^3)$ where, N_M is the total number of modifiers and L is the length of glass model as illustrated in Figure 5.5. Also, the $\langle N_i \rangle$ does not depend

on shape or position of search volume V_i but it does depend on V_i . The variation of N_i results will be displayed in histogram.

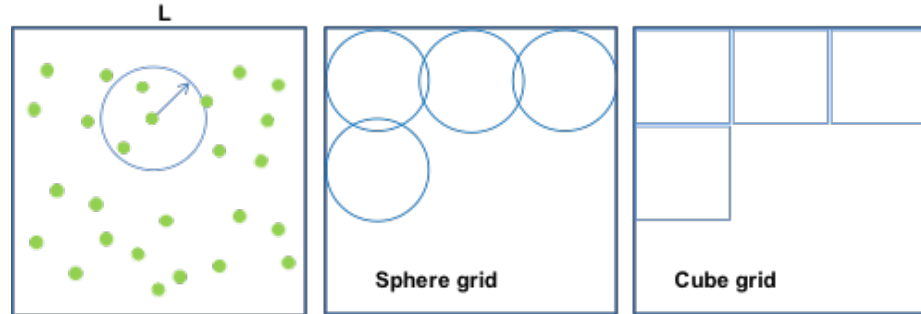


Figure 5.5 The model box showing the distribution of modifiers (green spheres) and sphere grid and cube grid search methods.

5.2.5 Theory of Poisson and binomial distributions

The modifier distribution in the glass model can be compared to statistical distributions, particularly by Poisson and binomial discrete distribution. The Poisson distribution describes random events that are independent and occur randomly but at a definite average rate over unit of time or space [18]. The random variable x that represents the number of events in a fixed unit of time or space has Poisson probability distribution function as follows:

$$P(x) = \frac{\lambda^x e^{-\lambda}}{x!} \quad \text{Equation 5.1}$$

where λ is expected average number of occurrences per unit of time or space and $P(x)$ is the probability of outcome (i.e. $x = 0, 1, 2, \dots, n$) but the number of trials n is indefinitely large i.e. $n \rightarrow \infty$.

On the other hand, the binominal distribution is a discrete probability function defined as:

$$P(x) = \binom{n}{x} p^x (1-p)^{n-x} \quad \text{Equation 5.2}$$

where x is discrete random variable and $x = 0, 1, 2, \dots, n$. The $P(x)$ is the probability of x successes in n trials and the binominal coefficient $\binom{n}{x} = \frac{n!}{x!(n-x)!}$ [19].

The Poisson distribution function is a simple because it's defined by single parameter λ and it can be linked with the distribution of cations where x are the different observed values of cations, N_i , in different regions of space and λ is average value, $\langle N_i \rangle$. However, there is nothing to stop atoms from stacking on top of the other atoms which is physically unrealistic. This will produce a wide distribution function as some search grid boxes have large value of x and some have small value of x .

In a physically realistic model, atoms are stopped from being too close and distribution will be narrower and the search grid box will have roughly an average number of atoms. Therefore, this affect can be achieved with binomial distribution functions where smallest volume for one atom is $1/n$ of the search volume and this may have one atom which is defined by p or may not have one atom which is defined by $(1 - p)$. Hence, in a search grid box the maximum number of atoms n will be the number of smallest volumes for one atom that fit in the search volume (i.e. maximum $x = n$ and on average $x < n$) and the average number of atoms, $\langle N_i \rangle$, is defined by pn (i.e. $pn = \langle N_i \rangle$).

5.3 Results

5.3.1 Modifier cation distribution in initial configurations

Figure 5.6 shows the pictorial distribution of only *Ba* modifier initial configurations in the glass model without the *Si* and *O* atoms. The top part of the figure with the pink spheres and green spheres are the distribution of *Ba* modifiers from the MD method and random method respectively for $25Ba - 75SiO_2$ glass model. Likewise, the bottom part of the figure with the pink spheres and green spheres are the distribution of *Ba* modifiers from

the MD method and random method respectively for $50Ba - 50SiO_2$ glass model. The random positions of modifiers are generated by randomly generating the total number of required modifier's x , y and z positions (i.e. between 0 and 1), and finally x , y and z positions are multiplied by the length of model box.

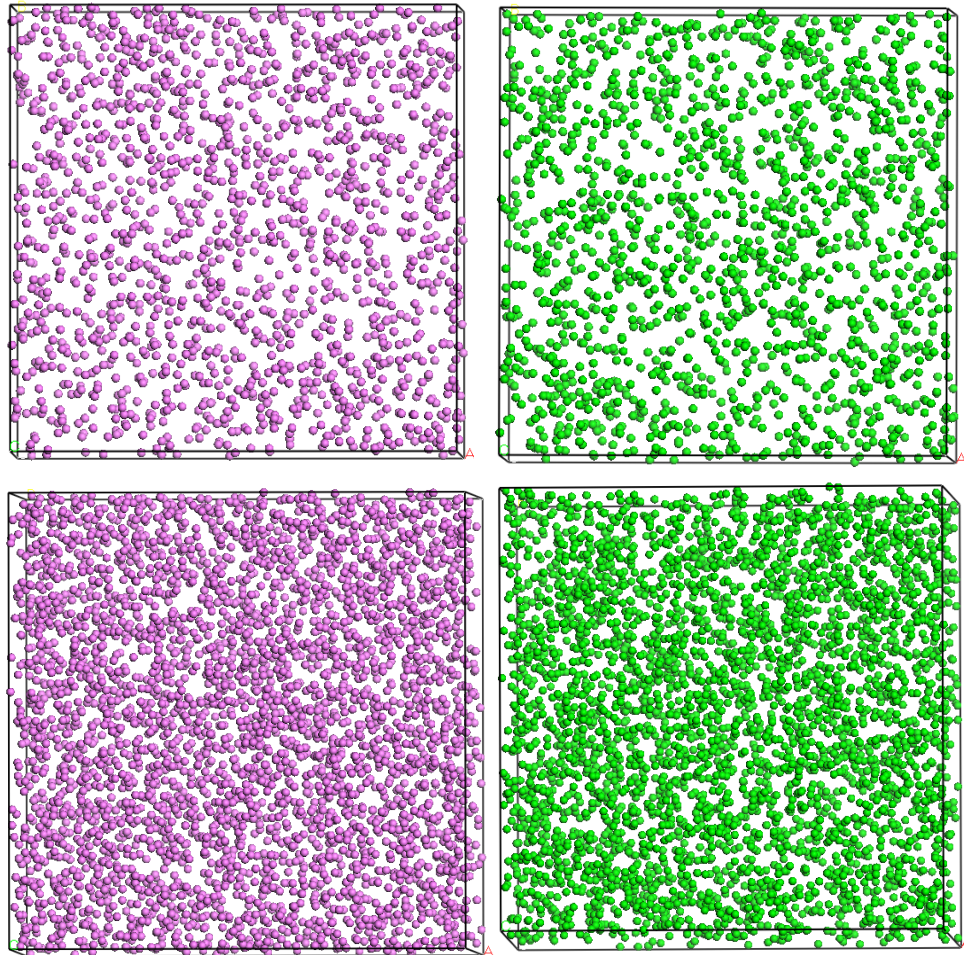


Figure 5.6 The initial configuration of $25BaO - 75SiO_2$ (top) and $50BaO - 50SiO_2$ (bottom) glass model only showing Ba modifiers. The distribution of pink spheres is from the MD configuration and the green spheres are from random method.

Figure 5.7 shows the distribution of modifiers M in $xMO - (x - 100)SiO_2$ glasses for $x = 25$ and 50 where $M = Mg, Ca$ and Ba . The results were obtained by the cubic sampling method where the glass model was divided into $8 \times 8 \times 8$ grid of cubic boxes and total number of cubic grid search boxes was 512. For $25MO - 75SiO_2$ glasses, the average number of modifiers in a search cube was 3.22 (i.e. $\langle N_i \rangle = \left(\frac{L}{8}\right)^3 \frac{N_M}{L^3}$). Similarly, in

$50MO - 50SiO_2$ glasses the average number of modifiers was 7.81. The cubic grid sampling of distributions of positions of modifiers from random method are broader compared to MD method. However, in MD method the configuration of the initial positions of modifier cations do not overlap each other as they are separated by roughly minimum value of inter atomic distance due to their similar charges which produces a narrower distribution as seen in Figure 5.7 (bottom).

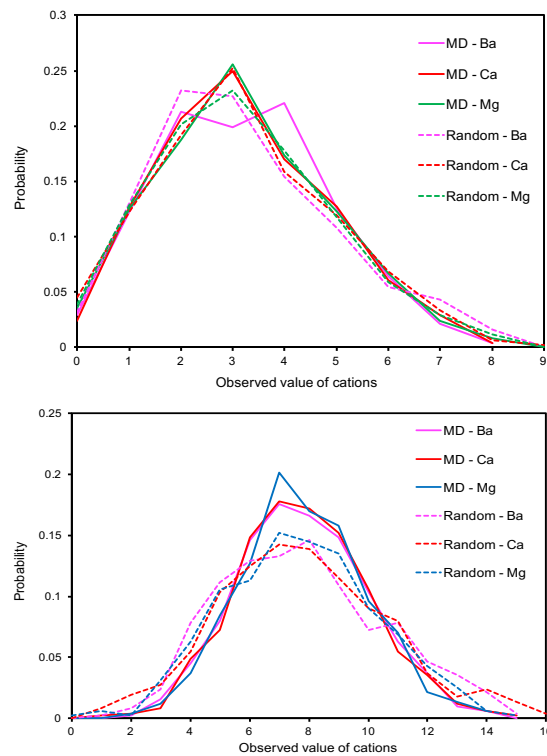


Figure 5.7 The cubic grid sampling of distributions of M modifiers in the initial configuration of glass model for $25MO - 50SiO_2$ (top) and $50MO - SiO_2$ (bottom) glass model with $M = Mg, Ca$ and Ba .

5.3.2 Modifier cation distribution in $50MO - 50SiO_2$ glasses with $M = Mg, Ca$ and Ba

Figure 5.8 shows the pictorial distribution of modifier cation M in $50MO - 50SiO_2$ glasses with $M = Mg, Ca$ and Ba . The figures do not contain Si and O atoms and green spheres are Mg cations in $50MgO - 50SiO_2$ glass, yellow spheres are Ca in $50CaO - 50SiO_2$ glass, and pink spheres are Ba cations in $50BaO - 50SiO_2$ glass. The distribution

of modifier M is expected to be homogenous. The cubic sampling with the total cubic grid search of 512 boxes were computed in the glasses, as shown Figure 5.9 (*top*). The observed values of cations in the cubic grid sampling box shows the highest probability at 8 but for Mg and Ba there is high probability at 7 as well. The resultant curve of Mg modifier is broader and lower than Ca and Ba modifiers.

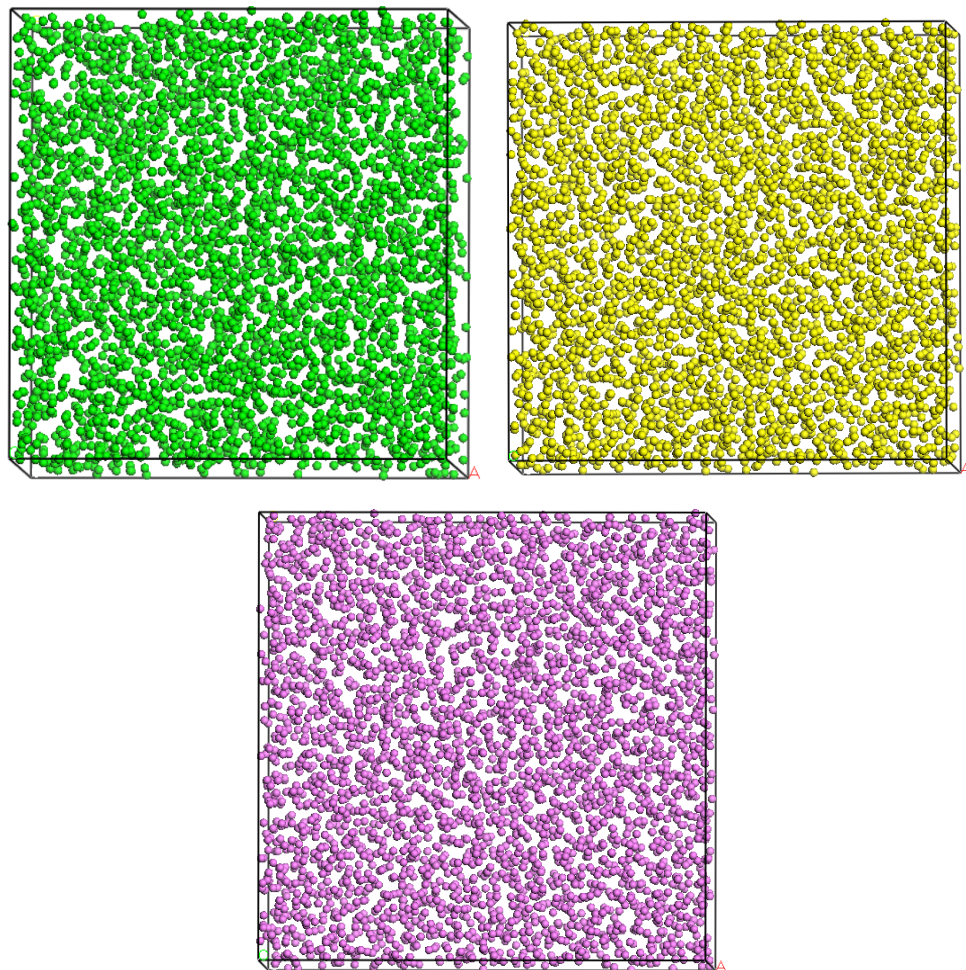


Figure 5.8 The distributions of M modifiers in $50MO - 50SiO_2$ glass models in the final configuration for $M = Mg, Ca$ and Ba . The green spheres are Mg , yellow spheres are Ca and pink spheres are Ba modifiers.

Figure 5.9 (*bottom*) compares the results of cubic sampling between the initial and final MD configurations. The modifier M from MD final configurations have narrow distribution indicating the high probabilities towards the expected of 7.81. The result is much more distinctive for Ba and Ca compared to Mg modifier. This characterised that there is

homogenous distribution of M modifiers in $50MO - SiO_2$ glasses. The homogeneity of modifiers is greater for larger alkaline earth size (e.g. $Ba > Ca > Mg$), this can be associated with the miscibility gap being large for binary magnesium silicate glasses compared to two other Ca and Ba silicate glasses as was mentioned in introduction.

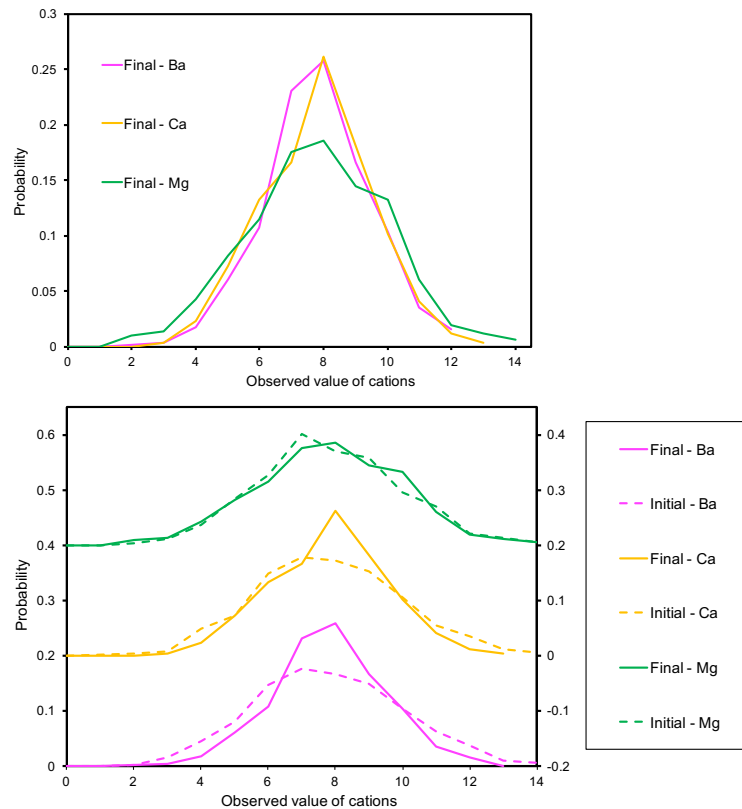


Figure 5.9 The cubic grid sampling of distributions of M modifiers in final configuration in $50MO - 50SiO_2$ glasses with $M = Mg, Ca$ and Ba (top). The comparison of cubic grid sampling of M modifier distributions between initial and final MD configuration in $50MO - 50SiO_2$ glasses (bottom). Vertical offsets of 0.2 have been used for display.

5.3.3 Modifier cation distribution in $25MO - 75SiO_2$ glasses with $M = Mg, Ca$ and Ba

Figure 5.10 shows the pictorial distributions of modifiers cations M in $25MO - 75SiO_2$ glasses (i.e. $M = Mg, Ca$ and Ba). In the figure Si and O atoms are lacking and green spheres are Mg cations in $25MgO - 75SiO_2$ glass, yellow spheres are Ca in $25CaO - 75SiO_2$ glass, and pink spheres are Ba cations in $25BaO - 75SiO_2$ glass. When the cubic

grid sampling with the total of 512 cubic search grid were computed the resultant curve of *Mg* modifier is broader and lower than *Ca* and *Ba* modifiers as shown Figure 5.11 (top). The curve for *Ca* is broader than *Ba* too. The probability of observed values of cations for *Mg* and *Ca* are high at 3 but for *Ba* is higher at 4. The distribution of *Mg* modifier is expected to be heterogeneous due to the miscibility gap.

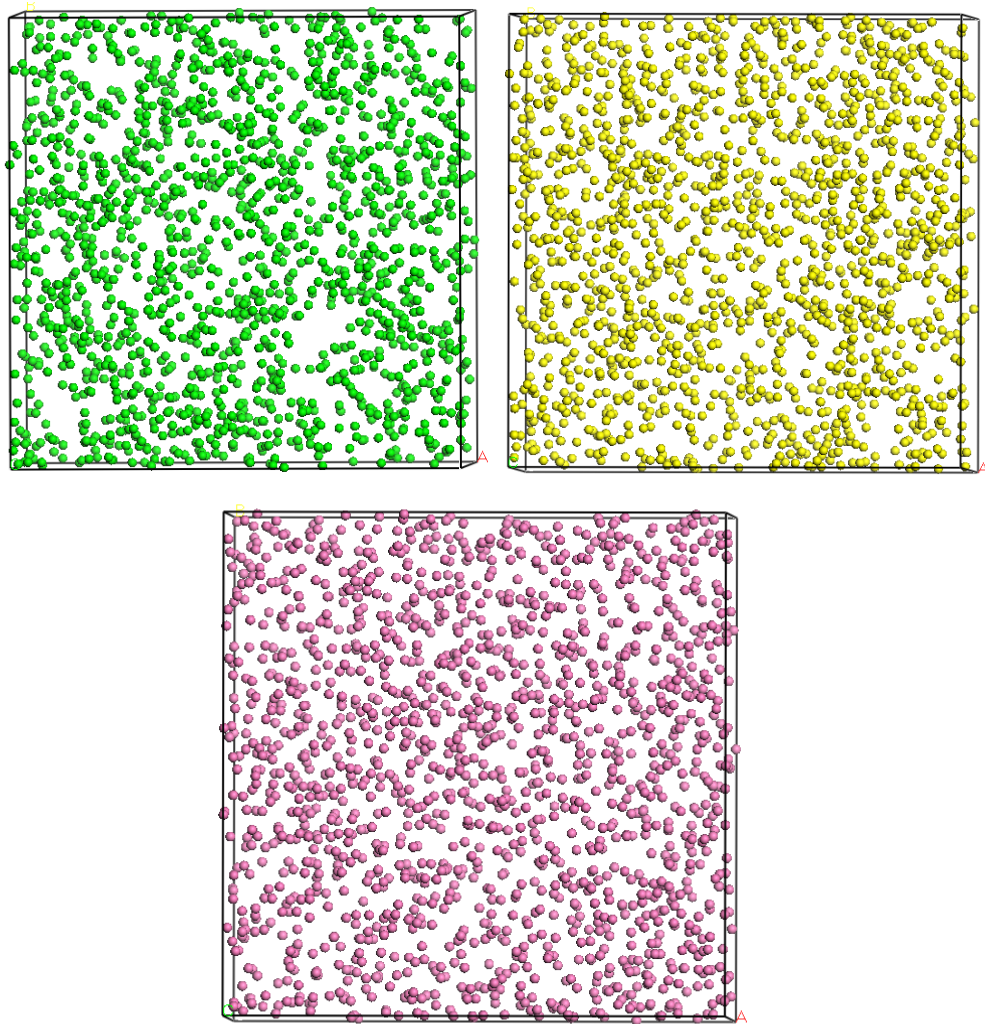


Figure 5.10 The distributions of *M* modifiers in $25MO - 75SiO_2$ glass models in the final configuration for $M = Mg, Ca$ and Ba . The green spheres are *Mg*, yellow spheres are *Ca* and pink spheres are *Ba* modifiers.

Figure 5.11 (bottom) compares the results of cubic sampling between the initial and final MD configurations. The curves from the initial and final configuration from MD follow different trends as for *Mg* it gets wider, for *Ca* it stays same and for *Ba* it gets narrower.

Therefore, the narrow curve indicating the high probabilities towards the expected value of 3.22. The wide-range observed for numbers, N_i , of Mg modifier in the MD final configuration of glass model characterised the heterogeneity of Mg modifier in $25MO - 75SiO_2$ glasses.

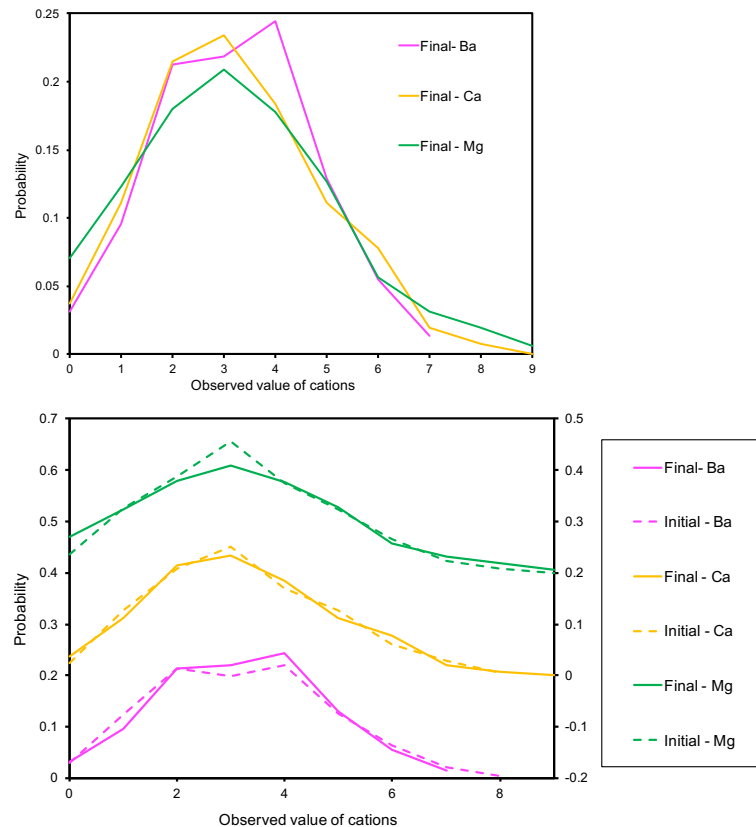


Figure 5.11 The cubic grid sampling of distributions of M modifiers in final configuration in $25MO - 75SiO_2$ glasses with $M = Mg, Ca$ and Ba (top). The comparison of cubic sampling of M modifiers distributions between initial and final MD configuration in $25MO - 75SiO_2$ glasses (bottom). Vertical offsets of 0.2 have been used for display.

5.4 Discussion

The cubic sampling results from MD initial configurations shows that modifiers M are not truly randomly distributed when it was compared with the initial configurations from the random method. The curves of modifiers M from random initial configuration are broader than from MD initial configuration. For both $25MO - 75SiO_2$ and $50MO -$

$50SiO_2$ (i.e. $M = Mg, Ca$ and Ba) glass models the Poisson distribution functions were calculated and presented in Figure 5.12 with the expected values of $\lambda = 3.22$ and $\lambda = 7.81$ respectively. Figure 5.12 also shows that truly random configurations agreeing with the Poisson results.

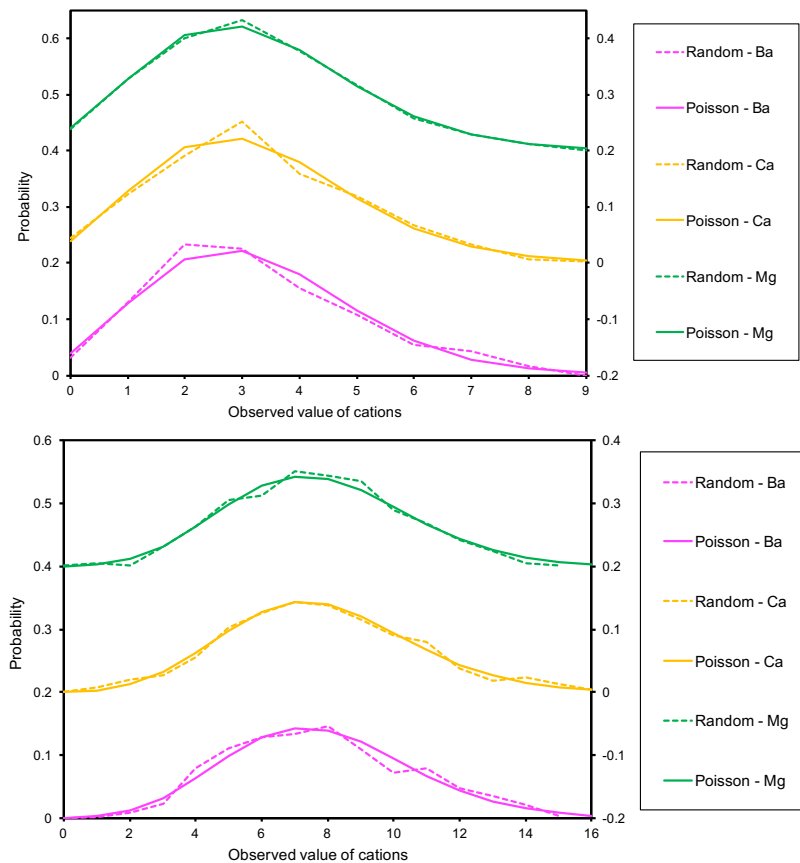


Figure 5.12 Comparison of the Poisson distribution function and cubic grid sampling of distributions of modifiers M in initial configuration from random method for $25MO - 75SiO_2$ (top) and $50MO - 50SiO_2$ (bottom) glasses with $M = Mg, Ca$ and Ba . Vertical offsets of 0.2 have been used for display.

The cubic sampling results from final MD configuration for distribution of modifiers M in $50MO - 50SiO_2$ glasses gave the full width at half maximum (FWHM) narrower than Poisson functions which is shown in Figure 5.13. Hence final MD configurations give less statistical fluctuations than random distributions. The figure also shows the final MD configuration matches the characteristics of binominal distribution function where $\langle N_i \rangle = \lambda = np = 7.81$. However, the two parameters that can be adjusted are n and p where $n =$

18 for Mg and $n = 11$ for both Ca and Ba , and $p = 7.81/n$. Modifiers are evenly distributed because of $i - i$ separation (i.e. $r_{ii} \geq R_{mm}$). This effect is incorporated in the binomial distribution because in cubic grid search boxes each smallest volume can have at most 1 modifier.

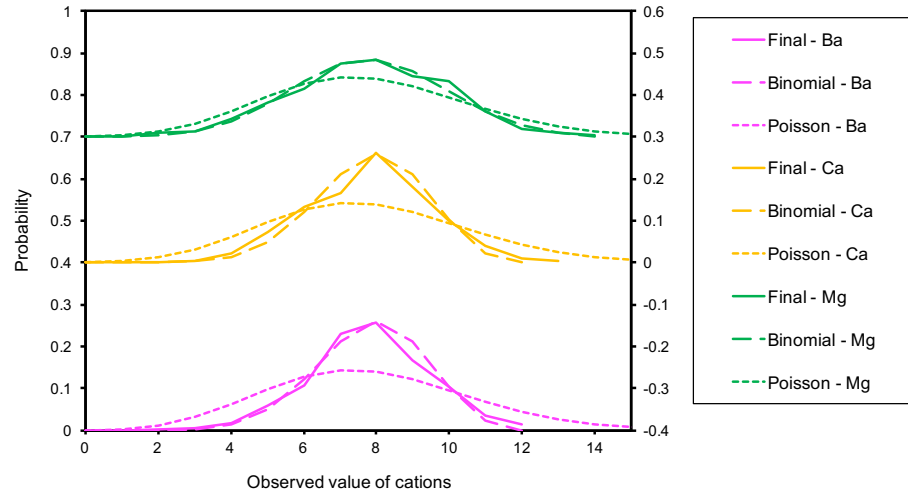


Figure 5.13 Comparison of cubic grid sampling distributions of modifiers M in the MD final configuration of $50MO - 50SiO_2$ glasses (i.e. $M = Mg, Ca$ and Ba), with Poisson and binomial distribution functions. Vertical offsets of 0.2 have been used for display.

The cubic sampling results from final MD configuration of distribution of modifiers M in $25MO - 75SiO_2$ glasses gave the full width at half maximum (FWHM) similar to Poisson function as shown in Figure 5.14. The result for Ba is narrow than random, Ca is similar to random and Mg is wider than random. This shows the greater effect for smaller alkaline earth size (i.e. $Mg < Ca < Ba$).

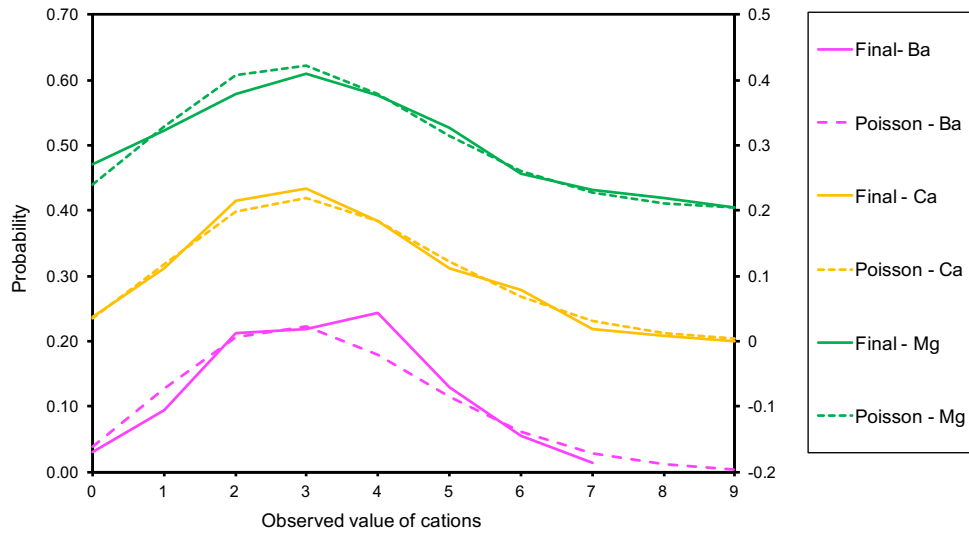


Figure 5.14 Comparison of cubic sampling ($l = 8 \text{ \AA}$) distributions of modifiers M in the MD final configuration of $25MO - 75SiO_2$ glasses (i.e. $M = Mg, Ca$ and Ba) with Poisson distribution functions. Vertical offsets of 0.2 have been used for display.

In MD, a large number of time-steps were performed in the melts before quench to see the effects on homogeneity of the glasses. This is so the melts have got enough time for a completely homogenous distribution to be achieved. Figure 5.15 shows that for Ba and Ca the large number of time-steps results in a distribution getting close to a random distribution. Instead Mg gets more different to a random distribution and in particular higher probability for $x = 0$ and for $x \geq 6$, and lower probability for $x = 3$. This shows the miscibility gap for Mg .

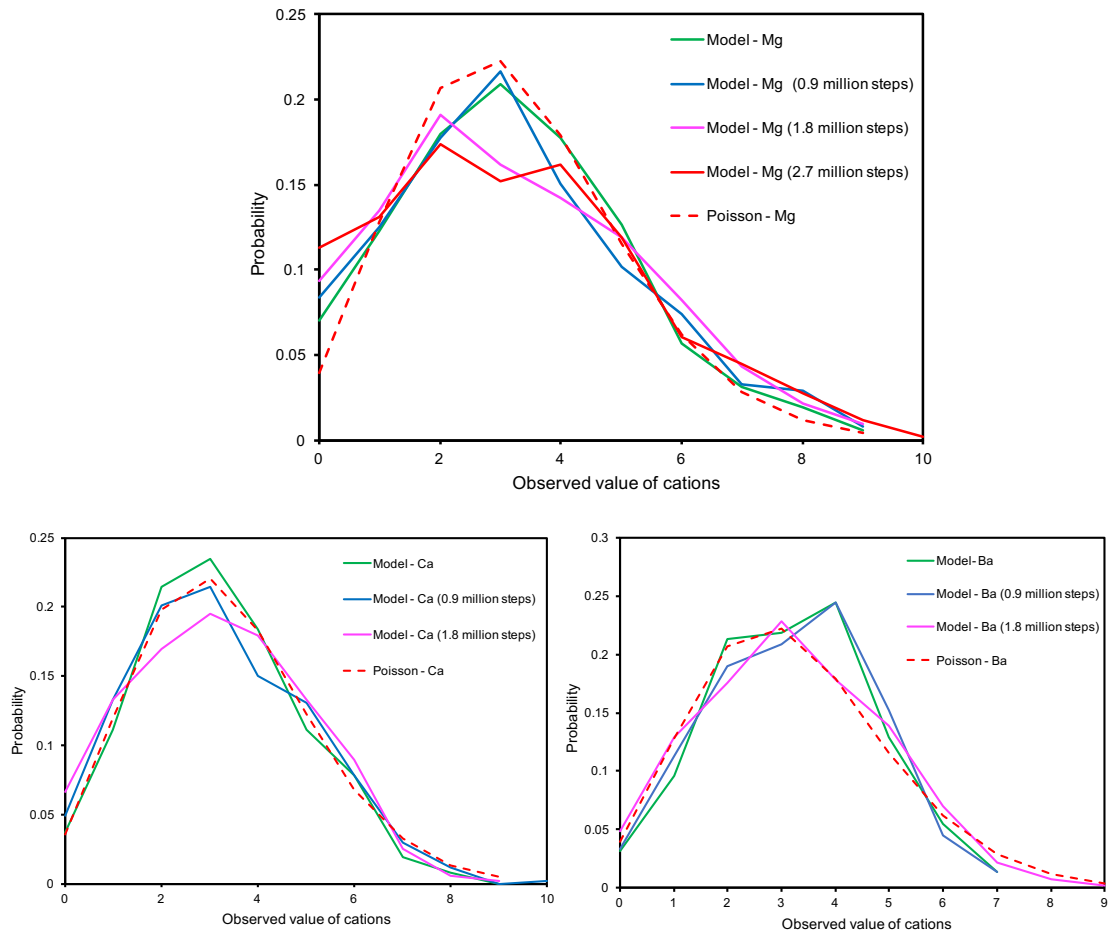


Figure 5.15 The result of cubic sampling distributions of modifiers M in the MD final configuration of $25MO - 75SiO_2$ glasses with $M = Mg$ (top), Ca (bottom-left) and Ba (bottom-right) from different time-steps used in the melt before quenching.

5.5 Conclusions

The phase diagram of alkaline earth silicate systems and the barium silicate glasses in Chapter 4 shows whether there is phase separation for $x \leq 25$ glasses. To see better in alkaline earth silicate glasses large models were made. These were investigated with a new method to quantify the distribution of modifiers, M , with the so called cubic grid search. When examining $50MO - 50SiO_2$ glasses the results show narrower than a random distribution. The physical reason is the minimum separation distances between the modifiers. This can be approximated by the binomial distribution. Instead for $25MO - 75SiO_2$ glasses where there is lower concentration of modifiers it is seen that Ba and Ca are similar to a

random distribution. However, for *Mg* it was wider than the random distribution which is a sign of the miscibility gap.

5.6 References

- [1] H. Rawson, Inorganic glass forming system: Nonmetallic solids, (1967).
- [2] R.H. Doremus, Glass Science, 2nd ed., Wiley, 1994.
- [3] P. Hudon, D.R. Baker, The nature of phase separation in binary oxide melts and glasses. I. Silicate systems, *J. Non Cryst. Solids*. 303 (2002) 299-345.
- [4] A.F. Craievich, E.E. Zanotto, P.F. James, Kinetics of sub-liquidus phase separation in silicate and borate glasses. A review, *Bull Mineral*. 106 (1983) 169-184.
- [5] J.E. Shelby, Introduction to Glass Science and Technology, Royal Society of Chemistry, 2005.
- [6] G. Mountjoy, B.M. Al-Hasni, C. Storey, Structural organisation in oxide glasses from molecular dynamics modelling, *J. Non Cryst. Solids*. 357 (2011) 2522-2529.
- [7] B.M. Al-Hasni, G. Mountjoy, A molecular dynamics study of the atomic structure of $x(\text{MgO})_{100-x}(\text{SiO}_2)$, *J. Non Cryst. Solids*. 400 (2014) 33-44.
- [8] M. Guignard, L. Cormier, Environments of Mg and Al in $\text{MgO}-\text{Al}_2\text{O}_3-\text{SiO}_2$ glasses: A study coupling neutron and X-ray diffraction and Reverse Monte Carlo modelling, *Chemical Geology*. 256 (2008) 111-118.
- [9] M. Wilding, M. Guthrie, C.L. Bull, M.G. Tucker, P.F. McMillan, Feasibility of in situ neutron diffraction studies of non-crystalline silicates up to pressures of 25 GPa, *Journal of Physics: Condensed Matter*. 20 (2008) 244122.
- [10] M.C. Wilding, C.J. Benmore, J.A. Tangeman, S. Sampath, Coordination changes in magnesium silicate glasses, *EPL (Europhysics Letters)*. 67 (2004) 212.
- [11] C.J. Benmore, E. Soignard, M. Guthrie, S.A. Amin, J.K.R. Weber, K. McKiernan, M.C. Wilding, J.L. Yarger, High pressure X-ray diffraction measurements on Mg_2SiO_4 glass, *Journal of Non-Crystalline Solids*. 357 (2011) 2632-2636.
- [12] R.N. Mead, G. Mountjoy, A Molecular Dynamics Study of the Atomic Structure of $(\text{CaO})_x(\text{SiO}_2)_{1-x}$ Glasses, *The Journal of Physical Chemistry B*. 110 (2006) 14273-14278.
- [13] G. Mountjoy, SRS Experimental Reports 2005, Daresbury Laboratory: Warrington. (2005).
- [14] C. Karlsson, E. Zanghellini, J. Swenson, B. Roling, D.T. Bowron, L. Brjesson, Structure of mixed alkali/alkaline-earth silicate glasses from neutron diffraction and vibrational spectroscopy, *Physical Review B*. 72 (2005) 064206.

- [15] E.D. Zanotto, P.F. James, A.F. Craievich, The effects of amorphous phase separation on crystal nucleation kinetics in BaO-SiO₂ glasses, *J. Mater. Sci.* 21 (1986) 3050-3064.
- [16] A.H. Ramsden, P.F. James, The effects of amorphous phase separation on crystal nucleation kinetics in BaO-SiO₂ glasses, *J. Mater. Sci.* 19 (1984) 2894-2908.
- [17] D. Teter, Private communication, (2004).
- [18] T.R. Forester, W. Smith, The DL_POLY_2. 0 user manual, CCLRC, Daresbury Laboratory, Warrington, UK. (1997).
- [19] J. Taylor, *Introduction to Error Analysis, the Study of Uncertainties in Physical Measurements*, 1997.

Chapter 6

Molecular dynamics modelling of barium zirconium fluoride $ZrF_4 - BaF_2$ glasses

6.1 Introduction

Glass formation based on the fluorozirconate system was discovered by Poulain et al. in 1975 [1]. It was first observed in the $ZrF_4 - BaF_2 - NaF$ ternary system and later in 1979 [2] it was observed in the $ZrF_4 - BaF_2$ binary system [3]. Zirconium tetrafluoride itself does not exist in the vitreous form but it can form binary glasses if associated with other fluorides, particularly BaF_2 [4]. Fluorozirconate glasses have a tendency for crystallization and the differences between the crystallization temperature and T_g are generally approximately 300 K, which is indicative of the instability of these glasses [5]. However, in the binary systems the combination of fluorozirconate with di- and trivalent fluorides like BaF_2 and LaF_3 can give rise to rather stable glasses, but over limited ranges of compositions [6]. A phase diagram of $ZrF_4 - BaF_2$ is shown in Figure 1 [7]. The first such binary glasses, $xZrF_4 - (100 - x)BaF_2$ reported by Poulain et al. [2] contained ZrF_4 between $x = 60$ to 70. Later, in 1981 with the same quenching rate Almeida et al. reported the glass forming region to be $x = 52$ to 74 [8].

The compositions of glass forming in the fluorozirconate system can be described by the ratio of F to Zr , which is independent of the compositions of the counter-cations such as Li , Na , K , Rb and Ba [9]. The ratio for the binary system $ZrF_4 - BaF_2$ is between 4.5 and 6 [9], i.e. glass-forming region around $x = 50$ to 82.

The chemical bonding ionicity estimated from the electronegative differences for ZrF_4 is 83% and BaF_2 is 91% [10]. This indicates that with the relatively high atomic number cations, the closed shell configuration of F^- is relatively undeformed, hence the heavy-metal fluoride bonding can be described by considering spherically symmetric interatomic

interactions [11]. Although the tendency towards the formation of complex ions ZrF_x^{4-x} in melts and crystals has been attributed to mixed ionic-covalent bond [5], it is a good first order representation of their interatomic potentials to be treated as ionic [11].

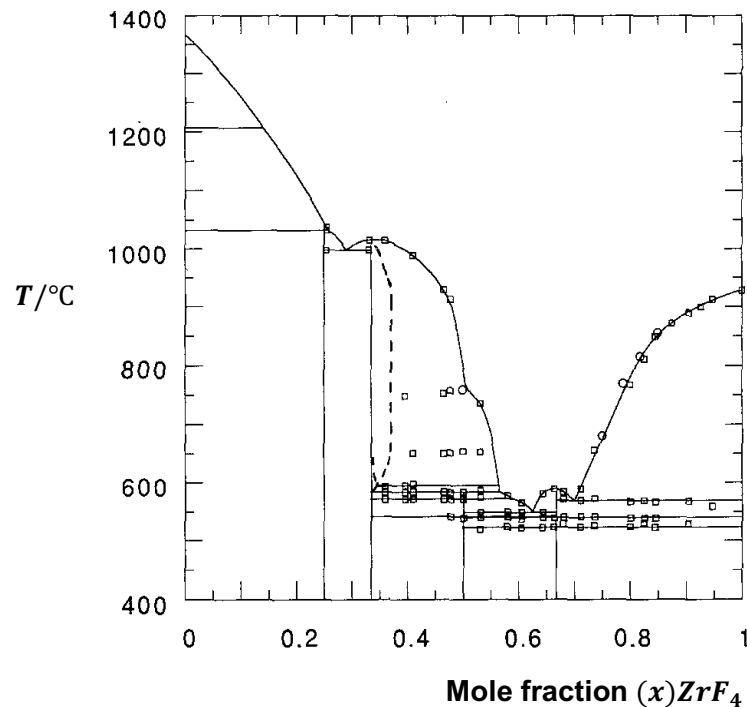


Figure 6.1 The phase diagram of binary system $ZrF_4 - BaF_2$ [7].

In term of glass structure, the fluorozirconate glasses do not follow Zachariasen's rules and ZrF_4 is considered the main component of glass former or glass progenitor [3] rather than the concept of network former that is common in oxide glasses. The barium fluorozirconate based binary systems are the simplest fluorozirconate glasses, where BaF_2 plays the role of network modifier [12] but this description remains controversial. For ionic system, such as heavy-metal fluoride glasses, the structural theory of random closed packed (RCP) model [13] is proposed (e.g. [14]) rather than common theory of modified random network or continuous random network (CRN) to describe the structural theories of glass formation.

The fluorozirconates are puzzling glass systems and the prominent reasons may be the extreme ability of Zr^{4+} ions to modify its own environment around F^- ions [15]. The

coordination number for F about Zr (N_{ZrF}) can be 6, 7 or 8, even in the fluorozirconate crystals [16]. Therefore, to understand heavy-metal fluoride glass structures that lack the structural units one has to grasp the knowledge on how these various polyhedra form a glassy material and how they are affected by the addition of modifiers or substitution of other glass formers [11].

The early short-range structure of fluorozirconate glasses were studied with infrared and Raman spectroscopy by Almeida and Mackenzie [8]. They reported structural characteristics for three different model glasses and comparing the Raman spectra to fluoride crystals based on stoichiometry [17]. The three model glasses that were investigated were barium dizirconate ($67ZrF_4 - 33BaF_2$ and $64ZrF_4 - 36BaF_2$), barium metazirconate ($52ZrF_4 - 48BaF_2$) and barium trizirconate ($74ZrF_4 - 26BaF_2$). They suggested that barium dizirconate glass was composed of zigzag chains of ZrF_6 octahedra (i.e. $N_{ZrF} = 6$ with 2 bridging fluorine atoms), cross linked by $Ba - F$ ionic bonds. For barium metazirconate and trizirconate, reported N_{ZrF} were 7 and 5 respectively. However, they concluded that all glasses appeared to have a small number of isolated ZrF_6^{2-} octahedra units and the structure of fluorozirconate glasses varies gradually with the ZrF_4 content. They also proposed that the inter-octahedral angle ($Zr - F - Zr$) was roughly 136° .

Later work done by Phifer et al [18] with Raman spectroscopy found that $BaZr_2F_{10}$ glass has N_{ZrF} between 7 and 8. However, for $52ZrF_4 - 48BaF_2$ glass, they reported N_{ZrF} was about 8 and for $74ZrF_4 - 26BaF_2$ glass was mostly 7, with some 6. Kawamoto et al [19] studied crystals structures of $ZrF_4 - BaF_2$ binary system with Raman scattering spectra and these were compared with the glass structures.

Several X-ray and neutron diffraction studies were carried out on $ZrF_4 - BaF_2$ binary glasses. The early X-ray studies were reported by Coupe' et al. [20] and they studied $xZrF_4 - (100 - x)BaF_2$ glass for compositions $x = 50$ to 82 . The average CN reported for

the zirconium atom were in the range of 7.08 to 8.35 that depended on the chemical compositions. The CN for barium with respect to fluorine atoms (N_{BaF}) were reported ranging from 8.1 to 10.7. They found the short-range order distances for $Zr - F$ (R_{ZrF}) and $Ba - F$ (R_{BaF}) from 2.09 – 2.11 Å and 2.61 – 2.68 Å respectively. They also reported the average values of the $Zr - F - Zr$ angle varying from 143° to 160° again depending on the chemical composition.

The X-ray diffraction study done on $50ZrF_4 - 50BaF_2$ glass by Kawamoto and Hori-saka [21] proposed that the basic structure of the glasses consists of chains of edge shared ZrF_8 dodecahedra polyhedra by comparing with the crystal structure of $\beta - BaZrF_6$ and $\alpha - BaZrF_6$. Etherington and Almeida et al. [22] studied $64ZrF_4 - 36BaF_2$ glass with X-ray diffraction and found $N_{ZrF} = 7.6$. They implied that results from the diffraction are consistent either with a structural model consisting of a three-dimensional random network of ZrF_8 structural units, or a chain model of the type proposed by Almeida and Mackenzie [8] on the basis of Raman data.

Almeida and Mackenzie [23] studied the $64ZrF_4 - 36BaF_2$ glass, by both methods of X-ray and neutron diffraction techniques by also found N_{ZrF} between 6 and 7. They also proposed that there is existence of both bridging and non-bridging fluorine atoms. XPS (X-ray photoemission spectroscopy) studies done by Almeida et al [24] on $xZrF_4 - (100 - x)BaF_2$ glasses of composition $x = 55$ to 75, also suggested the existence of an extensive degree of bridging fluorine in these glassy networks.

Wagner et al [25] studied $67ZrF_4 - 33BaF_2$ glass by both X-rays and neutron diffraction techniques in details. They reported the $Zr - F$ short-range distance order 2.06 Å for both X-ray and neutrons diffraction and slightly different $N_{ZrF} = 7.4$ for X-ray and 6.9 for neutrons. Le Bail et al [26] investigated $ZrF_4 - (100 - x)BaF_2$ glasses by neutron diffraction with compositions $x = 60, 67$ and 75. They only performed X-ray diffraction on

$67ZrF_4 - 33BaF_2$ glass and characterised it as the most detailed of their investigations. They reported N_{ZrF} between 7 – 7.5 and $N_{BaF} \sim 10$, with the details of pair distribution function over distances up to 6 Å.

Boulard et al. [27] studied the $xZrF_4 - (100 - x)BaF_2$ glasses by EXAFS for compositions $x = 60, 67$ and 75 . They reported the N_{ZrF} of 6.8, 7.1 and 8.1 respectively, with R_{ZrF} short-range order distance of roughly 2.1 Å. However, the EXAFS studies of $67ZrF_4 - 33BaF_2$ and $60ZrF_4 - 40BaF_2$ glasses performed by Fudging and Kunquan et al [28] reported the N_{ZrF} of 6 and R_{ZrF} short-range order distance between 2.03 – 2.05 Å. On the other hand, Almeida et al [29] studied Ba atom structural environments in $67ZrF_4 - 33BaF_2$ glass with EXAFS and reported $N_{BaF} = 7.4$ and $R_{BaF} = 2.71$ Å.

Youngman and Sen [30] studied $xZrF_4 - (100 - x)BaF_2$ glasses using high-resolution ^{19}F NMR spectroscopy for $x = 58$ to 78 . Their structural studies reported N_{ZrF} about 7.6 to 7.1. They also looked at bridging fluorine between corner sharing $Zr - F$ polyhedra and one non-bridging fluorine which is bonded to one Zr and one Ba atom or is bonded to one Zr and two Ba atoms. They concluded that the edge shared $Zr - F$ polyhedral in these binary glasses are insignificant.

Several other studies done on the structural modelling of $ZrF_4 - BaF_2$ binary glasses were by molecular dynamics (MD) techniques. One of the early modelling studies by Lucas et al [31] was performed on $64ZrF_4 - 36BaF_2$ glass and analysis was focused on $Zr - Zr$ distances due to the previous report of edge sharing like that observed in the crystal $\alpha - ZrF_4$. They reported that the CN of F by Zr was around 1.5 compared with 2.0 expected if each Zr were bridged by a single fluoride and CN of Zr by F about 7.7. On the other hand, Kawamoto et al [32] performed structural modelling on $50ZrF_4 - 50BaF_2$ glass. They found short-range order distances, $R_{ZrF} = 2.12$ Å and $R_{BaF} = 2.75$ Å and reported $N_{ZrF} = 8$ and $N_{BaF} = 10$. They also proposed that the structural units ZrF_n were mostly triangular

decahedron (Snub Disphenoid) and small amount of monocapped trigonal prism with $CN = 7$. Also, they summarised from the $Zr - Zr$ pair correlation function that the ZrF_n polyhedra were linked by 3:2 ratio of edge sharing and corner sharing.

Yasui and Inoue [33] studied $xZrF_4 - (100 - x)BaF_2$ glasses by both molecular dynamics simulations and X-ray diffraction for $x = 60$ and 75 . Their MD result revealed that the structural units in these glasses were mainly ZrF_8 polyhedra and they were either linked by corners or edges. They concluded that the edge shared structure was similar to the crystal $\beta - BaZrF_6$. Phifer et al [34] reviewed all the previous structural data and MD results for binary $ZrF_4 - BaF_2$ glasses and proposed a Zr_2F_{13} bi-polyhedra module based model, with strong edge sharing in $67ZrF_4 - 37BaF_2$ glass and also by considering structure of the same composition crystal $BaZr_2F_{10}$. Whereas Simmons et al [35] did MD studies of $xZrF_4 - (100 - x)BaF_2$ glasses for $x = 50$ to 75 and reported that the Zr^{4+} ions are primarily 8-fold coordinated to F^- ions.

Structural studies of this binary glass system by first principles (quantum mechanics) MD technique performed by Voit et al [36] and Lin-xiang et al [37] also reported that CN of Zr can be equal to 7 or 8 and connection is mixed by edges or corners. From all the previous structural studies, the basic structural units of these glasses are not firmly established and it is not clearly determined the manner in which these structural units are interconnected. Also, there is the puzzling glass structure interpretation by either random packing or random network theories. Therefore, we are making new MD models of the binary $ZrF_4 - BaF_2$ glasses in order to carry out detailed analysis of structural units and for this purpose we will make use of results for rotational invariants, Q_l , presented in Chapter 3.

6.2 Method

6.2.1 Structure of barium fluorozirconate crystals

The crystal structures are studied to compare the structural units and the short-range order to the corresponding glasses. It also tests the validity of the inter-atomic potential parameters used for the structural studies of the glasses by MD.

6.2.1.1 $\alpha - ZrF_4$

The alpha zirconium tetrafluoride crystal polyhedra [38] with the $Zr - F$ $CN = 8$ is shown in Figure 6.2. The calculated density of the crystal is 4.60 gcm^{-3} . The lattice parameters are: $a = 7.896 \text{ \AA}$, $b = 7.896 \text{ \AA}$ and $c = 7.754 \text{ \AA}$ with $\alpha = 90^\circ$, $\beta = 90^\circ$ and $\gamma = 90^\circ$.

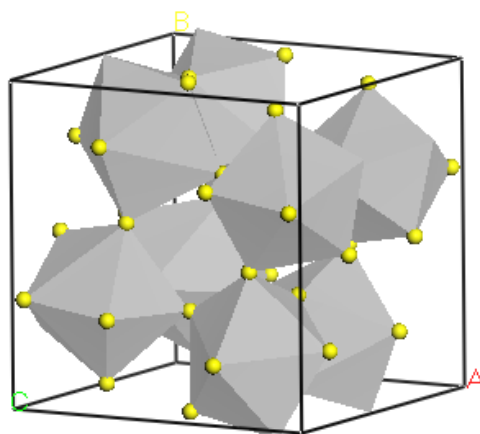


Figure 6.2 The unit cell of $\alpha - ZrF_4$ with ZrF_n polyhedra indicated in grey and the yellow spheres are fluorine atoms.

6.2.1.2 $\beta - ZrF_4$

The beta zirconium tetrafluoride crystal polyhedra [39] is shown in Figure 6.3. This crystal has peculiar CN with some Zr having $CN = 6$ and some having $CN = 8$. Likewise, Zr with $CN = 8$ for this particular crystal has been reported elsewhere [20]. The lattice parameters are $a = 9.570 \text{ \AA}$, $b = 9.930 \text{ \AA}$ and $c = 7.730 \text{ \AA}$ with $\alpha = 90^\circ$, $\beta = 94.28^\circ$ and $\gamma = 90^\circ$.

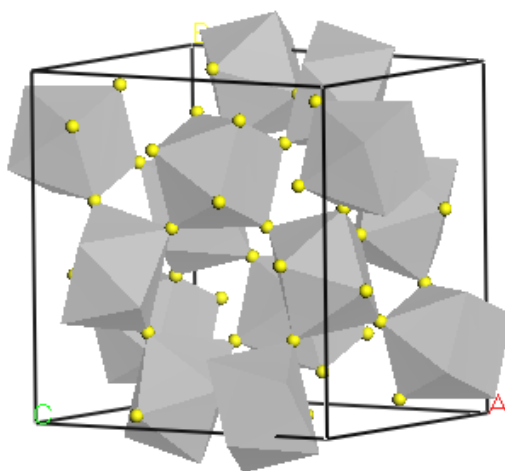


Figure 6.3 The unit cell of $\beta - ZrF_4$ with ZrF_n polyhedra indicated in grey and the yellow spheres are fluorine atoms.

6.2.1.3 $\beta - BaZr_2F_{10}$

The beta barium dizirconate crystal [40] is shown in Figure 6.4. The two distinctive polyhedra are $Zr - F$ with $CN = 7$ indicated by grey polyhedra and $Ba - F$ with $CN = 11$ indicated by blue polyhedra. The calculated density of the crystal is 4.35 gcm^{-3} . The lattice parameters are $a = 6.064 \text{ \AA}$, $b = 15.383 \text{ \AA}$ and $c = 9.057 \text{ \AA}$ with $\alpha = 90^\circ$, $\beta = 112.98^\circ$ and $\gamma = 90^\circ$.

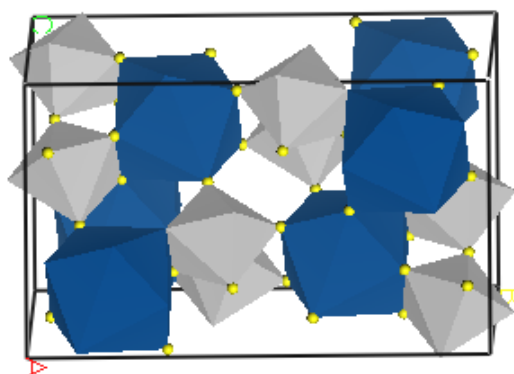


Figure 6.4 The unit cell of $\beta - BaZr_2F_{10}$ crystal, grey indicating the ZrF_n polyhedra and blue indicating BaF_n polyhedra.

6.2.1.4 $\alpha - BaZrF_6$

The alpha barium metafluorozirconate crystal [41] is shown in Figure 6.5. The grey polyhedra are $Zr - F$ with $CN = 8$ and the blue polyhedra are $Ba - F$ with $CN = 11$. However, for $\alpha - BaZrF_6$ crystal, $Zr - F$ with $CN = 7$ can be found elsewhere [19]. The $\beta - BaZrF_6$ crystal polyhedra having $Zr - F$ with $CN = 8$ and $Ba - F$ with $CN = 10$ is also reported [20]. The calculated density of the crystal is 5.01 gcm^{-3} . The lattice parameters are $a = 6.493 \text{ \AA}$, $b = 9.530 \text{ \AA}$ and $c = 9.203 \text{ \AA}$ with $\alpha = 90^\circ$, $\beta = 127.09^\circ$ and $\gamma = 90^\circ$.

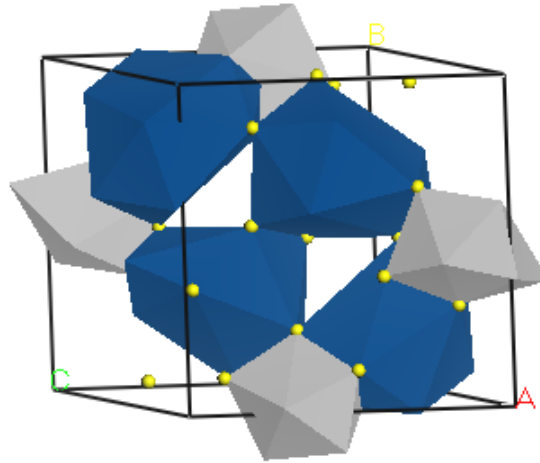


Figure 6.5 The unit cell of $\alpha - BaZrF_6$ crystal, grey indicating the ZrF_n polyhedra and blue indicating BaF_n polyhedra.

6.2.1.5 $\alpha - Ba_2ZrF_8$

The $\alpha - Ba_2ZrF_8$ crystal [42] is shown in Figure 6.6. The grey polyhedra are $Zr - F$ with $CN = 8$ and the blue polyhedra are $Ba - F$ with $CN = 11$. The calculated density of the crystal is 5.29 gcm^{-3} . Its lattice parameters are: $a = 9.740 \text{ \AA}$, $b = 5.614 \text{ \AA}$ and $c = 11.887 \text{ \AA}$ with $\alpha = 90^\circ$, $\beta = 90^\circ$ and $\gamma = 90^\circ$.

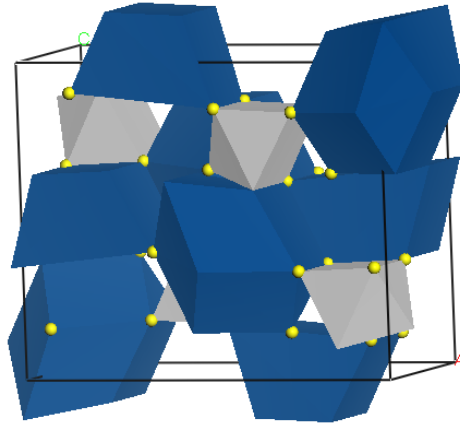


Figure 6.6 The unit cell of $\alpha - Ba_2ZrF_8$ crystal, grey indicating the ZrF_n polyhedra and blue indicating BaF_n polyhedra.

6.2.1.6 BaF_2

The structural unit cell of barium fluoride crystal [43] is shown in Figure 6.7 with $Ba - F$ having $CN = 8$. The calculated density of the crystal is 4.89 gcm^{-3} . Its lattice parameters are: $a = 6.196 \text{ \AA}$, $b = 6.196 \text{ \AA}$ and $c = 6.196 \text{ \AA}$ with $\alpha = 90^\circ$, $\beta = 90^\circ$ and $\gamma = 90^\circ$.

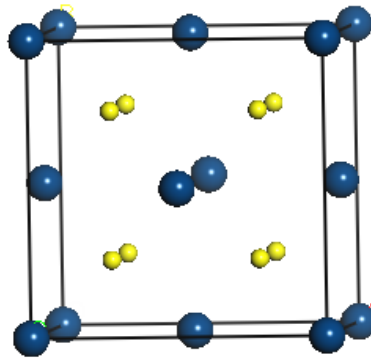


Figure 6.7 The unit cell of BaF_2 crystal, blue spheres representing barium atoms and yellow spheres representing fluorine atoms.

6.2.2 Potentials for barium fluorozirconate systems

The interaction between the pairs of ions in $ZrF_4 - BaF_2$ binary system was described by using the Buckingham rigid ion interatomic potentials. The form of Coulomb and Buckingham potentials are given in Equation 2.2 – 2.4. The potential parameters used were derived by Teter [44] and these are listed in Table 6.1 for $Zr - F$, $Ba - F$ and $F - F$ interactions.

Table 6.1 Teter potential parameters for $ZrF_4 - BaF_2$ binary system.

$i - j$	$q_i(e)$	$A_{ij}(eV)$	$\rho_{ij}(\text{\AA})$	$C_{ij}(eV\text{\AA}^{-6})$
$Zr - F$	2.4	216847.86	0.150759	0.06858
$Ba - F$	1.2	472934.92	0.190284	140.80
$F - F$	-0.6	11510.58	0.225005	29.53

6.2.3 Testing of potentials

Before the application of MD simulation to the modelling of melt quenched glasses to study the atomic structure, at first one has to test the interatomic potentials. Therefore, to evaluate the legitimacy of Teter interatomic potential energy function parameters, they were applied in the energy minimisation algorithm of well-known crystal structures of $\alpha - ZrF_4$, $\beta - ZrF_4$, $\beta - BaZr_2F_{10}$, $\alpha - BaZrF_6$, $\alpha - Ba_2ZrF_8$ and BaF_2 . In $ZrF_4 - (100 - x)BaF_2$ glasses these correspond to $x = 100, 75, 67, 50$ and 0 respectively. The principle and algorithms of the energy minimisation method to test these potential parameters by the General Utility Lattice Program (GULP) are explained in Chapter 2. The results obtained from the GULP minimisation process are given in the following Tables 6.2 – 6.7.

Table 6.2 The result from the GULP energy minimisation for $\alpha - ZrF_4$ crystal initial and final structures displaying the low percentage errors.

Parameter	Unit	Initial Value	Final Value	Difference	Percent
Volume	\AA^3	481.566	471.044	-10.521	-2.18
a	\AA	7.896	7.849	-0.046	-0.59
b	\AA	7.896	7.849	-0.046	-0.59
c	\AA	7.724	7.644	-0.79	-1.02
α	Degree	90.000	89.99	-0.001	0.00
β	Degree	90.000	89.99	0.001	0.00
γ	Degree	90.000	89.99	-0.002	0.00
$Zr - F$ distance	\AA	2.216	2.091	-0.125	-5.63
$Zr - F$ CN		8	8	0	0

Table 6.3 The result from the GULP energy minimisation for $\beta - ZrF_4$ crystal initial and final structures displaying the low percentage errors except for the change in $Zr - F$ CN.

Parameter	Unit	Initial Value	Final Value	Difference	Percent
Volume	\AA^3	732.534	717.016	-15.517	-2.12
a	\AA	9.570	9.444	-0.125	-1.31
b	\AA	9.930	9.910	-0.019	-0.20
c	\AA	7.730	7.679	-0.059	-0.66
α	Degree	90.000	90.000	0.000	0.00
β	Degree	94.280	94.010	-0.269	-0.29
γ	Degree	90.000	90.000	0.000	0.00
$Zr - F$ distance	\AA	2.232	2.098	-0.134	-6.00
$Zr - F$ CN		6.700	7.700	1.00	14.8

Table 6.4 The result from the GULP energy minimisation for $\beta - BaZr_2F_{10}$ crystal initial and final structures displaying the low percentage errors.

Parameter	Unit	Initial Value	Final Value	Difference	Percent
Volume	\AA^3	777.812	760.148	-17.663	-2.27
a	\AA	6.064	6.096	0.032	0.54
b	\AA	15.383	15.582	0.199	1.30
c	\AA	9.057	8.759	-0.297	-3.29
α	Degree	90.000	90.000	0.000	0.00
β	Degree	112.980	114.010	1.030	0.91
γ	Degree	90.000	90.000	0.000	0.00
$Zr - F$ distance	\AA	2.050	2.026	-0.024	-1.16
$Zr - F$ CN		7	7	0	0
$Ba - F$ distance	\AA	2.783	2.858	0.075	2.69
$Ba - F$ CN		10	10	0	0

Table 6.5 The result from the GULP energy minimisation for $\alpha - BaZrF_6$ crystal initial and final structures displaying the low percentage errors.

Parameter	Unit	Initial Value	Final Value	Difference	Percent
Volume	\AA^3	454.256	437.466	-16.790	-3.70
a	\AA	6.493	6.556	0.638	0.98
b	\AA	9.530	8.873	-0.656	-6.89
c	\AA	9.203	9.404	0.201	2.19
α	Degree	90.000	90.000	0.000	0.00
β	Degree	127.090	126.915	-0.174	-0.14
γ	Degree	90.000	90.000	0.000	0.000
$Zr - F$ distance	\AA	2.152	2.145	0.007	0.32
$Zr - F$ CN		8	8	0	0
$Ba - F$ distance	\AA	2.841	2.878	0.037	1.30
$Ba - F$ CN		11	12	1	9.1

Table 6.6 The result from the GULP energy minimisation for $\alpha - Ba_2ZrF_8$ crystal initial and final structures displaying the low percentage errors except for the change in $Ba - F$ CN.

Parameter	Unit	Initial Value	Final Value	Difference	Percent
Volume	\AA^3	650.078	625.065	-25.013	-3.85
a	\AA	9.740	9.061	-0.678	-6.97
b	\AA	5.614	5.628	0.013	0.25
c	\AA	11.887	12.255	0.368	3.10
α	Degree	90.000	90.000	0.000	0.00
β	Degree	90.000	90.000	0.000	0.00
γ	Degree	90.000	90.000	0.000	0.00
$Zr - F$ distance	\AA	2.098	2.098	0.000	0.00
$Zr - F$ CN		8	8	0	0
$Ba - F$ distance	\AA	2.811	2.852	0.041	1.46
$Ba - F$ CN		11	12.5	1.5	13.6

Table 6.7 The result from the GULP energy minimisation for BaF_2 crystal initial and final structures displaying the low percentage errors.

Parameter	Unit	Initial Value	Final Value	Difference	Percent
Volume	\AA^3	237.913	260.752	22.839	9.60
a	\AA	6.196	6.388	0.192	3.10
b	\AA	6.196	6.388	0.192	3.10
c	\AA	6.196	6.388	0.192	3.10
α	Degree	90.000	90.000	0.000	0.00
β	Degree	90.000	90.000	0.000	0.00
γ	Degree	90.000	90.000	0.000	0.00
$Ba - F$ distance	\AA	2.746	2.765	0.019	0.68
$Ba - F$ CN		8	8	0	0

6.2.4 Initial configurations for barium fluorozirconate glasses

Models were made of $xZrF_4 - (x - 100)BaF_2$ glasses with compositions $x = 50$, 60, 67 and 75. The initial random distributions (see Chapter 2), had numbers of atoms, cubic box length and density with details shown in Table 6.8. The densities of glasses reported in literature were 4.57 gcm^{-3} [20] for $75ZrF_4 - 25BaF_2$, 4.64 gcm^{-3} [22] for $64ZrF_4 - 36BaF_2$, 4.64 gcm^{-3} [25] for $67ZrF_4 - 33BaF_2$ and 4.37 gcm^{-3} [45] for $65ZrF_4 - 35BaF_2$ glasses. The densities used in the model were based largely on those reported in the literature and the comparing with the densities of related crystals.

Table 6.8 Initial configurations of the binary glasses $xZrF_4 - (x - 100)BaF_2$ with the compositions $x = 50$ to 75.

Chemical compositions of glasses (x)	Number of Zr atoms	Number of Ba atoms	Density (gcm^{-3})	Length (\AA)
50(ZB)	200	200	est. 4.76	28.79
60(Z3B2)	240	160	4.64	28.99
67(Z2B)	268	132	4.64	28.95
75(Z3B)	300	100	4.64	28.93

6.2.5 Parameters for MD modelling of barium fluorozirconate glasses

MD simulation of these binary glasses were performed in DL_POLY_2 as described in Chapter 2 (see section 2.4). Normally the equilibrations are performed in the certain temperature sequence e.g. shown in Table 2.3 (Chapter 2). However, Table 6.9 displays the new scheme that was applied here with many temperature stages to heat the system at high temperature and equilibrate the random configuration and quenched at 2,000 K. In this many stage method, the temperature was dropped by 100 K from 5,000 K until 2,000 K equili-

brating for 5,000 time-steps. The time-steps were 2 fs . At the final stage of bath with temperature 300 K , the first 80,000 time-steps was equilibrated and sample only was collected after 80,000 time-steps at every 400 time-steps. Typical control parameters for MD modelling of glasses are described in Chapter 2 (see Section 2.4.1). For the barium fluorozirconate glasses the cutoffs for short-range and long-range potentials were 7.0 \AA and 12.0 \AA with quench rate of $10^{13} Ks^{-1}$.

Table 6.9 MD stages for melt-quenched barium fluorozirconate glasses.

Stages	Temperature (K)	Time-steps	Process (NVT Berendsen thermostat)
1	5000	40000	Equilibrate
(30 stages)	4900 – 2000	5000	Equilibrate
3	2000	85000	Quench
4	300	160000	Equilibrate and collect

6.3 Results

Figure 6.10 shows the images of $xZrF_4 - (x - 100)BaF_2$ binary glass models for $x = 50, 60, 67$ and 75 . Networks of grey polyhedra are ZrF_n polyhedra forming the structural units of the glass or acting as network formers. The fluorine atoms as yellow spheres are present at every vertex of polyhedra structures and act as the bridging between these networks of polyhedra. The dark blue spheres are the barium atoms, whose increase in concentration seems to destroy these network polyhedra structures and give rise to the disorder in the models.

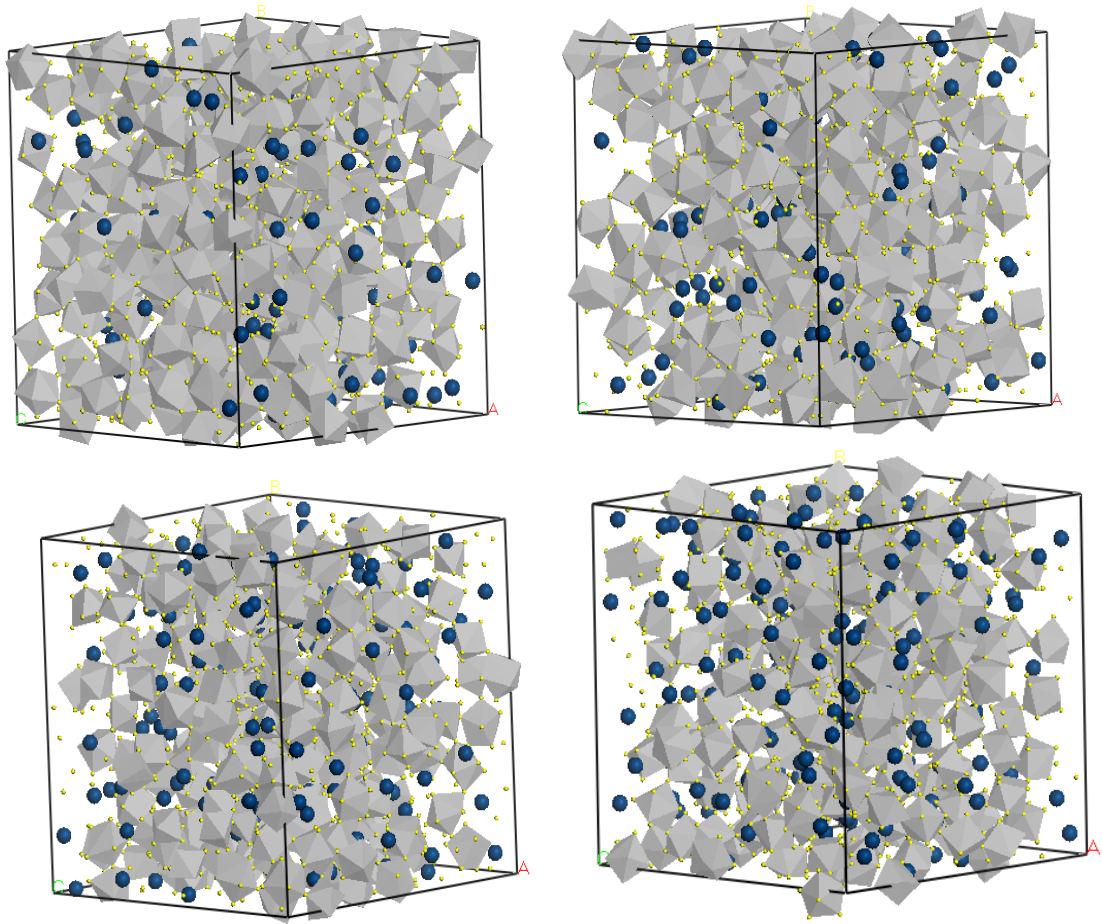


Figure 6.8 Image of (top-left) $x = 75$, (top-right) $x = 67$, (bottom-left) $x = 60$ and (bottom-right) $x = 50$ glass models.

6.3.1 Pair distribution function, nearest neighbour distances and coordination numbers

The pair distribution functions, $T_{ij}(r)$, for the binary glass model of $xZrF_4 - (x - 100)BaF_2$ for $x = 50, 60, 67$ and 75 are shown in Figure 6.9. The first prominent peaks in Figure 6.9 (top) and Figure 6.9 (bottom) i.e. $T_{ZrF}(r)$ and $T_{BaF}(r)$ represent $Zr - F$ and $Ba - F$ nearest neighbours respectively with the average bond length, R_{ij} . The area under these peaks determines coordination numbers, N_{ij} , around Zr and Ba atoms respectively. $T_{FF}(r)$ has the first peak around 2.55 \AA which represents $F - Zr - F$ average distance in ZrF_n polyhedra in the glass models. The second peak roughly at 3.95 \AA may indicate $F -$

$Ba - F$ average distance in BaF_n polyhedra. The correlation $T_{ZrZr}(r)$ shown in the secondary axis of Figure 6.9 (top), which peaks at 4.09 Å indicates the network connectivity, N_{ZrZr} , of ZrF_n polyhedra.

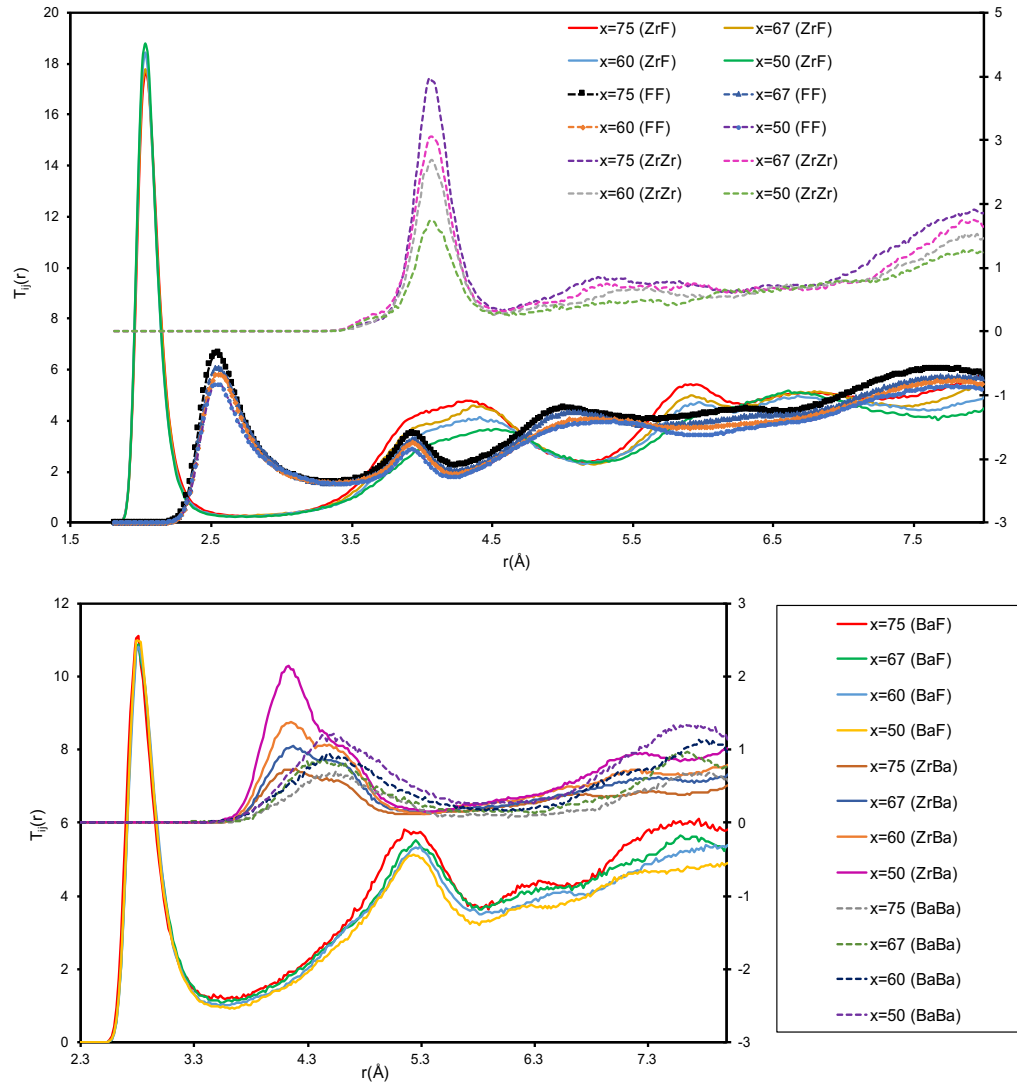


Figure 6.9 The pair distribution functions, $T_{ij}(r)$, for $x = 50, 60, 67$ and 75 glass models. T_{ZrF} , T_{FF} and T_{ZrZr} , (top). T_{ZrF} , T_{ZrBa} and T_{BaBa} (bottom).

Likewise, the correlation results shown in the secondary axis of Figure 6.9 (bottom) are $T_{BaBa}(r)$ and $T_{ZrBa}(r)$ which has first peak roughly at 4.6 Å and at 4.1 Å respectively. The average coordination number of fluorine atoms found under these correlations curves indicates the non-bridging fluorine atoms in the models i.e. $Ba - F - Ba$ or $Zr - F - Ba$. The R_{ij} and N_{ij} for all the glass models are given in Tables 6.10 – 6.11, where i and j are

either Ba , Zr or F atoms. The estimated error in the results are ± 0.02 Å for atomic separations, R_{ij} , and ± 0.1 in the coordination number, N_{ij} .

Table 6.10 Average bond length, R_{ij} , and the coordination number, N_{ij} , of $ZrF_4 - BaF_2$ binary glass models. The cutoff distances were 2.75 Å and ~ 4.5 Å for N_{ZrF} and N_{ZrZr} respectively.

x	$F:Zr$	R_{ZrF}	N_{ZrF}	R_{ZrZr}	$ZrZr$ $\langle n \rangle$ Model	$ZrZr$ $\langle n \rangle$ Theory	N_{ZrZr} PDF
50	6.00	2.03Å	7.5	4.11 Å	3.07	3.00	2.86
60	5.33	2.03Å	7.4	4.09 Å	4.14	4.32	4.02
67	4.99	2.03Å	7.4	4.07 Å	4.87	5.00	4.68
75	4.67	2.03Å	7.5	4.09 Å	5.63	5.66	5.55

Table 6.11 Average bond length, R_{ij} , and coordination number, N_{ij} , of $ZrF_4 - BaF_2$ binary glass models. The cutoff distances were 3.3 Å, ~ 6.0 Å and ~ 5.1 Å, for N_{BaF} , N_{BaBa} and N_{ZrBa} respectively.

x	R_{BaF}	N_{BaF}	R_{BaBa}	$BaBa$ $\langle n \rangle$ Model	N_{BaBa} PDF	R_{ZrBa}	N_{ZrBa} PDF
50	2.83Å	10.5	4.67 Å	8.98	6.59	4.27 Å	6.73
60	2.83Å	10.3	4.67 Å	7.87	5.08	4.37 Å	4.96
67	2.81Å	10.4	4.57 Å	7.31	4.31	4.39 Å	3.94
75	2.81Å	10.5	4.63 Å	5.84	3.35	4.37 Å	2.73

The theory behind the calculation of network connectivity initially assumes the corner sharing of ZrF_n polyhedra, where $\langle n \rangle$ is the number of bridging fluorine atoms. The bridging fluorine atoms are deduced from the chemical composition ratio of $F:Zr$ assuming the average $Zr - F$ CN to be 7.5 in the glass. Assuming the average connectivity, $\langle n \rangle$, can vary from $\langle n \rangle = 5.0$ when $x = 67$ to $\langle n \rangle = 3.0$ when $x = 50$, it can be estimated using $\langle n \rangle = (11x - 400)/x$.

The $T_{ij}(r)$ function shows that there is an overlap between $Ba - Zr$ and $Ba - Ba$ correlations between 3.5 – 5.4 Å. There are also clear indications of change in heights of the peaks as x changes from 50 to 75. Particularly the change in the height of the peaks are clearly visible in $Zr - Zr$, $Zr - Ba$, $Ba - Ba$ and $F - F$ correlations. The $T_{ZrZr}(r)$ correlation clearly shows that the $\langle n \rangle$ decreases as the composition of Zr ions decreases. The cutoff for N_{ij} were estimated from the minimum of the first peak of each respective $T_{ij}(r)$ correlation functions.

6.3.2 Bond angle distribution functions

Further information about the local structural units is provided by the bond angle distribution functions (BAD). Although it's the very common method for analysing the local structure of amorphous systems, to our knowledge this higher order correlation function has not been investigated for the $ZrF_4 - BaF_2$ binary glass system. Figure 6.10 displays $F - Zr - F$ and $F - Ba - F$ bond angle distribution functions of all glass models for cutoff distances of 2.75 Å and 3.3 Å respectively. In $F - Zr - F$ there are two prominent peaks, the primary peak at 75° and secondary peak at 141°. There is a minimum at 105° between these two peaks. Similarly, for the $F - Ba - F$, there are also two typical peaks at 55° and 109° but the secondary peak is broad and has wider shoulders. There is a minimum around 85° between these two peaks.

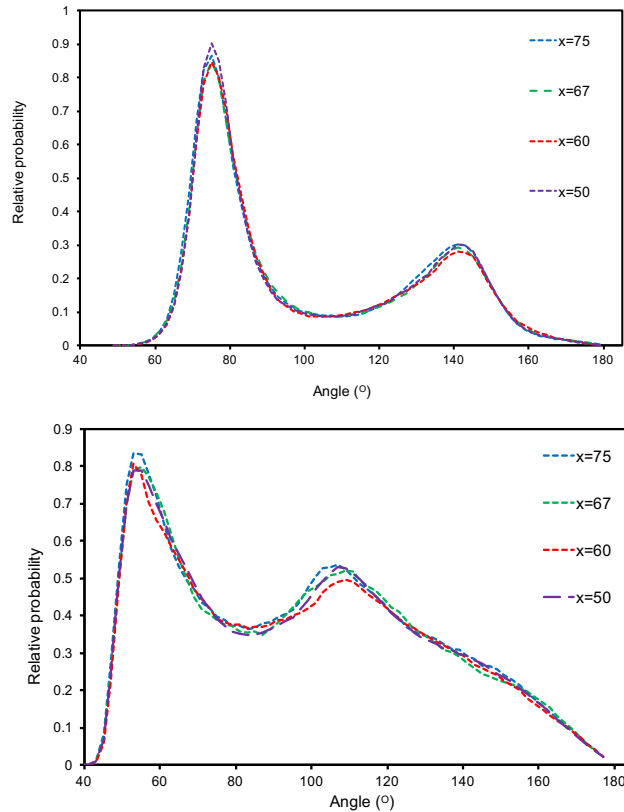


Figure 6.10 The bond angle distribution functions (BAD) of all the glass compositions. $F - Zr - F$ (top) and $F - Ba - F$ (bottom).

Figure 6.11 displays the BAD of glasses and related crystals, with compositions $x = 67$ and 50 . In addition it also shows the BAD for $\alpha - ZrF_4$, $\beta - ZrF_4$ and BaF_2 crystals. For $x = 67$ crystal, $F - Zr - F$ has two main peaks whereas $x = 50$ crystal has one main peak and two secondary peaks. Both crystals have a primary peak around 77° . There is secondary peak at 141° for $x = 67$ crystal but $x = 50$ crystal has two secondary peaks at 133° and 149° . Also, between the primary and secondary peaks there is a minimum at 117° and 109° for $x = 67$ crystal and for $x = 50$ crystal respectively. The BAD for pure $\alpha - ZrF_4$ shows two distinctive peaks, the primary peak at 75° and secondary peak 139° and a minimum in between those two peaks at 115° , whereas $\beta - ZrF_4$ crystal has three distinctive peaks at 75° , 115° and 141° . The peak at 115° is not seen in any other crystals or glasses.

Furthermore, the $\alpha - ZrF_4$ peaks are more widely distributed than $\beta - ZrF_4$. The BAD signature of both $x = 67$ and 50 crystals are similar to the glasses however $x = 50$ crystal has two secondary peaks.

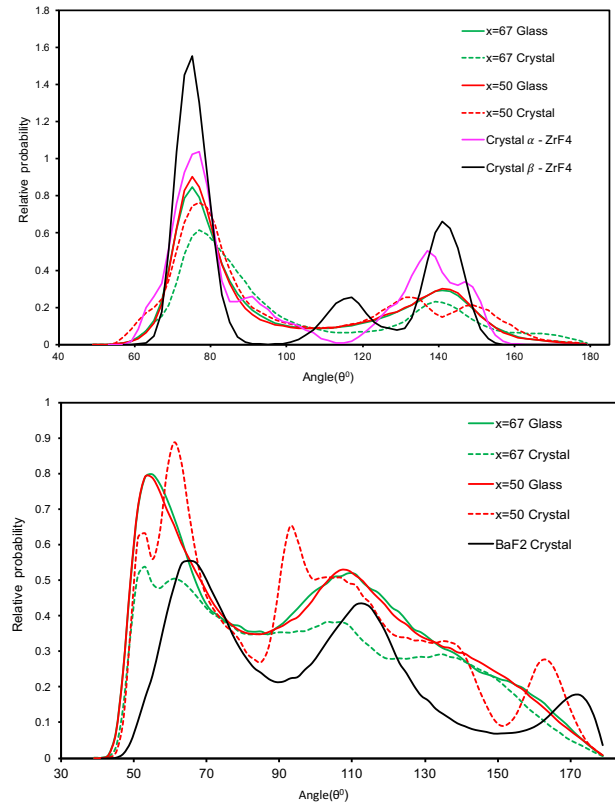


Figure 6.11 The bond angle distribution functions (BAD) of glasses and related crystals. (Top) $F - Zr - F$ of pure $\alpha - ZrF_4$ crystal, $\beta - ZrF_4$ crystals, and $x = 67$ and 50 glasses and its corresponding crystals. (Bottom) $F - Ba - F$ of pure BaF_2 crystal and $x = 67$ and 50 glasses and its corresponding crystals.

The BAD of $F - Ba - F$ (see Figure 6.11 bottom) in crystals show the range of angles with more characteristic peaks than glasses. Crystals $x = 67$ and 50 both have recognizable peaks at 53° , 61° and 137° . For $x = 67$ crystal another recognizable peak is at 105° and for $x = 50$ crystal other distinctive peaks are at 93° and 163° . The pure BaF_2 crystal has three distinctive peaks. The two peaks with similar intensities are at 65° and 113° and there is small third peak at 171° . The peaks of $x = 50$ crystal have higher intensities than other crystals. The BAD result for $x = 67$ crystal has similar signature to the glasses.

6.3.3 Network connectivity

From Table 6.10 the N_{ZrZr} denotes nearest neighbours and $\langle n \rangle$ denotes $Zr - F - Zr$ links per Zr (a formula was given in section 6.3.1). Figure 6.12 shows the proportion of Zr having different values of $Zr - F - Zr$ connectivity per Zr and the proportion of Ba having different values of $Ba - F - Ba$ connectivity per Ba (i.e. Q_{Zr}^n and Q_{Ba}^n respectively) in all the glass models. As the concentration of Zr increases the $\langle n \rangle$ also increases and the $\langle n \rangle$ mostly lies between 3 – 6. The $Ba - F - Ba$ connectivity is decreasing approximately linearly when percentage of Ba is reduced thus indicating no phase separation in the glass models.

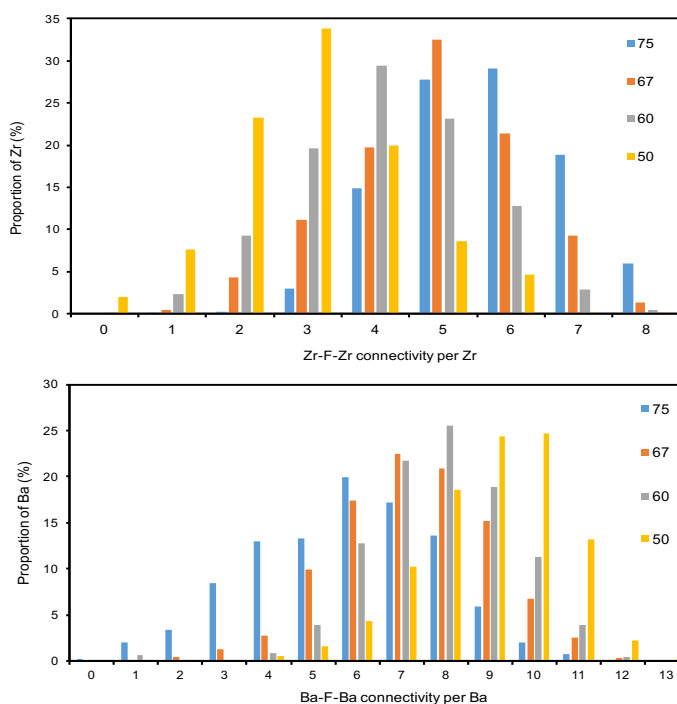


Figure 6.12 $Zr - F - Zr$ linkage per Zr (top) and $Ba - F - Ba$ linkage per Ba (bottom) for $xZrF_4 - (x - 100)BaF_2$ glass models.

Figure 6.13 shows average $Zr - F - Zr$ linkage per Zr and average $Ba - F - Ba$ linkage per Ba calculated from the two methods described in Chapter 2 (see section 2.6.4) with $Zr - Zr$ cutoff of 4.5 Å and $Ba - Ba$ cutoff of 6.0 Å. The $Zr - F - Zr$ linkage results compare very well between two methods because $Zr - F - Zr$ linkages are mostly corner

sharing but $Ba - F - Ba$ does not because $Ba - F - Ba$ is mostly edge sharing. The corner sharing and edge sharing between the $Zr - Zr$ network can also be deduced from these two methods using Equation 2.44 and the result is given Table 6.12.

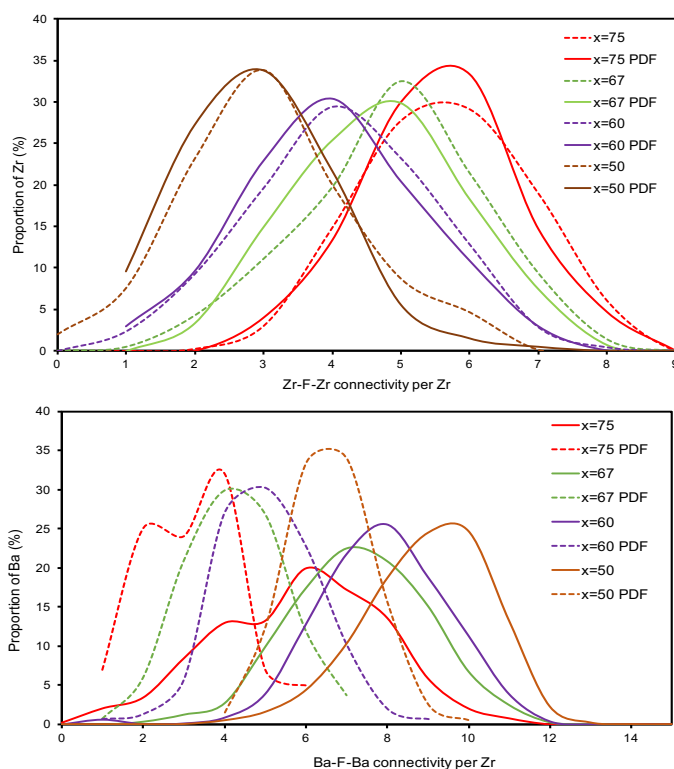


Figure 6.13 Comparisons of $Zr - F - Zr$ linkage per Zr (top) and $Ba - F - Ba$ linkage per Ba (bottom) for $xZrF_4 - (x - 100)BaF_2$ glass models computed from the pair distribution function and by “xhst-hsc” method (see Chapter 2 section 2.6.4).

Table 6.12 Percentage of $Zr - Zr$ corner sharing and edge sharing for $ZrF_4 - BaF_2$ glass models

x	% corner sharing	% edge sharing
50	86.25	13.75
60	94.01	5.99
67	92.32	7.68
75	96.98	3.02

The comparison between $Zr - F - Zr$ connectivity per Zr and $Ba - F - Ba$ connectivity per Ba for $x = 50$ and 67 glasses and related crystals is shown in Figure 6.14. The linkage of Zr and Ba compare well between $x = 50$ crystal and glass. The comparison of $x = 67$ crystal and glass indicates that the glass has higher average connectivity per Zr and

per Ba than the crystal. Probably, in the crystal there are more $Zr - F - Ba$ connections than in the glass.

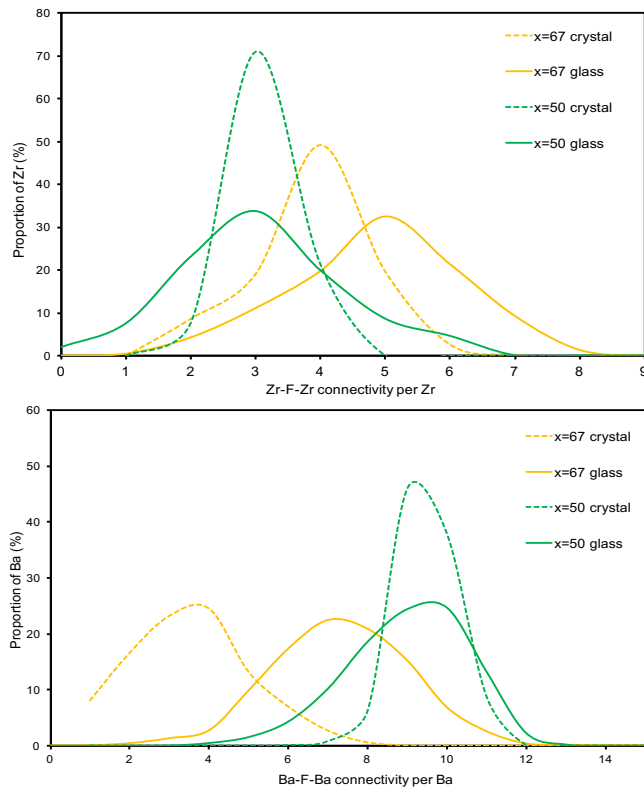


Figure 6.14 $Zr - F - Zr$ linkage per Zr (top) and $Ba - F - Ba$ linkage per Ba (bottom) for $x = 50$ and 67 glasses and its corresponding crystals.

6.3.4 Neutron and X-ray diffraction structure factors

Comparison between the glass models and experiments for the neutron and X-ray diffraction structure factors, $S(Q)$, are shown in Figure 6.15 and Figure 6.16 respectively. For the neutron diffraction $S(Q)$ of the glasses $x = 75$, 67 and 60 experimental results [26] agree very well with the glass models. On other hand, experimental results [21, 25, 26] for X-ray diffraction $S(Q)$ compare well with the $x = 67$ and 50 glass models. The experimental results for $x = 65$ [45] and 64 [22] are also compared with the $x = 67$ glass model, which gave good agreement.

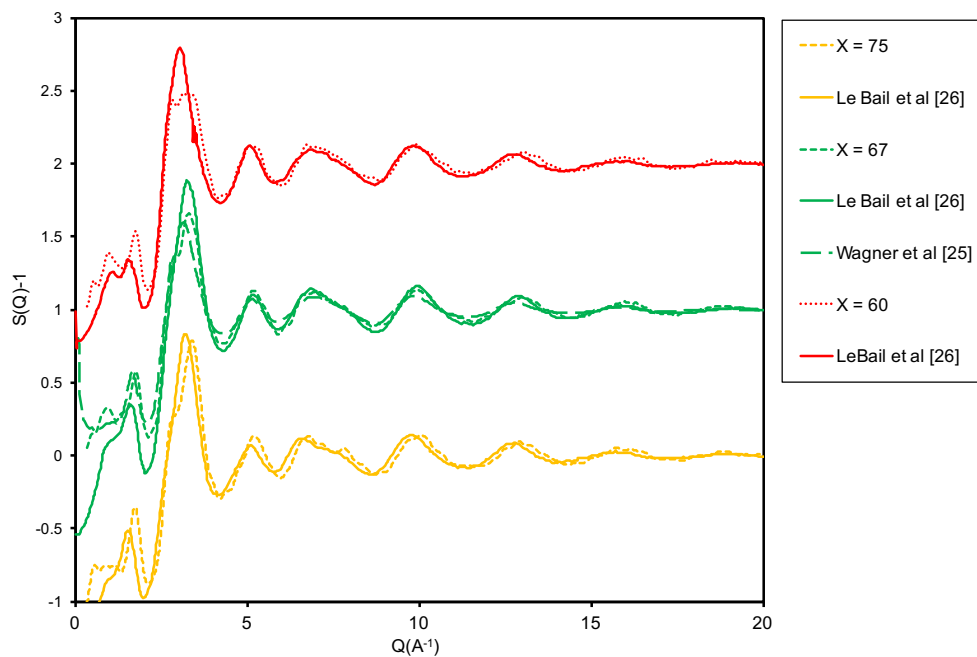


Figure 6.15 Neutron diffraction structure factors for $x = 67$, 60 and $x = 75$ glass models and experiments [25, 26].

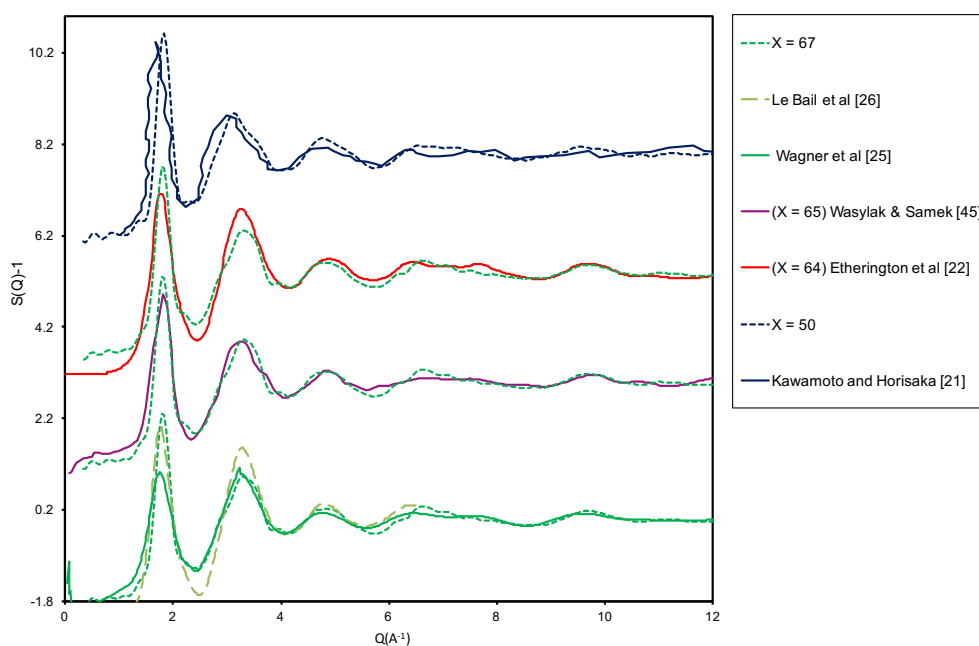


Figure 6.16 X-ray diffraction structure factors for $x = 67$ and $x = 50$ glass models and experiments [21, 22, 25, 26, 45].

6.3.5 Rotational invariants for Zr and Ba in $ZrF_4 - BaF_2$ binary glasses

The rotational invariants, Q_l , for the glass models are calculated by using Equation 3.9. Figure 6.17 shows the average values of Q_l for $l = 1$ to 10, for ZrF_n polyhedra with $CN = 7$ (top) and $CN = 8$ (bottom) respectively for the glass models $xZrF_4 - (x - 100)BaF_2$ with $x = 50, 60, 67$ and 75.

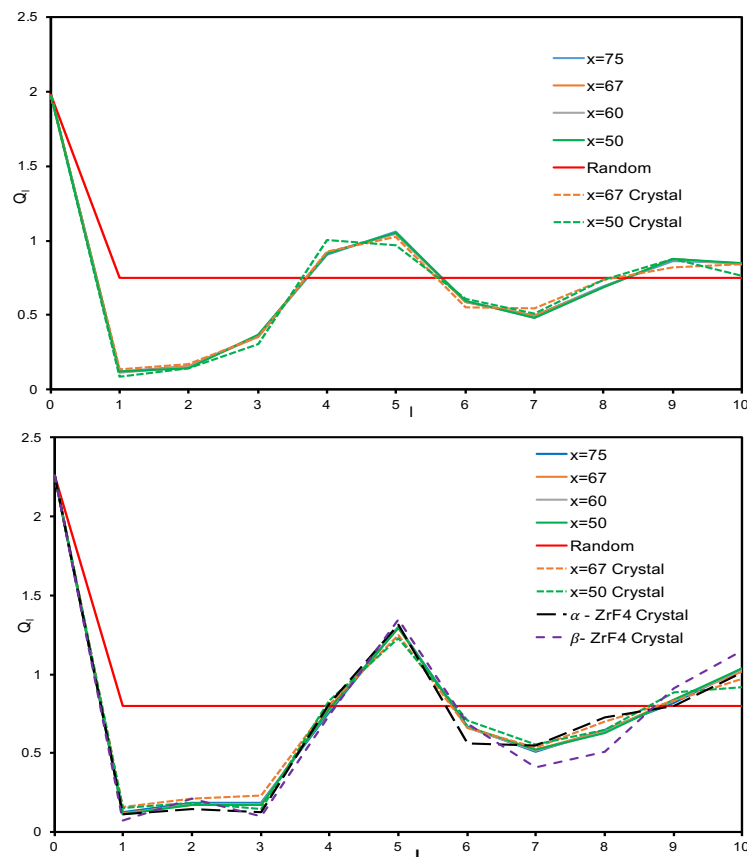


Figure 6.17 Rotational invariant, Q_l , of ZrF_n polyhedra $CN = 7$ (top) and $CN = 8$ (bottom) for glass models and compared with its corresponding crystals $x = 50$ and $x = 67$. The Q_l of α - ZrF_4 and β - ZrF_4 crystals both with $CN = 8$ is also compared (bottom).

The average value Q_l of ZrF_n polyhedra from the different glass models gave identical results for $CN = 7$ and for $CN = 8$. These average values Q_l for $x = 50$ and 67 glasses and its related crystals are compared also with the random distribution for $CN = 7$ and $CN = 8$. The glass models gave the mixture of $CN = 7$ and $CN = 8$ which is given by Table 6.13.

The average values Q_l for $x = 50$ and $x = 67$ crystals also gave the mixtures of CN but for α - ZrF_4 and β - ZrF_4 crystals deduced by the MD method gave the 100 % of $CN = 8$ and their average values Q_l are compared in Figure 6.17 (*bottom*). The uncertainty in the average values of Q_l for glasses were ± 0.05 (one standard deviation).

Table 6.13 Percentages mixtures of $CN = 7$ and $CN = 8$ in ZrF_n polyhedra from the glass models $xZrF_4 - (x - 100)BaF_2$ and in parentheses (red) for the corresponding crystals. ZrF_n polyhedra for $x = 67$ crystal was mainly dominated by mixture of $CN = 6$ (24.6%) and $CN = 7$ (58.3%).

x	% $CN = 7$	% $CN = 8$
50	49.0 (43.1)	48.5 (55.6)
60	56.3	40.8
67	48.9 (58.3)	44.8 (15.0)
75	46.0	50.7

For the ZrF_n polyhedra with $CN = 7$, the average value Q_l for crystal $x = 67$ is more similar to glasses than $x = 50$ crystal where its average values Q_l approaches towards random value Q_l at $l = 10$. For ZrF_n polyhedra with $CN = 8$, crystal $x = 50$ has an identical average value Q_l with the glass models. Also, α - ZrF_4 crystal average values Q_l has very similar result with the glasses compared to β - ZrF_4 crystal.

Figure 6.18 shows average values of Q_l for $l = 1$ to 10, for ZrF_n polyhedra with the $CN = 7$ (*top*) and $CN = 8$ (*bottom*) for $x = 67$ and $x = 50$ glass models compared with all the possible reference convex polyhedral of vertices, $N = 7$ and $N = 8$. Augmented Triangular Prism has very similar average values of Q_l compared to the glasses rather than other reference convex polyhedra for vertices, $N = 7$. For $CN = 8$, average values of Q_l for ZrF_n polyhedra of glasses have similar results with Biaugmented Triangular Prism, Square Antiprism and Snub Disphenoid polyhedra. However, average value of Q_l between glasses of ZrF_n polyhedra with $CN = 8$ and Biagumented Triangular Prism of vertices, $N = 8$, compares better than other references convex polyhedra of vertices, $N = 8$.

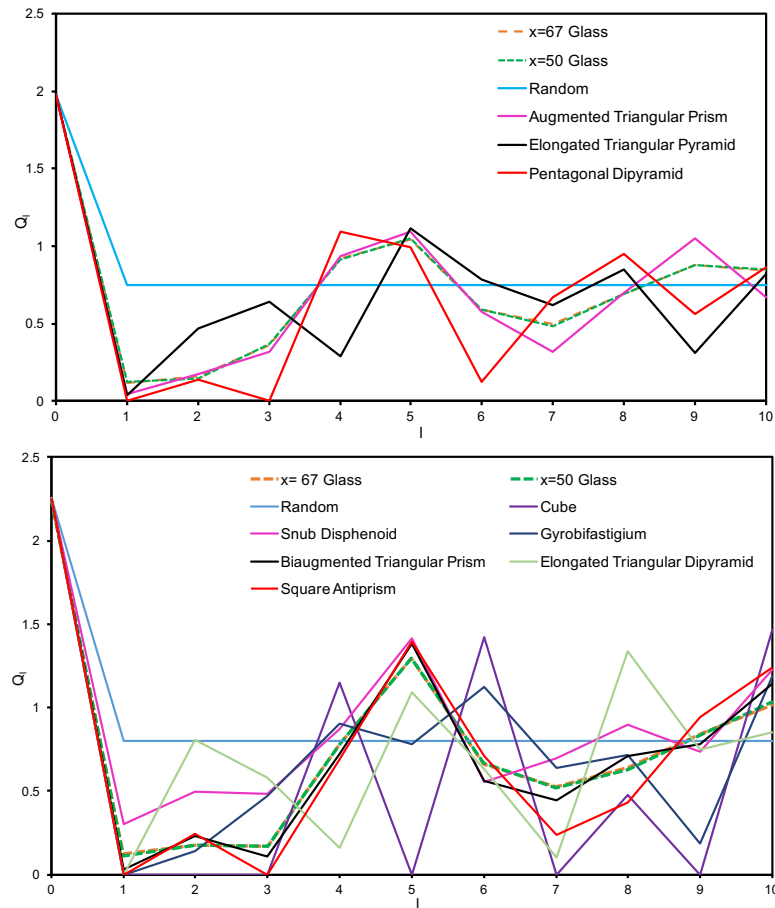


Figure 6.18 Rotational invariant, Q_l , of ZrF_n polyhedra from the glass models are compared with all the reference convex polyhedra of vertices, $N = 7$ (top) and $N = 8$ (bottom).

Figure 6.19 displays average value of Q_l for $l = 1$ to 10, for BaF_n polyhedra for $CN = 10$ (top) and $CN = 11$ (bottom) of the glass models $xZrF_4 - (x - 100)BaF_2$ for $x = 50, 60, 67$ and 75. The average value Q_l of BaF_n polyhedra from the different glass models gave identical results for $CN = 10$ and for $CN = 11$. There is a clear indication in glasses that CN of BaF_n polyhedra are mainly dominated by a mixture of $CN = 10$ and $CN = 11$, which is illustrated in Table 6.14. The average values Q_l for $x = 50$ and 67 glasses and its corresponding crystals are also compared with the random distribution for $CN = 10$ and $CN = 11$. The values of Q_l of $x = 67$ crystals are similar to the glasses and are closer to random values of Q_l .

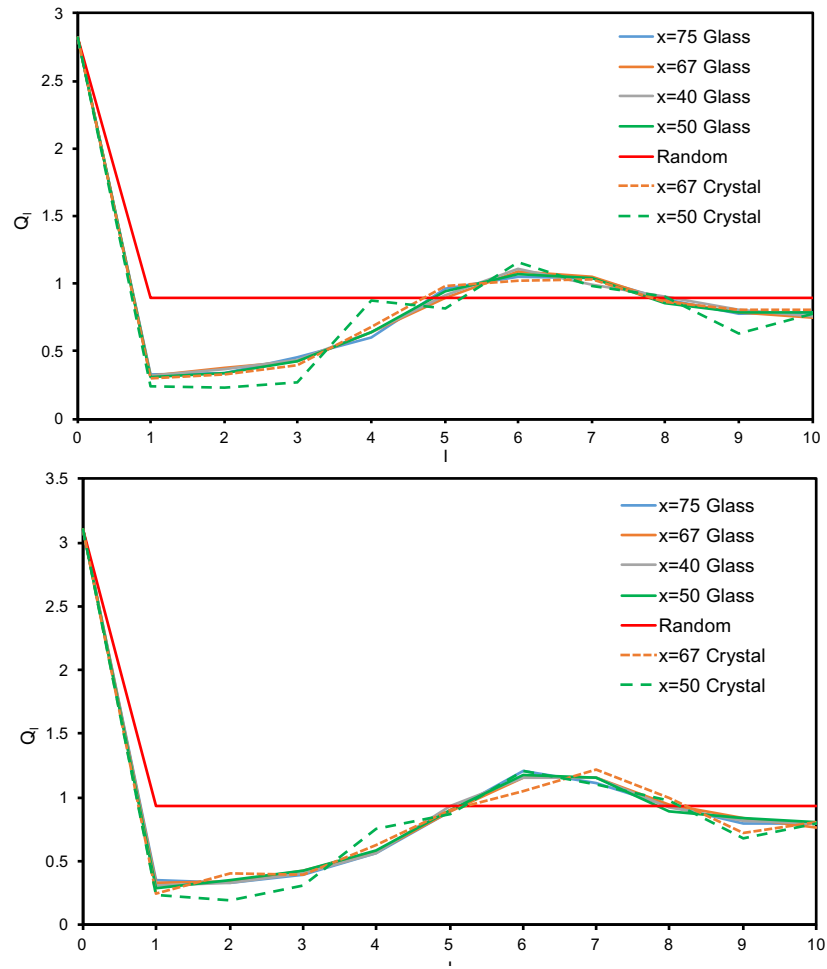


Figure 6.19 Rotational invariant Q_l of BaF_n polyhedra with $CN = 10$ (*top*) and $CN = 11$ (*bottom*) for the glass models are compared with corresponding crystals for $x = 50$ and $x = 67$ crystals.

Table 6.14 Percentages mixtures of $CN = 10$ and $CN = 11$ in BaF_n polyhedra from the glass models $xZrF_4 - (x - 100)BaF_2$ and in parentheses (red) for the corresponding crystals. For $x = 67$ crystal it is mainly a mixture of $CN = 9$ (26.7%) and $CN = 10$ (33.3%).

x	% $CN = 10$	% $CN = 11$
50	35.0 (55.6)	37.0 (44.4)
60	33.8	33.8
67	32.6 (33.3)	28.8 (6.7)
75	35.0	27.0

Figure 6.20 displays average values of Q_l for $l = 1$ to 10, for BaF_n polyhedra with the $CN = 10$ (*top*) and $CN = 11$ (*bottom*) of the glass models $x = 67$ and $x = 50$ compared with all the possible reference convex polyhedra with the vertices, $N = 10$ and $N = 11$. The

average values of Q_l for BaF_n polyhedra $CN = 10$ and $CN = 11$ from the glasses tend to be closer to the values of Q_l for Metabidiminished Icoashedron or Pentagonal Prism ($N = 10$) and Augmented Pentagonal Prism ($N = 11$). The average values of Q_l from the glasses gave a smooth curve compared to the values of Q_l from $x = 50$ crystal and from the references convex polyhedra.

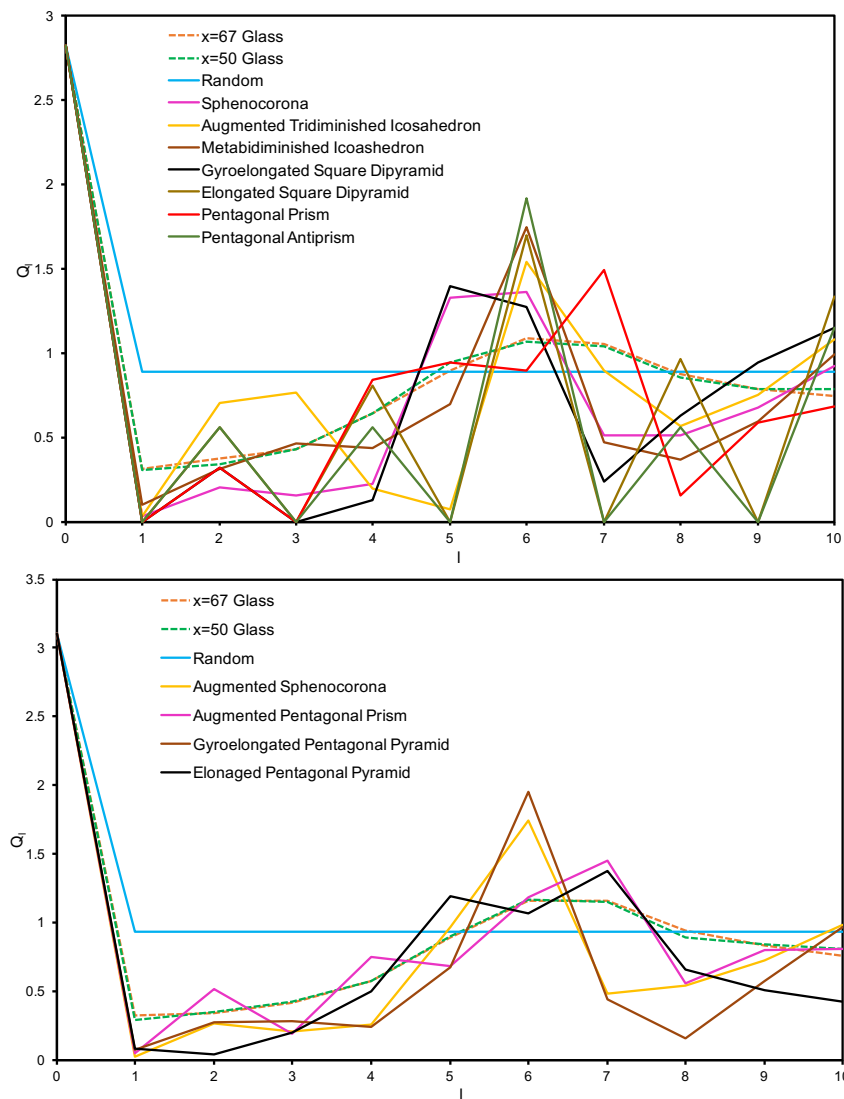


Figure 6.20 Rotational invariant Q_l of BaF_n polyhedra from glass models are compared with all the reference convex polyhedra of vertices, $N = 10$ (top) and $N = 11$ (bottom).

6.4 Discussion

The rigid ion potentials used to model the glasses gave good results when they were initially tested with the $xZrF_4 - (100 - x)BaF_2$ crystal structures. There were very low percentages of discrepancies in the volumes of crystals structures apart from BaF_2 crystal value around 10%. Short-range order in the crystals were fairly reproducible however, $\beta - ZrF_4$ crystal gave N_{ZrF} discrepancies, and N_{BaF} discrepancies were also found in $x = 50$ and $x = 33.3$ crystals.

The result from glass pair distribution functions indicates nearest neighbour distances are not changing with compositions x . The coordination number for Zr and Ba remains stable with changing composition x . The main changes are increase of $Zr - Zr$ coordination number, and decrease of $Zr - Ba$ and $Ba - Ba$ coordination numbers with increase of composition x . This effect is seen in pair distribution functions illustrated in Figure 6.21 for $x = 67$ and $x = 50$ crystals which show higher coordination numbers for $Ba - F$, $Zr - Ba$ and $Ba - Ba$ for $x = 50$ crystal.

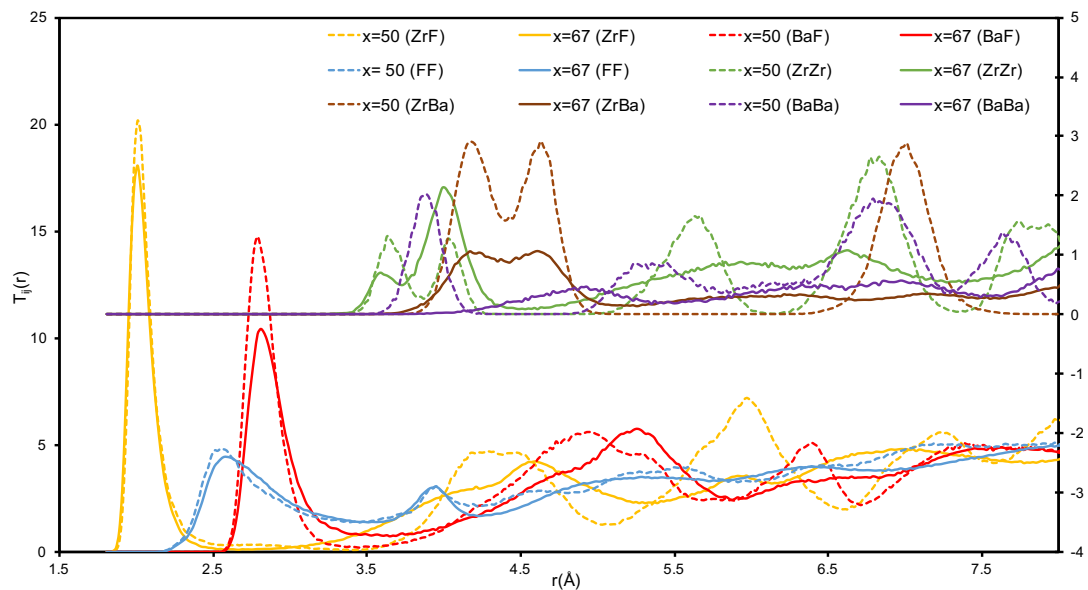


Figure 6.21 $T_{ij}(r)$ comparison between $x = 50$ and $x = 67$ crystal.

MD models of glasses and its related crystals are compared in term of pair distribution functions which are shown in Figure 6.22 for $x = 67$ glass and Figure 6.23 for $x = 50$ glass. Generally, in both glass models for $x = 50$ and $x = 67$, glasses show similar $T_{ij}(r)$ correlations with their associated crystals. Only slightly higher CN for $Ba - Ba$ and $Zr - Zr$ were seen at the same cutoff for glasses but $x = 50$ crystal gave higher CN for $Zr - Ba$ at the same cutoff.

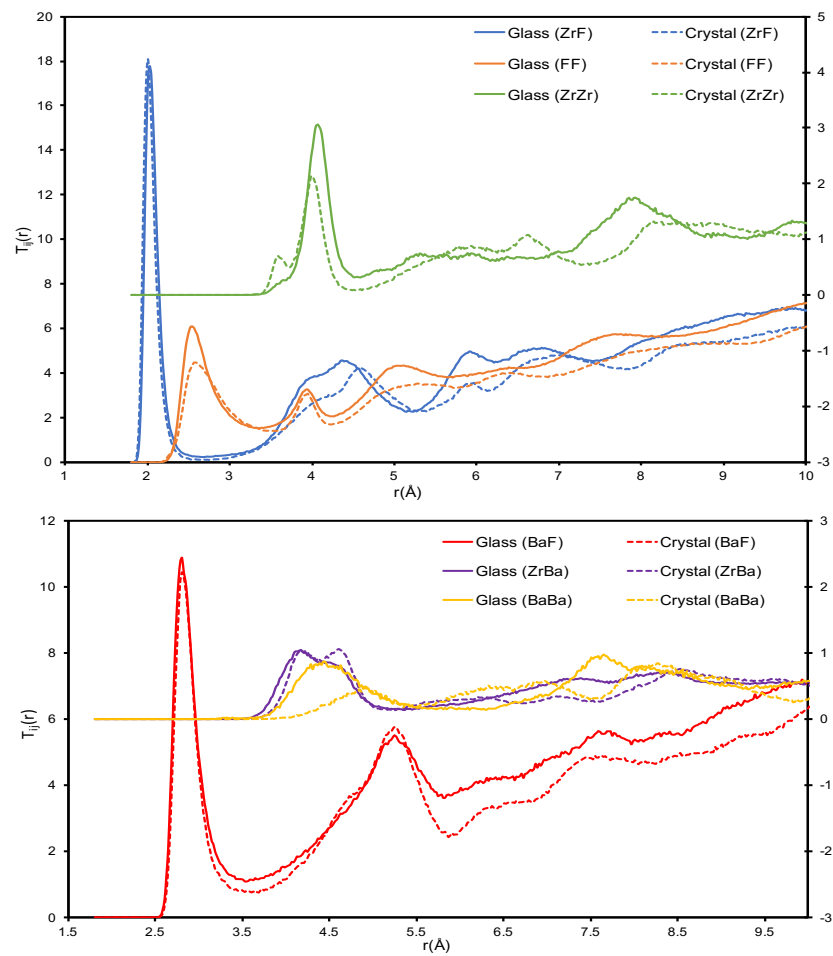


Figure 6.22 $T_{ij}(r)$ comparison between $x = 67$ glass and its related $BaZr_2F_{10}$ crystal.

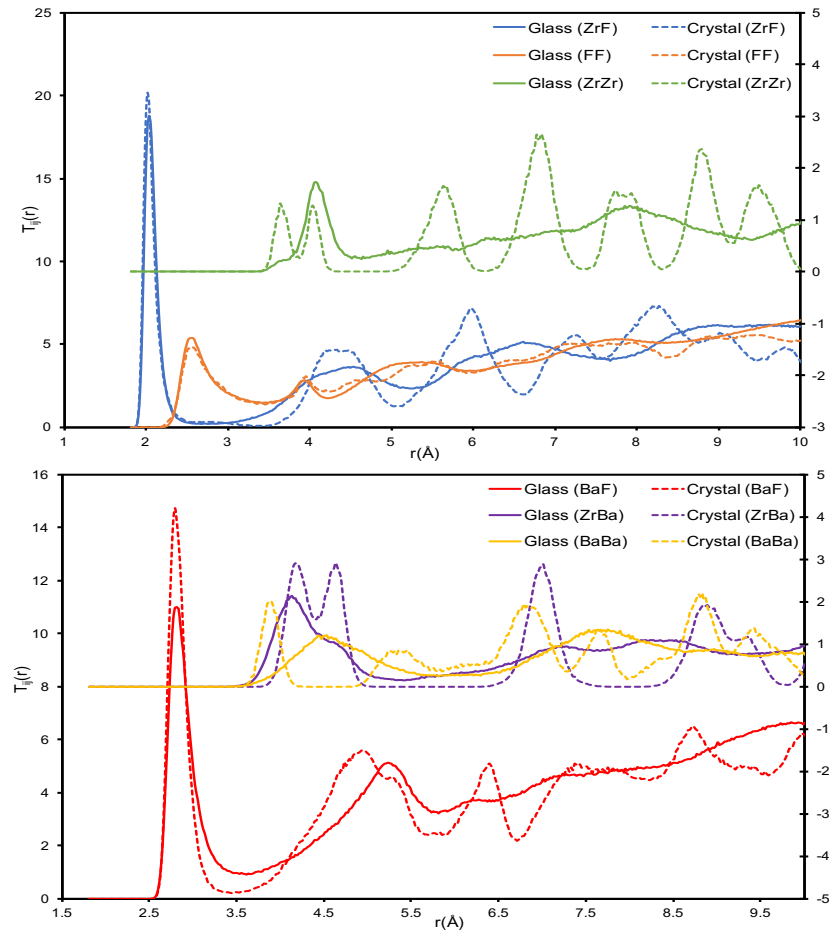


Figure 6.23 $T_{ij}(r)$ comparison between $x = 50$ glass and its related $BaZrF_6$ crystal.

At short-range $Zr - Zr$ distances the crystals have two prominent peaks compared to glasses having just one prominent peak. This first and second peaks indicate the edge sharing and corner sharing in the crystals $Zr - F - Zr$ networks respectively. It can be said there are significantly more edge sharing in the crystals than glasses, and glasses are predominately corner sharing. Both $x = 50$ and $x = 67$ glasses have more area under $Ba - Ba$ peak compared to crystals which suggest Ba is less mixed in the zirconium fluoride network. Furthermore, the $x = 67$ glass shows slightly more $Zr - F - Zr$ connectivity and more of $Ba - F - Ba$ connectivity than its related crystal, whereas $x = 50$ glass and corresponding crystal are approximately similar.

The results of the model glasses can be compared with the work of [18], who used Raman spectroscopy to study the CN . They reported the N_{ZrF} between 7 and 8 for $x = 67$

glass and for $x = 74$ glass N_{ZrF} between 7 and 6. However, here $x = 75$ glass N_{ZrF} was mostly between 7 and 8. The N_{ZrF} results from the work of [20, 21, 22, 23, 25 and 26], who used X-ray and neutron diffraction also reported CN mostly between 7 and 8. However, work by [20] found N_{BaF} between 8 and 10 but the work here shows it is mostly between 10 and 11. The $N_{ZrF} = 7.4$ result from the work of [25] by X-ray diffraction is similar to the result for $x = 67$ glass model. The results of short-range order distances $R_{ZrF} = 2.03 \text{ \AA}$ and $R_{BaF} = 2.71 \text{ \AA}$ for $x = 67$ glass from [27] by EXAFS compare well to results from the model.

The work from [30] done by ^{19}F NMR spectroscopy found that there was significant corner sharing ZrF_n polyhedra which coincided very well with the results found here. The results of ZrF_n polyhedra network connectivity by [31 and 33], who used by both MD and X-ray diffraction, proposed strongly edge sharing but the MD modelling study done here for $x = 50$ to 75 glasses suggested well above 85 to 95% of corner sharing. The trends in $Zr - F - Zr$ connectivity in the glasses also increase with the increase of x which can be predicted using a formula (see results section 6.3.1).

The BAD from the glasses and crystals can also be compared with the number of occurrences of polyhedra angles subtended from each vertex to vertex, which is given in Figure 6.24 for $CN = 7$ and Figure 6.25 for $CN = 8$. This technique was applied to BAD in metallic glasses [46]. For glasses and crystals, the average BAD includes both $CN = 7$ and $CN = 8$. Augmented Triangular Prism and Biaugmented Triangular Prism polyhedra have a similar bond angle distribution functions for $CN = 7$ and for $CN = 8$ respectively, which was also shown by the rotational invariant, Q_l , values.

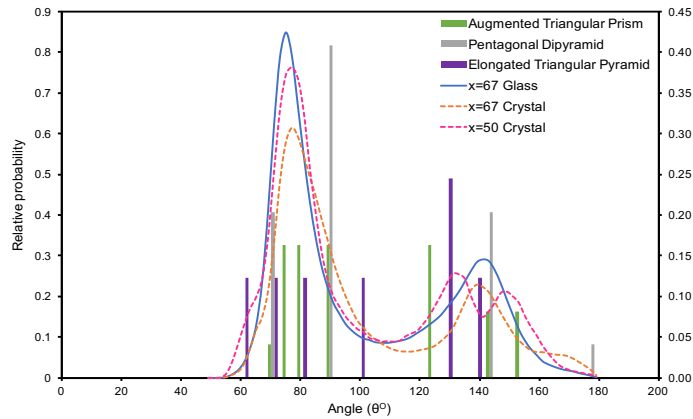


Figure 6.24 The average $F - Zr - F$ BAD for glass and crystals for $CN = 7$ compared with the $F - Zr - F$ BAD of all possible convex polyhedra with vertices, $N = 7$.

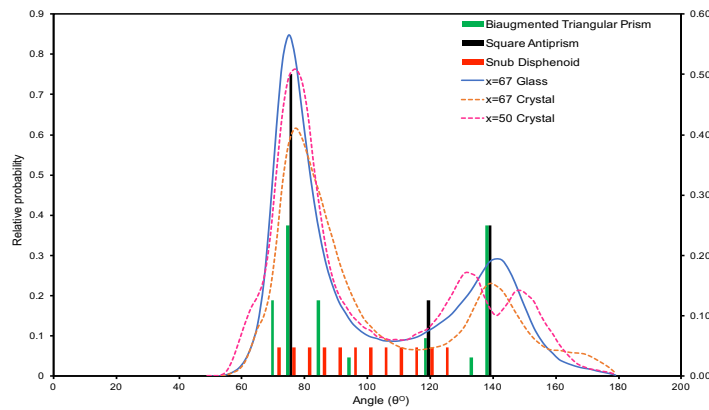


Figure 6.25 The average $F - Zr - F$ BAD for glass and crystals for $CN = 8$ compared with the $F - Zr - F$ BAD of three possible convex polyhedra (rest excluded due to very indifferent results) with vertices, $N = 8$.

Studies suggested the $F - Zr - F$ angle distribution varying from 136° [17] and 143° to 160° [20] but the results found here showed the average angle distribution function has the range from 53° to 179° with two prominent peaks, a primary peak at 75° and a secondary peak at 141° . However, the Q_l analysis here has provided the direct means to match between glasses and reference convex polyhedra structures as an alternative to the BAD comparison analysis (see Figure 6.24 and 6.25). Q_l analysis shows that in glasses the ZrF_n polyhedra with mixture of $CN = 7$ and 8 have very similar Zr cation sites to Augmented Triangular Prism and Biaugmented Triangular Prism respectively. For BaF_n polyhedra with the mixture of $CN = 10$ and 11 , both gave very similar Q_l results and their cation

sites can be roughly linked with the reference polyhedra like Metabidiminished Icoashedron or Pentagonal Prism and Augmented Pentagonal Prism respectively.

The result of Q_l values as shown in Figure 6.26 for static $\beta - BaZr_2F_{10}$ ($x = 67$) crystal unit cell have indicated that its structural unit is very close to Pentagonal Dipyramid as proposed by [40]. They also made a suggestion that the ZrF_7 Pentagonal Dipyramid structure units linked by Ba atoms are compactly preserved in glass, which may explain why these binary $ZrF_4 - BaF_2$ glasses have higher densities than crystals unlike common oxide glasses. But for the simulated $\beta - BaZr_2F_{10}$ crystal the result of Q_l values were similar to Augmented Triangular Prism. Fascinatingly, the result of Q_l values (i.e. 7 out of 10 Q_l values) for $x = 67$ glass is much more closed to Augmented Triangular Prism than its related crystal (see Figure 6.26). There was another proposal of the structural units of these glasses from the MD analysis [32] which suggest that it constitutes of mainly ZrF_8 polyhedra with small amount of ZrF_7 polyhedra but our analysis showed that there was almost similar amount of both types of polyhedra. They also proposed that the shape structure of ZrF_8 polyhedra were similar to Snub Disphenoid which contrasts to the result here and for the ZrF_8 polyhedra as they did not mention whether it is Elongated or Augmented Triangular Prism.

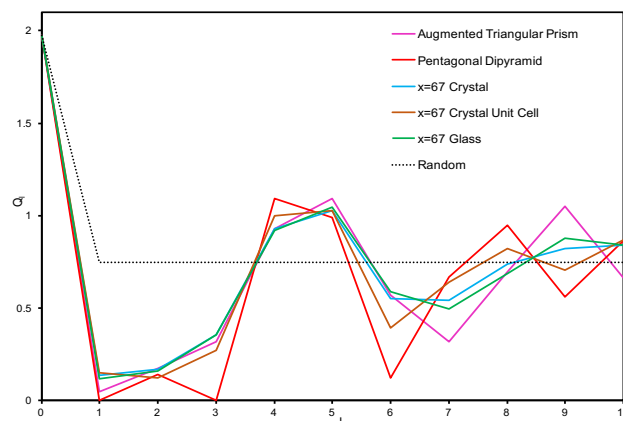


Figure 6.26 Rotational invariants, Q_l , of ZrF_n polyhedra for $x = 67$ crystal and $x = 67$ glass for $CN = 7$ compared with convex polyherda for vertices $N = 7$ (Elongated Triangular Pyramid not included due to very different Q_l values).

As discussed in Chapter 1 (section 1.3.3) from the theory of random close packing bonding criteria, ionic binary glasses like $ZrF_4 - BaF_2$ which have a large radius ratio and large values of CN will have more than one type of polyhedra of structural units [47]. Here the model results presented more than one ZrF_n polyhedra structural unit. Similarly, BaF_n polyhedra in glasses had mostly $CN \geq 10$, which leads to a less well-defined coordination polyhedra as was shown by the results of rotational invariants, Q_l .

6.5 Conclusions

The new molecular dynamics models of $xZrF_4 - (100 - x)BaF_2$ glasses presented here gave fair agreement with the experimental X-ray diffraction data for $x = 50$ and 67 glasses and with neutron diffraction data for $x = 60, 67$ and 75 glasses. The metazirconate ($x = 50$), dizirconate ($x = 67$) and trizirconate ($x = 75$) glasses shows mixtures of 7 and 8 coordinated Zr atoms and primarily 10 and 11 coordinated Ba atoms. The short-range order agrees very well with a previous EXFAS study. The metazirconate crystal ($x = 50$) gave similar results but the dizirconate crystal ($x = 67$) gave mixtures of 6 and 7 coordinated Zr atoms and 9 and 11 coordinated Ba atoms. The BAD and Q_l analysis showed that the ZrF_n polyhedra for $x = 67$ and 50 glasses and its related crystals are in fair agreement with the structural units of Augmented Triangular Prism ($N = 7$) for ZrF_7 polyhedra and Biaugmented Triangular Prism ($N = 8$) for ZrF_8 polyhedra. However, Q_l analysis offers more the direct comparison than BAD between these structural units. The network of ZrF_n polyhedra in glasses are found to be significantly corner sharing. Additionally, the Q_l results of BaF_n polyhedra in glasses showed that the Q_l values tend towards random as the $Ba - F$ coordination number increases.

6.6 References

- [1] M. Poulain, M. Poulain, J. Lucas, Verres fluores au tetrafluorure de zirconium proprietes optiques d'un verre dope au Nd^{3+} , Mater. Res. Bull. 10 (1975) 243-246.
- [2] M. Poulain, M. Poulain, J. Lucas, Etude comparee de verres fluores dans les diagramm ternaires ZrF_4 - BaF_2 - MF_n ($M= Na, Ca, La, Th; n = 1, 2, 3, 4$), Rev.Chim. Miner. 16 (1979) 267-276.
- [3] M. Poulain, Fluoride glass composition and processing, Fluoride Glass Fibre Optics. (1991).
- [4] C. Fouassier, Inorganic Solid Fluorides: Chemistry and Physics, Chap.Optical properties of fluorides. Academic Press Inc. (1985) 477-487.
- [5] C.M. Baldwin, R.M. Almeida, J.D. Mackenzie, Halide glasses, J. Non Cryst. Solids. 43 (1981) 309-344.
- [6] K.J. Rao, Structural Chemistry of Glasses, Elsevier, 2002.
- [7] T. Grande, S. Aasland, S. Julsrud, Phase equilibria in the glass-forming system ZrF_4 - BaF_2 , J. Non Cryst. Solids. 140 (1992) 73-76.
- [8] R.M. Almeida, J.D. Mackenzie, Vibrational spectra and structure of fluorozirconate glasses, J. Chem. Phys. 74 (1981) 5954-5961.
- [9] S. Aasland, T. Grande, Structure of fluorozirconate glasses and melts, Chemical Papers. 52 (1998) 21-28.
- [10] S.M. Brian, A. Mitchell, An introduction to materials engineering and science for chemical and materials engineers, Vol.1st Edition: Wiley Blackwell. (2004).
- [11] J.H. Simmons, C.J. Simmons, R. Ochoa, A.C. Wright, Fluoride glass structure, in: Anonymous Academic Press, San Diego, 1991, pp. 37-84.
- [12] G. de Leede, Crystallisation behaviour of a fluorozirconate glass, (1989).
- [13] R. Zallen, The Physics of Amorphous Solids, Wiley Classics Library Edition ed., John Wiley & Sons, 1998.
- [14] A.C. Wright, Diffraction studies of halide glasses, in: Anonymous Halide Glasses for Infrared Fiberoptics, Springer, 1987, pp. 75-117.
- [15] R.M. Almeida, Halide Glasses for Infrared Fiberoptics, NATO ASI serie E-123.(1987)1.
- [16] M.G. Drexhage, Heavy metal fluoride glasses, Treatise on materials science and technology. 26 (1985) 151-243.
- [17] S. Gross, D.G. Lancaster, H. Ebendorff-Heidepriem, T.M. Monro, A. Fuerbach, M.J. Withford, Femtosecond laser induced structural changes in fluorozirconate glass, Optical Materials Express. 3 (2013) 574-583.

- [18] C.C. Phifer, D.J. Gosztola, J. Kieffer, C.A. Angell, Effects of coordination environment on the Zr-F symmetric stretching frequency of fluorozirconate glasses, crystals, and melts, *J. Chem. Phys.* 94 (1991) 3440-3450.
- [19] Y. Kawamoto, F. Sakaguchi, Thermal properties and Raman spectra of crystalline and vitreous $BaZrF_6$, $PbZrF_6$, and $SrZrF_6$. *Bull. Chem. Soc. Jpn.* 56 (1983) 2138-2141.
- [20] R. Coupe, D. Louer, J. Lucas, A. Leonard, X-Ray Scattering Studies of Glasses in the System ZrF_4 - BaF_2 , *J Am Ceram Soc.* 66 (1983) 523-529.
- [21] Y. Kawamoto, T. Horisaka, Short-range structures of barium, lead, and strontium meta-fluorozirconate glasses, *J. Non Cryst. Solids.* 56 (1983) 39-44.
- [22] G. Etherington, L. Keller, A. Lee, C. Wagner, R.M. Almeida, An X-ray diffraction study of the structure of barium fluorozirconate and fluorohafnate glasses, *J. Non Cryst. Solids.* 69 (1984) 69-80.
- [23] R.M. Almeida, J.D. Mackenzie, Short range structures of Fluoride glasse, *Journal de Physique Colloques.* 46 (1985) 79.
- [24] R.M. Almeida, J. Lau, J.D. Mackenzie, XPS Studies of Fluorozirconates, 5 (1985) 465-470.
- [25] C. Wagner, S.B. Jost, G. Etherington, M.S. Boldrick, The Structure of Heavy Metal Fluoride Glasses, 19 (1987) 137-140.
- [26] A. Le Bail, B. Boulard, C. Jacoboni, Structure of Barium Fluorozirconate Glasses: A Quasi-Crystalline Modelling of " $BaZr_2F_{10}$ ", 19 (1987) 127-136.
- [27] B. Boulard, A. Le Bail, J.P. Laval, C. Jacoboni, Local environment of Zr in barium fluorozirconate glasses: The EXAFS point of view, *Le Journal de Physique Colloques.* 47 (1986) 794.
- [28] F. Ma, Z. Shen, L. Ye, M. Zhang, K. Lu, Y. Zhao, EXAFS study of glasses in the system BaF_2 - ZrF_4 , *J. Non Cryst. Solids.* 99 (1988) 387-393.
- [29] R.M. Almeida, M.I. de Barros Marques, M.C. Goncalves, EXAFS study of Ba and La structural environments in fluorozirconate glasses, *J. Non Cryst. Solids.* 168 (1994) 144-149.
- [30] R.E. Youngman, S. Sen, A high-resolution ^{19}F NMR spectroscopic study of barium fluorozirconate glasses and related crystals, *Solid State Nucl. Magn. Reson.* 27 (2005) 77-89.
- [31] J. Lucas, C.A. Angell, S. Tamaddon, Fluoride bridging modes in fluorozirconate glasses by X-ray and computer simulation studies, *Mater. Res. Bull.* 19 (1984) 945-951.
- [32] Y. Kawamoto, T. Horisaka, K. Hirao, N. Soga, A molecular dynamics study of barium meta-fluorozirconate glass, *J. Chem. Phys.* 83 (1985) 2398-2404.

- [33] I. Yasui, H. Inoue, Molecular dynamic simulations of changes in structure in ZrF₄ based glasses, *J. Non Cryst. Solids*. 71 (1985) 39-47.
- [34] C.C. Phifer, C.A. Angell, J.P. Laval, J. Lucas, A structural model for prototypical fluorozirconate glass, *J. Non Cryst. Solids*. 94 (1987) 315-335.
- [35] J.H. Simmons, G. O'Rear, T.P. Swiler, A.C. Wright, Structural modeling of the ZrF₄ - BaF₂ binary using molecular dynamics, *J. Non Cryst. Solids*. 106 (1988) 325-329.
- [36] E.I. Voit, A.V. Voit, V.I. Sergienko, Quantum-Chemical Justification of the Structure of Fluorozirconate Glasses1, *Glass physics and chemistry*. 27 (2001) 195-203.
- [37] Z. Lin-xiang, J.R. Hardy, X. Xin, Molecular Dynamics Simulation of Binary Fluorozirconate Glass ZrF₄-BaF₂, *Chinese physics letters*. 15 (1998) 326.
- [38] R. Papiernik, D. Mercurio, B. Frit, Structure du tétrafluorure de zirconium, α -ZrF₄, *Acta Crystallographica Section B: Structural Crystallography and Crystal Chemistry*. 38 (1982) 2347-2353.
- [39] C. Legein, F. Fayon, C. Martineau, M. Body, J. Buzaré, D. Massiot, E. Durand, A. Tressaud, A. Demourgues, O. Péron, ¹⁹F High Magnetic Field NMR Study of β -ZrF₄ and CeF₄: From Spectra Reconstruction to Correlation between Fluorine Sites and ¹⁹F Isotropic Chemical Shifts, *Inorg. Chem*. 45 (2006) 10636-10641.
- [40] J.P. Laval, B. Frit, J. Lucas, Crystal structure of the β -BaZr₂F₁₀ compound. Relations with the ReO₃-type and the fluorozirconate glasses, *Journal of Solid State Chemistry*. 72 (1988) 181-192.
- [41] J. Laval, R. Papiernik, B. Frit, α -BaZrF₆: une structure à anion complexe [Zr₂F₁₂]⁴⁻ *Acta Crystallographica Section B: Structural Crystallography and Crystal Chemistry*. 34 (1978) 1070-1074.
- [42] A. Le Bail, J. Laval, Synthesis and crystal structure of α -Ba₂ZrF₈ and Pb₂ZrF₈ determined ab initio from synchrotron and neutron powder diffraction data, *European journal of solid state and inorganic chemistry*. 35 (1998) 357-372.
- [43] A.S. Radtke G.E. Brown, Frankdicksonite, BaF₂, a New Mineral from Nevada, *Am. Mineral*. 59 (1974) 885-888.
- [44] D. Teter, Private Communication (2004).
- [45] J. Wasylak, L. Samek, Structural aspects of fluorozirconate glasses and some of their properties, *J. Non Cryst. Solids*. 129 (1991) 137-144.
- [46] J. Hafner, Bond-angle distribution functions in metallic glasses, *Le Journal de Physique Colloques*. 46 (1985) 78.
- [47] C.J. Simmons, O.H. El-Bayoumi, *Experimental Techniques of Glass Science*, Amer Ceramic Society, 1993.

Chapter 7

Molecular dynamics modelling of Eu^{3+} doped ZBLAN glasses

7.1 Introduction

The discovery fluoride based ternary glass $ZrF_4 - BaF_2 - NaF$ (ZBN) by Poulain et al [1] has triggered extensive study of the structures of glasses based on zirconium barium fluoride. Typically, interest was on fluorozirconate systems based on the $ZrF_4 - BaF_2 - LaF_3 - AlF_3 - NaF$ (ZBLAN) glass composition due to their stability against devitrification amongst the fluoride glasses [2]. It can also be doped with rare-earth ions, e.g. europium (Eu^{3+}), [3] for optical applications [4]. The glass formation regions are also found in $ZrF_4 - BaF_2 - LaF_3$ (ZBL) [5], $ZrF_4 - BaF_2 - LaF_3 - AlF_3$ (ZBLA) [6] and $ZrF_4 - BaF_2 - LaF_3 - NaF$ (ZBLN) [7] systems.

The glass transition temperature, T_g , of these heavy metal fluoride glasses are in range of 300 °C and melting temperature, T_m , between 450 °C and 600 °C depending on the glass compositions [8]. The stability of these glasses can be predicted by the Hruby factor, $H_r = (T_x - T_g)/(T_m - T_x)$, where T_x is the crystallization temperature [9]. The T_x and the glass formation regions for ZBN, ZBL, ZBLA, ZBLN and ZBLAN are well reported in [2], [10], [11], [12]. Generally, T_x ranges from 250 °C to 410 °C depending on composition.

The simple binary system of $ZrF_4 - BaF_2$ is considered the base component for these multicomponent fluorozirconate glasses. The reported glasses illustrate that ZrF_4 is a primary network former with roughly more than 50 mol % of ZrF_4 and BaF_2 as a modifier with at least 20 mol % of BaF_2 . The heavy metal fluoride glasses like ZBLAN which can be easily doped with rare earth ions are interesting for optical applications and are superior to binary and ternary glasses which exhibit large crystallization rates [13]. However, due to the multicomponent nature of these glasses there are very few structural studies reported.

Nevertheless, there are reports of their physical properties, and selected glass compositions were studied in this project.

Samek et al [14] studied a series of compositions for ZBL glasses by Raman spectroscopy and only reported the wavenumber caused by the vibrations of $[ZrF_6]^{-2}$ octahedra. Aasland et al [15] studied a series of ZBN ternary glass compositions constrained by a ratio $F/Zr = 5$ with infrared and Raman spectroscopies and they concluded that the glass structure is depended on the F/Zr ratio.

Wasylak and Samek [16] studied ZBLA glass containing mole percentage of $53ZrF_4 - 32BaF_2 - 9LaF_3 - 9AlF_3$ by X-ray diffraction. They reported the bond length of 2.1 Å and 2.7 Å for $Zr - F$ and $Ba - F$ respectively. They also reported nearest neighbour distances of 4.2 Å for $Ba - Ba$ cations, and for $Zr - Ba$ and $Zr - Zr$ ranging from 3.8 – 4.8 Å. Braglia et al [17] studied local atomic environment of ZBLAN glass containing mole percentage of $53ZrF_4 - 20BaF_2 - 4LaF_3 - 3AlF_3 - 20NaF$ by extended absorption fine structure (EXAFS) and anomalous X-ray scattering techniques. They reported the bond length of 2.1 Å for $Zr - F$, 2.6 Å for $Ba - F$ and nearest neighbour distances of 4.1 Å for both $Zr - Zr$ and $Ba - Ba$ cations.

Harrison and Denning [18] studied the Eu^{3+} doped ZBLAN glass by classical molecular dynamics method. The simulated glass contained 2 mol % of Eu and other components mole percentage were $53ZrF_4 - 20BaF_2 - 2LaF_3 - 3AlF_3 - 20Na$. They calculated the short-range order with bond length of 2.05 Å, 2.65 Å, 2.30 Å, and 2.25 Å for $Zr - F$, $Ba - F$, $Na - F$ and $Eu - F$ respectively. They also reported non-integer coordination numbers of 7.6, 8.5, and 7.5 for $Zr - F$, $Ba - F$ and $Eu - F$ respectively and 6.0 for $Al - F$.

The structure of ZBLAN glass are still not well understood. The compounds such as BaF_2 and NaF breakup the $Zr - F - Zr$ network [19]. Therefore, new MD models for ZBL,

ZBA, ZBN, ZBLA, ZBLAN and Eu^{3+} doped ZBLAN glasses are studied in this project to analyse the local environment of the cations in the glasses also by the method of rotational invariants, Q_l , presented in Chapter 3.

7.2 Method

7.2.1 Structures of multicomponent fluorozirconate crystals

The multicomponent fluorozirconate crystals are very rarely found. Only few ternary and quaternary crystals were found to compare short-range order and local structures with the ZBLAN glass system.

7.2.1.1 EuF_3

The unit cell of europium fluoride crystal [20] is shown in Figure 7.1. The calculated density of the crystal is 6.81 g cm^{-3} . Its lattice parameters are: $a = 6.616 \text{ \AA}$, $b = 7.013 \text{ \AA}$ and $c = 4.392 \text{ \AA}$ with $\alpha = 90^\circ$, $\beta = 90^\circ$ and $\gamma = 90^\circ$.

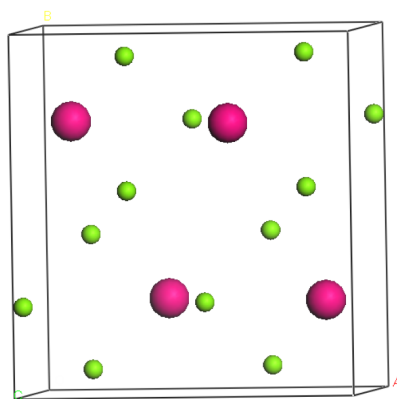


Figure 7.1 The unit cell of EuF_3 crystal. The violet spheres are europium atoms and green spheres are fluorine atoms.

7.2.1.2 LaF_3

The unit cell of lanthanum fluoride crystal [21] is shown in Figure 7.2. The calculated density of the crystal is 5.94 g cm^{-3} . Its lattice parameters are: $a = 7.185 \text{ \AA}$, $b = 7.185 \text{ \AA}$ and $c = 7.351 \text{ \AA}$ with $\alpha = 90^\circ$, $\beta = 90^\circ$ and $\gamma = 120^\circ$.

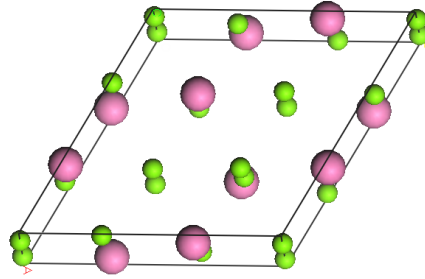


Figure 7.2 The unit cell of LaF_3 crystal. The light pink spheres are lanthanum atoms and green spheres are fluorine atoms.

7.2.1.3 AlF_3

The unit cell of aluminium fluoride crystal [22] is shown in Figure 7.1. The calculated density of the crystal is 3.19 g cm^{-3} . Its lattice parameters are: $a = 4.931 \text{ \AA}$, $b = 4.931 \text{ \AA}$ and $c = 12.445 \text{ \AA}$ with $\alpha = 90^\circ$, $\beta = 90^\circ$ and $\gamma = 120^\circ$.

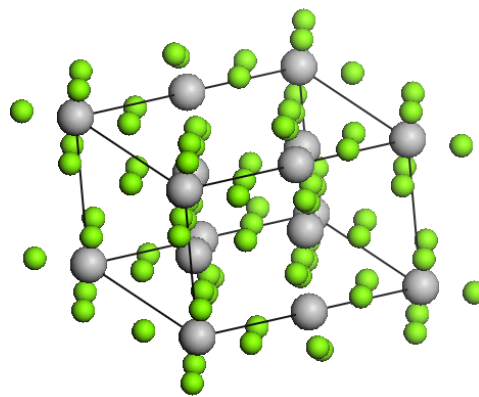


Figure 7.3 The unit cell of AlF_3 crystal. The silver spheres are aluminium atoms and green spheres are fluorine atoms.

7.2.1.4 NaF

The unit cell of sodium fluoride crystal [23] is shown in Figure 7.4. The calculated density of the crystal is 2.81 g cm^{-3} . Its lattice parameters are: $a = 4.630 \text{ \AA}$, $b = 4.630 \text{ \AA}$ and $c = 4.630 \text{ \AA}$ with $\alpha = 90^\circ$, $\beta = 90^\circ$ and $\gamma = 90^\circ$.

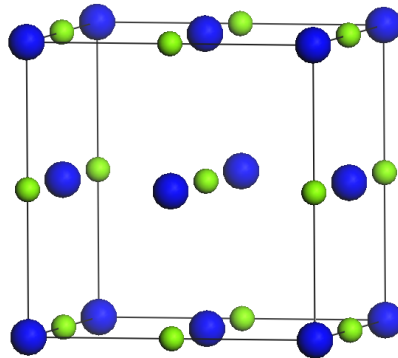


Figure 7.4 The unit cell of NaF crystal. The blue spheres are sodium atoms and green spheres are fluorine atoms.

7.2.1.5 $\text{Eu}_3\text{Zr}_3\text{F}_{15}$

The unit cell of europium zirconium fluoride crystal [24] is shown in Figure 7.5. The calculated density of the crystal is 4.64 g cm^{-3} . Its lattice parameters are: $a = 12.461 \text{ \AA}$, $b = 12.461 \text{ \AA}$ and $c = 11.344 \text{ \AA}$ with $\alpha = 90^\circ$, $\beta = 90^\circ$ and $\gamma = 120^\circ$.

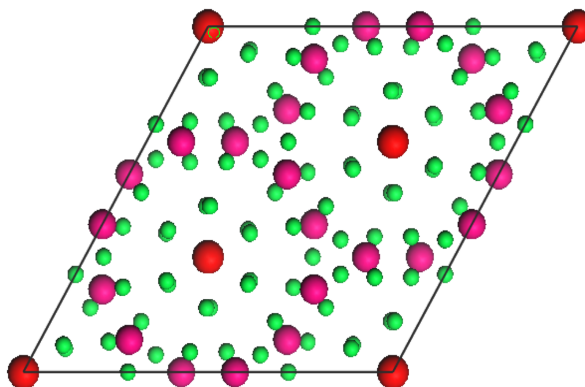


Figure 7.5 The unit cell of $\text{Eu}_3\text{Zr}_3\text{F}_{15}$ crystal. The violet spheres are europium atoms, red spheres are zirconium atoms and green spheres are fluorine atoms. The Eu sites are mixed occupancy of 0.3333 Eu and 0.6667 Zr.

7.2.1.6 $\text{Eu}_3\text{Ba}_4\text{F}_{17}$

The unit cell of tetrabarium heptadecafluorotrieuropate crystal [25] is shown in Figure 7.6. The calculated density of the crystal is 5.94 gcm^{-3} . Its lattice parameters are: $a = 11.179 \text{ \AA}$, $b = 11.179 \text{ \AA}$ and $c = 20.579 \text{ \AA}$ with $\alpha = 90^\circ$, $\beta = 90^\circ$ and $\gamma = 120^\circ$.

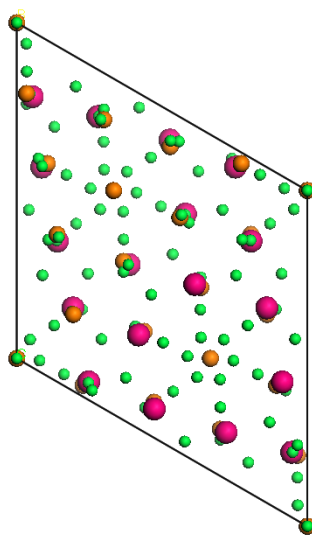


Figure 7.6 The unit cell of $\text{Eu}_3\text{Ba}_4\text{F}_{17}$ crystal. The violet spheres are europium atoms, brown spheres are barium atoms and green spheres are fluorine atoms.

7.2.1.7 $\beta - \text{EuNaF}_4$

The unit cell of β - sodium europium fluoride crystal [26] is shown in Figure 7.7. The calculated density of the crystal is 5.45 gcm^{-3} . Its lattice parameters are: $a = 6.04 \text{ \AA}$, $b = 6.04 \text{ \AA}$ and $c = 3.632 \text{ \AA}$ with $\alpha = 90^\circ$, $\beta = 90^\circ$ and $\gamma = 120^\circ$.

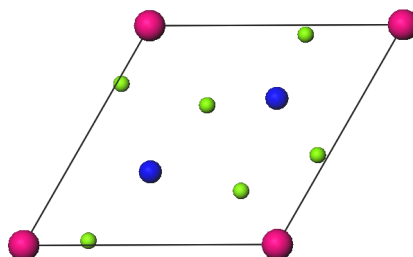


Figure 7.7 The unit cell of NaEuF_4 crystal. The violet spheres are europium atoms, blue spheres are sodium atoms and green spheres are fluorine atoms.

7.2.1.8 $\text{NaBaZr}_2\text{F}_{11}$

The unit cell of sodium barium zirconium fluoride crystal, $\text{NaBaZr}_2\text{F}_{11}$ [27] is shown in Figure 7.8. The calculated density of the crystal is 4.59 gcm^{-3} . Its lattice parameters are: $a = 8.233 \text{ \AA}$, $b = 8.233 \text{ \AA}$ and $c = 23.610 \text{ \AA}$ with $\alpha = 90^\circ$, $\beta = 90^\circ$ and $\gamma = 90^\circ$.

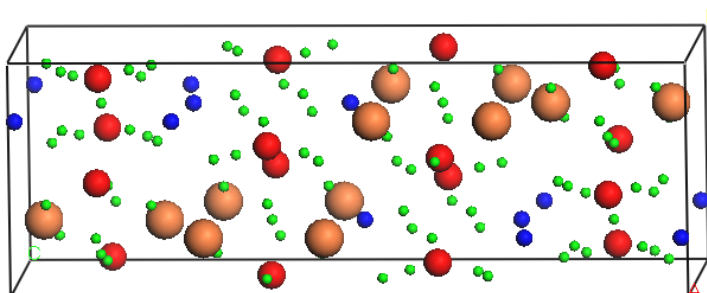


Figure 7.8 The unit cell of $\text{NaBaZr}_2\text{F}_{11}$ crystal. The red spheres are zirconium atoms, brown spheres are barium atoms, blue spheres are sodium atoms and green spheres are fluorine atoms.

7.2.1.9 NaBaZrF_7

The unit cell of sodium barium zirconium fluoride crystal, NaBaZrF_7 [28] is shown in Figure 7.9. The calculated density of the crystal is 4.49 gcm^{-3} . Its lattice parameters are: $a = 9.118 \text{ \AA}$, $b = 5.556 \text{ \AA}$ and $c = 11.236 \text{ \AA}$ with $\alpha = 90^\circ$, $\beta = 90^\circ$ and $\gamma = 90^\circ$.

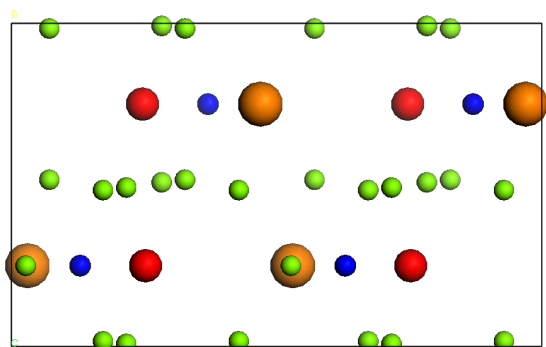


Figure 7.9 The unit cell of NaBaZrF_7 crystal. The red spheres are zirconium atoms, brown spheres are barium atoms, blue spheres are sodium atoms and green spheres are fluorine atoms.

7.2.2 Potentials for ZBLAN Systems including Eu^{3+}

The two-body interaction is considered for the multicomponent system. The interaction of ions in ZBLAN systems including Eu^{3+} was described by using the Buckingham rigid ion interatomic potentials. The form of Coulomb and Buckingham potentials are given in Equation 2.2 – 2.4. The potential parameters used were derived by Teter [29] and these are listed in Table 7.1 for $Zr - F$, $Ba - F$, $La - F$, $Al - F$, $Na - F$, $F - F$ and $Eu - F$ interactions.

Table 7.1 Teter potential parameters for multicomponent fluorozirconate systems.

$i - j$	$q_i(e)$	$A_{ij}(eV)$	$\rho_{ij}(\text{\AA})$	$C_{ij}(eV\text{\AA}^{-6})$
$Zr - F$	2.4	216847.86	0.150759	0.06858
$Ba - F$	1.2	472934.92	0.190284	140.80
$La - F$	1.8	74564.178	0.196472	49.873
$Al - F$	1.8	55493.596	0.147476	5.9767
$Na - F$	0.6	58286.14	0.169113	4.1555
$Eu - F$	1.8	23177.141	0.203968	11.188
$F - F$	-0.6	11510.594	0.225005	29.527

7.2.3 Testing of potentials

The potentials parameters used on the multicomponent fluorozirconate glass systems were initially used to mimic the crystal structures. The short-range order, coordination numbers and lattice parameters of crystals were compared to test the potentials and the results are shown in the Tables 7.2 – 7.10.

Table 7.2 The result from the GULP energy minimisation for EuF_3 crystal initial and final structures displaying the low percentage errors.

Parameter	Unit	Initial Value	Final Value	Difference	Percent
Volume	\AA^3	203.780	205.611	1.831	0.90
a	\AA	6.616	6.650	0.034	0.51
b	\AA	7.013	7.034	0.021	0.29
c	\AA	4.392	4.396	0.004	0.09
α	Degree	90	90	0	0
β	Degree	90	90	0	0
γ	Degree	90	90	0	0
$\text{Eu} - \text{F}$ distance	\AA	2.314	2.381	0.066	2.87
$\text{Eu} - \text{F}$ CN		9	9	0	0

Table 7.3 The result from the GULP energy minimisation for LaF_3 crystal initial and final structures displaying the low percentage errors.

Parameter	Unit	Initial Value	Final Value	Difference	Percent
Volume	\AA^3	328.648	319.359	-9.288	-2.83
a	\AA	7.185	7.11207	-0.073	-1.02
b	\AA	7.185	7.11207	-0.073	-1.02
c	\AA	7.351	7.291	-0.060	-0.82
α	Degree	90	90	0	0
β	Degree	90	90	0	0
γ	Degree	120	120	0	0
$\text{La} - \text{F}$ distance	\AA	2.58	2.56	-0.01	-0.56
$\text{La} - \text{F}$ CN		11	11	0	0

Table 7.4 The result from the GULP energy minimisation for AlF_3 crystal initial and final structures displaying the low percentage errors.

Parameter	Unit	Initial value	Final value	Difference	Percent
Volume	\AA^3	262.029	261.186	-0.843	-0.32
a	\AA	4.931	4.932	0.001	0.02
b	\AA	4.931	4.932	0.001	0.02
c	\AA	12.446	12.400	-0.046	-0.37
α	Degree	90	90	0	0.00
β	Degree	90	90	0	0.00
γ	Degree	120	120	0	0.00
$\text{Al} - \text{F}$ distance	\AA	1.797	1.737	-0.060	-3.32
$\text{Al} - \text{F}$ CN		6	6	0	0.00

Table 7.5 The result from the GULP energy minimisation for NaF crystal initial and final structures displaying the low percentage errors.

Parameter	Unit	Initial Value	Final Value	Difference	Percent
Volume	\AA^3	99.253	98.754	-0.499	-0.50
a	\AA	4.630	4.622	-0.008	-0.17
b	\AA	4.630	4.622	-0.008	-0.17
c	\AA	4.630	4.622	-0.008	-0.17
α	Degree	90	90	0	0.00
β	Degree	90	90	0	0.00
γ	Degree	90	90	0	0.00
$\text{Na} - \text{F}$ distance	\AA	2.315	2.311	-0.004	-0.17
$\text{Na} - \text{F}$ CN		6	6	0	0.00

Table 7.6 The result from the GULP energy minimisation for $\text{Eu}_3\text{Zr}_3\text{F}_{15}$ crystal initial and final structures displaying the low percentage errors.

Parameter	Unit	Initial Value	Final Value	Difference	Percent
Volume	\AA^3	508.489	495.687	-12.802	-2.52
a	\AA	8.128	8.042	-0.085	-1.05
b	\AA	8.128	8.042	-0.085	-1.05
c	\AA	8.128	8.042	-0.085	-1.05
α	Degree	100.097	99.566	-0.531	-0.53
β	Degree	100.097	99.566	-0.531	-0.53
γ	Degree	100.097	99.566	-0.531	-0.53
Zr – F distance	\AA	2.095	2.088	-0.007	-0.34
Zr – F CN		7	7	0	0.00
Eu – F distance	\AA	2.195	2.168	-0.027	-1.25
Eu – F CN		8	8	0	0.00

Table 7.7 The result from the GULP energy minimisation for $\text{Eu}_3\text{Ba}_4\text{F}_{17}$ crystal initial and final structures displaying the low percentage errors. Apart from Eu – F coordination number.

Parameter	Unit	Initial Value	Final Value	Difference	Percent
Volume	\AA^3	2227.078	2358.807	131.730	5.91
a	\AA	11.179	11.626	0.447	4.00
b	\AA	11.179	11.248	0.069	0.62
c	\AA	20.579	20.882	0.303	1.47
α	Degree	90	90.154	0.154	0.17
β	Degree	90	89.519	-0.481	-0.53
γ	Degree	120	120.247	0.247	0.21
Ba – F distance	\AA	2.773	2.778	0.005	0.20
Ba – F CN		9.604	9.333	-0.271	-2.82
Eu – F distance	\AA	2.357	2.406	0.050	2.11
Eu – F CN		10.5	9.306	-1.194	-11.38

Table 7.8 The result from the GULP energy minimisation for $\beta - \text{EuNaF}_4$ crystal initial and final structures displaying the low percentage errors.

Parameter	Unit	Initial Value	Final Value	Difference	Percent
Volume	\AA^3	114.74938	120.175	5.425	4.73
a	\AA	6.04	5.945	-0.095	-1.57
b	\AA	6.04	5.945	-0.095	-1.57
c	\AA	3.632	3.926	0.294	8.10
α	Degree	90	90	0	0.00
β	Degree	90	90	0	0.00
γ	Degree	120	120	0	0.00
$\text{Na} - \text{F}$ distance	\AA	2.374	2.390	0.016	0.67
$\text{Na} - \text{F}$ CN		7	7	0	0.00
$\text{Eu} - \text{F}$ distance	\AA	2.357	2.349	-0.008	-0.32
$\text{Eu} - \text{F}$ CN		9	9	0	0.00

Table 7.9 The result from the GULP energy minimisation for $\text{NaBaZr}_2\text{F}_{11}$ crystal initial and final structures displaying the low percentage errors.

Parameter	Unit	Initial Value	Final Value	Difference	Percent
Volume	\AA^3	1596.455	1642.429	45.975	2.88
a	\AA	8.223	8.322	0.099	1.2
b	\AA	8.223	8.317	0.094	1.14
c	\AA	23.610	23.731	0.121	0.51
α	Degree	90	90.035	0.035	0.04
β	Degree	90	89.972	-0.028	-0.03
γ	Degree	90	90.016	0.016	0.02
$\text{Zr} - \text{F}$ distance	\AA	2.127	2.275	0.148	6.95
$\text{Zr} - \text{F}$ CN		7.81	7.63	-0.18	-2.4
$\text{Ba} - \text{F}$ distance	\AA	2.751	2.708	-0.043	-1.61
$\text{Ba} - \text{F}$ CN		11	11	0	0.00
$\text{Na} - \text{F}$ distance	\AA	2.327	2.322	-0.005	-0.25
$\text{Na} - \text{F}$ CN		6.37	6.37	0	0

Table 7.10 The result from the GULP energy minimisation for $NaBaZrF_7$ crystal initial and final structures displaying the low percentage errors.

Parameter	Unit	Initial Value	Final Value	Difference	Percent
Volume	\AA^3	569.242	549.034	-20.208	-3.55
a	\AA	9.118	8.975	-0.143	-1.57
b	\AA	5.556	5.628	0.072	1.29
c	\AA	11.236	10.870	-0.366	-3.26
α	Degree	90	90	0	0.00
β	Degree	90	90	0	0.00
γ	Degree	90	90	0	0.00
$Zr - F$ distance	\AA	2.061	2.024	-0.037	-1.79
$Zr - F$ CN		7	7	0	0.00
$Ba - F$ distance	\AA	2.855	2.827	-0.028	-0.98
$Ba - F$ CN		12	12	0	0.00
$Na - F$ distance	\AA	2.430	2.418	-0.012	-0.51
$Na - F$ CN		8	8	0	0.00

7.2.4 Initial configurations for Eu^{3+} doped ZBLAN glasses

The glass models made are shown in Table 7.11. The particular compositions and experimental densities of these glasses are taken from the literature for ZBL [5] [10] [30] [31], ZBA [32], ZBN [29] [33], ZBLA [6] [34] [35], ZBLAN [36] [37] [38] [39] and Eu^{3+} doped ZBLAN [19] [40] glasses. The Eu^{3+} doped ZBLAN glass models had total number of atoms of 78900 with the box size of 101.5 \AA .

Table 7.11 Initial configuration of multicomponent ZBLAN glasses including Eu^{3+} doped. In parenthesis are the percentage of atoms compositions

Glasses	Number of Zr atoms	Number of Ba atoms	Number of La atoms	Number of Al atoms	Number of Na atoms	Number of Eu atoms	Density (gcm^{-3})	Length (Å)
ZBL	2170 (62%)	1155 (33%)	175 (5%)	0	0	0	4.69	59.63
ZBA	2100 (60%)	1050 (30%)	0	350 (10%)	0	0	4.43	59.59
ZBN	2000 (50%)	1000 (25%)	0	0	1000 (25%)	0	4.5	58.81
ZBLA	2052 (57%)	1224 (34%)	180 (5%)	144 (4%)	0	0	4.54	60.46
ZBLAN	2862 (53%)	1080 (20%)	216 (4%)	162 (3%)	1080 (20%)	0	4.50	65.68
ZBLAN – Eu1%	10600 (53%)	4000 (20%)	600 (3%)	600 (3%)	4000 (20%)	200 (1%)	4.52	101.51
ZBLAN – Eu2%	10600 (53%)	4000 (20%)	400 (2%)	600 (3%)	4000 (20%)	400 (2%)	4.52	101.55

7.2.5 Parameters for MD modelling of Eu^{3+} doped ZBLAN glasses

MD Simulations were performed in DL_POLY_2 with the parameters given in Table 7.12. The melts temperature, T_m , was taken from [41] and the quench rate used was 10^{12} K/s. This quench rate was possible due to the greater computing resources available at this stage of the project. The other parameters are same as for the binary ‘ZB’ glass simulations from the previous Chapter 6.

Table 7.12 The MD parameters and stages for melt-quenched ZBLAN glasses

Stages	Temperature (K)	Time-steps	Process (NVT Brendsen thermostat)
1	5000	80000	Equilibrate
2	3000	80000	Equilibrate
3	2000 (T_m) [41]	350000	Quench
4	300	150000	Equilibrate and collect

7.3 Results

Figures 7.10 – 7.12 display the models of ZBA, ZBL, ZBN, ZBLA, ZBLAN, 1% Eu doped ZBLAN and 2% Eu doped ZBLAN glasses. The pink polyhedra are ZrF_n , brown spheres are Ba cations and green spheres are F anions. Similarly, the blue polyhedra are AlF_n , yellow spheres, grey spheres and red spheres are La Na and Eu cations respectively in the glass models.

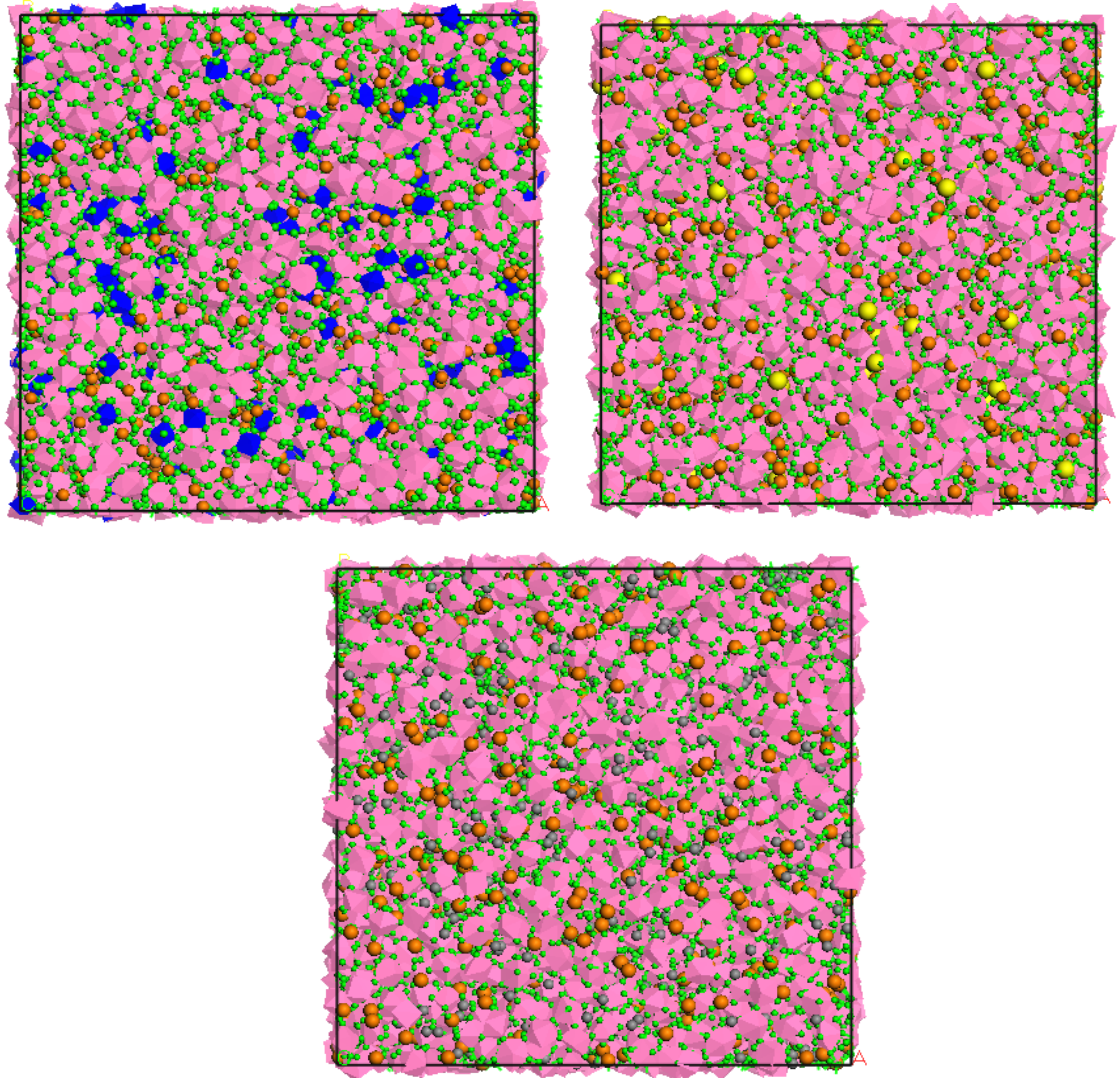


Figure 7.10 The model images of ZBA (*top-left*), ZBL (*top-right*) and ZBN (*bottom*) glasses. The pink polyhedra are ZrF_n , brown and green spheres are Ba cations and F anions. The blue polyhedra are AlF_n in ZBA, yellow spheres are La cations in ZBL, and grey spheres are Na cations in ZBN.

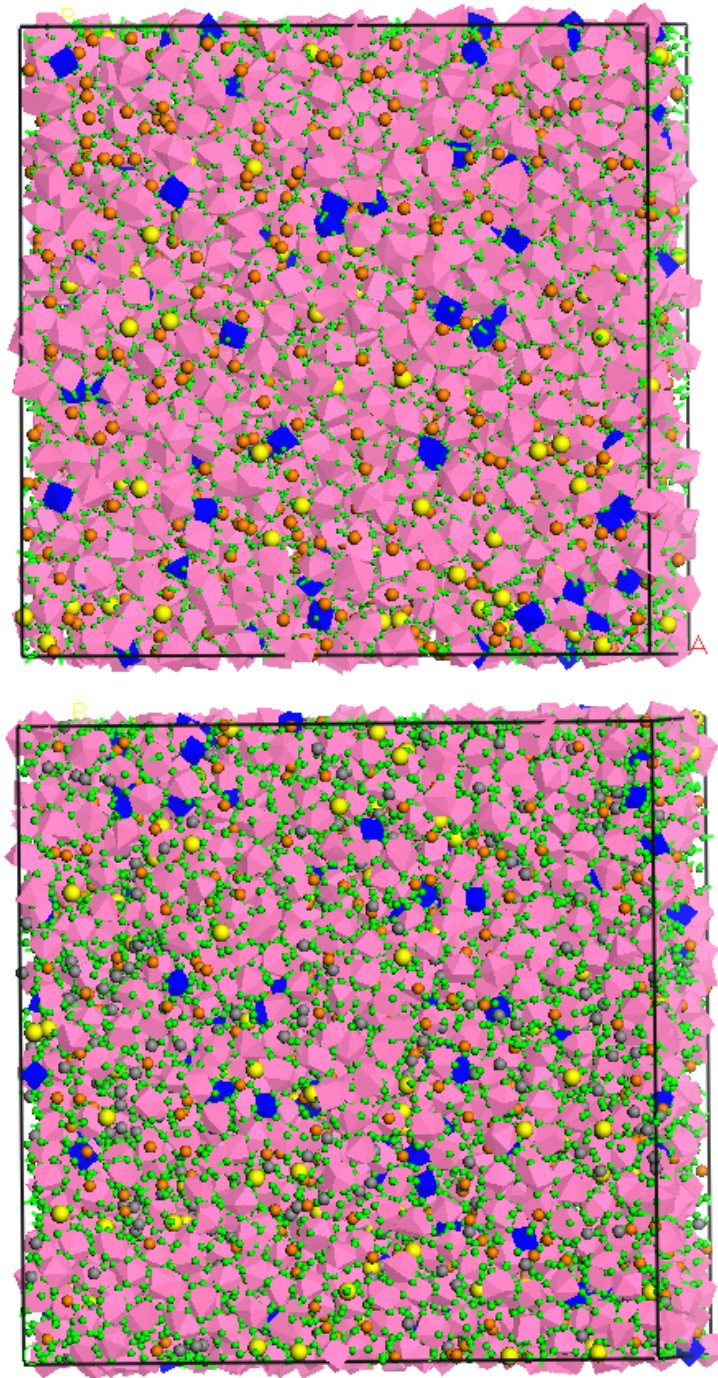


Figure 7.11 The model images of ZBLA (*top*) and ZBLAN (*bottom*) glasses. The pink polyhedra are ZrF_6 , brown and yellow spheres are Ba and La cations respectively, blue polyhedra are AlF_4 , and green spheres are F anions. The grey spheres are Na cations in ZBLAN.

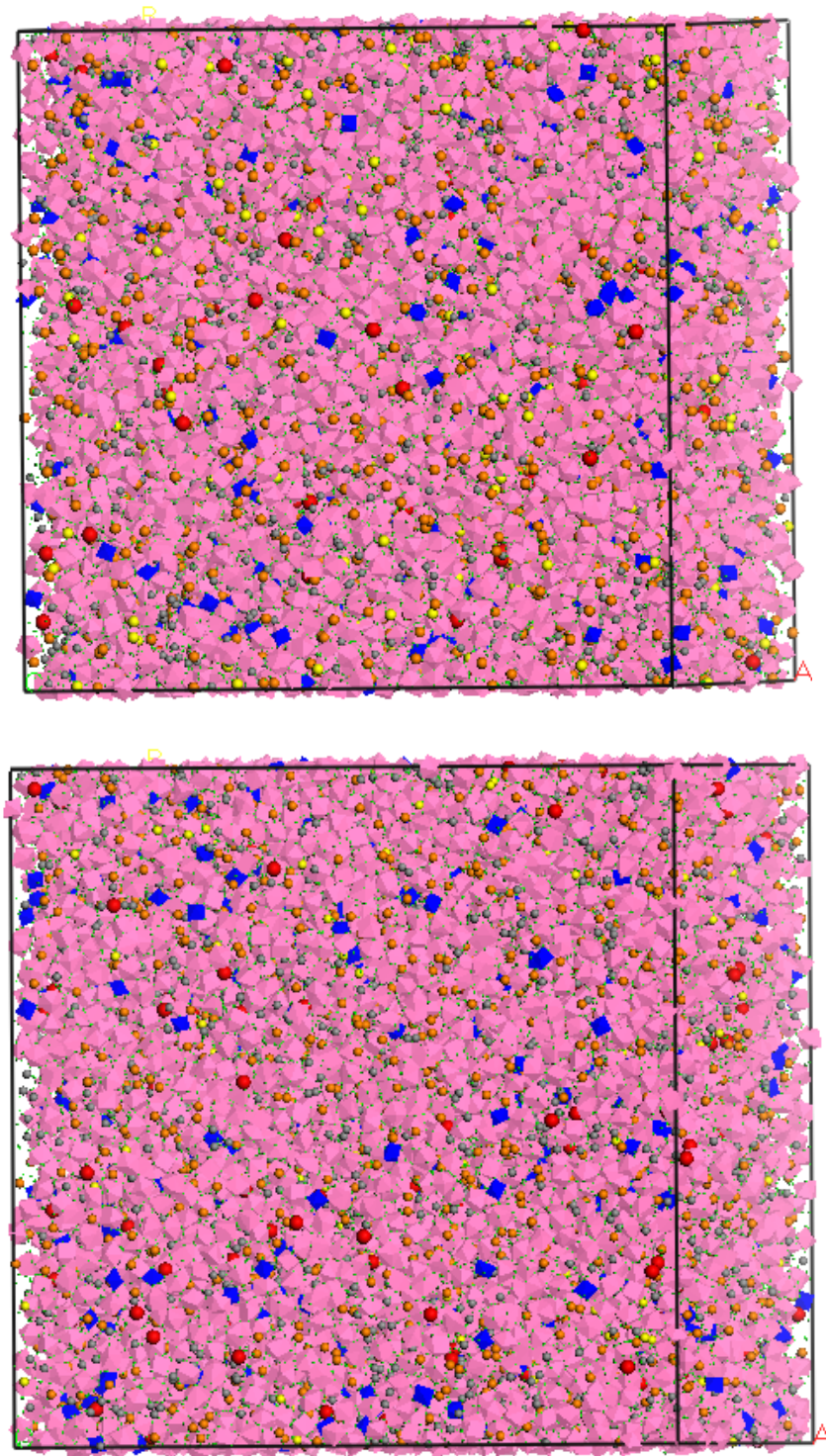


Figure 7.12 The model of ZBLAN doped with of 1% (*top*) and 2% (*bottom*) of Eu^{3+} . The pink and blue polyhedra are ZrF_6 and AlF_6 polyhedra structures. The red, brown, yellow, and grey spheres are Eu , Ba , La and Na cations respectively. The green spheres are F anions.

7.3.1 Pair distribution function, nearest neighbour distances and coordination numbers

The pair distribution functions, $T_{ij}(r)$, for ZBL, ZBA, ZBN, ZBLA and ZBLAN glasses are shown in Figure 7.13 and Figure 7.14. The partial correlation for j as fluorine ion and i either as zirconium, barium, lanthanum, aluminium or sodium ion is shown in the top part of Figure 7.13. Likewise, the bottom part of Figure 7.13 displays the partial correlation for i as zirconium ion and j as either zirconium, barium, lanthanum, aluminium or sodium ion. The partial correlation for i as barium ion and j either as barium, lanthanum, aluminium or sodium ion is shown in the top part of Figure 7.14. For i and j ions that are both lanthanum, or aluminium or sodium or either one or the other is shown in the bottom part of Figure 7.14.

Figure 7.15 and Figure 7.16 display $T_{ij}(r)$ for the Eu^{3+} doped ZBLAN glasses. The partial correlation for j as fluorine ion and i either as zirconium, barium, lanthanum, aluminium, sodium or europium ion is shown in the top part of Figure 7.15. The middle part of Figure 7.15 displays the partial correlation for i as zirconium ion and j as either zirconium, barium, lanthanum, aluminium, sodium or europium ion. The bottom part of Figure 7.15 displays the partial correlation for i as barium ion and j either as barium, lanthanum, europium, aluminium or sodium ion.

Likewise, top part of Figure 7.16 displays the pair correlation for i as lanthanum, aluminium or sodium ion and j as either lanthanum, aluminium or sodium ion. The bottom part of Figure 7.16 displays the partial correlation for i as lanthanum or europium ion and j as either aluminium, sodium or europium ion.

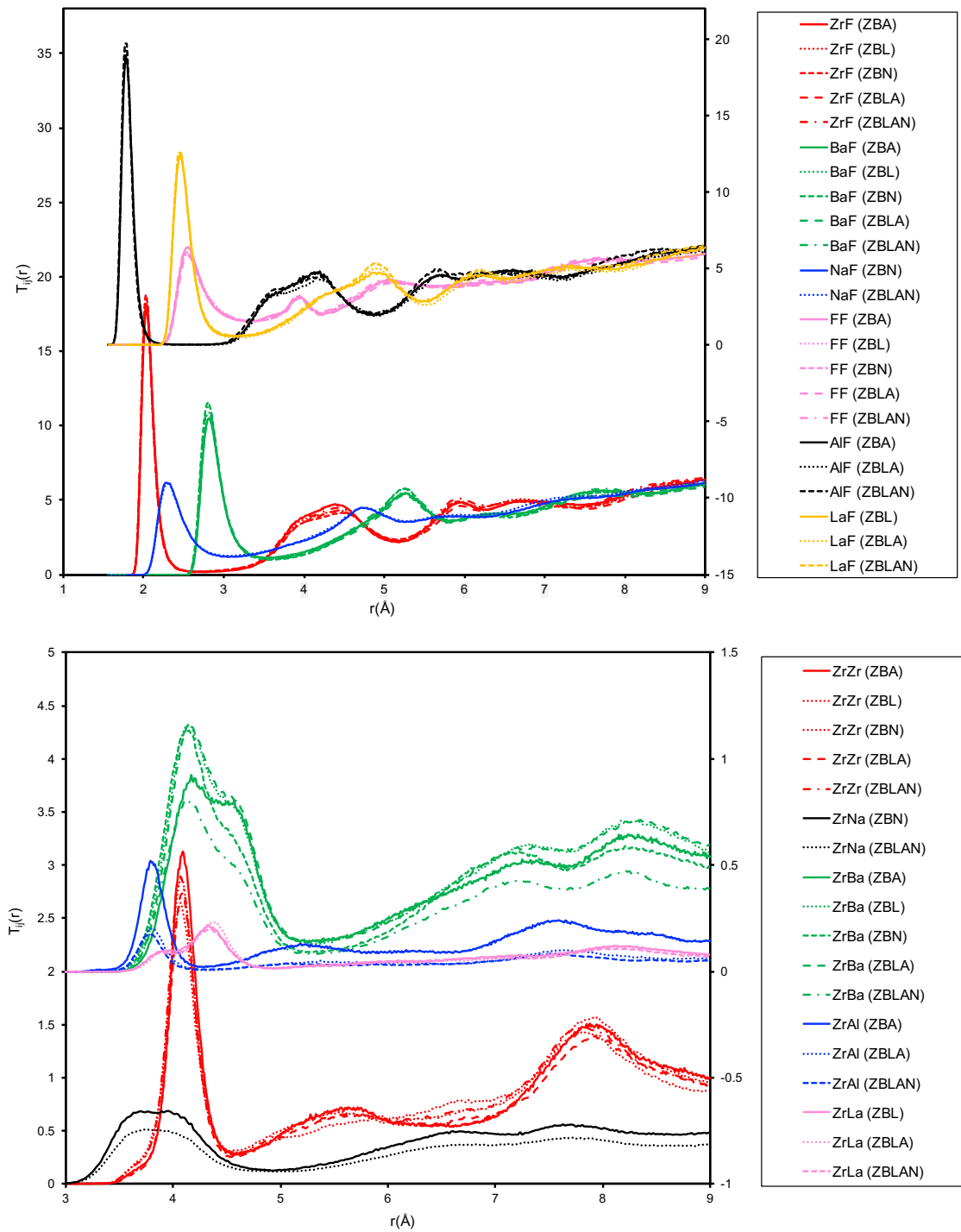


Figure 7.13 T_{ij} for ZBA, ZBL, ZBN, ZBLA and ZBLAN glass models. Top figure shows T_{ZrF} , T_{BaF} , T_{AIF} , T_{LaF} , T_{NaF} and T_{FF} , and bottom figure shows T_{ZrZr} , T_{ZrBa} , T_{ZrAl} , T_{ZrLa} and T_{ZrNa} .

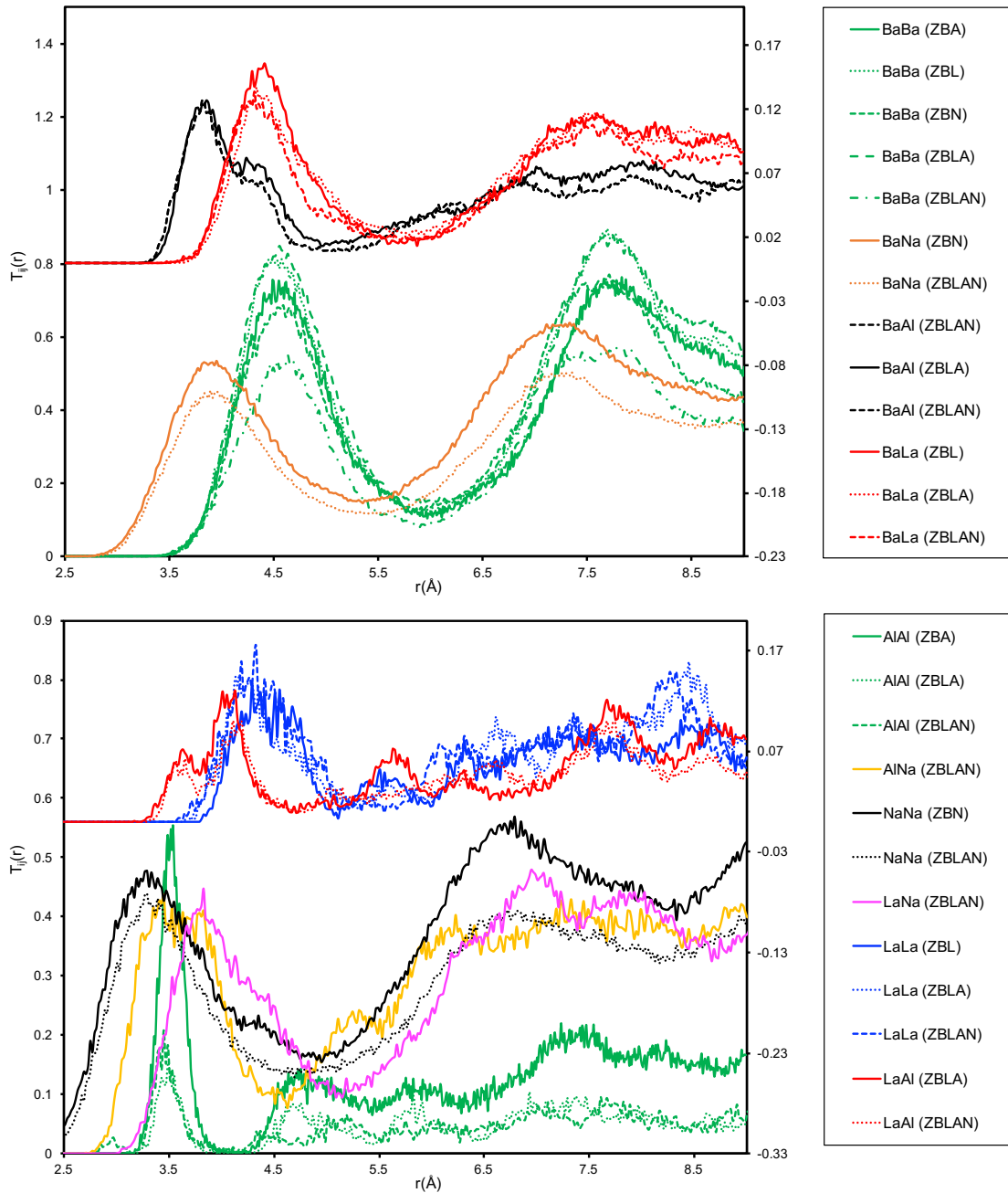


Figure 7.14 T_{ij} for ZBA, ZBL, ZBN, ZBLA and ZBLAN glass models. Top figure shows T_{BaBa} , T_{BaAl} , T_{BaLa} and T_{BaNa} , and bottom figure shows T_{AlAl} , T_{LaLa} , T_{NaNa} , T_{LaAl} , T_{LaNa} and T_{AlNa} .

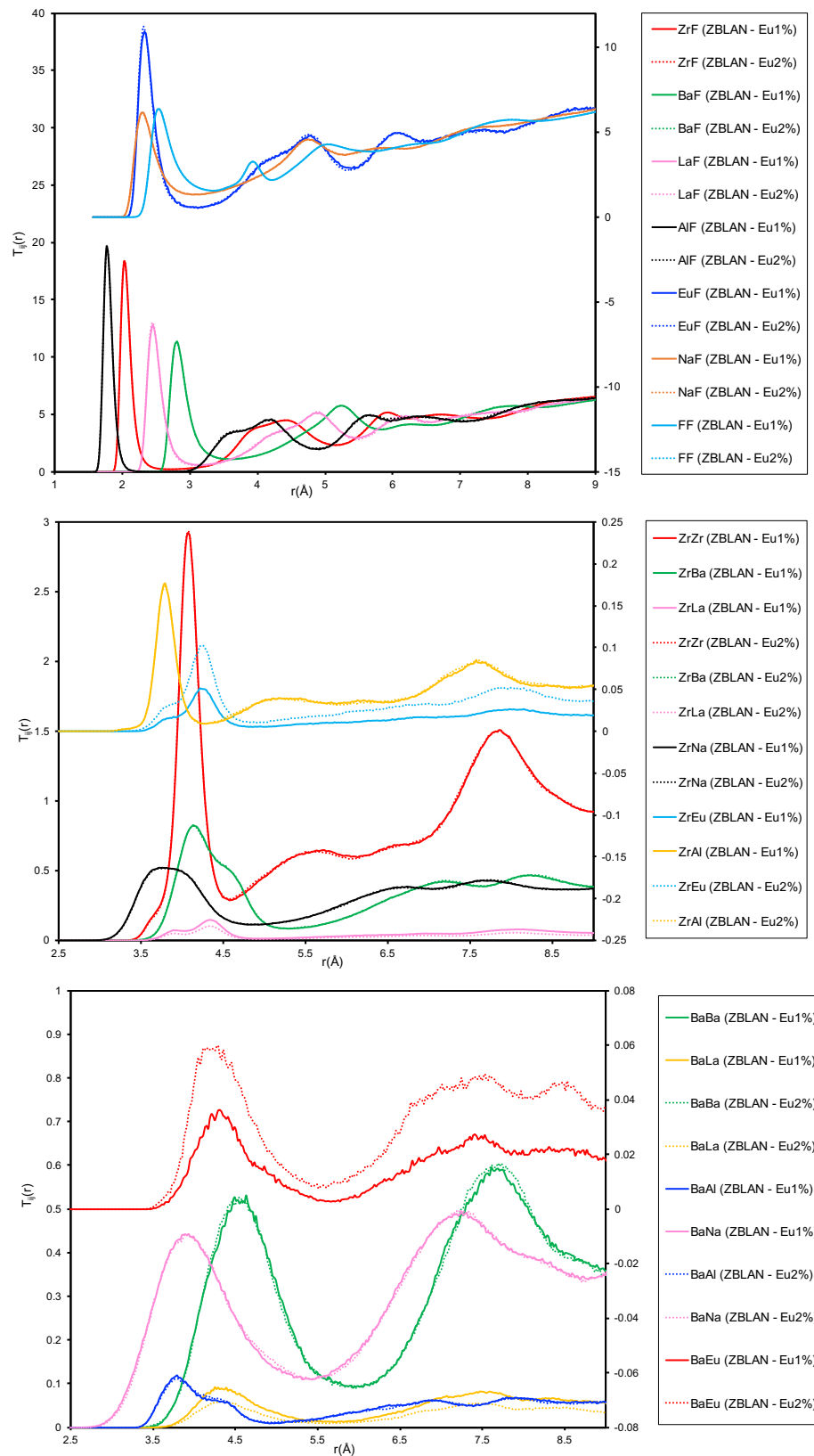


Figure 7.15 T_{ij} for ZBLAN – Eu1% and ZBLAN – Eu2% glass models. Top figure shows T_{ZrF} , T_{BaF} , T_{AlF} , T_{LaF} , T_{NaF} , T_{EuF} and T_{FF} , middle figure shows T_{ZrZr} , T_{ZrBa} , T_{ZrAl} , T_{ZrLa} , T_{ZrNa} and T_{ZrEu} , and bottom figure shows T_{BaBa} , T_{BaAl} , T_{BaLa} , T_{BaNa} and T_{BaEu} .

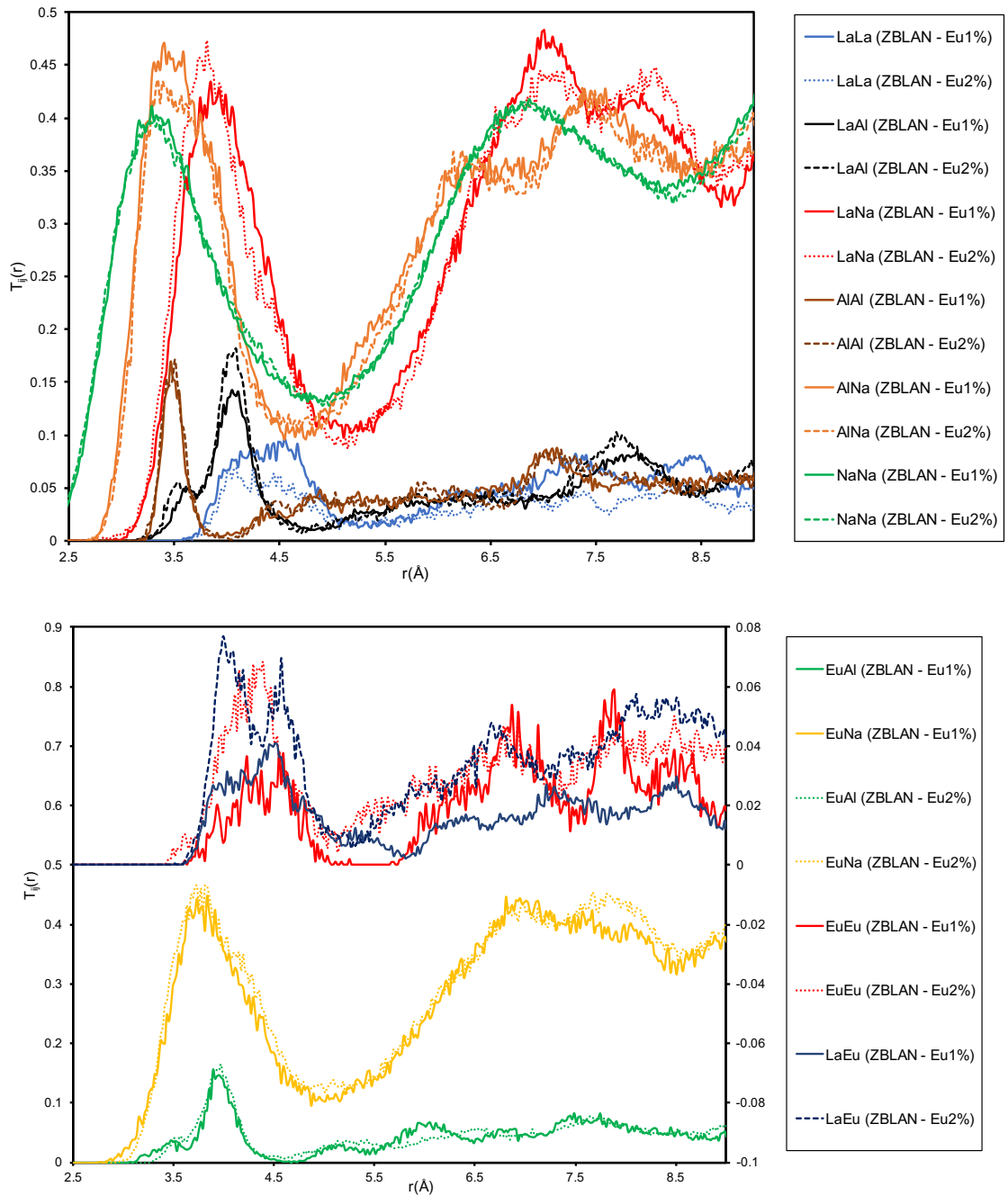


Figure 7.16 T_{ij} for ZBLAN – Eu 1% and ZBLAN – Eu 2% glass models. Top figure shows T_{LaLa} , T_{LaAl} , T_{LaNa} , T_{AlAl} , T_{AlNa} and T_{NaNa} , and bottom figure shows T_{EuEu} , T_{EuAl} , T_{EuNa} , and T_{LaEu} .

The prominent first peaks of $T_{ZrF}(r)$, $T_{BaF}(r)$, $T_{LaF}(r)$, $T_{AlF}(r)$, $T_{NaF}(r)$ and $T_{EuF}(r)$ provide the average bond length or the short-range order and the area under this curve determines the coordination number which are given in Tables 7.13 – 7.18. The partial functions $T_{FF}(r)$ in all the glass models have primary peaks at 2.54 – 2.57 Å indicating $F - Zr - F$ average nearest neighbour distances in ZrF_n polyhedra structures, and the second and third peaks are 3.93 – 3.95 Å and 5.03 – 5.09 Å respectively. These two secondary peaks include the average nearest neighbours' distances for $F - Ba - F$ in BaF_n polyhedra. The first peaks of $Zr - F$ and $Al - F$ correlation are narrower and reach to zero value after the first peak where as for other cations the first peaks are wider and it does not reach to zero value. This corresponds with the role of Zr and Al as network formers and the role of Ba , La and Na as network modifiers.

The $T_{ij}(r)$ where i is Zr and j are either Ba , La , Al or Na has average nearest neighbouring distances between 3.81 – 4.33 Å. There are peaks between 3.61 – 5.49 Å, 3.27 – 4.83 Å and 2.91 – 5.27 Å for T_{BaLa} , T_{BaAl} and T_{BaNa} respectively. Similarly, for T_{LaAl} , T_{LaNa} and T_{AlNa} primary peaks are between 3.31 – 4.73 Å, 3.03 – 5.17 Å and 2.91 – 4.53 Å respectively. These partial correlations indicate the non-bridging fluorides in the glass structures because it involves Ba , La , or Na . The exception is $Zr - Al$ which is bridging fluorine.

The partial correlations T_{ZrEu} and T_{BaEu} in the Eu^{3+} doped ZBLAN glasses has average neighbouring distances roughly at 4.19 Å and 4.29 Å (see Figure 7.15) respectively. There are prominent peaks between 3.63 – 4.97 Å, 3.07 – 4.49 Å and 3.05 – 4.89 Å for T_{LaEu} , T_{EuAl} and T_{EuNa} (see Figure 7.16) respectively.

Table 7.13 Average $Zr - F$ and $Zr - Zr$ nearest neighbour distance, R_{ij} , and coordination number, N_{ij} , for ZBLAN glasses and with Eu^{3+} doping. The cutoff distances were 2.75 Å and ~ 4.57 Å for N_{ZrF} and N_{ZrZr} .

Glass Models	R_{ZrF} (Å)	N_{ZrF}	R_{ZrZr} (Å)	$ZrZr$ < n > Model	N_{ZrZr} PDF
ZBA	2.03	7.35	4.1	4.40	4.20
ZBL	2.03	7.41	4.1	4.38	4.20
ZBN	2.03	7.53	4.1	4.15	4.12
ZBLA	2.05	7.35	4.1	3.89	3.81
ZBLAN	2.03	7.52	4.1	4.37	4.26
ZBLAN - Eu 1%	2.03	7.55	4.1	4.42	4.32
ZBLAN - Eu 2%	2.03	7.52	4.1	4.40	4.32

Table 7.14 Average $Ba - F$ and $Ba - Ba$ nearest neighbour distance, R_{ij} , and coordination number, N_{ij} , for ZBLAN glasses and with Eu^{3+} doping. The cutoff distances were 3.3 Å, 6.0 Å and 5.3 Å for N_{BaF} , N_{BaBa} and N_{ZrBa} respectively.

Glass Models	R_{BaF} (Å)	N_{BaF}	R_{BaBa} (Å)	$BaBa$ < n > Model	N_{BaBa} PDF	R_{ZrBa} (Å)	N_{ZrBa} PDF
ZBA	2.82	10.09	4.61	6.62	4.05	4.39	3.51
ZBL	2.83	10.60	4.57	7.07	4.34	4.31	4.10
ZBN	2.83	10.98	4.63	6.43	3.97	4.31	3.70
ZBLA	2.83	10.17	4.61	7.12	4.63	4.33	4.15
ZBLAN	2.83	10.91	4.67	5.25	2.90	4.33	2.80
ZBLAN - Eu 1%	2.83	10.89	4.57	5.24	2.89	4.31	2.80
ZBLAN - Eu 2%	2.83	10.88	4.57	5.27	2.87	4.31	2.80

Table 7.15 Average $Al - F$ and $Al - Al$ nearest neighbour, R_{ij} , and coordination number, N_{ij} , for ZBLAN glasses and with Eu^{3+} doping. The cutoff distances were 2.5 Å and 4.0 Å for N_{AlF} and N_{AlAl} .

Glass Models	R_{AlF} (Å)	N_{AlF}	R_{AlAl} (Å)	$AlAl$ < n > Model	N_{AlAl} PDF
ZBA	1.79	5.95	3.53	0.55	0.54
ZBLA	1.79	5.99	4.09	0.14	0.14
ZBLAN	1.79	5.99	3.47	0.21	0.18
ZBLAN - Eu 1%	1.79	5.99	3.47	0.16	0.15
ZBLAN - Eu 2%	1.79	5.97	3.49	0.17	0.16

Table 7.16 Average $La - F$ and $La - La$ nearest neighbour distance, R_{ij} , and coordination number, N_{ij} , for ZBLAN glassed and with Eu^{3+} doped. The cutoff distances were 3.1 Å and 5.3 Å for N_{LaF} and N_{LaLa} .

Glass Models	R_{LaF} (Å)	N_{LaF}	R_{LaLa} (Å)	$LaLa$ < n > Model	N_{LaLa} PDF
ZBL	2.47	9.04	4.49	0.54	0.40
ZBLA	2.47	8.72	4.27	0.67	0.45
ZBLAN	2.47	9.24	4.43	0.79	0.58
ZBLAN - Eu 1%	2.47	9.25	4.55	0.57	0.40
ZBLAN - Eu 2%	2.47	9.04	4.35	0.38	0.26

Table 7.17 Average $Na - F$ and $Na - Na$ nearest neighbour distance, R_{ij} , and coordination number, N_{ij} , for ZBLAN glasses and with Eu^{3+} doping. The cutoff distances were 3 Å and 5.0 Å for N_{NaF} and N_{NaNa} .

Glass Models	R_{NaF} (Å)	N_{NaF}	R_{NaNa} (Å)	$NaNa$ < n > Model	N_{NaNa} PDF
ZBN	2.33	6.95	3.39	3.21	2.55
ZBLAN	2.35	6.92	3.41	2.73	2.13
ZBLAN - Eu 1%	2.33	7.0	3.35	2.78	2.16
ZBLAN - Eu 2%	2.33	7.15	3.35	2.79	2.17

Table 7.18 Average $Eu - F$ and $Eu - Eu$ nearest neighbour distance, R_{ij} , and coordination number, N_{ij} , for ZBLAN glasses and with Eu^{3+} doping. The cutoff distances were 3 Å and 5.2 Å for N_{EuF} and N_{EuEu} .

Glass Models	R_{EuF} (Å)	N_{EuF}	R_{EuEu} (Å)	$EuEu$ < n > Model	N_{EuEu} PDF
ZBLAN - Eu 1%	2.33	8.34	4.37	0.13	0.10
ZBLAN - Eu 2%	2.33	8.24	4.35	0.26	0.22

7.3.2 Bond angle distribution functions

The bond angle distribution functions (BAD) between $j - i - j$ where j is fluoride ion and i are the cations of Zr or Ba or La or Al or Na or Eu are shown in Figure 7.17. The BAD when i is Zr (or Al) has two well separated peaks, primary at 75° (or 89°) degree and secondary at 141° (or 173°) respectively. There is a strong minimum at 103° for $F - Zr - F$ and $F - Al - F$ has zero probability between 120° and 150° . We associated these type of BAD with the role of network former.

The BAD for other cations of Ba , La and Eu has a similar shape with the two main peaks, primary peaks at 53° , 67° and 68° respectively, and secondary peaks at 107° , 125° and 135° respectively. These peaks are much broader than those for $F - Zr - F$ and there is less deep minimum at 81° , 101° and 103° for Ba , La and Eu respectively. The BAD for Na cation have main peak at 65° with a very shallow minimum at 101° before secondary peak at 123° .

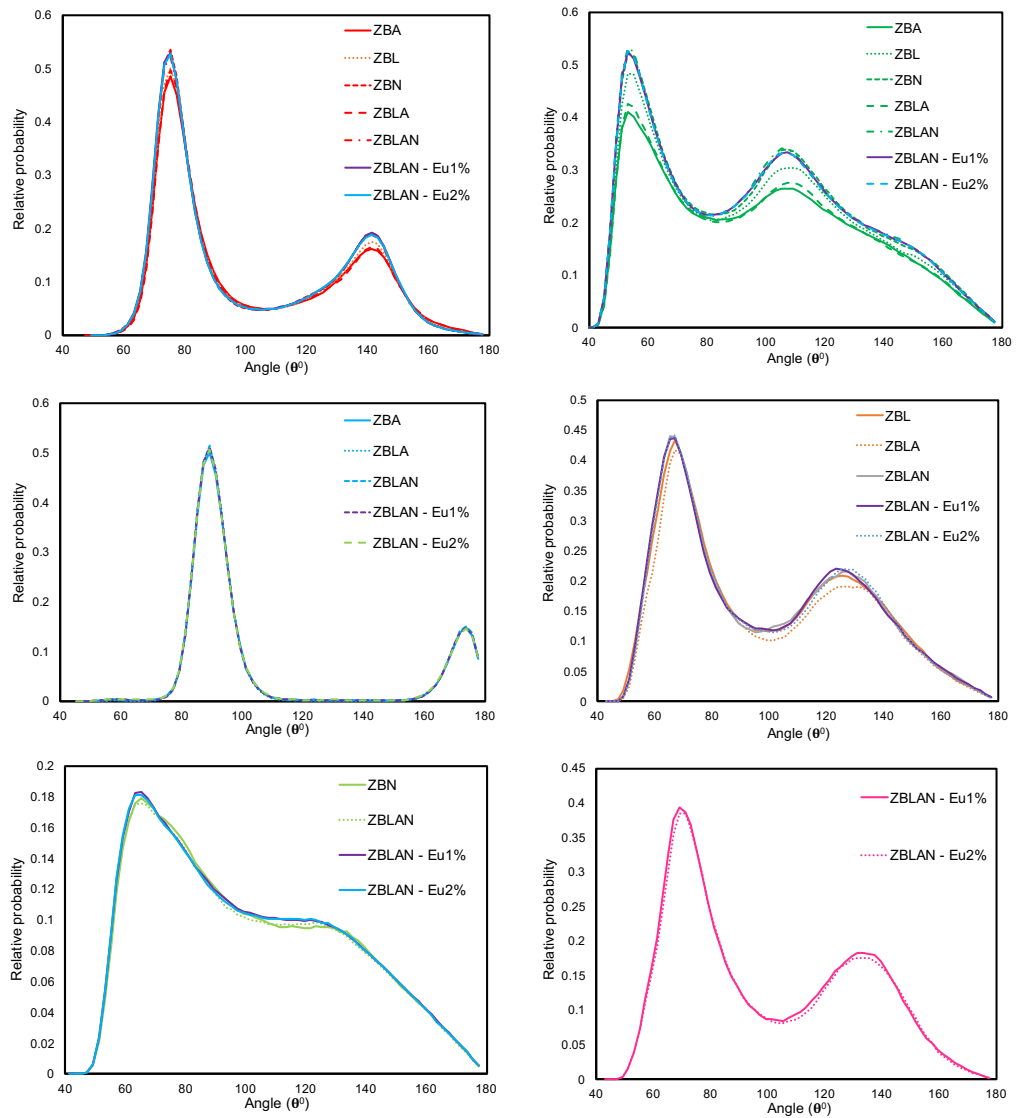


Figure 7.17 The BAD of glasses (*top-left*) $F - \text{Zr} - F$, (*top-right*) $F - \text{Ba} - F$, (*middle-left*) $F - \text{Al} - F$, (*middle-right*) $F - \text{La} - F$, (*bottom-left*) $F - \text{Na} - F$ and (*bottom-right*) $F - \text{Eu} - F$.

7.3.3 Network connectivity

Figure 7.18 shows $i - j - i$ connectivity per i where j is F and i is either Zr , Ba , La , Al , Na or Eu^{3+} cations for modelled glasses. The compositions in these glasses were between 50 – 62% for ZrF_4 and 20 – 34% for BaF_2 with addition of different compositions of other cations. Tables 7.13 and 7.14 show the average connectivity for Zr were roughly 4 and for Ba ranges from 5 to 7. Tables 7.15, 7.16 and 7.18 show the $i - j - i$

linkage per i for La , Al and Eu is distributed from 0 – 4 with very high proportion of 0 values due to lower concentration of these cations and hence this gives the average connectivity for these cations less than 1. For, $\text{Na} - \text{F} - \text{Na}$ the linkage per Na in Table 7.17 were roughly 3 reflecting compositions of 20 – 25% for NaF .

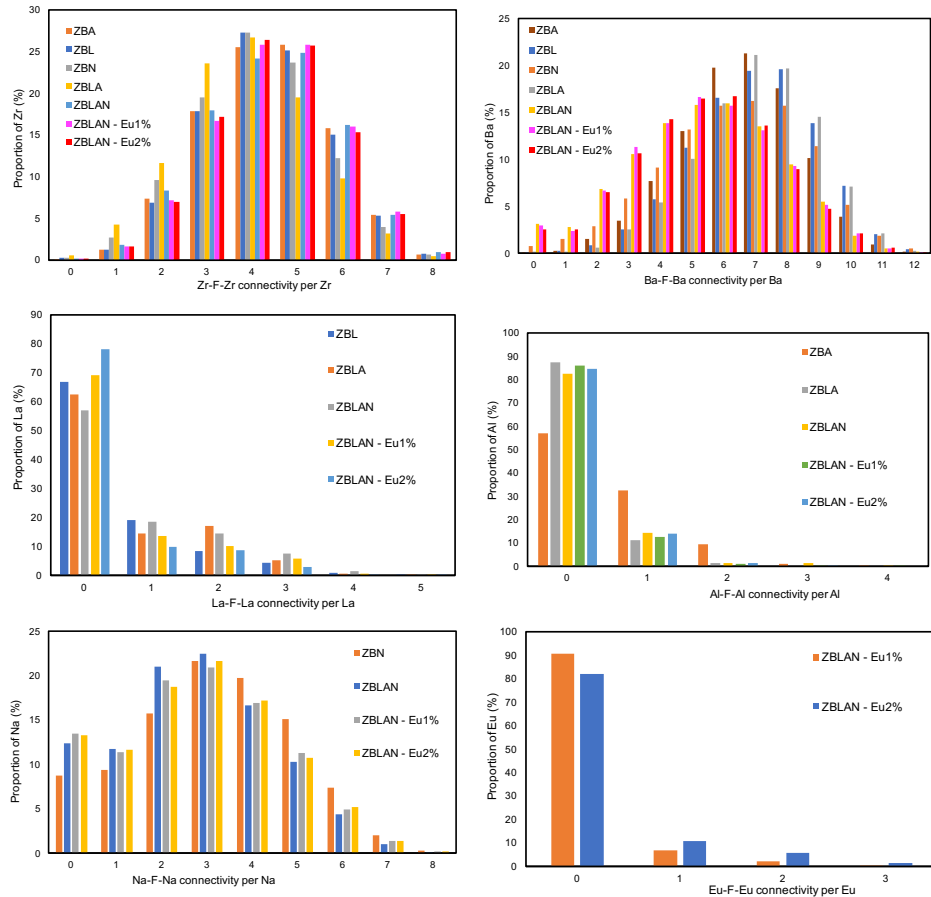


Figure 7.18 $\text{Zr} - \text{F} - \text{Zr}$ linkage per Zr (top-left), $\text{Ba} - \text{F} - \text{Ba}$ linkage per Ba (top-right), $\text{La} - \text{F} - \text{La}$ linkage per La (middle-left), $\text{Al} - \text{F} - \text{Al}$ linkage per Al (middle-right), $\text{Na} - \text{F} - \text{Na}$ linkage per Na (bottom-left) and $\text{Eu} - \text{F} - \text{Eu}$ linkage per Eu (bottom-right) for modelled glasses.

The average connectivity was computed by two methods mentioned in Chapter 2 (see section 2.6.4). The results were illustrated in Tables 7.13 – 7.18 that gives the average connectivity, $\langle n \rangle$, from the model i.e. by “xhst-hsc” and from PDF as a direct method. Furthermore, from these two results the corner sharing and edge sharing in $\text{Zr} - \text{F} - \text{Zr}$ and $\text{Ba} - \text{F} - \text{Ba}$ connectivity were computed using Equation 2.44 with the results given in

Table 7.19. Although the average connectivity is less than 1 for other cations La , Al and Eu the difference between the average connectivity calculated by the two methods were less than 0.7. This signified there are mixture of corner sharing and edge sharing networks in those cations except in $Al - F - Al$ with high corner sharing connectivity. The high corner sharing of Zr and Al is associated with their role as network formers.

Table 7.19 Percentage of majority corner sharing or edge sharing of $i - j - i$ connectivity glasses models where j are fluorine ions and i are cations.

Glass Model	$Zr - F - Zr$ % corner sharing	$Ba - F - Ba$ % edge sharing	$Na - F - Na$ % corner sharing	$La - F - La$ % edge sharing	$Al - F - Al$ % corner sharing	$Eu - F - Eu$ % corner sharing
ZBL	91.78	77.23	-	51.85	-	-
ZBA	90.91	77.64	-	-	96.36	-
ZBN	98.55	76.52	58.88	-	-	-
ZBLA	95.89	69.94	-	65.67	100	-
ZBLAN	94.97	89.52	56.04	53.16	71.43	
ZBLAN - Eu 1%	95.48	89.69	55.40	59.65	87.50	53.85
ZBLAN - Eu 2%	96.36	91.08	55.56	63.16	88.24	69.23

7.3.4 X-ray diffraction structure factor for ZBLA and ZBLAN glasses

The only X-ray diffraction experimental data in the literature were for ZBLA [16] and ZBLAN [17] glasses. The structure factors $[S(Q) - 1]$ for ZBLA glass model is shown in the top of Figure 7.19, which computed from T_{ij} by using Equation 2.68 and it is compared with the experiment data. The total pair distribution function, $T(r)$, for undoped ZBLAN glass [17] is compared with the ZBLAN model that is computed by using equation, $T(r) = \sum_{ij} w_{ij} T_{ij}(r)$, where w_{ij} are weighting factor for XRD explained in Equation 2.71.

There are fair agreements on the both comparisons although ZBLA glass model and experiment have slightly different compositions between them.

The total pair distribution function of reported ZBLAN glass shows first peak at 2.07 Å which complements the model result and is due to the $\text{Zr} - \text{F}$ correlation and the second peak at 2.62 Å are mostly due $\text{F} - \text{F}$ and $\text{Ba} - \text{F}$ due to their high content. However, the model clearly shows more detailed peaks at 2.50 Å and 2.79 Å which are due to $\text{La} - \text{F}$, $\text{F} - \text{F}$ and $\text{Ba} - \text{F}$ respectively. That model does not clearly show the contribution of high content of $\text{Na} - \text{F}$ correlation at 2.35 Å due to low X-ray scattering power of Na although it seems to contribute the experiment result.

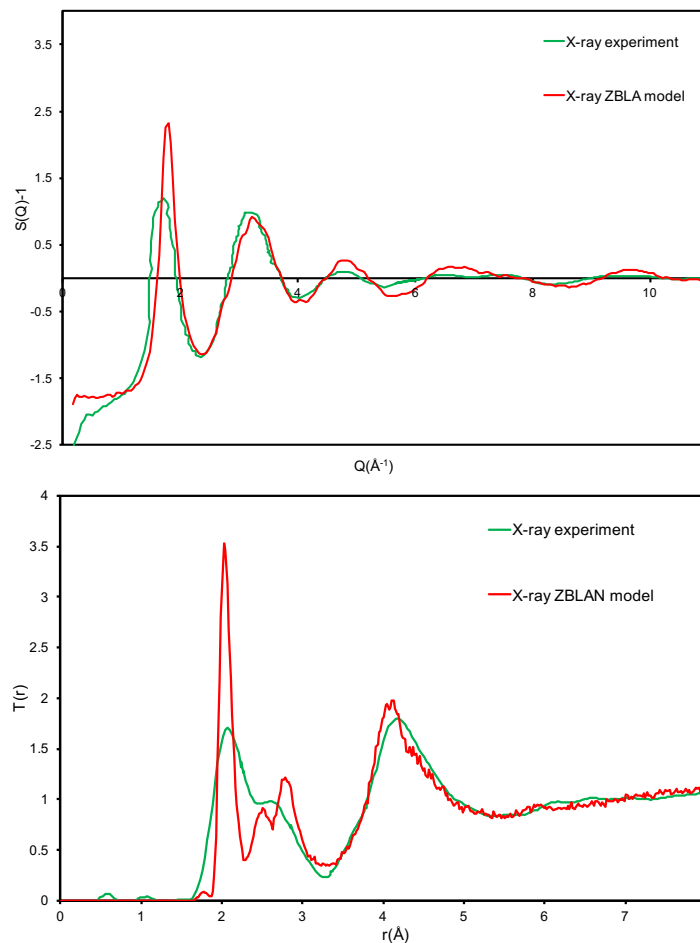


Figure 7.19 X-ray diffraction structure factor for ZBLA glass model and experiment [16] (*top*) and the total pair distribution functions, $T(r)$, for ZBLAN glass obtained from experiment [17] compared with the model glass (*bottom*).

7.3.5 Rotational invariants for Zr , Ba , La , Al , Na and Eu cations in ZBLAN and Eu^{3+} doped ZBLAN glasses

The calculation of rotational invariants, Q_l , as described in Chapter 3 has been carried out for all the cations involved in these model glasses. Most of these cations in the glasses don't seem to have well-defined single coordination numbers and their percentage mixtures of coordination numbers are illustrated in Tables 7.20 – 7.21. The exception is AlF_n polyhedra which gave well-defined single $CN = 6$. The percentage mixture of CN for the cations varies between the glasses. The average coordination number for ZrF_n polyhedra for ZBL , ZBA and $ZBLA$ glasses has high percentage of $CN = 7$ and for ZBN , $ZBLA$, $ZBLAN$ and Eu^{3+} doped ZBLAN glasses has high percentage of $CN = 8$. For BaF_n polyhedra in ZBA and $ZBLA$ glasses there is a has high percentage of $CN = 10$ and others glasses have a high percentage of $CN = 11$. However, for NaF_n , EuF_n and LaF_n , polyhedra, all the glasses have high percentage of $CN = 7$, 8 and 9 respectively.

Table 7.20 Percentage mixtures CN for $Zr - F$, $Ba - F$ and $Al - F$ for model glasses.

Model Glasses	% Zr $CN 7$	% Zr $CN 8$	% Ba $CN 9$	% Ba $CN 10$	% Ba $CN 11$	% Ba $CN 12$	% Al $CN 6$
<i>ZBL</i>	53.5	43.3	14.2	30.3	33.0	15.2	96.32
<i>ZBA</i>	57.1	38.0	22.5	34.4	24.1	9.4	98.88
<i>ZBN</i>	46.0	51.6	8.5	26.3	36.7	21.2	97.38
<i>ZBLA</i>	59.1	36.8	21.7	33.0	26.3	10.0	98.90
<i>ZBLAN</i>	46.1	51.0	9.2	26.0	34.1	22.2	97.38
<i>ZBLAN - Eu 1%</i>	44.4	53.0	9.4	26.7	34.4	21.2	97.06
<i>ZBLAN - Eu 2%</i>	45.5	52.0	9.7	26.3	34.4	22.1	96.03

Table 7.21 Percentage mixtures CN for $\text{La} - \text{F}$, $\text{Na} - \text{F}$ and $\text{Eu} - \text{F}$ for model glasses.

Model Glasses	% La CN 8	% La CN 9	% La CN 10	% Na CN 6	% Na CN 7	% Na CN 8	% Eu CN 7	% Eu CN 8	% Eu CN 9
ZBL	30.78	51.20	15.65	-	-	-	-	-	-
ZBN	-	-	-	26.3	36.7	21.2	-	-	-
ZBLA	32.86	51.62	9.96	-	-	-	-	-	-
ZBLAN	21.25	51.41	23.72	27.16	37.01	21.10	-	-	-
ZBLAN – Eu 1%	21.25	51.41	24.37	25.89	36.86	22.64	10.99	47.91	36.50
ZBLAN – Eu 2%	22.00	51.15	23.41	26.07	36.25	22.12	12.61	51.05	32.98

Figures 7.20 - 7.22 display the average values of Q_l for $l = 0$ to 10 for the cations polyhedra found in all the glass structures. Apart from this, Q_l were calculated for $CN = 7$ and 8 for ZrF_n polyhedra, $CN = 10, 11$ and 12 for BaF_n polyhedra, $CN = 8, 9$ and 10 for LaF_n polyhedra, $CN = 6, 7$ and 8 for NaF_n polyhedra, and $CN = 8$ and 9 for EuF_n polyhedra. Additionally, for ZBA and ZBLA glasses the Q_l for $CN = 9$ for BaF_n polyhedra were calculated as those glasses had mixture of CN mostly between 9 – 11. The rotational invariant results show that the structures of these cation fluorine polyhedra in these multicomponent fluorozirconate glasses do not change with the compositions. The uncertainty in the average values of Q_l for glasses were ± 0.05 (one standard deviation).

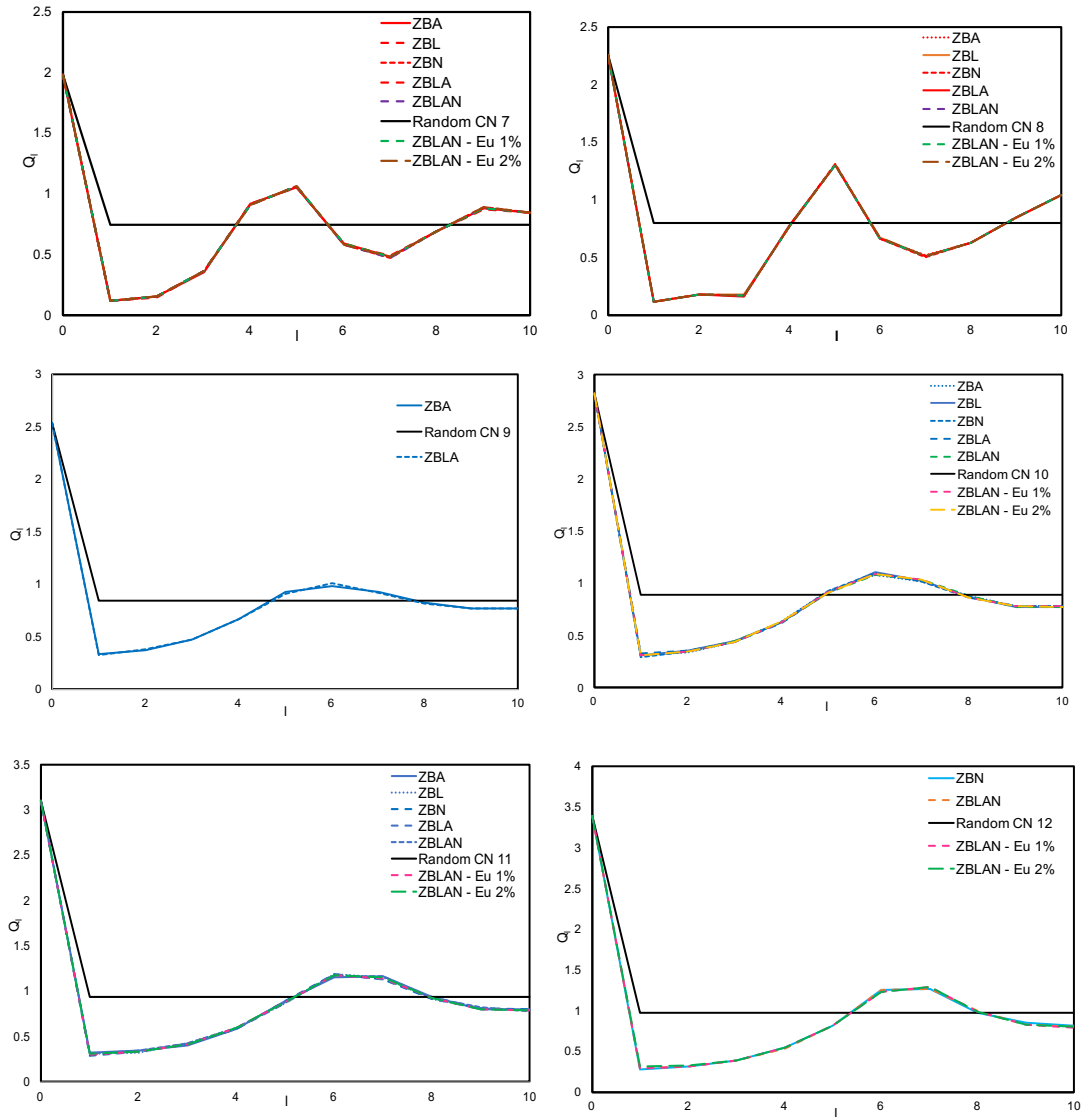


Figure 7.20 The average Q_l values for $l = 0$ to 10 for ZrF_n polyhedra for $\text{CN} = 7$ (top-left) and 8 (top-right), and BaF_n polyhedra for $\text{CN} = 9$ (middle-left), 10 (middle-right), 11 (bottom-left) and 12 (bottom-right) in multicomponent fluorozirconate glasses.

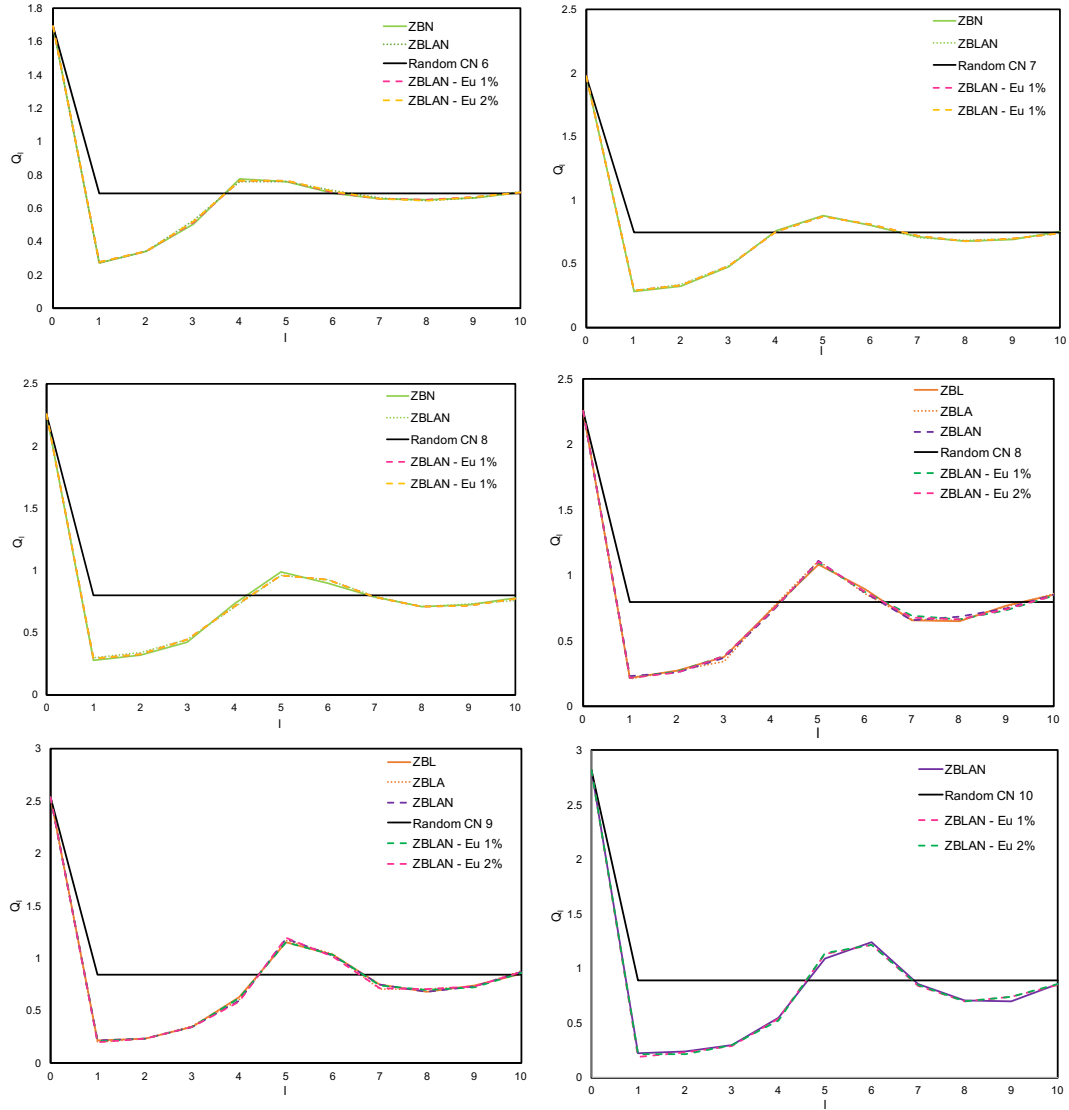


Figure 7.21 The average Q_l values for $l = 0$ to 10 for NaF_n polyhedra for $\text{CN} = 6$ (top-left), 7 (top-right) and 8 (middle-left), and LaF_n polyhedra for $\text{CN} = 8$ (middle-right), 9 (bottom-left) and 10 (bottom-right) in multicomponent fluorozirconate glasses.

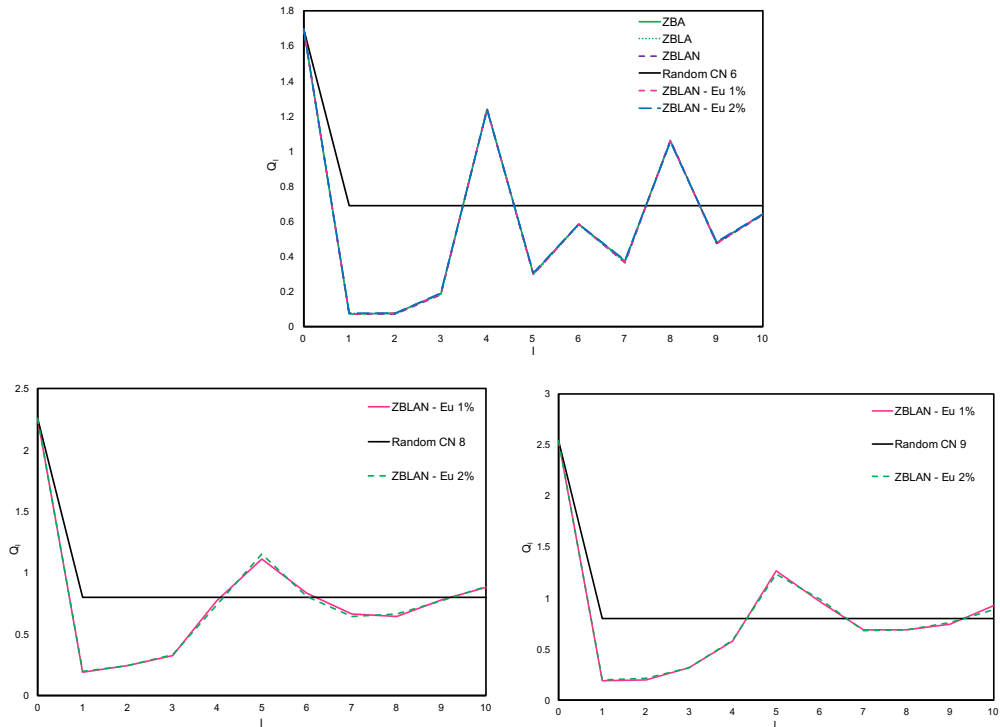


Figure 7.22 The average Q_l values for $l = 0$ to 10 for AlF_n polyhedra for $CN = 6$ (top), and EuF_n polyhedra for $CN = 8$ (bottom-left) and 9 (bottom-right) in multicomponent fluorozirconate glasses.

The results comparing the average values of Q_l for $l = 0$ to 10 for the different cations with the similar coordination numbers are displayed in Figures 7.23 to 7.25. Furthermore, it shows the comparison of Q_l values between all the possible references convex polyhedra for vertices, $N = 6$ to 12, and the cations polyhedra from the model glasses. For the AlF_6 polyhedra the average value of Q_l is similar to Octahedron but for NaF_6 polyhedra the average value of Q_l for $l = 4$ to 10 is close to random values. The average Q_l for ZrF_7 polyhedra and Augmented Triangular Prism very similar but for NaF_7 polyhedra the Q_l for $l = 5$ to 10 values are close to random. In the case of ZrF_8 polyhedra the Q_l values are very close to that of Biaugmented Triangular Prism. In the case of LaF_8 and EuF_8 polyhedra Q_l results are very similar and they do not closely retain the shape of ZrF_8 polyhedra. On other hand NaF_8 polyhedra have broadly similar Q_l to LaF_8 and to EuF_8 but the Q_l values for $l = 5$ to 10 are closer to random values.

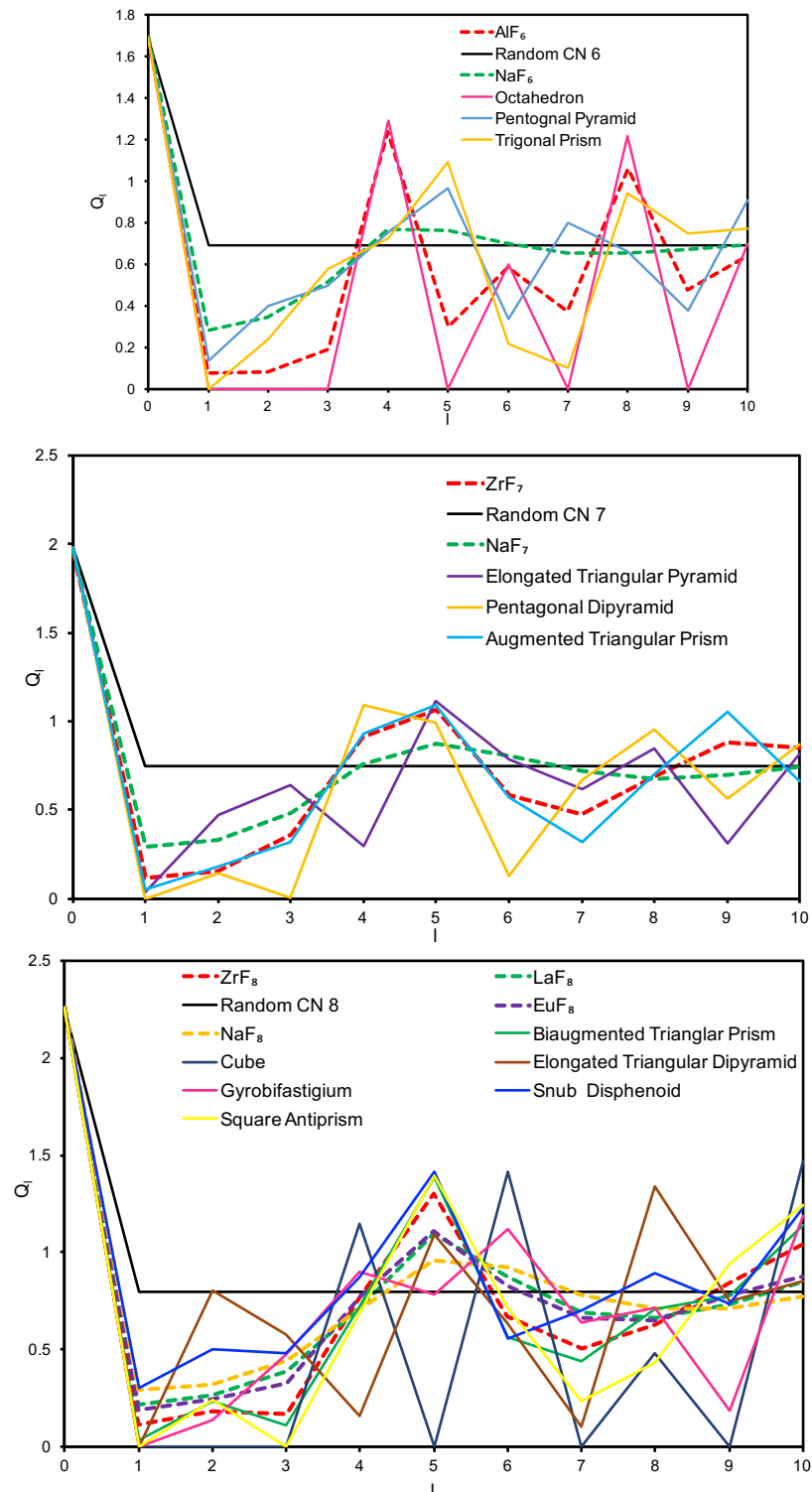


Figure 7.23 Rotational invariant Q_l of AlF_6 and NaF_6 polyhedra (top), ZrF_7 and NaF_7 polyhedra (middle), and ZrF_8 , LaF_8 and NaF_8 polyhedra (bottom) are compared with all possible reference convex polyhedra of vertices, $N = 6, 7$ and 8 respectively.

Figure 7.24 (*top*) displays the results of average values of Q_l for BaF_9 , LaF_9 and EuF_9 polyhedra. For LaF_9 and EuF_9 polyhedra the Q_l results are similar. However, BaF_9 polyhedra gave different Q_l values particularly for $l = 4$ to 10 which are closer to random values. The average Q_l values of Gyroelongated Square Pyramid and Triaugmented Triangular Prism are very similar from $l = 3$ to 10. Also EuF_9 and LaF_9 roughly retain the shape of these two polyhedra. The result of Q_l values for LaF_{10} and BaF_{10} polyhedra are shown in the Figure 7.24 (*bottom*) For BaF_{10} polyhedra the shape is flatter and closer to random compared to LaF_{10} mainly in Q_l values for $l = 4$ to 10.

The result of Q_l values for BaF_{11} polyhedra shown in Figure 7.25 (*top*) indicates that the shape does not match with any of the reference convex polyhedra with vertices, $N = 11$. However, the Q_l values for BaF_{11} polyhedra are close to Augmented Pentagonal Prism. For BaF_{12} polyhedra the Q_l result is shown in Figure 7.25 (*bottom*) compared with all the possible reference convex polyhedra for vertices, $N = 12$. The Q_l result of BaF_{12} is close to Sphenomegacorna and also retain the shape mainly in Q_l values for $l = 5$ to 10.

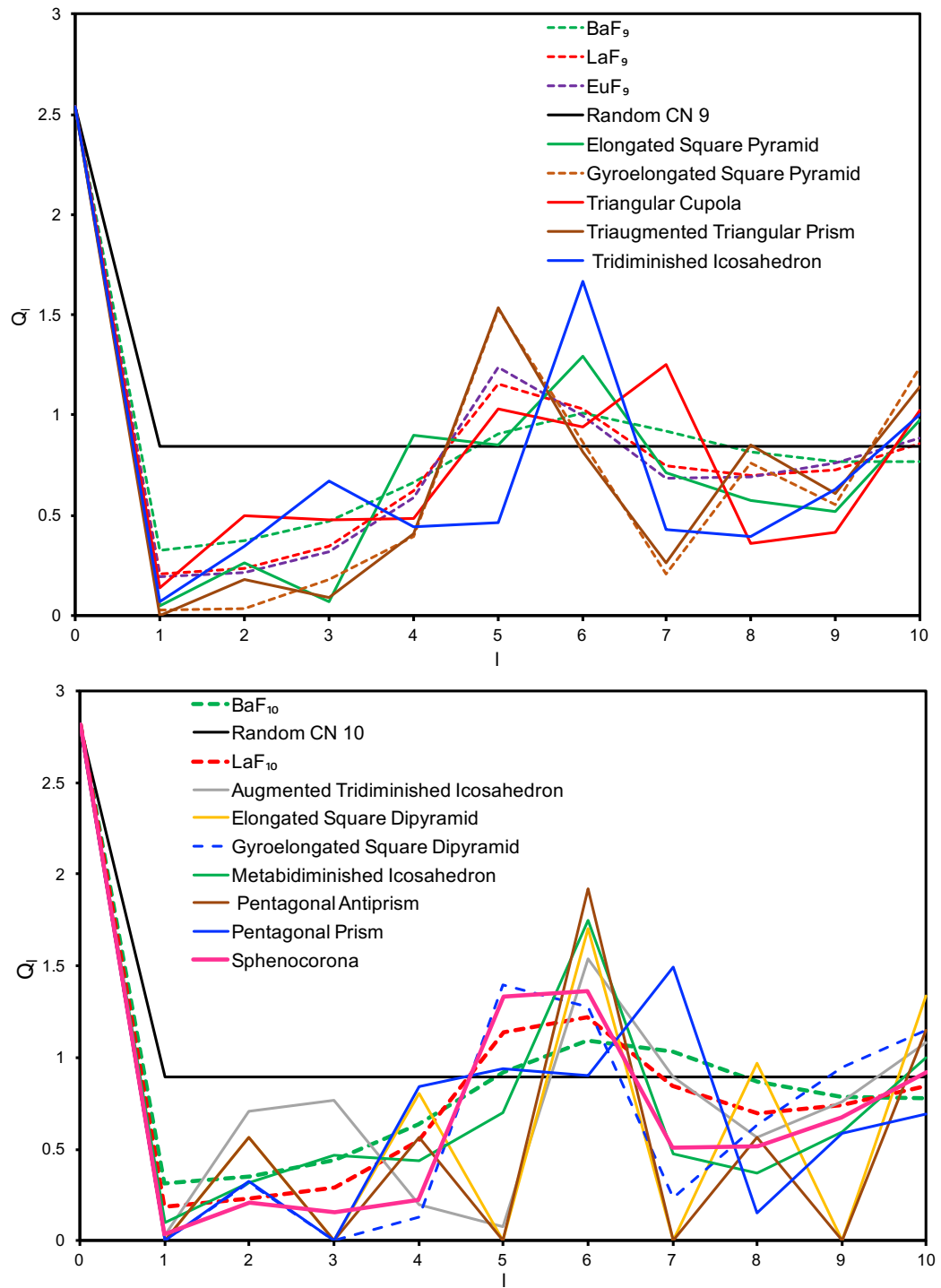


Figure 7.24 Rotational invariant Q_l of BaF_9 , LaF_9 and EuF_9 polyhedra (*top*), and BaF_{10} and LaF_{10} polyhedra (*bottom*) are compared with all possible reference convex polyhedra of vertices $N = 9$ and 10 respectively.

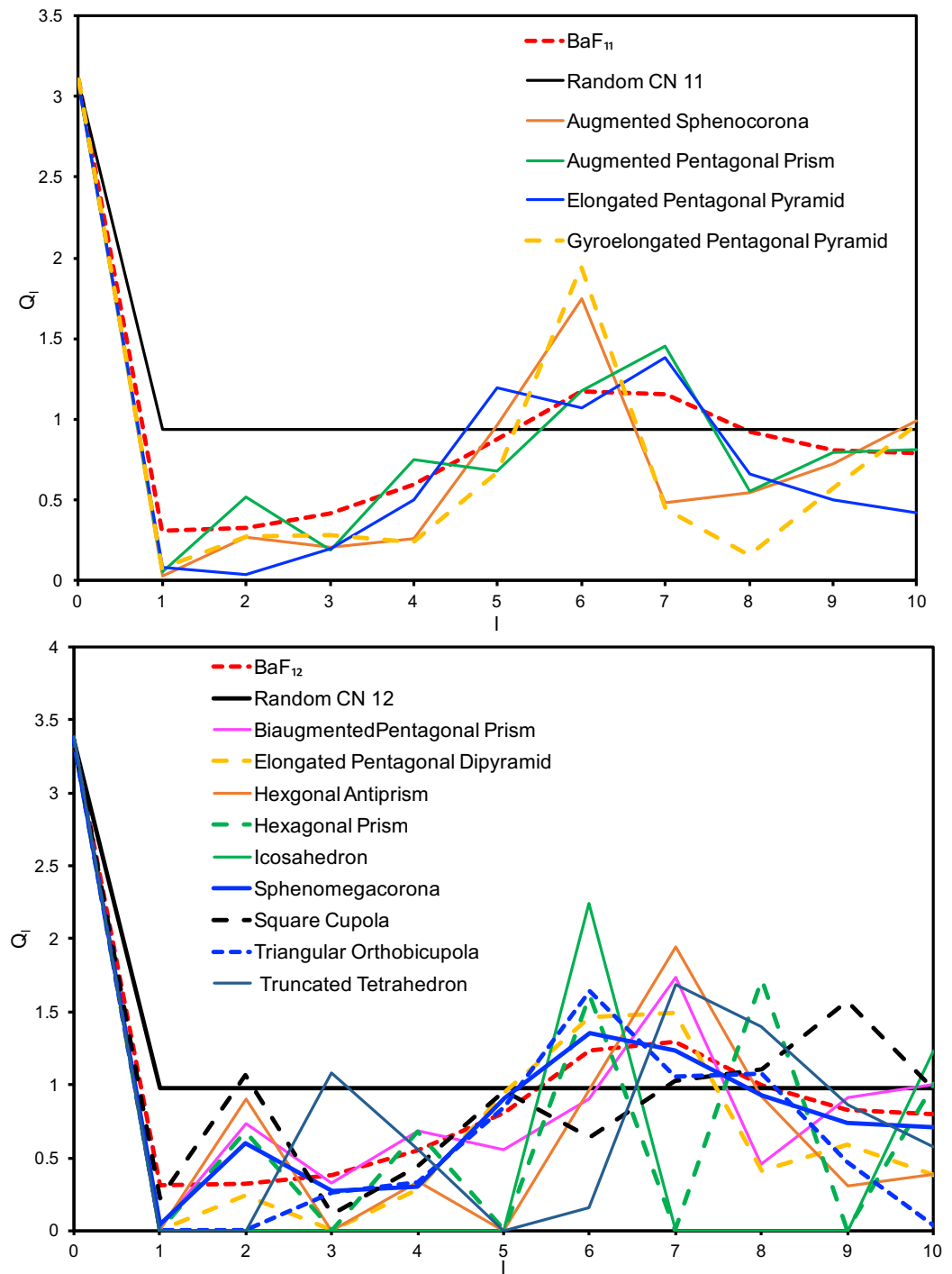


Figure 7.25 Rotational invariant Q_l of BaF_{11} polyhedra (top) and BaF_{12} polyhedra (bottom) are compared with all possible reference convex polyhedra of vertices, $N = 11$ and 12 respectively.

7.4 Discussion

The rigid ion potential parameters used to model these multicomponent fluorozirconate glasses initially tested in the crystal structures produce fair results. Tables 7.2 to 7.10 show that there is good agreement in short range order and the coordination number found in EuF_3 , LaF_3 , AlF_3 , NaF , $\text{Eu}_3\text{Zr}_3\text{F}_{15}$, $\text{Eu}_3\text{Ba}_4\text{F}_{17}$, $\beta - \text{EuNaF}_4$, $\text{NaBaZr}_2\text{F}_{11}$ and NaBaZrF_7 crystals. The biggest discrepancies were on the coordination numbers mainly for $\text{Eu} - \text{F}$ in $\text{Eu}_3\text{Ba}_4\text{F}_{17}$ crystal.

The similar results from the pair distribution functions and the bond angle distribution functions between Zr and Al suggest that Al act as network former. However, La and Na cations acts more of a modifier as their results are more similar to Ba cation. The multicomponent fluorozirconate glasses seems to retain the properties similar to binary ‘ ZB ’ glasses in term of short-range order and the coordination numbers for $\text{Zr} - \text{F}$ and $\text{Ba} - \text{F}$. The only slight differences are in the coordination numbers specially for $\text{Ba} - \text{F}$ which are slightly higher in multicomponent fluorozirconate glasses for ZBN , ZBLAN and Eu^{3+} doped ZBLAN glasses, i.e. with the Na cations added to the glass.

In the national chemical database, there was only $\text{NaBaZr}_2\text{F}_{11}$ and NaBaZrF_7 crystal found that are directly related to multicomponent fluorozirconate glasses. In addition, $\text{NaBaZr}_2\text{F}_{11}$ crystal has similar composition ($50\text{ZrF}_4 - 25\text{BaF}_2 - 25\text{NaF}$) with the ZBN model glass and their pair distribution functions were compared, which is illustrated in Figure 7.26. The similarity of the first peaks of $T_{\text{ZrF}}(r)$, $T_{\text{BaF}}(r)$, $T_{\text{FF}}(r)$ and $T_{\text{NaF}}(r)$ correlations imply a fair agreement at short-range order. However, ZBN glass has slightly lower coordination number for $\text{Zr} - \text{F}$ and slightly high coordination number for $\text{Na} - \text{F}$ than its related crystal. In terms of $\text{Zr} - \text{F} - \text{Zr}$ connectivity from $T_{\text{ZrZr}}(r)$, the crystal shows higher percentage of mixed edge sharing (61%) and corner sharing (38%) compared

to the ZBN glass where the connectivity is almost 99% corner sharing. Figure 7.26 also shows glass has more shorter distances for $\text{Na} - \text{Na}$ and $\text{Ba} - \text{Na}$ nearest neighbours.

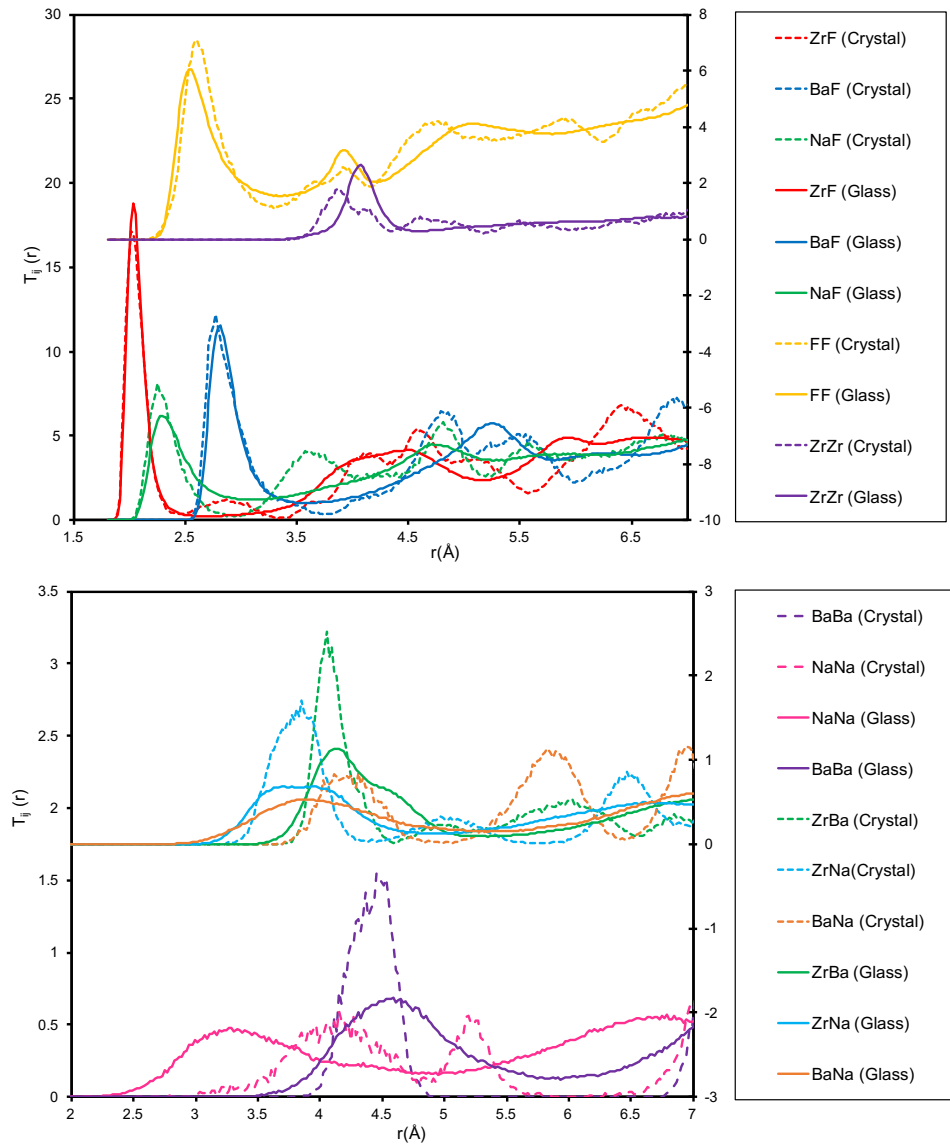


Figure 7.26 The comparison of $T_{ij}(r)$ between ZBN glass and its related $\text{NaBaZr}_2\text{F}_{11}$ crystal.

The comparison of T_{ij} between $\text{NaBaZr}_2\text{F}_{11}$ and NaBaZrF_7 crystals of the same system $\text{ZrF}_4 - \text{BaF}_2 - \text{NaF}$ in Figure 7.27 illustrates the slight change in short-range order and coordination numbers because of different amounts of ZrF_4 (see Tables 7.9 and 7.10).

The result also shows differences in cations nearest neighbour distances. The largest difference is in $\text{Zr} - \text{Zr}$ where nearest neighbour distances are very long for NaBaZrF_7 crystal which has less Zr than ZBN glass.

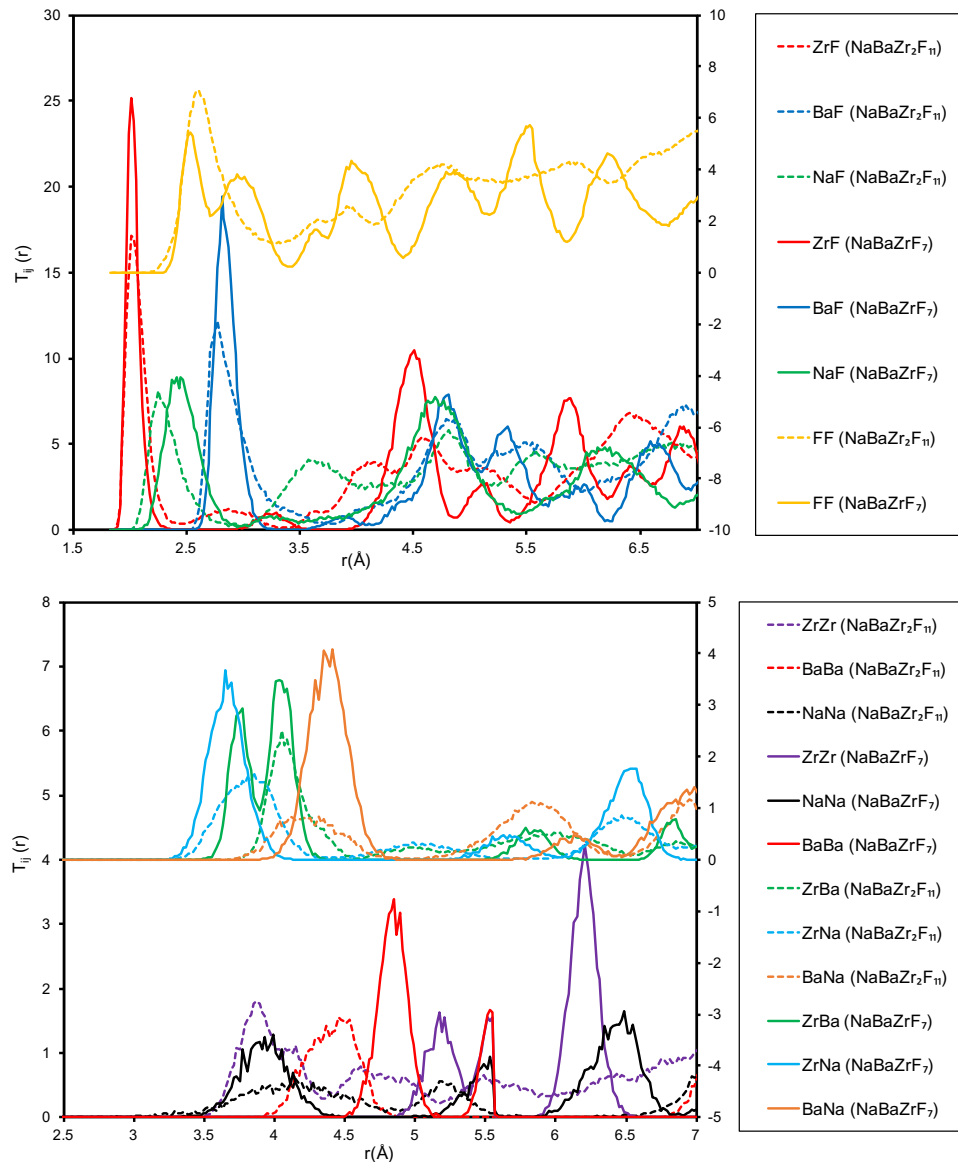


Figure 7.27 The comparison of $T_{ij}(r)$ between $\text{NaBaZr}_2\text{F}_{11}$ and NaBaZrF_7 crystal.

The result from the bond angle distribution functions suggested that Na and La cations in multicomponent fluorozirconate glasses act more like modifiers like Ba cations in the glass matrix. The BAD for ZBN glass was compared with its related similar composition $\text{NaBaZr}_2\text{F}_{11}$ crystal and with different composition NaBaZrF_7 crystal in Figure 7.28. It

shows that the crystal $\text{NaBaZr}_2\text{F}_{11}$ has similar trend to that of glass for $F - \text{Zr} - F$, $F - \text{Ba} - F$ and $F - \text{Na} - F$ bond angles.

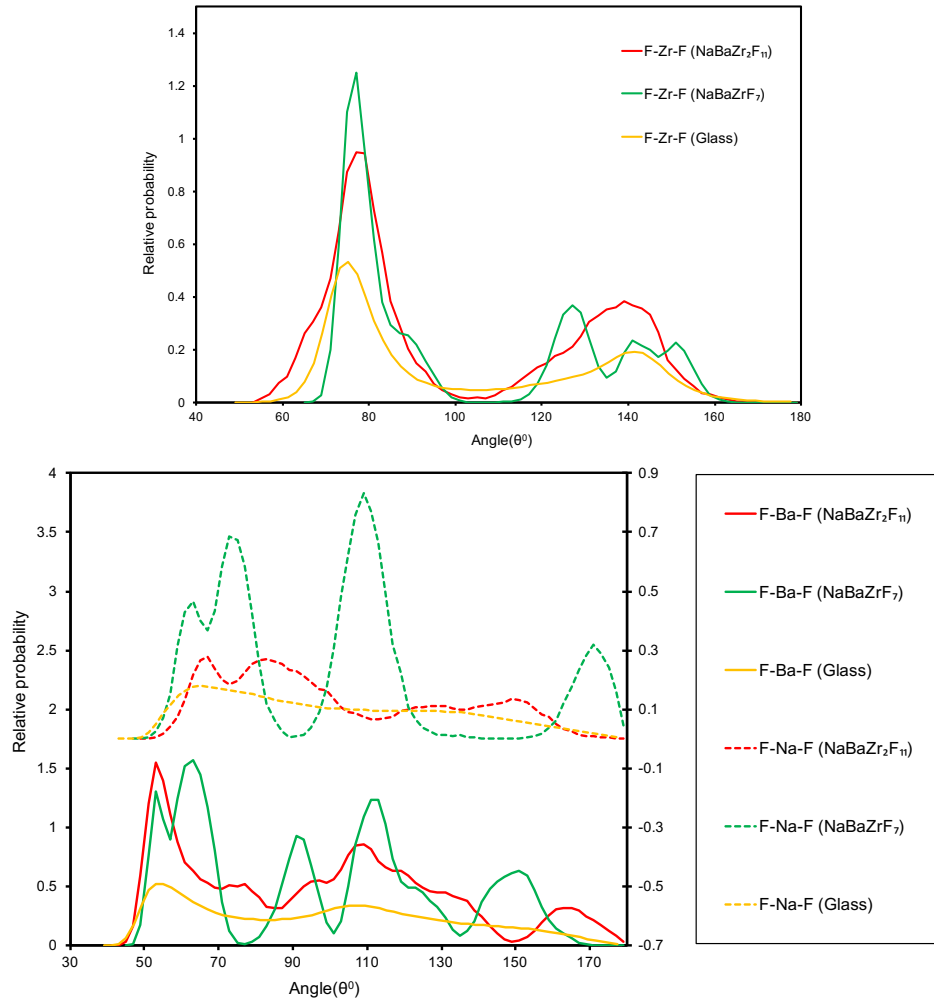


Figure 7.28 Comparison of the BAD between the ZBLN glass, its related $\text{NaBaZr}_2\text{F}_{11}$ crystal and different composition NaBaZrF_7 crystal. Top part of the figure shows BAD of $F - \text{Zr} - F$ and bottom part of the figure shows BAD of $F - \text{Ba} - F$ (*primary axis*) and $F - \text{Na} - F$ (*secondary axis*).

The Al cations are considered as the network former in the glass matrix where its average connectivity $\text{Al} - \text{F} - \text{Al}$ is less than 1 (see Figure 7.18). However, when the connectivity is calculated combining both network formers Zr and Al cations at cutoff 2.75 \AA , the average connectivity of Al increases approximately to 4 as expected due to the very high content of Zr cations, which is illustrated in Figure 7.29. Conversely, combining $\text{Zr} - \text{F} -$

Zr and $\text{Zr} - \text{F} - \text{Al}$ to get $\text{Zr} - \text{F} - \text{Zr}/\text{Al}$ as shown in Figure 7.29 there is only a slight increase in the average connectivity of Zr compared to the result from Figure 7.18 because of very low composition of Al in the glass matrix.

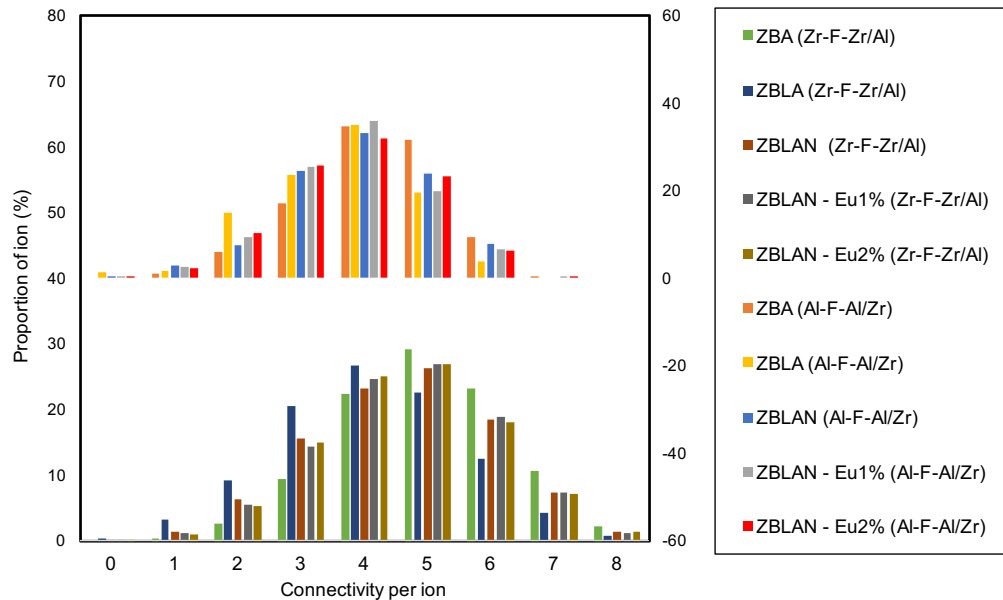


Figure 7.29 $\text{Zr} - \text{F} - \text{Zr}/\text{Al}$ linkage per Zr/Al (primary axis) and $\text{Al} - \text{F} - \text{Al}/\text{Zr}$ linkage per Al/Zr (secondary axis).

Similarly, the average connectivity for La , Na and Ba cations were calculated in combination as a modifier at the cutoff 3 \AA for La and Na , and 3.3 \AA for Ba . As expected there was increased in the average connectivity for La due to the high proportion of Na and Ba cations in the glass matrix as illustrated in Figure 7.30. The glass matrices have equal amount of Ba and Na but very less amount of La which will not much affect the high average connectivity for Ba and Na . The change in average connectivity for Na increases from ~ 3 to ~ 5.5 when they were calculated with other modifiers but for Ba it increases from 7 to 8.

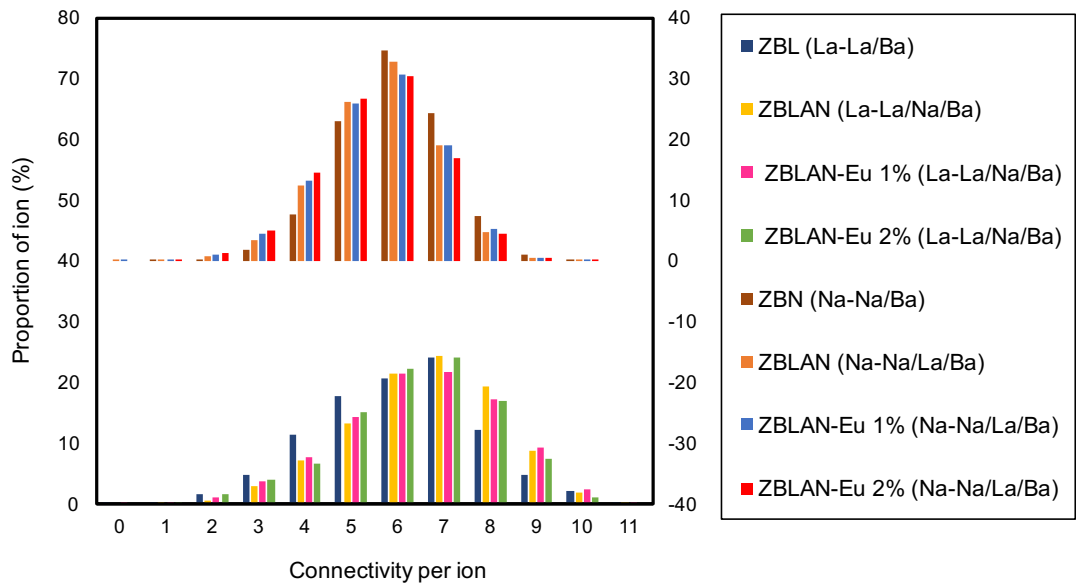


Figure 7.30 $\text{La} - \text{F} - \text{La}/\text{Na}/\text{Ba}$ linkage per $\text{La}/\text{Na}/\text{Ba}$ (primary axis) and $\text{Na} - \text{F} - \text{Na}/\text{La}/\text{Ba}$ linkage per $\text{Na}/\text{La}/\text{Ba}$ (secondary axis).

Zr and Ba cations retain their properties of connectivity $\langle n \rangle$ the same as in binary ‘ ZB ’ glasses. Zr is a network former with very high proportion of corner sharing and Ba is a modifier with high proportion of edge sharing. However, La and Na cations have mixture of edge and corner sharing as illustrated in Table 7.19. There is decrease in connectivity for Ba when its content is decreased and similarly in connectivity of Al when glass matrix is mixed with Na compositions.

For the binary $\text{ZrF}_4 - \text{BaF}_2$ system, the network connectivity, N_{ZrZr} , could have been predicted by the theory based on two types of fluorine. The ‘bridging’ F in $\text{Zr} - \text{F} - \text{Zr}$ and ‘non-bridging’ F in $\text{Zr} - \text{F} - \text{Ba}$. However, multicomponent fluorozirconate glasses have other types of fluorine which will not be included, e.g. the fluorine in $\text{Al} - \text{F} - \text{Al}$ and $\text{Al} - \text{F} - \text{Ba}$. Furthermore, in the binary ‘ ZB ’ glasses the connectivity $\langle n \rangle$ for Zr depends on F/Zr ratio. For e.g. ‘ ZB ’ glass with 60% ZrF_4 has F/Zr ratio 5.33 and has $N_{\text{ZrZr}} = 4.1$. Looking at the multicomponent fluorozirconate glasses the same way, the model glasses have ZrF_4 content between 50 to 62%. The corresponding F/Zr ratio is

between 5.3 to 5.6 and N_{ZrZr} from 3.9 to 4.4. There is slightly higher connectivity $\langle n \rangle$ in the multicomponent fluorozirconate glasses compared to binary ‘ZB’ glass with 60% ZrF_4 .

The structural study on ZBLA glass [16] and undoped ZBLAN glass [17] by X-ray diffraction reported $R_{ZrF} = 2.1 \text{ \AA}$ and $R_{BaF} = 2.7 \text{ \AA}$ that were similar to the model glass but R_{BaF} from [17] was 2.6 \AA . For the ZBLA glasses reported R_{BaBa} , R_{ZrBa} are shorter and R_{ZrZr} is longer than the model results. Whereas for ZBLAN glass the reported nearest neighbour distances for all of these cations were 4.1 \AA which are shorter than ZBLAN model results. The X-ray diffraction for praseodymium (Pr^{3+}) doped ZBLAN glass [17] also reported differential correlation functions for $Pr - F$ and these can be compared to $La - F$ since Pr and La have similar size. Besides, X-ray diffraction is based on high atomic number that is highly affected by Zr , Ba and La and less by F , Na and Al . But the reported first peak for $Pr - F$ is at 2.75 \AA which seems too long compared to 2.47 \AA for $La - F$ from the model.

The MD results [18] reported for 2% of Eu^{3+} doped ZBLAN glass compares well for the short-range order of $Zr - F$ and $F - F$ found by current glass models. However, results from [18] for bond length for $Ba - F$, $Eu - F$ and nearest neighbour distance for $Zr - Zr$ were shorter than results found in these current glass models. Consequently, the coordination numbers reported for $Ba - F$ and $Eu - F$ are lower as well. The previous very small model [18] has only used 393 atoms with cell length of 17.36 \AA but the current model has 78,600 atoms with cell length of 101.5 \AA which should be more reliable.

In terms of the $Zr:Ba$ ratio in the glass matrix, the higher $Zr:Ba$ ratio in ZBL, ZBA and ZBLA glasses have coordination numbers of 7.3 and 10.1 for $Zr - F$ and $Ba - F$. In contrast, for lower ratio $Zr:Ba$ in ZBN, ZBLAN and Eu^{3+} doped ZBLAN glasses which have Na added gave coordination numbers of 7.5 and 10.9 for $Zr - F$ and $Ba - F$. This

can be explained that by adding Na cations in the glass matrix increase the coordination of $\text{Zr} - \text{F}$ and $\text{Ba} - \text{F}$ as displayed in Table 7.20. However, in $\text{ZrF}_4 - \text{BaF}_2$ binary glass, the $\text{Zr} - \text{F}$ and $\text{Ba} - \text{F}$ coordination numbers were not affected by the $\text{Zr} : \text{Ba}$ ratio.

The Zr sites in these glasses are mainly in the mixture of ZrF_7 and ZrF_8 polyhedra, which were also seen in ‘ ZB ’ binary glasses. The ternary $\text{NaBaZr}_2\text{F}_{11}$ crystal also gave the mixture of $\text{CN} = 7$ and 8 for $\text{Zr} - \text{F}$ and its average Q_l values were compared with the ZBN glass model which is illustrated in Figure 7.31. It also shows that the glass and crystal average Q_l values are highly correlated to Augmented Triangular Prism and Biaugmented Triangular Prism respectively. This strongly suggests that in the glass the network former ZrF_n polyhedra retain its sites as in its related crystal. This is further supported by the results from AlF_6 polyhedra in the glass models where its average Q_l values are highly correlated to Octahedron (see Figure 7.23).

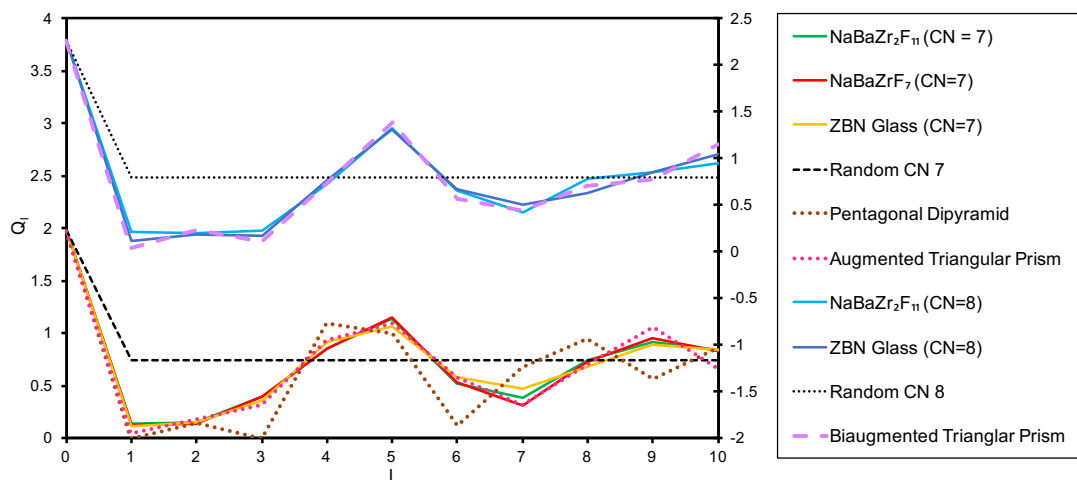


Figure 7.31 The Q_l values for ZrF_7 (primary axis) and ZrF_8 (secondary axis) polyhedra of ZBN glass with its related $\text{NaBaZr}_2\text{F}_{11}$ crystal and different composition NaBaZrF_7 crystal. These Q_l values are compared with reference polyhedra of vertices, $N = 7$ (Augmented Triangular Prism, Pentagonal Dipyramid) and $N = 8$ (Biaugmented Triangular Prism) respectively.

In contrast, modifier Ba cation sites in the glass are very different to that of its related crystals as illustrated in Figure 7.32 where BaF_{11} polyhedra for the crystal are much more

similar to Augmented Pentagonal Prism than the glass of related composition. This result can be further seen in the NaF_6 polyhedra between same composition of ZBN glass and crystal where the average Q_l values for crystal are much closer to Pentagonal Pyramid than the glass.

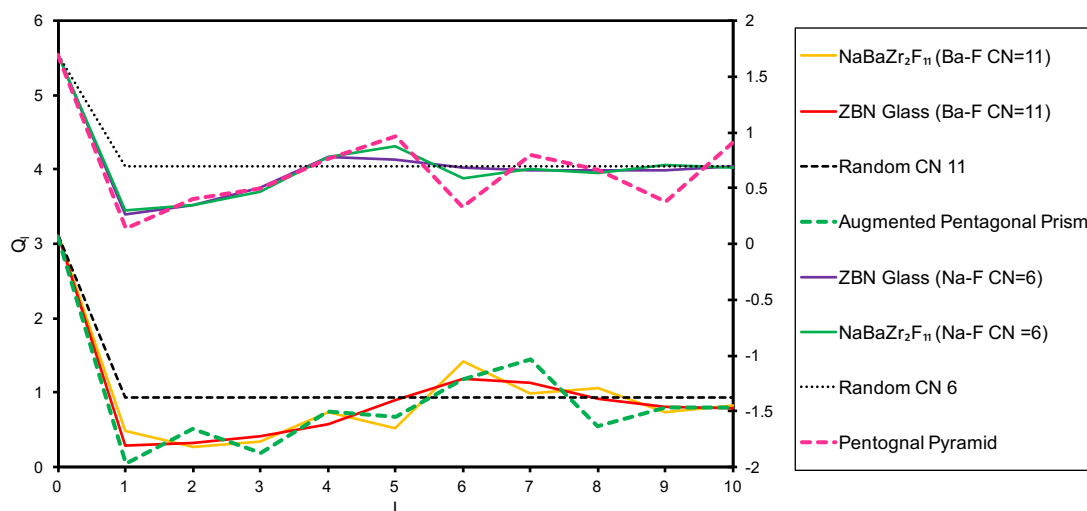


Figure 7.32 The Q_l of ZBN glass and its related $\text{NaBaZr}_2\text{F}_{11}$ crystal for BaF_{11} polyhedra (*primary axis*) and NaF_6 polyhedra (*secondary axis*) compared with the reference convex polyhedra Augmented Pentagonal Prism ($N = 11$) and Pentagonal Pyramid ($N = 6$) respectively.

In the glass Eu^{3+} dopant short-range order has $\text{Eu} - \text{F}$ distance of 2.3 Å which agrees roughly with various EuF_3 associated crystals but those crystals show $\text{Eu} - \text{F}$ coordination number ranging from 7 to 10.5 whereas in the glass it is around 8.3, with high percentage mixture of coordination numbers 8 and 9. The shape of the bond angle distribution is similar to that of La cation that act more like a modifier in the glass matrix (see Figure 7.17). Similarly, EuF_n and LaF_n for $n = 8$ and 9 have similar rotational invariants, Q_l , result (see Figure 7.23 and 7.24). Also, the Q_l results for EuF_8 are between Biaugmented Triangular Prism, Snub Disphenoid and Gyrobifastigium reference polyhedra (see Figure 7.23). For EuF_9 polyhedra Eu^{3+} cation sites can be roughly modelled by Gyroelongated Square Pyramid and Triaugmented Triangular Prism (see Figure 7.24).

The result from connectivity (see Figure 7.18) shows that the 1% doped Eu^{3+} is more isolated than 2% in ZBLAN glasses. If the Eu^{3+} cations are not isolated than they are connected to neighbouring Eu^{3+} cations by mixture of corner and edge sharing (see Table 7.19). For good optical properties, Eu ions should be isolated and distributed homogeneously in the glass matrix. The result from Figure 7.33 illustrate that the distribution of Eu^{3+} cations in ZBLAN glasses are homogenous as the mean expected number of Eu atoms in a cubic box of length 4 Å are 3 for 1% (i.e. for 400 Eu atoms) and 6 for 2% (i.e. for 600 Eu atoms) as predicated (refer to cubic grid analysis in Chapter 5).

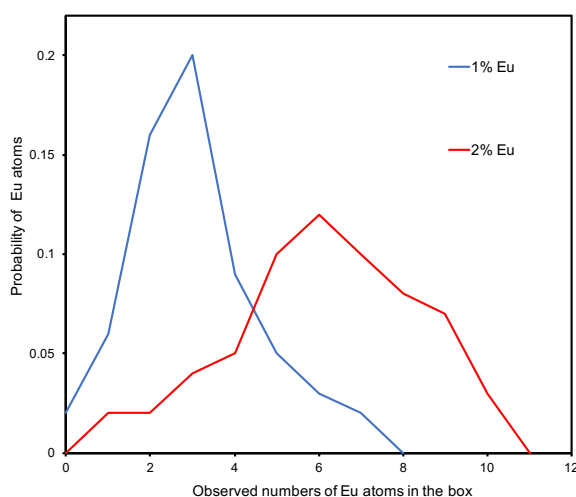


Figure 7.33 The distribution of Eu ions in box size 4 Å in ZBLAN glass models with cell length of 101.51 Å and total number of 78,600 atoms.

7.5 Conclusions

The new and large molecular dynamics models for fluorozirconate based multicomponent glasses including Eu^{3+} dopant with the box sizes ranging from 61 Å to 102 Å are presented here. The only previous multicomponent glass MD model was reported for ZBLAN doped with 2% of Eu^{3+} but it had only total numbers of 393 atoms with no comparison of diffraction data with the experiments. The new model of ZBLA and ZBLAN

glasses gave a fair agreement with experimental X-ray diffraction data. All these ZBL, ZBA, ZBN, ZBLA, ZBLAN and Eu^{3+} doped ZBLAN glasses gave the mixture of coordination numbers of 7 and 8 for Zr and mostly 10, 11 and 12 for Ba atoms. The slight change in coordination numbers seen in these glasses for higher and lower Zr:Ba ratio can be explained by the introduction of Na cations in the glass matrix which may have increased the coordination numbers for Zr and Ba cations at lower Zr:Ba ratio. The related $NaBaZr_2F_{11}$ crystal for ZBN glass also gave the mixture of 7 and 8 coordination number for Zr. Although Zr – F and Ba – F short-range order of these multicomponent glasses were similar to that of binary ‘ZB’ glasses but the change in Zr:Ba ratio did not affected the coordination numbers for ‘ZB’ glasses.

The results from the pair distribution functions, bond-angle distribution functions and network connectivity suggested that Al cations act as a network former whereas La and Na cations act more as modifiers in these multicomponent glass matrices. The Al cations in the glass very much retain its short-range order and coordination number like that of AlF_6 crystal. The rotational invariants, Q_l , analysis further suggested that cations sites for Zr and Ba are in similar to binary ‘ZB’ glasses and its related crystals.

The tiny percentage of Eu^{3+} ions as a dopant in the glass roughly retain the short-range order that of EuF_3 crystal but it gave the mixture of coordination numbers of 8 and 9 with high percentage of 8. The network connectivity result showed that Eu cations in the glass are largely isolated and rotational invariants analysis suggested that its sites are similar to La cations. The model also concluded that Eu^{3+} ions are homogenously distributed in the glasses.

7.6 References

- [1] M. Poulain, M. Poulain, J. Lucas, Verres fluores au tetrafluorure de zirconium proprietes optiques d'un verre dope au Nd^{3+} , Mater. Res. Bull. 10 (1975) 243-246.
- [2] A.A. Babitsyna, T.A. Emel'yanova, V.A. Fedorov, Glass Formation in the $\text{ZrF}_4\text{-BaF}_2\text{-LaF}_3\text{-AlF}_3\text{-NaF}$ System, Inorganic materials. 39 (2003) 981-987.
- [3] B. Phebus, B. Getman, S. Kiley, D. Rauser, M. Plesha, R.H. Terrill, Preparation and analysis of Eu^{3+} and Eu^{2+} - doped ZBLAN and ZBLALi fluorozirconate glasses, Solid State Ionics. 176 (2005) 2631-2638.
- [4] S.J. Ribeiro, R. Diniz, Y. Messaddeq, L.A. Nunes, M.A. Aegerter, Eu^{3+} and Gd^{3+} spectroscopy in fluoroindate glasses, Chemical physics letters. 220 (1994) 214-218.
- [5] A. Lecoq, M. Poulain, Lanthanum fluorozirconate glasses, J. Non Cryst. Solids. 34 (1979) 101-110.
- [6] R. Lebullenger, M. Poulain, Influence of barium substitution on the physical characteristics of ZBLA glass, J. Non Cryst. Solids. 213 (1997) 353-357.
- [7] J.M. Parker, G.N. Ainsworth, A.B. Seddon, A. Clare, The crystallisation of $\text{ZrF}_4\text{-BaF}_2\text{-NaF}$ glasses, Physics and chemistry of glasses. 27 (1986) 219-227.
- [8] J. Adam, Fluoride glass research in France: fundamentals and applications, J. Fluorine Chem. 107 (2001) 265-270.
- [9] T. Nakajima, B. Žemva, A. Tressaud, Advanced Inorganic Fluorides: Synthesis, Characterization and Applications, Elsevier, 2000.
- [10] M. Poulain, A. Soufiane, Y. Messaddeq, M.A. Aegerter, Fluoride glasses: Synthesis and properties, (2009).
- [11] V.A. Fedorov, A.A. Babitsyna, T.A. Emel'yanova, Glass Formation in the $\text{ZrF}_4\text{-LaF}_3\text{-BaF}_2\text{-NaF}$ System, Glass physics and chemistry. 27 (2001) 512-519.
- [12] A.A. Babitsyna, T.A. Emel'yanova, V.A. Fedorov, Glass Formation in the $\text{ZrF}_4\text{-BaF}_2\text{-AlF}_3\text{-NaF}$, $\text{ZrF}_4\text{-BaF}_2\text{-LaF}_3\text{-NaF}$, and $\text{ZrF}_4\text{-BaF}_2\text{-LaF}_3\text{-AlF}_3$ Systems, Inorganic materials. 38 (2002) 512-521.
- [13] V. Nazabal, M. Poulain, M. Olivier, P. Pirasteh, P. Camy, J. Doualan, S. Guy, T. Djouama, A. Boutarfaia, J. Adam, Fluoride and oxyfluoride glasses for optical applications, J. Fluorine Chem. 134 (2012) 18-23.
- [14] L. Samek, J. Wasylak, The glassy area, structure and some properties of glasses on the ZrF_4 basis, Bol.Soc.Esp.Ceram.Vidr. 29 (1990).
- [15] S. Aasland, M. Einarsrud, T. Grande, P.F. McMillan, Spectroscopic investigations of fluorozirconate glasses in the ternary systems $\text{ZrF}_4\text{-BaF}_2\text{-AF}$ (A= Na, Li), J. Phys. Chem. 100 (1996) 5457-5463.

- [16] J. Wasylak, L. Samek, Structural aspects of fluorozirconate glasses and some of their properties, *J. Non Cryst. Solids*. 129 (1991) 137-144.
- [17] M. Braglia, C. Bruschi, G. Dai, J. Kraus, S. Mosso, C. Meneghini, A. Balerna, F. Boscherini, S. Pascarelli, C. Lamberti, Local structure of Pr^{3+} in fluorozirconate glasses, *J. Non Cryst. Solids*. 256 (1999) 83-88.
- [18] M.T. Harrison, R.G. Denning, Site selective spectroscopy and molecular dynamics simulation of Eu (III) ZBLAN glasses, *J Lumin.* 69 (1996) 265-285.
- [19] M.C. Goncalves, R.M. Almeida, Influence of the modifying cations on physical properties of fluorozirconate glasses, *Mater. Res. Bull.* 31 (1996) 573-580.
- [20] V.F. Zinchenko, N.P. Efrushina, O.G. Eryomin, V.Y. Markiv, N.M. Belyavina, O.V. Mozkova, M.I. Zakharenko, Synthesis, structure and optical properties of EuF_3 film-forming material, *J. Alloys Compounds*. 347 (2002) L3.
- [21] A. Zalkin, D.H. Templeton, T.E. Hopkins, The atomic parameters in the lanthanum trifluoride structure, *Inorg. Chem.* 5 (1966) 1466-1468.
- [22] P. Daniel, A. Bulou, M. Rousseau, J. Nouet, J.L. Fourquet, M. Leblanc, R. Burriel, A study of the structural phase transitions in AlF_3 : X-ray powder diffraction, DSC and Raman scattering investigations of the lattice dynamics and phonon spectrum, *Journal of Physics: Condensed Matter*. 2 (1990) 5663-5677.
- [23] A. W. Hull, The Positions of Atoms in Metals, *Transactions of the American Institute of Electrical Engineers*. XXXVIII (1919) 1445-1466.
- [24] J.P. Laval, J.F. Gervais, L. Fournès, J. Grannec, P. Gravereau, A. Abaouz, A. Yacoubi, Cationic Distribution in $\alpha\text{-MZr}_3\text{F}_{15}$ Series (M= Y, In, Ln, Tl), *Journal of Solid State Chemistry*. 118 (1995) 389-396.
- [25] S.N. Achary, S.J. Patwe, A.K. Tyagi, Powder XRD study of $\text{Ba}_4\text{Eu}_3\text{F}_{17}$: A new anion rich fluorite related mixed fluoride, *Powder Diffraction*. 17 (2002) 225-229.
- [26] D. Zakaria, R. Mahiou, D. Avignant, M. Zahir, Single-crystal structure refinement and luminescence analysis of $\beta\text{-NaEuF}_4$, *J. Alloys Compounds*. 257 (1997) 65-68.
- [27] J.P. Laval, A. Abaouz, Crystal structure of $\text{BaNaZr}_2\text{F}_{11}$: A phase recrystallizing from fluorozirconate glasses, *Journal of Solid State Chemistry*. 101 (1992) 18-25.
- [28] Y. Gao, J. Guery, C. Jacoboni, X-ray powder structure determination of NaBaZrF_7 , *European journal of solid state and inorganic chemistry*. 29 (1992) 1285-1293.
- [29] D. Teter, Private communication, (2004).
- [30] A.K. Varshneya, *Fundamentals of Inorganic Glasses*, Elsevier, 2013.
- [31] A. Konishi, H. Izumi, R. Kanno, Y. Kawamoto, Physicochemical properties of $\text{ZrF}_4\text{-BaF}_2\text{-LnF}_3$ glasses (Ln= Y or rare-earth elements), *J. Mater. Sci.* 29 (1994) 1584-1588.

- [32] X. Zhao, S. Sakka, Properties of glasses in the ZrF₄-AlF₃-BaF₂-RF (R= Li, Na or K) system, *J. Mater. Sci.* 23 (1988) 3455-3458.
- [33] S. Aasland, T. Grande, Structure of fluorozirconate glasses and melts, *Chemical Papers.* 52 (1998) 21-28.
- [34] W.C. Hasz, C.T. Moynihan, Physical properties of ZrF₄-based glass-forming melts and glasses, *J. Non Cryst. Solids.* 140 (1992) 285-292.
- [35] R. Lebullenger, S. Benjaballah, C. Le Deit, M. Poulain, Systematic substitutions in ZBLA and ZBLAN glasses, *J. Non Cryst. Solids.* 161 (1993) 217-221.
- [36] D. Mncke, D. Ehrt, Structure and properties of mixed phosphate and fluoride glasses, *Physics and chemistry of glasses.* 46 (2005) 67-71.
- [37] A. Herrmann, D. Ehrt, Green and Red Er³⁺ Photoluminescence Behavior in Various Fluoride Glasses, *International Journal of Applied Glass Science.* 1 (2010) 341-349.
- [38] W.C. Hasz, J.H. Whang, C.T. Moynihan, Comparison of physical properties of ZrF₄- and HfF₄-based melts and glasses, *J. Non Cryst. Solids.* 161 (1993) 127-132.
- [39] Institute for Photonics, Advanced Sensing, Institute for Photonics and Advanced Sensing, *Coordinates.* 34 (2009) 138.604513.
- [40] H. Inoue, K. Soga, A. Makishima, Simulation of the optical properties of Er: ZBLAN glass, *J. Non Cryst. Solids.* 298 (2002) 270-286.
- [41] J.M. Parker, Fluoride glasses, *Annual Review of Materials Science.* 19 (1989) 21-41.

Chapter 8

Conclusions

In this thesis, atomic structures of glasses are analysed from the results of computer simulation where the classical molecular dynamics modelling technique is used. The validity of glass model was scrutinised by comparing with available experimental diffraction data and also comparing structure of short-range order with its related crystal (i.e. simulated at same conditions). Furthermore, the new method of rotational invariants was used to carefully study the structural units in the glass. Also, very large size models of alkaline earth silicate glasses were made to study immiscibility where a new grid analysis method was introduced to see the distributions of alkaline earth cations.

The models of $x(\text{BaO}) - (100 - x)\text{SiO}_2$ glass gave fair agreement with experimental diffraction data for $x = 33.3$ (both neutron and X-ray) and $x = 40$ (only neutron). In short-range order, the bond length and coordination number for *Ba* were 2.97 Å and approximately 7 respectively which was similar to $x = 50$ crystal and inconsistent with $x \leq 40$ crystals. As expected the result of rotational invariants, Q_l , for structural units of *Si* cations were extremely similar to tetrahedral geometry. A previous neutron diffraction study of $x = 40$ glass [1] was hypothesised to be evidence of “quasi-Bragg planes” in the glass structure that was not seen in the model in which there was no layer-like ordering of *Ba* cations. The $T_{\text{BaBa}}(r)$ correlation function showed smooth progression from $x = 25$ to 50, with no deviation at $x = 25$, hence the glass models indicating no phase separation in $x \leq 33.3$ glasses.

Very large size models of $25MO - 75\text{SiO}_2$ (i.e. $M = \text{Mg}, \text{Ca}$ and *Ba*) glasses were made to study the immiscibility gaps in the alkaline earth silicate systems. The new method of grid analysis was introduced to see the distribution of these alkaline earth cations. Addi-

tionally, very large size models of $50MO - 50SiO_2$ glasses were made, in order to understand the distribution of alkaline earth cations in comparison to Poisson and binominal random distributions. The distribution of alkaline earth cations in $50MO - 50SiO_2$ glasses were described by the binominal random distributions (i.e. homogenously distributed). In the case of $25MO - 75SiO_2$ glasses the distribution of alkaline earth cations of these low M contents were approximated by Poisson distribution where Ba and Ca were similar to random distributions. However, the distribution of Mg was wider than the Poisson distribution indicating immiscibility gap in $25MO - 75SiO_2$ glasses.

One of the interesting reasons to model binary barium fluorozirconate ‘ ZB ’ glass was to carefully study its structure because it does not follow the general Zachariasen rules for glass formation. Models of $xZrF_4 - (100 - x)BaF_2$ glasses gave fair agreement with X-ray diffraction for $x = 50$ and $x = 67$ and with neutron diffraction data for $x = 60, 67$ and 75 glasses. From the theory of random close packing bonding criteria, it is expected that a large ionic radius ratio and large values of coordination number will have more than one type of polyhedra structural units which was seen in the case of ‘ ZB ’ binary glasses for both ZrF_n and BaF_n .

In the models of ‘ ZB ’ glasses the coordination number of Zr was a mixture of 7 and 8 which was seen in the $x = 50$ crystal. From the $T_{ZrZr}(r)$ correlation functions of $x = 50$ and 67 crystals showed that there was significantly more edge sharing in crystals than glasses. In a previous study [2], it was reported that the ZrF_7 structural unit in the $x = 67$ crystal was similar to Pentagonal Dipyramid polyhedra and suggested that this structural unit was compactly preserved in glass and that this may be the reason ‘ ZB ’ glasses have higher densities than its related crystals (unlike oxide glasses). The rotational invariants analysis (Q_l values) showed otherwise, as the crystals have structural units which are similar to Augmented Triangular Prism and interestingly the glasses have structural units which are much closer to Augmented Triangular Prism than in related crystals. Also, previous MD structural

studies of glass [3] suggested that ZrF_8 structural units are similar to Snub Disphenoid polyhedra but the rotational invariants analysis suggested they are similar to Biagumented Triangular Prism. In glasses Ba has $CN \geq 10$ which leads to a less well-defined coordination polyhedra which was shown when its Q_l values were compared with reference convex polyhedra.

The large multicomponent glass matrix of Eu^{3+} doped $ZBLAN$ glass was modelled as it was heavily studied for optical applications. Initially the new large models for ZBL , ZBA , ZBN , $ZBLA$ and $ZBLAN$ glasses were made to check for any structural changes in ZrF_n and BaF_n polyhedra. The short-range order of Zr and Ba in these complex glasses was similar to that of binary ‘ ZB ’ glasses but there was slight change in coordination numbers seen between higher and lower $Zr:Ba$ ratio (although the change in $Zr:Ba$ ratio did not affect binary ‘ ZB ’ glasses). Also, the ZBN glass is seen to have short-range order similar to its related $NaBaZr_2F_{11}$ crystal with a mixture of CN for Zr .

From the pair distribution functions, bond angle distribution functions and network connectivity for models of $ZBLAN$ glasses it can be established that Al acts as a network former that has octahedra structural units whereas La and Na behave like modifiers in the glass with the mixture of coordination numbers 8 and 9 for La and coordination numbers of 6 and 7 for Na cations. Doped Eu atoms have short-range $Eu - F$ distance of 2.33 Å that roughly agrees with the EuF_3 and related crystals and have mixture of coordination numbers 8 and 9 but predominantly coordination number of 8. The connectivity results show that Eu atoms are isolated from each other and grid analysis shows they are uniformly distributed in the glass.

In the future work, it could be good to do more modelling of binary $BaO - SiO_2$ glasses this is to compare with phase separation found in experiments (e.g. [3]) because the results from the present $BaO - SiO_2$ glass models did not show any phase separation. The grid analysis used here to see the distribution of single alkaline earth cations (such as Mg ,

Ca, and *Ba*) can be applied to alkali cations such (e.g. *Na*) and to multicomponent silicates glasses that have more than one modifier. It would be interesting to look at the distribution of mixed modifiers compared to the single modifier cations studied in the present work.

The results of the bond angle distribution functions (BAD) of glasses based on barium fluorozirconate can be directly compared with the bond angle distribution of reference polyhedra. However, here only the glass structural units of ZrF_7 and ZrF_8 polyhedra were directly compared with all the reference polyhedra of vertices 7 and 8. Further such analysis might help to give a clearer understanding between rotational invariants, Q_l , and more general method of BAD in regards to identifying the glass structural units. Furthermore the Q_l values depend on symmetry and interaction between cations and anions. The reference polyhedra have symmetrical faces, e.g. equilateral triangles, similar to those in crystals. Glass has similar interactions to crystals but does not have well-defined symmetry, and the polyhedra have distorted faces, e.g. non-equilateral triangles. The software used in this project is only able to calculate the average shape of polyhedra from the model, and rotational invariants analysis might be improved by also calculating the distortion of the polyhedra faces.

In order that the large models of *ZBLAN* glasses including *Eu* doped results presented in this thesis can be rigorously compared and complimented one can perform experiments (e.g. diffraction) on *ZBLAN* glasses to have a better atomic structural understanding of these glasses.

8.1 References

- [1] L. Cormier, P.H. Gaskell, S. Creux, Comparison of the low-Q features in diffraction data for silicate glasses and crystals containing Sr or Ba, *J. Non Cryst. Solids*. 248 (1999) 84-91.
- [2] J.P. Laval, B. Frit, J. Lucas, Crystal structure of the β -BaZr₂F₁₀ compound. Relations with the ReO₃-type and the fluorozirconate glasses, *Journal of Solid State Chemistry*. 72 (1988) 181-192.
- [3] Y. Kawamoto, T. Horisaka, K. Hirao, N. Soga, A molecular dynamics study of barium meta-fluorozirconate glass, *J. Chem. Phys.* 83 (1985) 2398-2404.

-
- [4] E.D. Zanotto, P.F. James, A.F. Craievich, The effects of amorphous phase separation on crystal nucleation kinetics in BaO-SiO₂ glasses, *J. Mater. Sci.* 21 (1986) 3050-3064.